Stimulated Brillouin Scattering in Integrated Circuits: Platforms and Applications

A thesis submitted in fulfillment of the requirements for the degree of Doctor of Philosophy

By:
Blair Morrison

in the

School of Physics
The University of Sydney

2018

Declaration of Authorship

I, Blair Morrison, declare that this thesis titled, "Stimulated Brillouin Scattering in Integrated Circuits: Platforms and Applications" and the work presented in it are my own. To the best of my knowledge, this thesis contains no copy or paraphrase of work published by another person, except where duly acknowledged in the text. This thesis contains no material that has been previously presented for a degree at the University of Sydney or any other university.

— Blair Morrison

Abstract

Coherent interactions between light and sound have been of significant interest since the invention of the laser. Stimulated Brillouin scattering (SBS) is a type of coherent interaction where light is scattered from optically generated acoustic waves. SBS is a powerful tool for optical and microwave signal processing, with applications ranging from telecommunications and Radar, to spatial sensing and microscopy. Over the last decade there has been increasing interest in the investigation of Brillouin scattering at device scales smaller than the wavelength of light. New interactions with the waveguide boundaries in these systems are capable of altering the strength of SBS, from complete suppression to orders of magnitude increases. The landmark demonstration of Brillouin scattering in planar waveguides, just six years ago, represents a new frontier for this field.

This work explores the effective generation and harnessing of stimulated Brillouin scattering within modern photonic circuits. After establishing the foundations of linear and nonlinear optical circuits, we investigate the Brillouin processes available in multimode waveguides. We experimentally demonstrate giant Brillouin amplification using spiral waveguides consisting of soft-glass materials. We then integrate this soft-glass onto the standard platform for photonic circuits, silicon on insulator, without any reduction in performance. We apply these advanced devices to the field of microwave photonics and create high suppression microwave filters with functionality far beyond traditional electronic circuits.

This thesis is a significant step towards Brillouin enabled integrated photonic processors.

Acknowledgements

Throughout my PhD, and even before that, I have been incredibly fortunate to interact with and be supported by so many amazing people. It is hard to truly grasp or put into words the chances and opportunities that have enabled me to reach this position. To all of those who have helped along the way: I want to thank you for changing my life and know that I appreciate every interaction we have had. If you do not receive a mention below, please chalk it up to my softening memory of former times (it has been awhile!), rather than any form of slight.

I will start by thanking my supervisor, Prof. Benjamin J. Eggleton, for providing both the opportunity to work within your group and support along the way. Working within the CUDOS Sydney group has been a truly transformative experience for me, and I want to thank you for bringing together such a talented and amazing group of researchers and students, for providing funding for the many facilities and equipment I used, and for the multitude of opportunities to travel and speak at international conferences. I greatly appreciate your attention to detail for public speaking, including the time devoted to all the presentation practice sessions, and the importance of story and detail in scientific work. These are skills which I will value for the rest of my career. The many successes of the students you have supervised in Sydney are a testament to your prowess as a supervisor. I will miss our frequent (though sometimes heated) discussions around technical points and the unexpected, but always relevant, personal anecdotes.

My deepest thanks belong to my associate supervisor David Marpaung, without whose steady head and rational discussions I would have abandoned my PhD on more than one occasion. For this I will forever owe you a great debt. In technical, professional and even social aspects, you have been an incredible role model, and I am still in awe of your writing ability and complete mastery of the academic literature. You are incredibly selfless, giving over as much of your time as necessary to the discussion and teaching of differing technical points while supporting your young family. I will forever count myself very lucky to have been one of you students; it is not possible to find a better associate supervisor. Thank you, David.

My considerable thanks go to Alvaro-Casas Bedoya, my unofficial associate supervisor, who introduced me to Silicon photonics and integrated optics design. Thank you for providing continued optimism and energy, at times even in the face of my determined negativity! Additionally, thank you for the many things you did for the group during my time there, such as organising the imec fabrication runs, teaching me ipkiss, facilitating our external collaborations and being great to work with in the lab. Many of my successes are due to your kind assistance, I hope that you achieve all that you wish in your further career.

I also want to thank the other amazing post-docs in the SBS group at USyd. Ravi Pant, for introducing me to Brillouin scattering and teaching me so much in the early days in lab, such as chip coupling, and also providing the base results through which the SBS group was formed; Irina Kabakova, a guiding presence in my early group meetings; Amol Choudhary and Birgit Stiller, thank you both for being amazing people to work with every day. The last three years went so quickly with your helpful discussions, assistance and understanding on equipment sharing and supporting the group. I have found your tireless efforts, high quality papers and presentations and technical knowledge a continued inspiration.

During my time in CUDOS I shared many varied experiences with a multitude of students. Having worked in five different offices meant that I was fortunate to make friends with many awesome office mates. To those that did not make it to the end of the PhD grind at CUDOS: Rachel, Andrew, Iman, Steph and El-Abed, thanks for the shared experiences and I wish you all the best of luck.

To the ”first wave” of submissions: Yvan Paquot, for sharing an oversized cocktail at my first conference; Tomonori Hu, for being a continued inspiration, great presenter and amazing leader; Young ”jeeeeesus” Zhang, for being an impressive experimentalist and thinker and for all the help and advice over the years; Neetesh Singh, for being a determined worker, for teaching me some COMSOL tricks and for being the most honest person I have met; Jiakun He, thanks for always lighting up the office and congrats on your great job; Fernando Diaz: the best BBQer on the south side of the harbour, thanks for being second best at bin basketball, taking care of my rabbits more than once, and being a very practical researcher: I miss you mate! A special shout-out to Matt Collins, thanks for the good advice, awesome chats and even better sneaky lunch beers.

To the ”’Tijn” crew and peak officemates: Scott ”Frownface” Brownless, thanks for being the most reliable Thai Train parter and hooking me up with LaTeX tricks; Caitlin Fischer, for being the best OSA student chapter vice-president I have known, a good friend, dropping some amazing burns, and also for rabbits-sitting duties; and Björn Sturmberg, for our many conversations, getting me hooked on Inkscape alignment and general coding tips, and constantly raising the bar: we'll see you in Hobart, one day. To the final CUDOS students: Bruce Zhang, thanks for your equipment loans, incessant office sleeping and deadpan humour: I'm glad we've never played poker; and to Loris Marini, thanks for somehow both pushing me further and keeping me grounded, for the fresh pasta and espresso martinis, constant support, and all the conversations still to come.

A shoutout to my fellow students from the SBS group, it was so amazing to work with you all. To the visiting students: Kai, Hengyun, Victor, Julia and Kevin; thanks for enriching our office. To Luke McKay, for stepping up in the student chapter, I am sorry I did not have the time to get to know you better. Thomas Büttner, thanks for the awesome discussions and Tuesday Flodge sessions. To Yang Liu, for turning average ideas into great ones and being the hardest person to convince. Atiyeh Zarifi, for never giving up nor hesitating to tell me to shut-up. Iman Aryanfar, for only blowing up some of the components and making the broadest notch filters since 2013 - congratulations on finishing mate and best of luck in the future. A special shoutout to Moritz Merklein, for taking a bullet on the invited talks and winning all the prizes. Jokes aside, Moritz, you are the best presenter I have seen and an even better researcher. I count myself lucky to have done my PhD with you. An extra special thanks to Mattia Pagani, my nonlinear integrated microwave photonics partner in crime. Thanks for making the first years of my PhD so enjoyable with your wry humour, enduring the CUDOS showcase with a grin and letting me always be right. If I had even half the capacity and expertise you do my PhD would have only taken three years. Working with you was a constant pleasure and I have no doubt you will continue to succeed in your chosen career.

To all of the students, thank you for the Atom Thai lunches and even better Campos coffee sessions! Thanks also to Owen Brasier, a former CUDOSer, for getting in on the lunch antics over the many years, providing more than your fair share of amazing conversations, and being so awesome during the Vivid festival. Atom Thai - thank you for providing delicious affordable food so close to campus, and a special thank you to Campos, shout out to Dan, for making me realise that coffee is actually awesome and fuelling my academic output for many years.

While staring into my bleak americano in the Nothern Hemisphere I still dream about your creamy affogatos and crisp espresso.

My PhD would not have been possible without the amazing collaborators which I dealt with day in and day out. To the ANU chalcogenide fabrication team of Khu Vu, Duk-Yong Choi and Steve Madden, thank you for the hundreds of emails and calls, and always persevering beyond the frustrations inherent in the fabrication process. To the RMIT team of Guanghui Ren, Thach Nguyen and Arnan Mitchell, thank you for pushing the envelope for rapid prototyping. To our theory collaborators in UTS and Macquarie, Christian Wolff, Mikolaj Schmidt, Kokou Dossou, Mike Smith, Christopher Poulton and Mike Steel, thank you for providing a solid basis for discussions and travelling to USyd for our group meetings. A special shout-out, again, to Björn Sturmberg, for joining the SBS side and implementing Numbat: it was great to be able to extend our Thai lunches after you finished as a student. Also to Daniel Dolfi, Stephanie Molin and all the team in the opto-electronics group at the Thales-TRT in Palaiseau France, thank you for hosting me in 2015 and enriching my PhD more than I could have hoped to expect. I still regret not succeeding with the planned experiments.

I want to thank all of the other post-docs and researchers in CUDOS at Sydney, for assisting me with discussions, equipment sharing and especially guiding the experience at conferences: Alex Clarke, Alex Judge, Chad Husko, Jochen Schröder, Simon Lefrancois, Joel Carpenter, Elias Giacoumidis, Trung Vo, Alessandro Tuniz, Andrea Blanco-Redondo, Allessio Stefani and Darren Hudson. Thanks also to the senior researchers and Profs: Mark Pelusi, Boris Kuhlmey, Stefano Palomba, Simon Flemming and Martijn De Sterke.

A thank you to the CUDOS lab staff for your support and assistance: Enbang Li, Joseph Zheng and Shayan Sahnia. An extra special thanks to Eric Mägi, our lab manager extraordinaire, for his herculean effort over the years in supporting so many of the experiments, general lab and ordering support and working with the various filter prototypes. Eric, I enjoyed every one of our discussions and your incredibly broad technical knowledge was a key enabler in many experiments. I still incredibly impressed that a prototype was taken overseas and worked with such success.

A special thank you to the admin team of CUDOS, in particular Vera Brinkel, Silke Weiss and Simone Kingston. Thank you for making the daily pain of university bureaucracy a much more manageable experience. A special thank you to Shelley Martin for always fighting for the students, promoting the group and organising the amazing CUDOS workshops every year. I also want to thank the admin and support staff of the School of Physics and, in particular Alexis George, Cynthia Kiu and David Beech, and the head of school Tim Bedding.

Even before I started my PhD I was incredibly lucky to be supported in my interest of physics. Thanks to all the teachers from Uki Primary and Mt St Patricks College, in particular Mark Hoy for sacrificing his Tuesday afternoons to teach Extension maths and Narelle Sherrah for creating such an amazing environment with accelerated science program. Special thanks to my original bus driver, Matt Prior, for his inquisitive discussions and music taste. I also want to thank my undergraduate supervisors, David McClelland and Jong Chow, for fostering my research experience and suggesting the Sydney CUDOS group as place for a valuable PhD experience. An additional thanks go to the Australian Government, for funding my education and PhD scholarship. It is incredibly lucky to live in a country where growing up outside of a small town does not prevent you from reaching the highest quality education institutions.

Thank you to all my friends, in particular: Tim and Lisa, for showing what the light looks like at the end of the tunnel, and for strategy boardgames; Pat and Vicky, for providing welcome distractions, health(y) discussions, and gin nights; the Brig Crew: Tim, Christopher, Yasin, Dan and Steve, thanks for Tequila Sixes, Brigalow Fridays, Mattress Couch and for never being the Big Bang Theory; and Christopher, again, for cocktail shenanigans, intense conversations, amazing food, and always proving that knowledge and the pursuit of it is invaluable. Thanks for always being both interested and interesting.

And with so many people already thanked I shall close with the most important people of all, my family. I want to thank everyone in my family: my parents, siblings, nieces and nephews, aunts and uncles and grandparents. All of of you have provided me tremendous support and inspiration. To be able to move freely around with the world with only positivity and no expectations, has made everything I had to do easier on the way. I know that I do not communicate often enough, but I miss you all constantly. I hope that I have made you proud, and inspired some of you to. I would also like to thank the Blackburn family for welcoming me so kindly into their midst, for supporting me throughout this journey, and for humouring my physics-related lectures.

Finally to Jess, the love of my life. Thank you for always being interested in my work and assisting with my poor English grammar. Thank you for making every day special, putting up with my odd behaviour and choosing to share your life with me. I would not have made it through this journey without you, and I hope I can pay back the many weekends and evenings with amazing experiences in the next phase of our lives.

Original Works and Contributions Presented in this Thesis

The following outlines the original works in this thesis and the contributions of authors for the published works. The thesis author has been bolded for clarity.

Chapter 6

Sections: 6.2 - 6.4 **B. Morrison**, A. Casas-Bedoya, G. Ren, K. Vu, Y. Liu, A. Zarifi, T. G. Nguyen, D–Y. Choi, D. Marpaung, S. J. Madden, A. Mitchell, B. J. Eggleton, "Compact Brillouin devices through hybrid integration on silicon", Optica **4**, 847 (2017)

B. M. designed and performed mask layout for the As_2S_3 structures. A. C–B. prepared mask layout for base Si chip. G. R., K. V., T. G. N. and D–Y. C. fabricated the As_2S_3 structure. B. M. performed the experimental measurements, with assistance from A. C–B. and Y. L. Helpful discussions were provided by D. M., A. C–B., A. Z., Y. L. and B. J. E. The project was supervised by S. J. M., A. M. and B. J. E. The manuscript was prepared by B. M. with contributions from all authors.

Chapter 7

Section: 7.2 **B. Morrison**, Y. Zhang, M. Pagani, B. J. Eggleton, D. Marpaung, "Four-wave mixing and nonlinear losses in thick silicon waveguides", Optics Letters **41**, 2418 (2016)

B. M. performed the experiment. Split-step simulations were performed by Y. Z. Helpful discussions were provided by M. P., D. M. and B. J. E. The project was supervised by D. M. and B. J. E. The manuscript was prepared by B. M. with contributions from all authors.

Chapter 8

Section: 8.2 **B. Morrison**, D. Marpaung, R. Pant, E. Li, D-Y. Choi, S. Madden, B. Luther-Davies, B. J. Eggleton, "Tunable microwave photonic notch filter using on-chip stimulated Brillouin scattering", Optics Communications **313**, 85-89 (2014)

B. M., D. M and R. P. performed the experiments. D–Y. C. and S. J. M. fabricated the samples. D. M., B. L. D and B. J. E supervised the project. D. M., B. M. and R. P. prepared the manuscript with contributions from all authors.

Section: 8.3 D. Marpaung, **B. Morrison**, R. Pant, B. J. Eggleton, "Frequency agile microwave photonic notch filter with anomalously high stopband rejection", Optics Letters **38**, 4300 (2013)

B. M., D. M and R. P. performed the experiments. B. J. E. supervised the project. D. M. prepared the manuscript with contributions from all authors.

Section: 8.4 D. Marpaung, **B. Morrison**, M. Pagani, R. Pant, D-Y. Choi, B. Luther-Davies, S. Madden, B. J. Eggleton "Low-power, chip-based stimulated Brillouin scattering microwave photonic filter with ultrahigh selectivity", Optica **2**, 76 (2015)

B. M and M. P performed the experiments with assistance from D. M. and R. P. Fabrication was performed by D–Y. C. and S. J. M. The project was supervised by D. M. and B. J. E. The manuscript was prepared by D. M. with contributions from all authors.

Chapter 9

Section: 9.2 A. Casas-Bedoya, **B. Morrison**, M. Pagani, D. Marpaung, B. J. Eggleton, "Tunable narrowband microwave photonic filter created by stimulated Brillouin scattering from a silicon nanowire", Optics Letters **40**, 4154 (2015)

A. C–B., B. M and M. P performed the experiments. A. C–B. performed additional fabrication steps on the sample. D. M, B. M and M. P. provided useful discussion. B. J. E supervised the project. A. C–B. prepared the manuscript with contributions from all authors.

Section: 9.3 D. Marpaung, **B. Morrison**, R. Pant, C. Roeloffzen, M. Hoekman, R. Heideman, B. J. Eggleton, "Si_3N_4 ring resonator-based microwave photonic notch filter with an ultrahigh peak rejection", Optics Express **21**, 23286 (2013)

B. M. performed the experiments. C. R, A. L., M. H. and R. H. fabricated the samples. R. P. provided useful discussions. B. J. E supervised the project. D. M. prepared the manuscript with contributions from all authors.

Supervisor Attestment

As supervisor for the candidature upon which this thesis is based, I can confirm that the authorship attribution statements above are correct.

Benjamin J. Eggleton 31/08/2018

Contents

Chapter 1

Introduction

The interaction of light and sound has been of interest to scientists for more than a century. If two counterpropagating beams of light pass through a material, separated in frequency by twice the speed of sound divided by the optical wavelength, an acoustic wave will be coherently generated. This acoustic wave will backscatter the higher energy light beam and Doppler shift its frequency, like a moving optical grating, to precisely that of the lower energy light wave. This phenomenon is known as stimulated Brillouin scattering (SBS), and it was one of the first optical nonlinear effects measured upon the invention of the laser.

After the first studies of SBS in optical fibers more than 50 years ago it was promptly identified as a nuisance; a fundamental issue to be avoided at all costs in optical communications systems. This sentiment was reinforced through further publications at the time and is certainly still held by many in telecommunications research. However, in the past decade Brillouin scattering has been repeatedly demonstrated as a flexible and powerful tool for optical and microwave signal processing. Among the many intriguing applications of SBS are a few oddities, such as the capability to spectrally purify optical waves and the ability to coherently store light as sound.

Following these developments, there has been a renewed interest from researchers into optical devices in which Brillouin scattering can be effectively harnessed. Progress in the field has accelerated since the first demonstration of SBS in planar waveguides in 2011. These highly nonlinear planar waveguides were used in a number of demonstrations, performing functionalities previously restricted to systems using kilometres of optical fiber. At the same time theoretical results indicated that, in certain materials and geometries, new interactions generated at the waveguide boundaries could greatly increase the strength of the Brillouin processes.

Objective and Outline

This thesis is devoted to an exploration of Brillouin processes in modern photonic circuits, investigating materials, devices and applications. The body of work in this thesis was performed in the context of two driving questions:

1. How can we generate strong Brillouin interactions in photonic circuits?

2. Can we utilise on-chip SBS to create high performance integrated microwave photonic processors?

To address these questions we have to understand concepts from three fields of photonics: nonlinear optics, integrated optics and microwave photonics. The thesis has been designed to a be a reference material for future researchers and students interested in these fields and the structure has been prepared accordingly. The content is organised into ten chapters, formed within 3 main parts, and has the following structure:

Part I: Background and Theory In Part I of the thesis we provide the background and theory which enables an understanding of the concepts presented throughout the rest of the thesis. This is commenced with a thorough historical overview of Brillouin scattering in Chapter 2. This overview explores the early experimental works of the 20th century, the changes with the development of the laser and optical fibers, and also describes modern devices and the current state of the art of Brillouin scattering in waveguides and resonators.

Chapter 3 presents the material required for the understanding and development of nonlinear photonic circuits. To build an intuition this chapter starts with the theory of simple slab waveguides and nonlinear optics. The second section focuses on the optimal ways in which to design nonlinear photonic circuits in current photonic platforms, and highlights issues which arise in circuits designed for linear and nonlinear purposes. The chapter finishes with an overview of the current photonic foundries open to academic users.

In the final chapter of Part I, we explore the theory of Brillouin scattering in waveguides. Chapter 4 begins by describing the physical mechanisms behind Brillouin scattering in bulk materials, and the phase matching of SBS in such devices. This leads into the markedly different regime of waveguides, and how additional Brillouin processes exist in guided wave devices, due to the altered acoustic mode families in acoustic waveguides. We describe the phase-matching and dynamics of the different Brillouin processes and close with a discussion on how to calculate the gain coefficient, correctly incorporating the vectorial nature of the interacting fields and additional forces which arise due to boundary interactions.

Part II: Brillouin Scattering in Circuits In Part II we move beyond theory and shift our focus to generating large Brillouin interactions in photonic circuits. In Chapter 5 we demonstrate greater than 50 dB of Brillouin amplification in soft-glass chalcogenide waveguides. This demonstration was built upon an understanding of the importance of acoustic confinement and geometry choice, and improvements to fabrication processes. We provide measurements for multiple different device systems and describe the development of these circuits over the course of multiple years. The material also covers previous results in chalcogenide fibers, different methods of measuring Brillouin scattering parameters and the fabrication process of soft-glass waveguides.

Chalcogenide glasses are highly suitable materials for generating Brillouin interactions, but they not capable of front-end photonic integration. In Chapter 6, the key work in this thesis, we demonstrate the hybrid integration of As_2S_3 glass with an silicon on insulator (SOI) circuit obtained from imec. This demonstration required the adoption of a number of strategies discussed in Chapter 3, in particular the use of adiabatic bends in the heavily multimode waveguides. This hybrid integration enabled a Brillouin amplification of more than 20 dB in a silicon-based chip, utilising a compact spiral confined in less than a single mm^2. In this work we also demonstrate Brillouin lasing for the first time in a planar circuit.

In the search for alternative platforms for Brillouin scattering, in Chapter 7 we investigate 3 µm thick silicon waveguides available from VTT. While no Brillouin scattering was observed in these circuits, we found that the linear performance of the devices was very high. The long effective interaction lengths from the low loss waveguides enabled the generation of idler waves through Kerr four wave mixing.

Part III: Microwave Notch Filters using Photonic Devices The final Part of the thesis focuses on an application of Brillouin scattering: microwave signal processing. In particular we investigate the creation of high suppression microwave notch filters using integrated devices, in particular on-chip SBS. The start of Chapter 8 provides an overview of microwave photonics, and the simple operation of optical modulation and detection. We then describe integrated microwave photonic devices and key parameters for radio frequency notch filters. The chapter then shifts to experimental and published work on microwave filters using Brillouin scattering. We introduce a new technique for achieving high suppression cancellation based notch filters, and apply this technique with our soft-glass waveguides. The obtained results posses an impressive combination of high suppression and frequency tunability, while operating with very narrow linewidths. In Chapter 9 we explore the benefits of the cancellation technique in other photonic circuit technologies, using forward Brillouin scattering in an SOI circuit and a ring resonator in an Si_3N_4 device.

Finally, Chapter 10 provides a summary of the key results in the thesis, a perspective of future opportunities and possible new materials, and an outlook on future applications and devices utilising Brillouin scattering in photonic circuits.

Part I

Background and Theory

Chapter 2

Historical Overview of Brillouin Scattering

A tremendous amount of research has gone into the topic of Brillouin scattering over the past century. In this overview we will focus on the key results in early literature leading up to ″modern″ devices demonstrated within the past 10 years. Particular attention will be given to works which significantly improved understanding at the time and early experimental observations of different systems. This overview is split into 4 main sections

- The context and origins of Brillouin scattering theory and early experimental work.
- The advent of stimulated scattering processes, following the availability of the laser.
- Brillouin scattering in early optical fibers.
- Brillouin scattering in modern devices and the current state of the art.

The chapter concludes with a list of historic, and more recent, review papers which may be of use to readers interested in these topics.

2.1 Origins of Brillouin Scattering

At the turn of the 20th century there was a significant interest in the interaction and scattering of light with different materials. From the 1880s to 1900 Lord Rayleigh published a number of articles describing the scattering of light from particles much smaller than the wavelength, in an effort to describe the origin of the blue colour of the sky [1]. In this way he corrected understanding at the time by showing that the intensity of the *elastically* scattered light scaled following λ^{-4} i.e the intensity of scattered blue light is 16 times that of red. He later showed that this scattering originates from the individual molecules making up the atmosphere themselves (and summed for the total number of molecules), rather than considering some foreign particles embedded in a material such as a solid or liquid [2].

The idea that the scattering Rayleigh described could occur from individual molecules, which meant that the scattering sources would act independently from each other, was quite surprising at the time. In 1919, the year of Rayleigh's passing, J. Larmor published "*The principle of molecular scattering of radiation*" in which he discussed implications of Rayleigh's work [3]. He states that:

> The condition necessary for this independence is that the disturbances (such as strain, velocity) must arrive from the scattering particles in phases which are entirely uncorrelated...

Finding a lack of correlation unlikely, due to the sheer number of particles in close proximity, Larmor instead considers the effects on the scattering process if the motions of some of the particles are indeed correlated to some degree. Larmor expected that there should be a component of scattering due to these fluctuations, which will have a small Doppler shift due to the motion of the particles.

The work of Larmor consisted purely of postulations and no analysis, no descriptions of any magnitude of this possible Doppler shift were given. In 1922, C. Raman addressed this point in his work "*Optical Observation of the Thermal Agitation of the Atoms in Crystals*" published in *Nature* [4]. He considers the theory of Debye [5], based on earlier work by Einstein [6], which details that:

> the thermal energy of a solid is made of elastic vibrations in its material, the frequencies of such vibrations ranging from very small values up to a maximum limit determined by the ultimate molecular or atomic structure

This would mean that even an optically transparent material, free from defects or impurities, could not be considered "homogeneous" due to these elastic vibrations. It then follows, according to Raman, that light traversing the medium would be deviated and appear as scattered light, with the intensity of the scattering being related to the "thermal agitation" of the crystal. Raman makes an argument based on the Einstein relation (or Einstein-Smoluchowski formula) for the intensity of the scattering and concludes that transparent quartz should observe 10 times as much scattering as dust free air. Though no images or measurements are provided, Raman also states that he had observed such scattering in his laboratory.

2.1.1 Interlude: Discovery of Raman Scattering

As well as a focus on the scattering from acoustic waves within a media, Raman was interested in scattering from individual molecules, inspired in particular by the work of Rayleigh. Experimental work commenced in this area in 1922 and early on Raman's group observed an effect which they termed "weak fluorescence". Highly focused sunlight was spectrally filtered and passed through a material, typically a very pure (>10 distillations) liquid, with the transmitted and scattered light measured spectroscopically [7]. A thorough cataloguing of more than 60 liquids showed the uniformity of this effect, though the strength of the effect varied between materials. Work in this area stalled for a few years, until 1928 when Raman realised that he may in fact be observing an optical analogue of Compton scattering, the inelastic scattering of light from electrons, and not fluorescence at all. Experiments then recommenced with K. Krishnan, the student who performed the earlier study, and the idea was supported by the fact that the scattered light was highly polarised, to a similar degree of the transmitted light, whereas typical fluorescence is unpolarised. These observations lead Raman to publish the paper "*A New Type of Secondary Radiation*",a brief letter, dated February 16th 1928 [8].

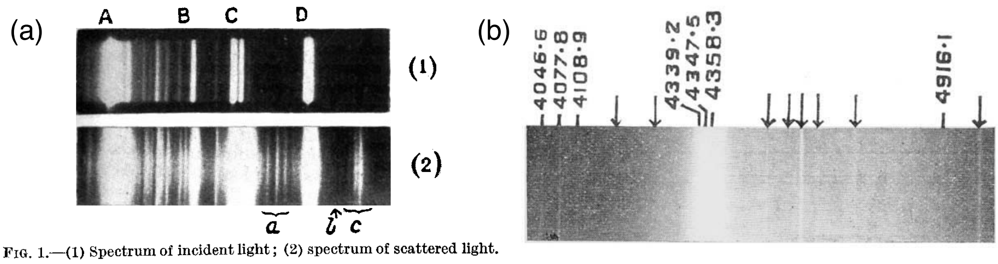

Figure 2.1: Experimental measurements of Raman scattering from two of Raman's *Nature* papers (a) [9] and (b) [10].

Work progressed very rapidly over the coming months. However an issue with the previous measurements was the poor spectral resolution of the source light from filtered sunlight. A setup similar to that of Woods, using the emission lines of an intense mercury lamp, improved the measurements greatly, allowing for the magnitude of the spectral shift to be observed [11]. This work was definitively confirmed in the paper "*The Optical Analogue of the Compton Effect*" by Raman, dated the 22nd March. The scattered light was clearly observable, as shown in Figure 2.1, and accurate measurements of the shift could now be taken [9]. This flurry of *Nature* publications was concluded in the paper, quite dramatically titled, "*The Negative Absorption of Radiation*", dated the 15th May [10]. In this work they identify a number of lines with sufficient accuracy, and find that the frequency spacing of these lines from the pump source matches the infrared absorption lines of the measured material (i.e molecular properties). What is even more remarkable is that they identify lines of higher frequency than the pump source, and associate these lines with emission from high energy states. The relative intensity of the higher frequency lines matches somewhat to the expected population of the molecular states at room temperature, as determined from standard thermodynamic arguments.

This flurry of results generated an incredible focus of this effect, soon confirmed by a number of different groups, with more than 60 papers published in 1928 on this topic alone [12]. For this body of work Raman received the Nobel Prize in 1930, somewhat contentiously [13], and Raman scattering has become one of the most ubiquitous measurement techniques in modern material science. For interested readers we have provided a number of references of perspectives, written throughout the 20th century, from different groups which worked on this topic [12, 14, 15]. Significant work investigating this form of scattering was also occurring in Russia at the time, for which a detailed overview can be found in the work of Fabelinskii [16].

2.1.2 Early Acoustic Scattering: Developing Understanding and Remarkable Experiments

Léon Brillouin also investigated the problem of light scattering from *acoustic* waves. Brillouin followed a similar approach to Raman's 1922 theory paper, considering the earlier work of Debye and Einstein, and applied his derived approach to the possible sources of inelastic scattering of X-rays [17]. Acting independently of Raman's work, Brillouin provided a more thorough analysis of the expected scattering effect and the analysis was based on two main ideas

- For a primary light ray $\vec{S_0}$, and a scattered ray $\vec{S}$, only sound waves travelling in the direction of the vector $\vec{s} = \vec{S} - \vec{S_0}$ are important for scattering
- Of the sound waves satisfying this condition, only waves with a wavelength $\Lambda = \lambda/s$ will contribute to scattering, where λ is the wavelength of the primary ray and s is the length of the vector $\vec{s}$.

The second condition is akin to satisfying the Bragg condition for constructive interference from a typical optical grating. The sound wave moves at the speed of sound in the medium, v_{ac}, and could be going in either direction, $+\vec{s}$ or $-\vec{s}$. The frequency of the scattered light will thus be shifted, according to the Doppler effect, and the scattered light will occur at two frequencies around the input frequency v_0.

$$v = v_0 \left[1 \pm 2\, n \frac{v_{\mathrm{ac}}}{c} \sin(\theta/2)\right] \tag{2.1}$$

where c is the speed of light in vacuum, θ is the angle between $\vec{S_0}$ and $\vec{S}$ and n is the refractive index of the scattering medium. On the basis of this work, the inelastic scattering of light from thermal acoustic waves is thus referred to as Brillouin scattering in the literature.

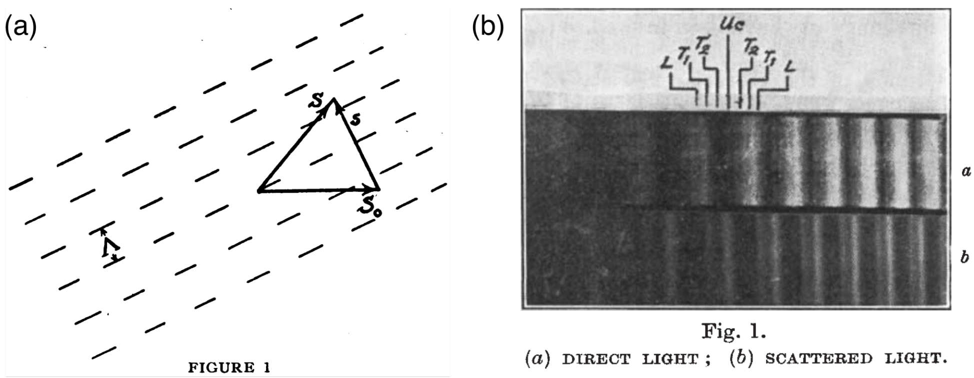

Figure 2.2: (a) Diagram explaining conditions for SBS in bulk media from the work of Debye [18] (b) Photograph of spectrographic measurements of SBS by Raman in quartz crystal [19].

Experimental demonstrations of Brillouin scattering were very difficult in the early 1900s due to the strict equipment requirements. Typical Brillouin shifts are on the order of 10 GHz to 50 GHz, very close to pump sources, putting stringent requirements on optical spectrometers and possible requirements for filters that remove non-shifted (or Rayleigh scattered) components. The first claimed experimental measurements of Brillouin scattering come from the work of E. Gross, published in *Nature* in 1930 [20], titled "*Change of Wavelength of Light due to Elastic Heat Waves at Scattering in Liquids*". Gross passed the 435.8 nm emission line of a mercury lamp through a number of materials, primarily liquids, and used a highly resolving spectrometer to measure the output radiation. Significant care needed to be taken to prevent hyperfine mercury lines from obscuring any of Doppler scattered pump input. Gross observed a doublet of peaks around a main unshifted peak in liquids such as water, benzene and Ethyl alcohol and also crystalline quartz. The measured shifts were a reasonable match with those expected from theory, and Gross postulates that this connection indicates that the accurate measurement of scattered light may provide a new tool for characterising materials. Gross did not provide any images of the of the measured spectra or data plots of any kind.

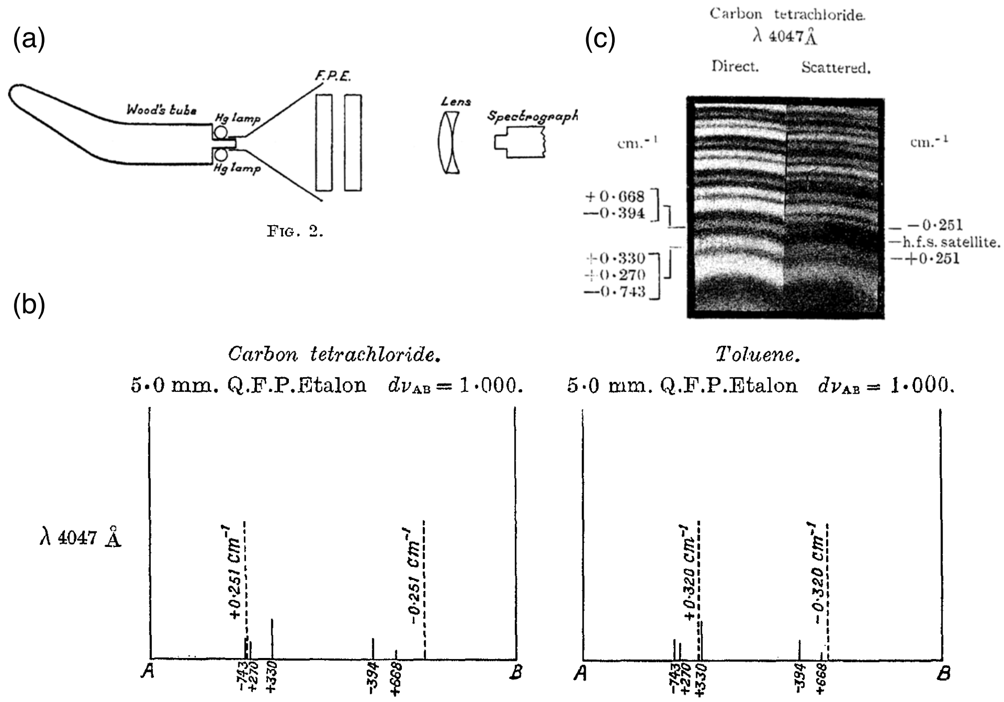

Figure 2.3: (a) Setup used by Rao to measure Brillouin scattering in liquids (b) Measured peaks from scattering in Carbon tetracholoride and Touline. The solid lines are hyperfine lines of the mercury lamp source, dashed lines are the Doppler shifted components (c) Spectrographic images of Carbon Tetrachloride using the 404.7 nm mercury line as a pump [21].

An unexpected observation by Gross was that, for some of the liquids (and for the quartz), multiple sets of lines were observed, at harmonics of the expected frequencies. This observation caused quite a stir in the literature and a number of researchers set out to address the issue. The work of Debye [18], attempted to address this by inducing supersonic acoustic waves directly on the liquid and observing the scattered wave. The measurements showed a significant number of orders and also a preference for scattering depending on the input orientation. While the measured velocities did match up with the expectation (from input frequencies of around 2 MHz), the question again was asked, why do these extra orders appear? It was postulated that the oscillations in the material where not pure sinusoidal waves and then some harmonics should be generated, but such a simple description could not explain the relative intensity of the different scattered lines. To address these new observations in the work of Debye and Sears, Raman and Nath theoretically investigated the configuration of their experiments over the course of five articles [22], titled *"The diffraction of light by High Frequency Sound Waves"*. They found that the observed effects occur in a regime were the acoustically driven grating is "weak", and the interaction region is short compared to the optical wavelength, and that the nth scattering order involves n phonons. In the case of a strong grating the more typical Bragg scattering occurs, with an individual photon and phonon, similar to the case of Brillouin scattering.

While the work of Raman and Nath developed understanding for some of the observations, it still was not clear why Gross was measuring multiple lines, in particular for the quartz crystal. Further experimental work by a student of Raman, B. Raghavendra Rao, attempted to clarify earlier results. In two papers titled *"Examination of molecularly scattered light with a Fabry-Perot Etalon"*, Rao performs highly detailed experiments measuring the scattered light using a Fabry-Perot etalon [21]. No series of lines were observed here, with a number of different mercury lines being explored as pumps. Rao's paper provided highly detailed schematics of different experimental equipment, such as the general design of the mercury lamps, and also photographs of interferograms as shown in fig. 2.3. Raman followed this work in 1938 with the first photographs of measurements in quartz crystal, elucidating the early work of Gross [19].

Following this, further understanding in crystals developed from advances in experimental apparatus, such as superior spectrometers, crystal sources and light sources. In 1951 V. Chandrasekharan investigated the effects different of orientations of diamond for the scattered Brillouin components [23]. Due to the birefringent nature of the crystal, and the effects of symmetry on the propagation of the acoustic wave, multiple components were observed, with up to 12 theoretically predicted [24, 25]. In 1955 R. Krishnan experimentally explored this effect, and identified the new possibilities of material characterisation [26]. In his paper, *"Elastic constants of crystals from light scattering measurements"*, Krishnan accurately identifies the various elastic constants and acoustic velocities for different orientations of a number of crystals, such as diamond, quartz and calcite. These observations were shown directly in photographic measurements, an excerpt of some data is given in fig. 2.4.

Birefringent Crystals

Crystal	Light incident along	Light scattered along	Angle of scattering in degrees	Direction of elastic wave-normal	Nature of Brillouin components	Shift observed in cm.$^{-1}$	Effective elastic constant		
							Theoretical expression	Value calculated from observed shifts $\times 10^{-11}$ dynes/cm.^{2}	Value calculated from known elastic constants $\times 10^{-11}$ dynes/cm.^{2}
α-Quartz	[0$\bar{1}$0]	[001]	90	[011]	Longitudinal	1·90	..	10·80	9·83
,,	[010]	[001]	90	[01$\bar{1}$]	Longitudinal	2·07	..	12·82	12·91
,,	[100]	[001]	90	[101]	Longitudinal	1·96	..	11·23	11·69
,,	[100]	[010]	90	[110]	Longitudinal	1·75	..	9·16	9·02
,,	[100]	[$\bar{1}$00]	180	[100]	Longitudinal	2·36	c_{11}	8·33	8·54
,,	[010]	[0$\bar{1}$0]	180	[010]	Longitudinal	2·22	$\frac{1}{2}(c_{11}+c_{44}) + \sqrt{\frac{1}{4}(c_{11}-c_{44})^2+c_{14}^2}$	7·37	9·32

Figure 2.4: An excerpt of a table of measured results from the work of Krishnan [26].

While the possibility of using Brillouin scattering for material characterisation was clearly demonstrated, the lack of suitable light sources prevented experiments in a wide range of materials, with results mostly limited to mercury lamps. With the invention of the laser this issue was addressed, and the subsequent high powers available opened up a wide range of new physics, which will be explored in the next section.

2.2 The Laser: Enabling *Stimulated* Scattering

The discovery of the laser in the 1950s, with the first experimental demonstration of a Ruby laser by Maiman in 1960 [27], truly changed the face of optics, photonics and technology in general. For optics, the laser provides a coherent and powerful light source, which can be tailored to emit over a wide range of spectral regions. Of relevance to this thesis is the birth of nonlinear optics, where the interaction of an intense optical field with a medium changes material properties, which can alter the conditions of a transmitted probe wave. Interactions which had been observed to occur spontaneously, in particular Raman and Brillouin scattering, were discovered to have *stimulated* analogs. Here I will detail the initial discoveries of stimulated scattering and investigations which led from these discoveries.

Though initial lasers were much more powerful than previous optical sources, these stimulated processes were not observed until the invention of Q-switched lasers [28]. In Q-switched lasers the properties of the lasing cavity are varied in time, allowing for the large internal circulating powers to be rapidly released as optical pulses which can have orders of magnitude higher powers than the input laser. When performing experiments with their Q-switched Ruby laser, Woodbury and co-authors found an emission of a second set of frequencies, accompanying the normal lasing output, which did not correspond to any fluorescence in Ruby [29]. Further experiments led to the realisation that this emission was due to the nitrobenzene material in the laser cavity used to perform the Q-switching, and that the emission frequency matched Raman emission frequencies [30]. These diligent experiments were performed with a number of liquids, such as toulene and benzene, and in all cases anomalous emission was observed which matched to measured Raman peaks. Furthermore, some experiments found laser action which was accompanied with no clear measurable absorption, i.e from a material resonance, indicating that Raman scattering was providing the optical *gain* for the lasing process.

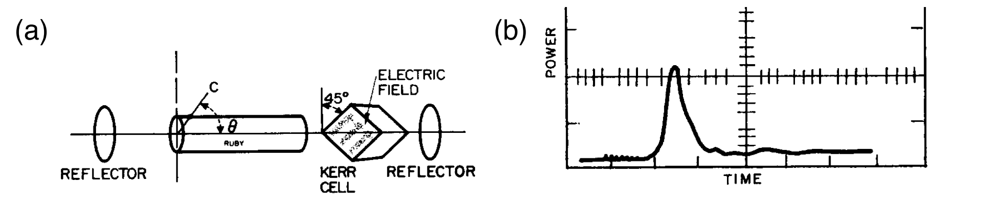

FIG. 1. Schematic diagram of the pulsed reflector laser.

FIG. 2. Output from the maser after switching the shutter. The time calibration is 0.2 μ sec/cm. The timing signal for the shutter switch appears as the beginning of the small oscillation on the trace before the output pulse.

Figure 2.5: (a) Experimental setup of Q-switched ruby laser [28] (b) "Giant" pulsations measured from Q-switched system. The origin of the pulses were discovered later to be stimulated Raman scattering in the Kerr cell medium.

While emission at the Raman frequencies indicates that Raman scattering was indeed the cause, it was not completely clear if the scattering was of a stimulated or spontaneous nature. In the 1963 work "*Theory of Stimulated Raman Scattering* [31], Hellwarth, a co-author of the previous works, provided details on how Raman scattering could provide gain similar to that of a typical lasing system. A large number of works quickly explored this area, summarised in this review from late 1963 [32] which covers the Woodbury results and later developments. Of significant importance were experiments observing *multiple* orders of stokes and anti-stokes emission [33, 34]. Thresholding effects were observed for different orders, and the directions of emissions varied between the different orders, with anti-stokes lines featuring cone-like emission in the forward directions. These results brought about a new realisation for the mechanisms causing these effects [35], as indicated by this quotation from Stoicheff,

> Consider that the intense maser radiation excites by means of the Raman effect a set of molecules vibrating coherently at the Raman frequency. The resulting variation in refractive index acts like a "phase grating" which then modulates and scatters the original light, thus producing sidebands or many Stokes and anti-Stokes frequencies.

The realisation that stimulated Raman scattering may be thought of as coherent molecular oscillations, i.e coherent optical phonons, induced by the pump light led the members of Townes group at MIT to ask the question: what about coherent oscillations of *acoustic* phonons? Experiments investigating this question led to the first demonstration of SBS, published in *Physics Review Letters* in 1964 [36]. The introduction to the work shows the clear inspiration of earlier results,

> Stimulated Brillouin scattering of an intense maser beam, involving coherent amplification of a hypersonic lattice vibration and a scattered light wave, has been detected in quartz and sapphire. This process is analogous to Raman maser action, but with molecular vibration replaced by an acoustic wave of frequency near 3×10^{10} cps, and with both the acoustic and scattered light waves being emitted in specific directions.

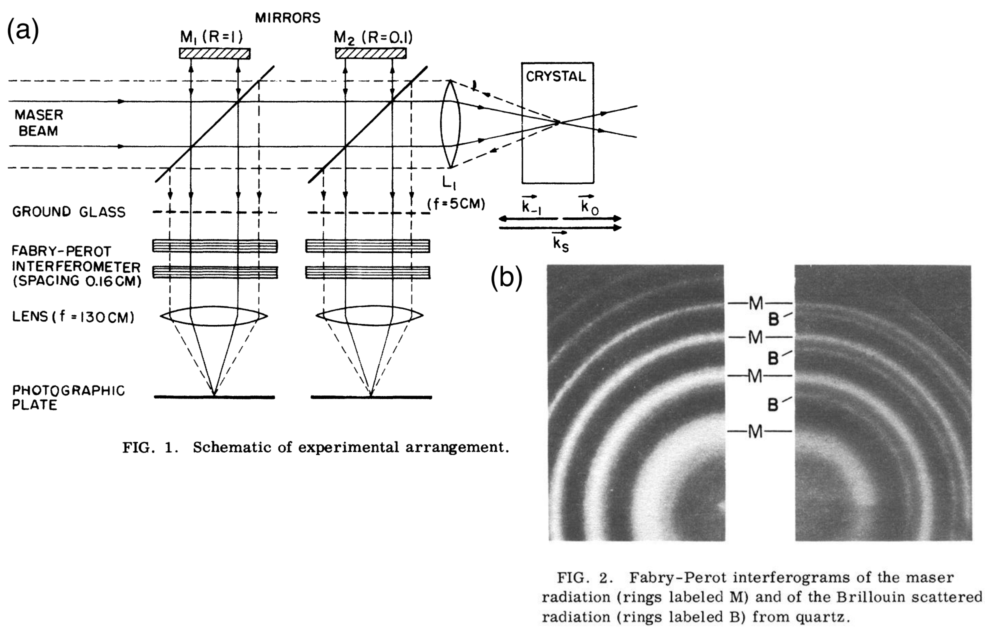

Figure 2.6: (a) The experimental configuration used in the work of Chiao, a member of the group of Townes [36] (b) The images from the two photographic plates. The reference plate captures the initial pump beam while the secondary plate shows the Brillouin scattered components.

The configuration of the experiment is shown in fig. 2.6 with the Brillouin scattering occurring within a quartz or sapphire crystal. Fabry-Perot interferograms were used to monitor the scattered light, with a reference interferogram measuring the input pump, with the very clear scattered Brillouin lines shown in fig. 2.6. The scattered light was of comparable power to the input pump, orders of magnitude larger than any expected spontaneous scattering, indicating that significant buildup of the acoustic wave was occurring. Finally, it was claimed that the quartz and sapphire crystals experience extensive internal fractures from the optically induced acoustic waves.

With initial demonstrations of SBS established in crystals, subsequent work experimented with different pumping configurations and materials, such as liquids [37]. Theory work on the dynamics of SBS rapidly progressed over the following years [38], in particular the work of Tang [39] explored depletion effects, conditions for spontaneous Brillouin generation and the effect of pump pulse shape on gain efficiency. The theory work investigating pump pulses was reinforced by the experimental work of Pohl [40], which used an interesting amplifier-oscillator configuration, shown in fig. 2.7, to accurately characterise phonon lifetimes and Brillouin gain coefficients in six liquids.

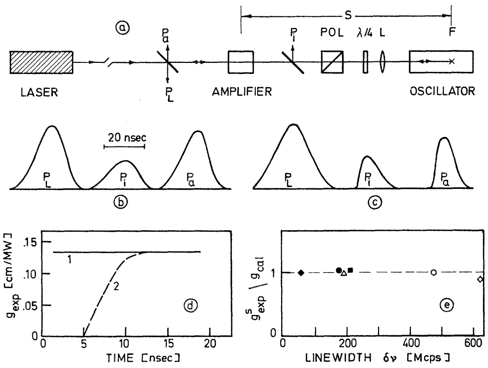

FIG. 1. (a) Schematic of the experimental system. (b) Oscilloscope traces depicting the laser pulse P_L, the incoming signal P_i, and the amplified signal P_a ($\Delta\nu = 0$). (c) same as (b) with abruptly rising signal P_i ($\Delta\nu = 0$). (d) Experimental gain factor of CS_2 versus time ($\Delta\nu = 0$): (1) slowly rising P_i and (2) abruptly rising P_i. (e) Ratio $g_{exp}{}^S/g_{cal}$ versus phonon linewidth $\delta\nu$ for six different liquids: solid diamond, CS_2; solid circle, acetone; triangle, methanol; solid square, n-hexane; open circle, toluene; and open diamond, CCl_4.

Figure 2.7: Amplifier oscillator configuration utilised in the work of Pohl [40]. The relative phonon lifetime and gain coefficient could be characterised to high precision.

2.3 Brillouin Scattering in Early Optical Fibers

With a basic understanding of SBS well established within a few years of the laser gaining wide use, investigations extended to newer areas, such as investigating acoustic properties of semiconductors and understanding Brillouin scattering in fibers and surfaces.

For nonlinear optics, optical fibers and waveguides provided significant advantages to previous free space experiments. Fibers provide tight mode confinement and diffraction free environment, with attainable interaction lengths orders of magnitude beyond free space propagation in bulk media. These benefits were first demonstrated in the 1970 publication of Eric Ippen, in which a Raman oscillator was formed with the primary gain medium being a 1 m long liquid core optical fiber [41]. A similar experiment was later repeated with a glass fiber medium by Stolen and Ippen [42]. In these experiments both single pass and resonator configurations were explored and the Raman gain was characterised in both cases. SBS was also observed in a 9 m long single pass fiber during these experiments, however the Raman response was dominant due to the wide spectral width of the pump source. The authors identified the multi-THz wide Raman response in the glass fibers as a possible gain medium for amplifiers, a very prescient prediction when one considers that fiber based Raman amplifiers are still in use today.

While fibers proved to be a suitable medium for performing nonlinear optics, it was quickly understood that they may be *too* effective. In 1972 Smith investigated the optical power handling capacity of low loss fibers, which had developed quickly after the predictions of Kao [43], due to the effects of Brillouin and Raman scattering [44]. It is important to keep in mind that due to the guidance conditions, unlike in a bulk medium, fibers only allow for optical propagation in forward and backwards directions. To determine the threshold Smith summed up the contributions of *spontaneous* scattering along the length of the medium and used this as an effective input probe at the far end of the medium. This probe then experiences Brillouin amplification due to the pump wave and, if the output probe is of similar power to the input pump, then depletion will occur and the output pump power will become saturated. Smith formulates a simple equation to determine the "critical power" at which depletion should occur, which will be discussed in section 4.4.4. Smith determined that the critical power to be in the range of 35 mW, using parameters of state of the art fibers, a value which was certain to be a severe limitation to fiber communication systems. Experimental confirmation of the work of Smith was performed by Ippen [45]. Ippen performed single pass SBS experiments with short fibers, around 20 m length and with quite high loss of 1.3 dB /m, and observed SBS threshold effects with pulses with peak powers less than 1 W. The setup and some results from this work are shown in fig. 2.8. After comparing the results with the formula of Smith it was concluded that

> From these experiments, it is clear that SBS can indeed occur at low power levels in optical fibers. In particular SBS limits the amount of narrow-band power which one can transmit through a fiber.

The power limitation caused by SBS became a significant issue as fiber losses improved. A number of strategies were developed to mitigate the effects of SBS in fiber including: tailoring the fiber properties, broadening or dithering the pump beams frequency, and using pulses shorter than the acoustic lifetime to prevent acoustic wave buildup [46].

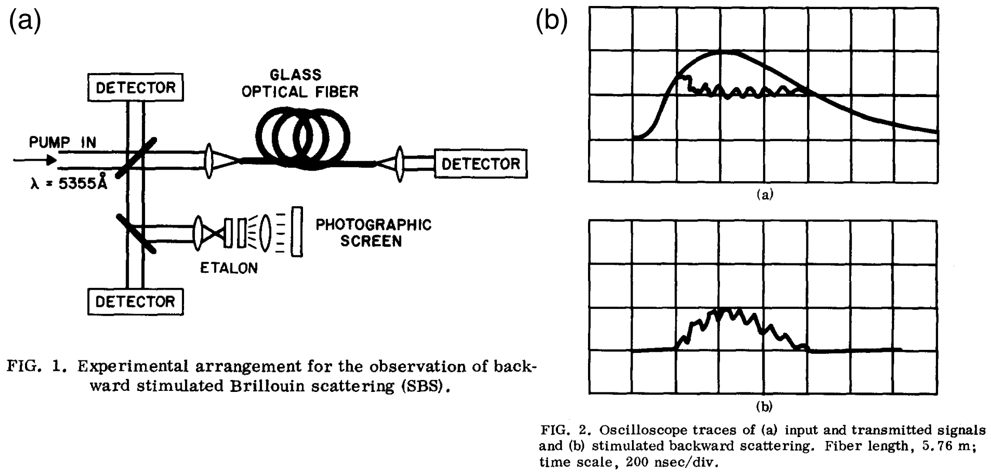

Figure 2.8: Single pass SBS measurements in a glass optical fiber [45]. (a) The experimental setup detectors measuring the input, transmitted and reflected pulses (b) The oscilloscope traces demonstrating the effects of pump depletion and the Stokes generated pulse in the back direction.

The strong buildup of SBS in long lengths of fiber enables the possibility of low threshold Brillouin lasers. In 1976, Hill formed the first continuous wave (CW) Brillouin laser using a fiber ring within a free space cavity [47]. The 10 m cavity length required a Fabry-Perot filter to select one longitudinal cavity mode.

The lasing threshold was a low CW power of 250 mW, significantly reduced from the multi W peak powers in the earlier work of Ippen and Stolen. In the same year, Hill also experimented with a Fabry-Perot configuration, where partially reflective mirrors were placed at each end of fiber [48]. Significant cascading was observed with up to 14 new frequency lines generated, with both anti-Stokes and Stokes waves being observed. No mechanism for the relative distribution of power between all the generated waves was given. The threshold improvement in these cavities is due, in part, to the high circulating powers within the resonator. In 1982, Stokes demonstrated an all fiber resonator, with a fiber directional coupler being used instead of mirrors, which enabled significant reduction to optical losses [49]. Predicting that such cavities would greatly improve nonlinear effects, Stokes then demonstrated Brillouin lasing with a sub mW threshold of 0.43 mW. It was shown that a correct cavity configuration can enhance the circulating power of the pump *and* scattered light, leading to the drastically reduced thresholds observed in the experiments [50]. Setups and measurements from these early works is shown in fig. 2.9.

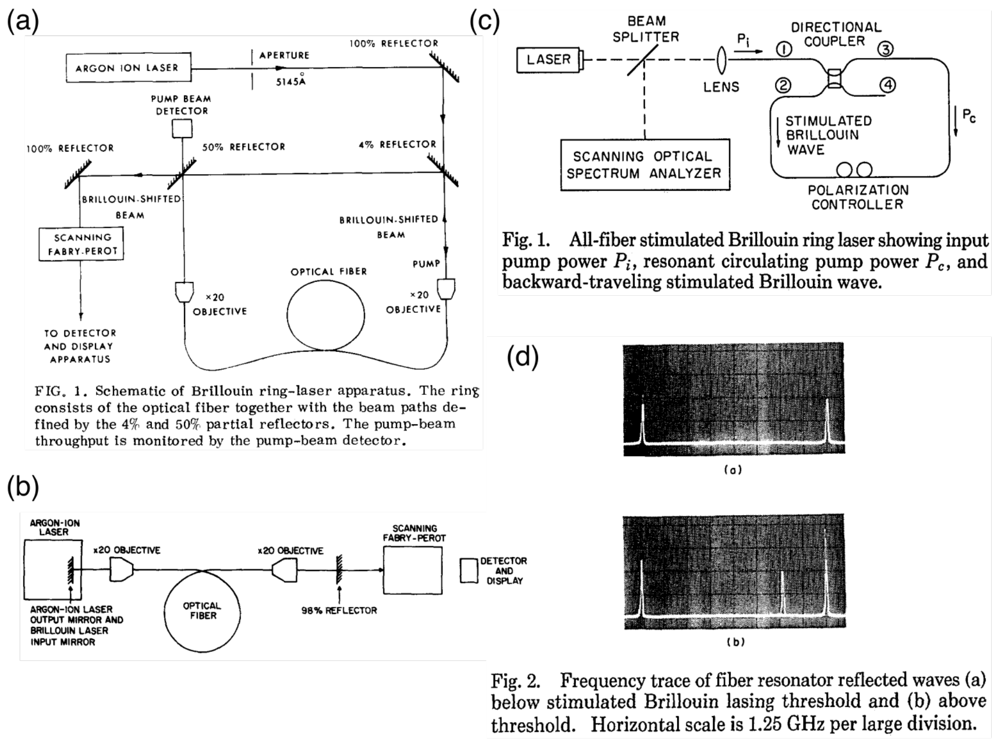

Figure 2.9: Brillouin laser apparatus used by Hill in (a) loop [47] and (b) Fabry-Perot [48] configurations. (c) The all-fiber laser used by Stokes [50] (d) Measurement above lasing threshold.

These initial works investigating Brillouin scattering in fiber assumed that the acoustic properties of the scattering medium to be the same as a bulk medium. In 1972 Sandercock, following experiments investigating Brillouin scattering in Silicon and Germanium [51], continued his research by performing experiments on thin films of various media [52]. This work, titled *"Structure in the Brillouin Spectra of Thin Films"*, found that sharp boundaries in the thin films investigated greatly change the nature of propagation of acoustic waves, in particular for structures suspended in air. The slab formed an acoustic cavity, similar to an optical Fabry-Perot etalon, yielding multiple individual lines under the Brillouin lifetime envelope, as shown in fig. 2.10.

The group of Stegeman followed up the initial results of Sandercock with a number of investigations in films, externally probing the slab from free space and also propagating light through the slab waveguide [53]. In this work they mention the effects of the waveguide boundary, and the additional "corrugation forces" which appeared due to the presence of the boundaries in these new devices. These boundary forces are of critical importance to modern small core waveguides, which we explore throughout this thesis in a number of areas, in particular in section 4.5.2. They developed early theory looking at the importance of guidance in the case of fibers [54], and concluded that only below certain dimensions should guidance become significant for typical backwards SBS [55]. The experimental measurements were very precise, utilising an automated Fabry-Perot system [56], and could separate scattering contributions from the core and cladding regions of the investigated fiber, as shown in Figure 2.10. The discussion of the paper is also highly detailed and mentions points such as

> With a suitable choice of cladding material, it would be possible to vary the lifetime of the acoustic normal modes and thus change the threshold for stimulated Brillouin scattering

and also suggests using Brillouin lasing in a fiber resonator as a rotation sensor. It is clear that, having developed an understanding for thin film conditions, the importance of guidance of acoustic waves in fibers was becoming understood.

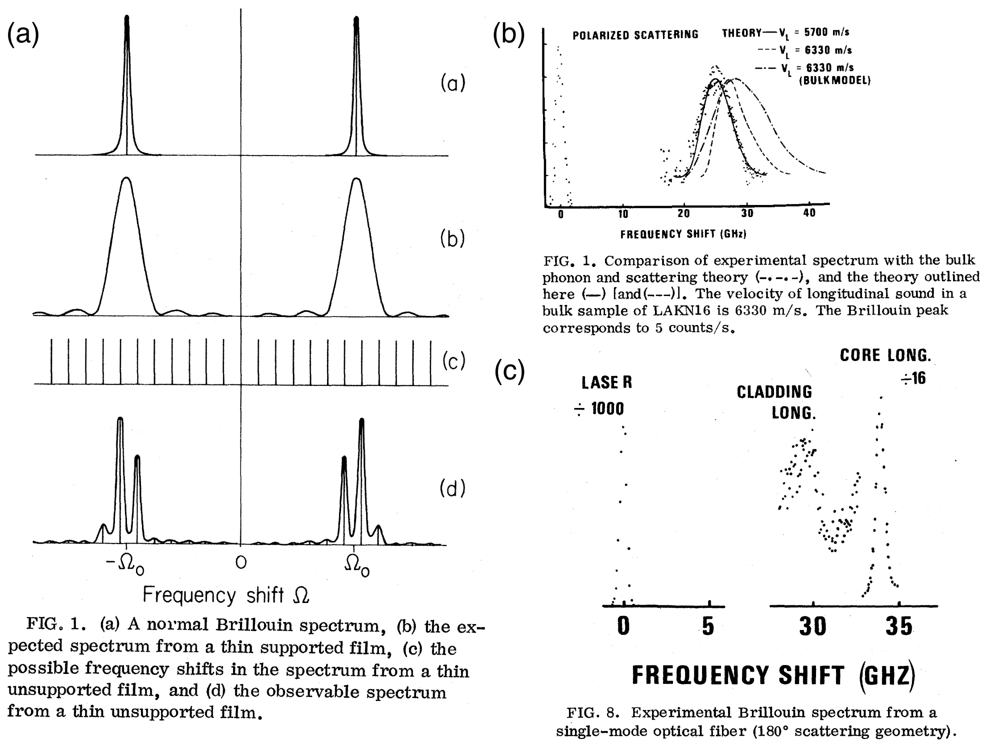

Figure 2.10: (a) Brillouin scattering properties of thin films [52] (b) Measured Brillouin scattering in slab waveguide [53]. The measured shift differs from predictions of bulk material (c) Brillouin spectrum from a single mode fiber, discriminating contributions from the waveguide core and cladding [55]

2.3.1 Guided Wave Brillouin Scattering and Early SBS Applications

Interest in nonlinear optics in fibers extended far beyond stimulated scattering, as reviewed by Stolen in 2006 [57], and even at this early stage applications were extending into a wide range of areas, such as quantum physics. The squeezing of vacuum noise below the quantum limit was of significant interest [58] and experiments were still being conducted in 1985 to achieve the first demonstration. Nonlinear effects in fibers had been identified as a possible mechanism for squeezing, and during their work, experimentalists at IBM identified a new noise source which may prevent measuring squeezing below the vacuum level. This noise source is due to spontaneous Brillouin scattering, in the *forward* propagation direction. Over two seminal papers Shelby discusses the effect [59, 60], termed guided acoustic wave Brillouin scattering (GAWBS). In a bulk medium, under the standard Bragg conditions and acoustic dispersion in bulk, forward scattering should produce a zero frequency shift. However, in fiber the acoustic modes are guided by a cylindrical structure, with the boundary conditions producing sets of transverse acoustic modes which induce strain (mixed torsional modes) or "dilate" the core (radial modes). The result of these oscillating acoustic modes is, somewhat surprisingly, that of a phase or polarisation modulation which occurs at the relative acoustic frequencies of the different modes. This modulation was predicted to produce significant amounts of noise and a further theory paper detailed how to suppress both SBS and GAWBS within a fiber system [61]. Following these developments Shelby demonstrated the first fiber squeezing results, using a 100 m fiber resonator cooled to 4 K [62]. The observed squeezing was achieved within a limited bandwidth due to a number of GAWBS peaks. Results of the combined works are shown in Figure 2.11.

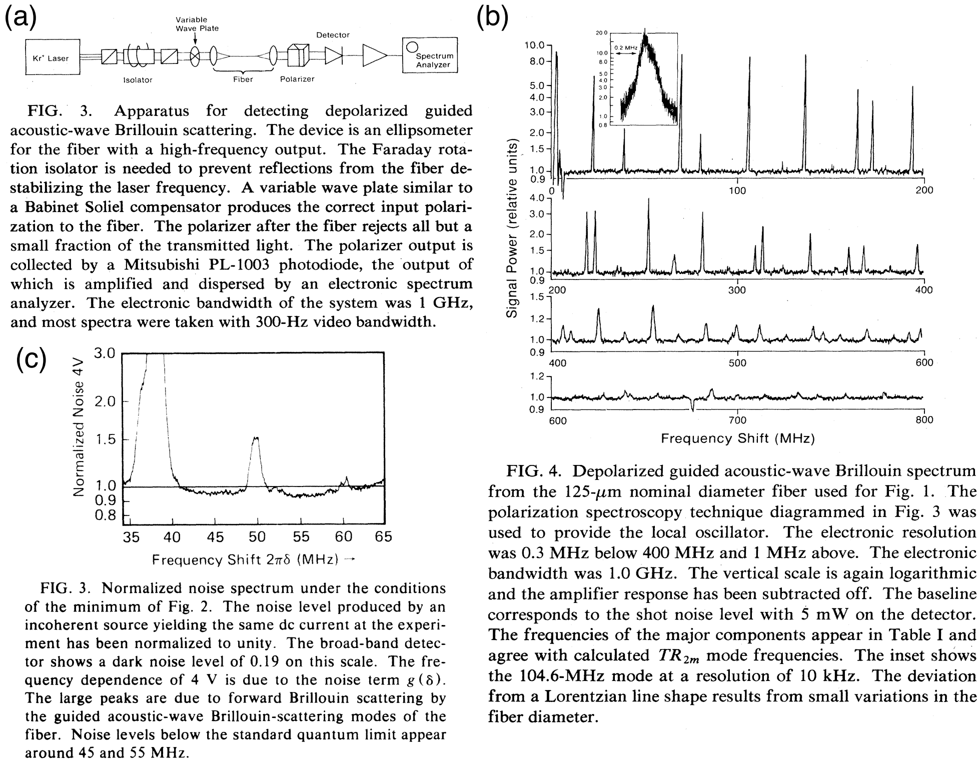

Figure 2.11: (a) Setup for measuring depolarised GAWBS (b) Measured GAWBS [59] (c) Frequency dependence of squeezed light in fiber [62]

In a more traditional realm, research into key components for telecommunications was still undergoing significant focus in the mid 80s [63]. Due to the narrowband range, significant strength and ease of tunability, Brillouin scattering, in the form of fiber Brillouin amplifiers (FBA) was receiving interest for use as amplifiers within telecommunications systems [64, 65]. Initial results were quite promising, with SBS in fiber used to amplify communications signals on the order of 20 dB, and achieve error free transmission. However it was quickly found that the significant noise from amplified spontaneous Brillouin scattering in these amplifiers was a serious issue that had to be designed around [66]. The severity of this effect arises due to the number of thermal phonons at room temperature, and was first described in detail in the work of Tang [39]. If a strong probe signal is used the effects are diminished, however the dynamic range of the amplifier suffers. The invention of the erbium doped fiber amplifier (EDFA) in 1987, capable of providing high gain and low noise figure within a few years [67–69], has led to Brillouin amplifiers only being used in niche applications. As described in the conclusion of one of these early papers by Tkach and Kraplyvy [66]:

> The large noise figure effectively removes the FBA from consideration for receiver pre-amplifier applications, since present direct-detection receivers are within 20 dB of the quantum limit...Thus, the FBA may not find wide application as an amplifier *per se*, but instead as a tunable optical filter.

Brillouin amplification has indeed found applications as tunable optical filters, in particular in the area of microwave photonics, which will be discussed in further detail in Chapter 8.

An interesting application explored during the mid 80s was that of acousto-optical frequency shifters or filters, utilising mode conversion induced by guided acoustic waves. Mode conversion using collinear acoustic waves had previously been explored in integrated waveguides, but this was accompanied by high optical insertion losses [73, 74]. In 1986 Kim et al published the work "*All-fiber acousto-optic frequency shifter*" in *Optics Letters* [70]. A guided acoustic wave, induced by an external acoustic oscillator and acoustic horn, is used to efficiently convert light from the LP_{01} fiber mode to the LP_{11} mode. This mode conversion is accompanied by a frequency shift corresponding to the frequency of the utilised guided acoustic mode. Finally a spliced fiber was used to strip any of the remaining LP_{01} mode after transmission, providing high extinction between the frequency shifted wave and the original input. A detailed theory paper following the experimental work is was published in 1988 [75]. While the above work uses guided acoustic waves for mode conversion, they are induced by an external source, unlike typical Brillouin scattering. Following this, Russell published some initial experimental work on forward Brillouin scattering between two modes of a dual mode fiber [72]. A detailed theory paper soon followed, describing a number of different aspects of this interaction [71]. The paper indicated that this scattering process, which we refer to as forwards intermodal Brillouin scattering (FIBS), is distinct from GAWBS due to the stimulated nature of the interaction occurring between the different optical and acoustic waves, being

> ...based on a genuine collinear phase matching between the three distinct guided waves and displaying a stimulated threshold... The inter-modal beating between the pump and Brillouin light excite, via electrostriction, a flexural acoustic wave that couples power between the modes.

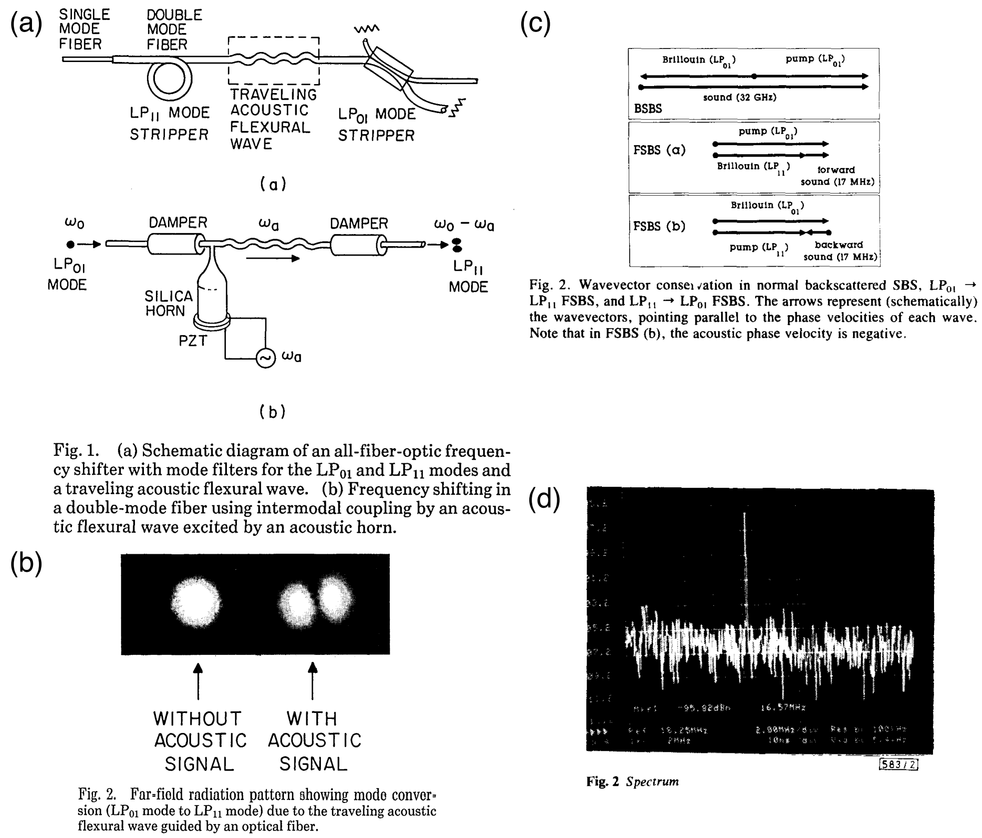

Figure 2.12: (a) Scheme for mode conversion and frequency shifting using acousto-optic effect [70] (b) Measured mode shifting with appropriate acoustic signal (c) Phasematching conditions for SBS, and inter-mode scattering [71] (d) Experimental measurement of forward inter-mode SBS in optical fiber [72]

The comprehensive paper by Russell explores the dynamics of this process, highlights how the gain scales with geometry and compares the relative thresholding effects between normal SBS and FIBS. While later work on acousto optics devices continued to use external acoustic generation [76], further work exploring FIBS would not occur for another decade, when new fiber waveguides based on photonic crystals began to emerge. We will discuss this, and the new dynamics which were realised with these devices, in section 2.4.

2.4 Brillouin Scattering in Modern Devices

Now that we have established historical context for Brillouin scattering, we will focus on key research within the past decade, particularly on investigations of waveguide devices with wavelength-scale geometries. For the sake of clarity, this section will split waveguide devices from resonators so that progress can be tracked in both areas independently.

2.4.1 Brillouin Scattering in Small Core and Photonic Crystal Fibers

As discussed in section 2.3, it was quickly understood that the guided nature of acoustic waves in fiber may affect the interaction when compared to that in a bulk media [54, 55]. In the work of Thomas [55], it was predicted that the diameter of the core would need to be in the range of a 4× the wavelength before guidance would significantly affect the *longitudinal* acoustic modes of the core, for waveguides where $v_{\mathrm{ac}}^{\mathrm{core}} > v_{\mathrm{ac}}^{\mathrm{clad}}$. Later theory and experimental work showed the situation could be even more complex and that for many fiber dopants *leaky* acoustic modes also should be considered [77–79], in particular for the case of $v_{\mathrm{ac}}^{\mathrm{core}} \approx v_{\mathrm{ac}}^{\mathrm{clad}}$. In 2002 Yeniay performed sensitive characterisation measurements of 4 different fibers: Allwave, Truewave, dispersion compensating and high-Ge doping [80], with remarkably varied responses observed in the different fibers, further cementing the importance of these considerations.

It is within this context that the group of Phillip Russell was exploring acoustic and optical confinement within photonic crystal fibers (PCFs) [81]. In particular, they found that tailoring the geometry of the holes within a fiber preform could create a phononic bandgap, in the MHz frequency range, which may allow for the enhancement or *suprression* of light sound interactions. In 2006 the group of Russell, led by Dainese [82], investigated SBS in PCFs with large air holes and small cores with varying diameters. The results of this work show the typical fiber SBS peak located at 11 GHz split into 3 peaks centered around 10 GHz, for core diameters $< 4\,\mu\mathrm{m}$. Simulations in the paper indicate that the geometry acts close to that of a solid core suspended in air. Detailed calculations with the fabricated device geometry showed the highly varied Brillouin spectra as the diameter was changed, as summarised in fig. 2.13. Another curious result was the large *increase* in the SBS threshold, even though the effective area of the fiber is *reduced*. The majority of the reduction is due to poor overlap of the highly confined acoustic modes with the optical modes, with a small amount being caused by the strong z-component of the electrical field (which is opposite for the forward and backward travelling optical waves).

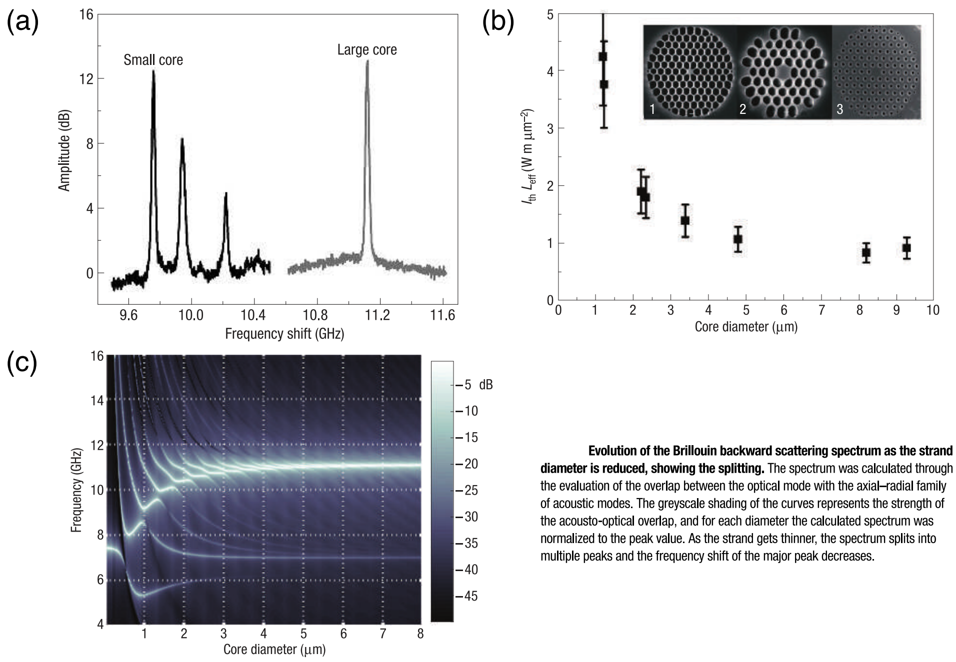

Figure 2.13: (a) SBS spectrum from small core PCFs (b) Increase in SBS threshold as core diameter is *reduced* (c) Simulations of SBS spectra for a range of core diameters. Significant mode splitting occurs, as described in the figure caption [82]

While the modification of SBS in small core PCFs, mostly due to the change in guided acoustic wave properties, has some physical intuition based on the prior SBS literature, a far more remarkable result was also demonstrated by the group of Russell in 2006. This work, titled "*Raman-like scattering from acoustic phonons in photonic crystal fiber*" and published in *Optics Express*, describes a configuration where the scattered light within a PCFs displays "Raman-like" properties, with dynamics unlike any previously observed Brillouin interaction [83]. The strong acoustic confinement, provided by GHz phononic bandgaps formed by the PCFs geometry, results in a high overlap of optical and *transverse* acoustic modes. These transverse modes have a non-zero frequency for scattering in the forward direction, similar to GAWBS but at higher frequencies and altered modal properties due to the tight confinement in the small suspended core. The experiments investigating the stimulated Raman-like scattering (SRLS) used short laser pulses, in the 50 ps range, to excite acoustic waves and monitor their response on a quasi-CW pulse. The frequency response was calculated from Fourier transforms of the measured time domain response. While highly intriguing, the dynamics of this interaction were not deeply explored until follow up work was published in 2009 in *Nature Physics* [84]. A PCFs with a high air-filling fraction of 74 % and diameter of 1.6 µm resulted in a strong photon-phonon interaction with a 1.8 GHz R_{01}-like transverse acoustic wave. Pump-probe measurements were performed with two CW waves spaced by the 1.8 GHz acoustic shift and co-propagated through the PCFs, and determined a gain coefficient of $1.5\,\mathrm{m}^{-1}\,\mathrm{W}^{-1}$. When the dual frequency pump was increased in strength, cascaded energy transfer occurred between multiple lines and a 14 line frequency comb spaced by the 1.8 GHz acoustic frequency was generated.

In 2010 the group of Russell again explored Brillouin interactions in small core air clad PCFs [85]. In this case they looked at forward *inter-polarization* scattering (SIPS), equivalent to the FIBS which Russell had investigated 20 years prior in fiber [72] as discussed in section 2.3.1. The same PCFs was capable of SIPS and SRLS allowing the dynamics of the different schemes to be explored with the same experimental system. Unlike SRLS, where strong cascading was easily observed, the SIPS interaction occurred only between two co-propagating waves due to the strict phasematching conditions. We explore the phasematching requirements in fine detail in section 4.4. SIPS is capable of exponential gain, like typical SBS, but the modified phase matching conditions result in a different frequency dependency with wavelength [86]. The SIPS interaction was later used as a reconfigurable isolator, utilising the directional (and frequency) dependence of the phase matching process to attenuate (or amplify) a wave in one direction but not the other [87].

2.4.2 Brillouin Scattering in Planar Waveguides

While SBS was well established in fiber, with some preliminary measurements of Brillouin scattering in thin films during the 70s (see section 2.3), the first demonstration of SBS in a planar optical waveguide was not achieved until 2011 [88]. Central to this result was the use of soft glass chalcogenide waveguides, made of amorphous As_2S_3, which provided acoustic confinement and large opto-acoustic overlap while on a SiO_2 substrate. The waveguide consisted of an 7 cm long 850 nm thick As_2S_3 rib waveguide, with a width of 4 µm and a 30 % partial etch, cladded with a thin 150 nm layer of SiO_2. A strong quasi-CW pump laser was used to perform back scattering measurements, which determined an SBS frequency shift of around 7.7 GHz, in line with previous SBS demonstrations in As_2S_3 fiber [91]. Pump-probe measurements determined a natural linewidth of 34 MHz and a Brillouin gain coefficient of $300\,\mathrm{m}^{-1}\,\mathrm{W}^{-1}$, on the order of 1000× higher than

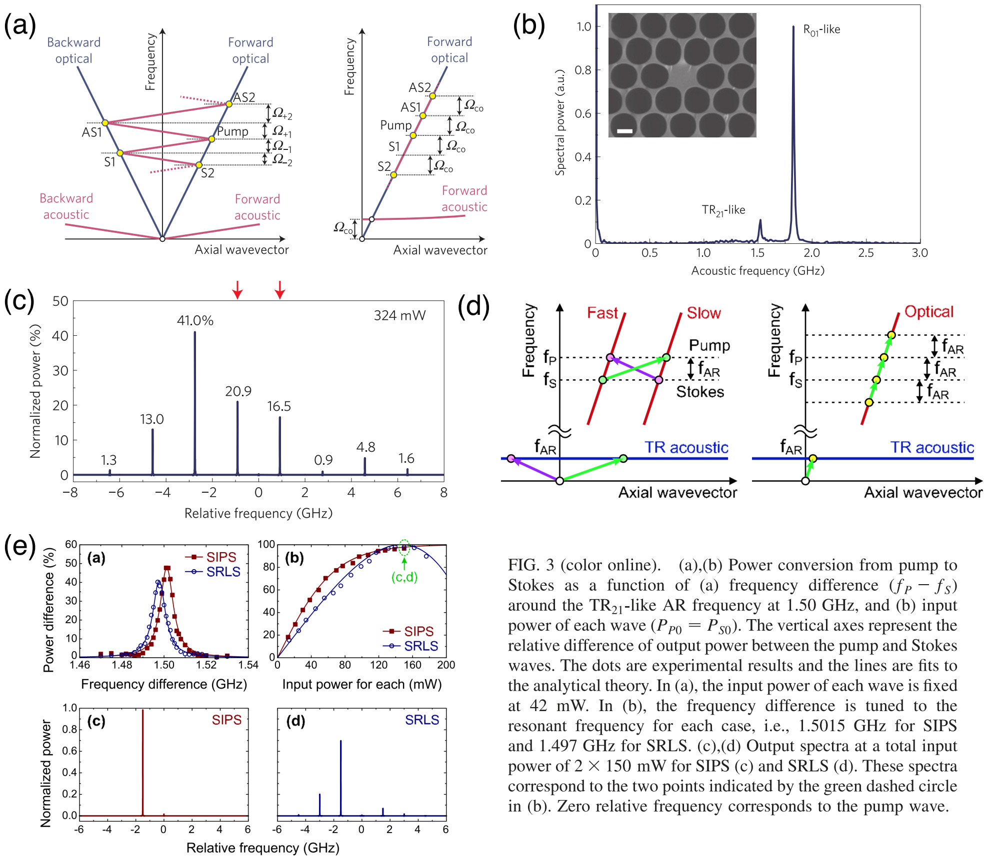

Figure 2.14: (a) Phasematching considerations for typical backwards SBS and stimulated Raman-like scattering (b) Acoustic modes in PCFs capable of generating SRLS (c) Continuous energy transfer between cascaded Stokes lines from SRLS process [84] (d) Phasematching process for SRLS and forward inter-mode scattering (e) Comparison of dynamics of inter-mode scattering and SRLS from [85].

SMF-28 fiber with a typical gain of around $0.2\,\mathrm{m^{-1}\,W^{-1}}$. SBS amplification of 16 dB, and later 22 dB [92], was achieved for coupled powers of a few 100 mW. These waveguides were used to demonstrate a number of applications including slow light [92], dynamic gratings [93], controlling nonlinearities [90] and optical filtering [94] in the following years. Improved versions of these devices have recently been demonstrated with up to 50 dB of gain utilising long effective lengths [89]. Results of these works are summarised in Figure 2.15 and SBS in soft glass waveguides is discussed in fine detail in Chapter 5 of this thesis.

Traditional SBS devices, bulk media and waveguides, rely purely on interactions induced via electrostriction in the medium. Following significant research into cavity optomechanics [97–99], which focuses primarily on *boundary* forces, Rakich published a theory paper investigating the control of optical forces in waveguides in 2010 [100]. This work incorporates the effects of electrostriction and radiation pressure, and finds that the forces interfere constructively or destructively depending on material properties and device geometry. In 2012 this work was reformulated to look specifically at the changes in SBS gain, with the significant effects represented in the title "*Giant Enhancement of Stimulated Brillouin Scattering in the Subwavelength limit*" [95]. The SBS gain of a silicon nanowire surrounded by air, in forward and backwards configurations, was explored for a variety of geometries. Compared to previous scalar theory, massive increases to the Brillouin gain were expected, with coefficients reaching values above $10^3\,\mathrm{m^{-1}\,W^{-1}}$

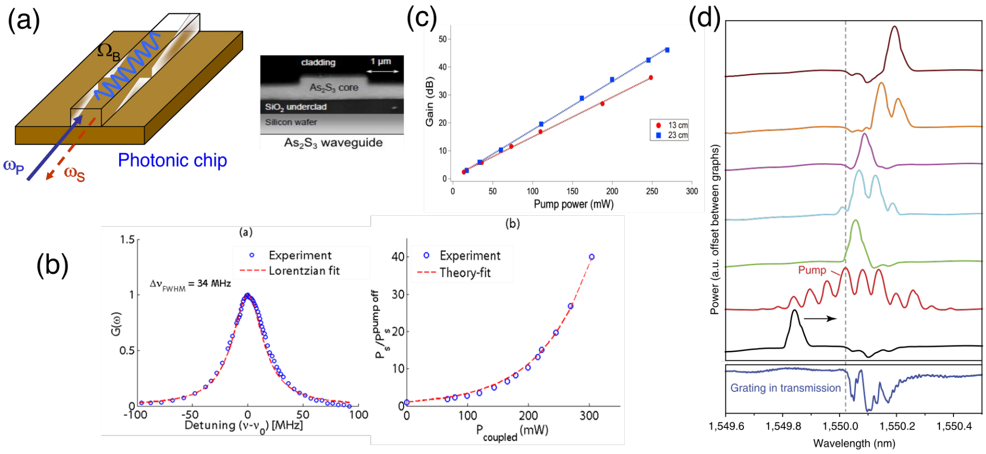

Figure 2.15: (a) Schematic of soft glass As_2S_3 waveguide used for first on-chip demonstration of SBS [88]. (b) Gain profile and on-off amplification of As_2S_3 waveguide (c) Demonstration of up to 50 dB of amplification in recent As_2S_3 devices [89] (d) Density states control of SBS using gratings in As_2S_3 waveguides [90]

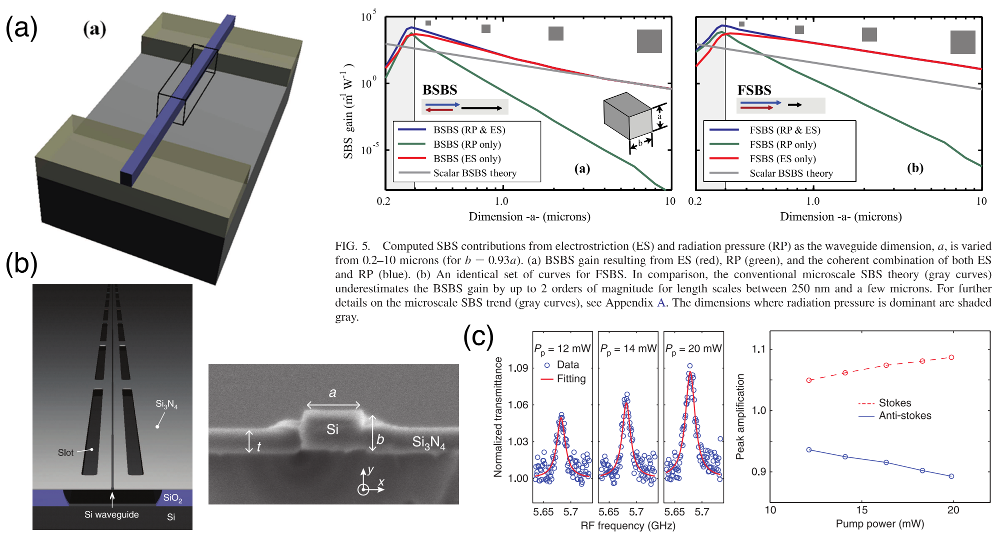

Figure 2.16: (a) Giant Brillouin gain predicted in small core silicon waveguides [95] (b) Hybrid Si and Si_3N_4 membrane waveguides (c) Brillouin amplification of 0.4 dB in hybrid membrane [96]

for backwards SBS. The enhancement was even more significant for forward Brillouin scattering (FBS) (equivalent to the SRLS of Russell) with values beyond 10^4 m^{-1} W^{-1} with the assumed material properties. The key result of this work was the unexpected massive increases to SBS gain coefficient in these sub-wavelength waveguides, kicking off significant experimental research in this area. Finally, a further reformulation of the theory in 2013, again involving Rakich, makes simulations more accessible through the use of standard device parameters and overlap integrals of optical and acoustic modes [101]. We discuss calculations of the Brillouin gain coefficient in fine detail in section 4.5.

The theory work of Rakich was followed soon by initial experimental results. The 2012 work "*Tailorable stimulated Brillouin scattering in nanoscale silicon waveguides*", published in *Nature Communications* and headed by Rakich, demonstrated FBS in a hybrid photonic-phononic waveguide formed of Si and Si_3N_4 [96]. A silicon core (313 nm × 194 nm) confined the optical mode while a membrane of Si_3N_4 with a thickness of 124 nm supported the waveguide in air. This membrane had periodic air holes (100 µm length) which provided lateral acoustic confinement, and the width of the membrane would determine the properties of the guided acoustic waves. Very high gain coefficients in the range of 2500 m^{-1} W^{-1} were measured, however Brillouin amplification was restricted to 0.4 dB due to high linear losses of 7 dB /cm and short physical device lengths of a few mm. An interesting extension of this work focused on an emitter receiver concept published in 2015 [102]. A phononic crystal was formed, instead of the large air gaps previously utilised, around the main membrane structure. This greatly improved the mechanical quality factor, with MHz range linewidth, and allowed for the possibility of placing a second waveguide in close proximity. An acoustic wave generated in one waveguide could then tunnel into the other waveguide, inducing modulation on a travelling optical probe wave, with optical responses with very fast falloffs akin to a 2nd order optical filter.

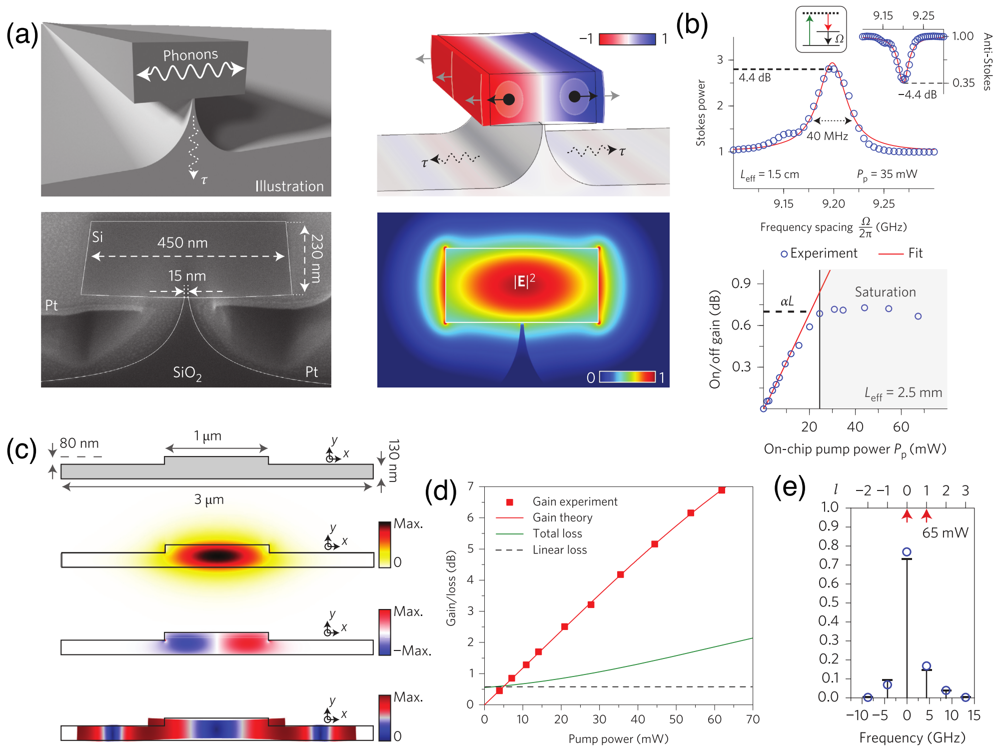

Figure 2.17: (a) Partially underetched Si waveguide geometry demonstrating high confinement of acoustic, top right, and optical, bottom right, modes [103] (b) Brillouin gain spectrum of underetched structure, nonlinear saturation was observed for coupled optical powers greater than 25 mW (c) All Si membrane geometry [104] (d) Large Brillouin amplification in membrane (e) Cascaded scattering in Si membrane structures

Rakich's experimental work confirmed the strong Brillouin interactions were accessible in sub-wavelength waveguides, however the short device lengths and high propagation losses prevented large Brillouin amplification from occurring. The 2015 work of Van Laer addressed this an an unexpected way: the silicon nanowires (of the typical 450 nm × 220 nm silicon photonics geometry) were *partially* underetched [103]. The narrow SiO_2 pillar, from 10 nm to 50 nm width, significantly reduced acoustic leakage while providing structural support sufficent for centimetre long structures in compact spirals. The all Si geometry generated large opto-acoustic overlap and, with the narrowest pillars of 15 nm, gain coefficients up to 3200 m^{-1} W^{-1} were measured, along with propagation losses of 2.6 dB /cm. The long effective lengths allowed for on-off gains of 4.4 dB to be measured, not sufficient enough to enable net gain, with higher gains prevented due to significant nonlinear losses above 25 mW on chip power. Linewidth broadening was observed for different waveguide lengths, and while the work focuses on FBS, weaker SBS was measured with results provided in the supplementary.

To achieve net amplification, of interest for a number of applications including lasing, in silicon waveguides required further device optimisation. Van Laer again investigated silicon nanowires, but now the gain medium was formed by a series of short fully underetched structures (25 µm long) and even shorter anchors (5 µm) [105]. Fully underetching the waveguide removed any leakage in the guiding region and improved the gain coefficient up to 6500 m^{-1} W^{-1}, approaching the range of the Rakich theory work. An increased propagation loss of 5.5 dB /cm did not prevent the first demonstration of net gain, with 0.4 dB net gain being achieved for an on-off gain of 2 dB in a 2.5 mm long device. This work also brought to light the issues of dimensional broadening, as significant variation in the mechanical quality factor was observed when the anchor length and number of components was varied. Theory work by Wolff [106] identified the intrinsic issues and causes of this dimensional broadening. Small continuous device perturbations alter the properties of the optical and acoustic mode, which slightly alter the Brillouin frequency shift along the waveguide and result in broadened peaks. Wolff also explored the SBS dynamics in the presence of nonlinear loss and calculated a figure of merit, which determined the maximum attainable amplification for a set of given device parameters [107, 108].

Table 2.1: Summary of demonstrated SBS performance in planar integrated waveguide devices

Device	Year	Type	Gain dB	Net Gain dB	G_{SBS} /W /m	A_{eff} µm^2	$G_{SBS} \times L_{eff}$
As_2S_3 Rib [92]	2012	B	22	16.5	320	2.3	13
Si/Si_3N_4 Membrane [96]	2013	F	0.4	–	2500	0.1	3
Si nanowire pillar [103]	2015	F	4.4	–	3200	0.1	50
Si nanowire [105]	2016	F	2.0	0.5	6500	0.1	12
Si membrane [104]	2016	F	6.9	5	1150	0.25	31
As_2S_3 Rib spiral [89]	2016	B	52	40	500	1.5	40
Si membrane [109]	2017	F_{SIMS}	3.5	2.3	470	0.35	10

*Silicon devices are suspended in air, F, FBS; F_{SIMS}, forward stimulated inter-modal scattering; B, backwards SBS; G_B, Brillouin gain coefficient; A_{eff}, effective mode area

The analysis of SBS with nonlinear losses by Wolff indicated that achieving large net gain requires the use of long low loss waveguides [108]. Achieving low propagation losses in high index contrast systems is very difficult, and the added issues of dimensional broadening further harm this proposition. In 2016 the group of Rakich dealt with both issues simultaneously through the use of a suspended all silicon rib waveguide [104]. The shallow etched rib design reduced propagation losses to 0.2 dB /cm, the free carrier lifetime to less than 2 ns and minimised effects of dimensional broadening. The increased A_{eff} resulted in a lower SBS gain coefficient of 1100 m^{-1} W^{-1}, however the increased L_{eff} greatly compensated this with these devices achieving the highest on-off gain in silicon SBS devices, with 7 dB, and more impressively, a significantly improved net gain of 5 dB. Highly efficient cascading was also observed under suitable pumping conditions. The overall available gain was still limited by nonlinear losses present at 1550 nm. In very recent work Kittlaus demonstrated that these devices are also capable of forward *inter-mode* scattering [110]. What makes this work particularly exciting is the ability to use on-chip mode multiplexers within planar circuits, enabling significantly enhanced functionality beyond what has been demonstrated in PCFs. A summary of the results of this section are provided in the form of Table 2.1, with extracted images presented in fig. 2.17.

2.4.3 Brillouin Scattering and Lasing In Resonators

The conditions for achieving strong Brillouin interactions in resonators are quite distinct from those in waveguides. Large circulating powers, achieved through high finesse optical cavities, place less importance on the SBS gain coefficient and more focus on cavity design. Significant interest had developed in microresonators during the 1990s [111], with impressive results being achieved through low loss spherical resonators formed by melting the end of an optical fiber. The importance of these devices for nonlinear optics was made clear in the 2002 paper by Spillane [112], which demonstrated Raman lasing with 50 µW of optical power in a spheres with diameters in the tens of µm range and optical quality factors of 10^9. While SBS was not observed generally, the authors state that they could observe SBS if the azimuthal mode splitting satisfied the SBS shift (no plots were given). In the same year the group of Vahala also demonstrated toroid based resonators fabricated on a silicon chip, with optical Q factors reaching 10^8 [113]. This breakthrough enabled significantly higher device density than previous works, though external coupling with fiber tapers was still standard. Raman lasing was consequently observed in these chip based toroid devices in 2004, with no observation of Brillouin scattering due to the lack of appropriate mode families spaced at the SBS shift [114].

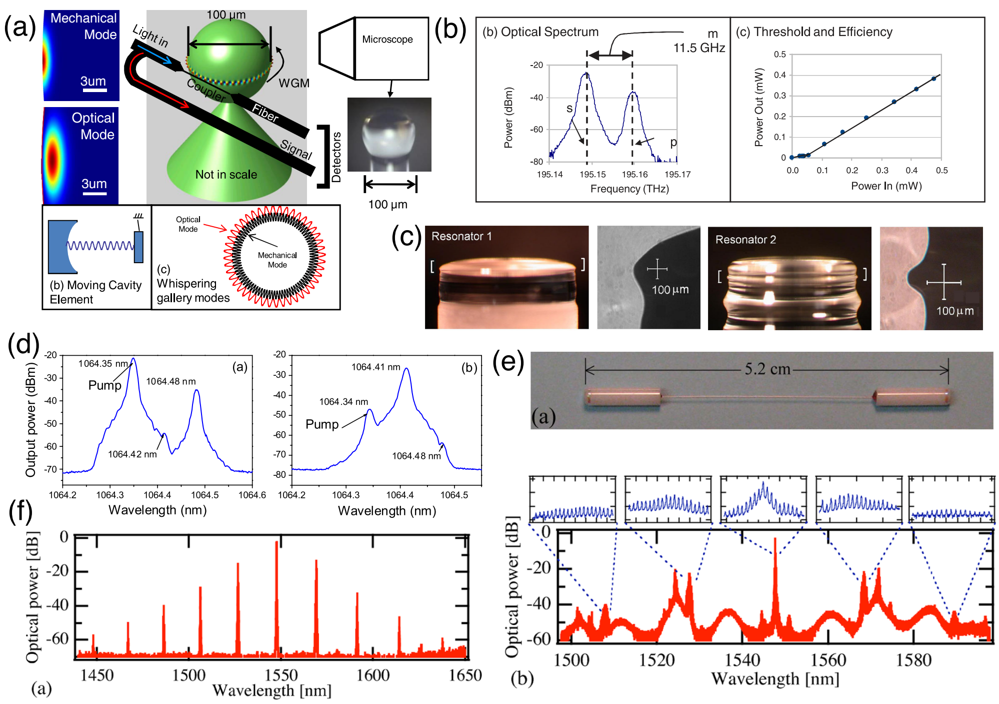

Figure 2.18: (a) Brillouin lasing scheme in silica microresonator [115] (b) Measured optical spectrum and slope efficiency of Brillouin laser (c) Crystalline resonators with mm diameters [116] (d) Optical spectrum in the forward (left) and backwards (right) positions, above the lasing threshold (e) HNLF Fabry-Perot resonator configuration [117] (f) Spectral measurements of comb output, Brillouin lines shown in inset on right.

In 2009 three groups definitively observed SBS in chip scale devices with quite distinct configurations, all published in *Physical Review Letters* [115–117]. The work of Tomes and Carmon observed SBS in a 100 µm diameter spherical silica resonator [115]. In these devices both the optical and acoustic modes are whispering gallery modes. Azimuthal mode families with approximately 11 GHz mode spacing were used to match the expected SBS shift at the 1550 nm pump wavelength. The 300×10^6 optical Q enabled Brillouin lasing with less than 0.1 mW of pump power, and a high slope efficiency of 90 % was achieved with appropriate coupling. The group of Maleki investigated Brillouin lasing in a crystalline CaF_2 whispering gallery mode resonator [116]. This resonator has a diameter of 5.5 mm such that the longitudinal cavity spacing was close to the expected SBS shift of 17.7 GHz at the 1064 nm pump wavelength. The large size of the cavity length meant that the acoustic wave did not build up significantly over a round trip, and would act more like SBS in a bulk sample. Although two different resonators were tested with slightly different transverse geometries, lasing was only observed in a resonator which had an "abundance" of modes spaced by 10s of MHz, relaxing the precise diameter matching required for phase matching. With these conditions Brillouin lasing was demonstrated with a threshold of 10 µW, with significant cascading and other nonlinear effects observed as the power was increased. The final demonstration was quite distinct from the other two works, the group of Diddams demonstrated the interaction of multiple nonlinearities in a Fabry-Perot resonator formed of highly nonlinear fiber (HNLF) with polished facets [117]. This monolithic device was 5.2 cm long and had reflectivities of 99.9 %, achieving a finesse greater than 550, and thus large circulating powers. The mode spacing was around 2 GHz, a fifth of the expected SBS shift, and external coupling was performed with free space lenses. When pumped above 500 mW a number of lines spaced at around 2 THz were generated from four wave maxing, with a Brillouin comb filling the spectrum at a spacing of 10 GHz. These works are summarised in Figure 2.18.

While the 2009 results demonstrated traditional backwards SBS, there was also interest in forward scattering in resonators. In 2011 Bahl, within the group of Carmon, demonstrated forward *inter-mode* Brillouin scattering between different whispering gallery modes, in a 100 µm diameter silica microsphere [118]. Acoustic modes with frequencies ranging from 50 MHz to 1.5 GHz were observed as an external pump laser was slowly swept from 1520 nm to 1570 nm. The experiments focused on low frequency acoustic waves, due to the exceptionally high *mechanical* quality factors available for 100 MHz range surface acoustic waves. A phonon lifetime of 40 µs was measured for a 134 MHz Rayleigh mechanical wave. In the following year Bahl used these acoustic waves to observe spontaneous Brillouin *cooling* [119]. The anti-Stokes scattering process wave was generated selectively by pumping at a wavelength where the Stokes wave could not resonate. Because the upshifted anti-Stokes wave *removed* acoustic phonons from the system, the number of spontaneous phonons in the mode was reduced, effectively cooling the resonance mode. The mechanical linewidth increased, resulting in less integrated power, by a factor of 10 as the pump power was increased from 10 µW to 100 µW. By swapping the pump to the higher frequency optical mode only Stokes scattering can occur and heating was also experimentally demonstrated.

These early demonstrations of Brillouin lasing in microresonators achieved phasematching by relying on somewhat random spacing between different optical mode families. In 2012 the group of Vahala introduced a new device paradigm with on-chip ultra high Q silica wedge resonators which were defined *completely*

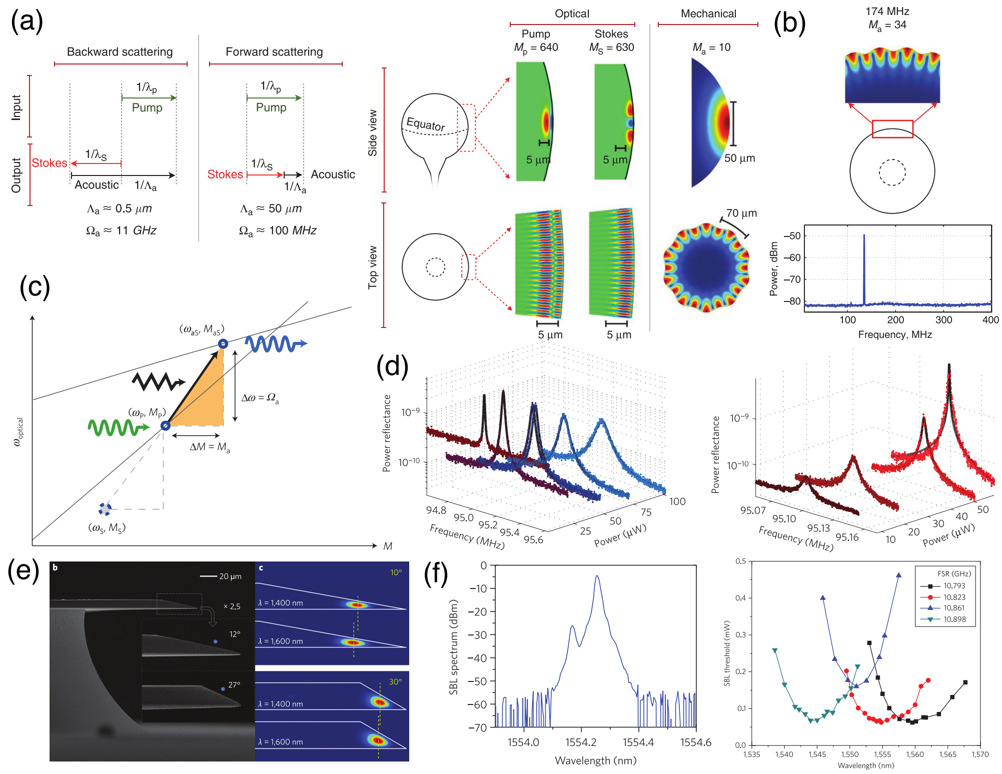

Figure 2.19: (a) Scheme describing SBS using surface acoustic waves in microresonators [118] (b) Simulated acoustic wave and generated beatnote from 130 MHz acoustic wave (c) Phasematching requirements for spontaneous cooling. Only the Stokes or anti-Stokes process is excited due to density of states control in microresonator [119] (d) Experimental measurements of spontaneous cooling (e) Geometry of on-chip Ultrahigh-Q wedge resonators [120] (f) Brillouin lasing in wedge resonator. Precise diameter control enables low threshold lasing over desired wavelength ranges

through lithographic processes [120]. This enabled exquisite dimensional control, allowing sub MHz precision for GHz resonator spacings. Exceptional low losses were also possible for the appropriate wedge design, unloaded optical Q factors approaching a *Billion* were achieved in larger devices. With such accurate control the spacing between two cavity modes was deterministically controlled to enable Brillouin lasing with 50 µW thresholds. Extra experiments demonstrated that significant Stokes linewidth narrowing occurs in these devices, with sub-Hz linewidths achieved for KHz pump sources [121]. Controlling the coupling conditions to the resonator allowed for cascading of several lines with only mW pump levels. In 2013 the group of Vahala demonstrated pure microwave generation by beating cascaded Brillouin lines generated from the on-chip microresonator [122]. The noise of the generated microwave tones were comparable with commercial signal generators. More recently the low noise counter-propagating cascaded Stokes were used as an optical gyroscope [123]. The spacing between cascaded Stokes lines is inherently stable due to the generation from a single pump laser, the demonstrated rotation sensitivity was a factor of 40 higher than previous micro-optic based systems.

Microresonators can achieve very low power SBS operation, but integrating these devices in an optical circuit is difficult. One alternative is to use waveguide based schemes, where a large SBS gain coefficient can compensate for lower optical Q factors. After the initial demonstration of on-chip SBS in soft glass waveguides [124], a number of different schemes for enhancing SBS with resonators were investigated. The first scheme used weak (around 17 %) reflections off the facets of a straight 4 cm As_2S_3 waveguide to act as a Fabry-Perot cavity [125]. The SBS threshold was reduced by a factor of 4 and cascading of 2 Stokes and 1 anti-Stokes lines was observed for a pump peak power of 1.3 W. In 2013 Kabakova achieved efficient lasing by using the As_2S_3 chip as a short gain medium within a 20 m fiber loop cavity [126]. To minimise the roundtrip loss this particular device utilised on chip tapers [127], reducing the total insertion loss to 5.5 dB. A slope efficiency of 30 % was measured above the threshold of 330 mW, and the SBS laser linewidth was narrowed by a factor of 10 compared to the pump. Finally, Büttner inspected the Fabry-Perot configuration [128] with a a slight twist: an internal waveguide grating was used to enhance further the SBS process [90]. A quasi-CW pulse with peak powers of 2 W would generate 7 cascaded SBS lines, symmetrically spaced around the pump. Significant effort was placed on investigating the temporal dynamics of the cascading process. It was found that the different Stokes lines were phase locked, likely through four wave mixing [129], and that the pulse to pulse time dynamics were practically identical, as shown in Figure 2.20.

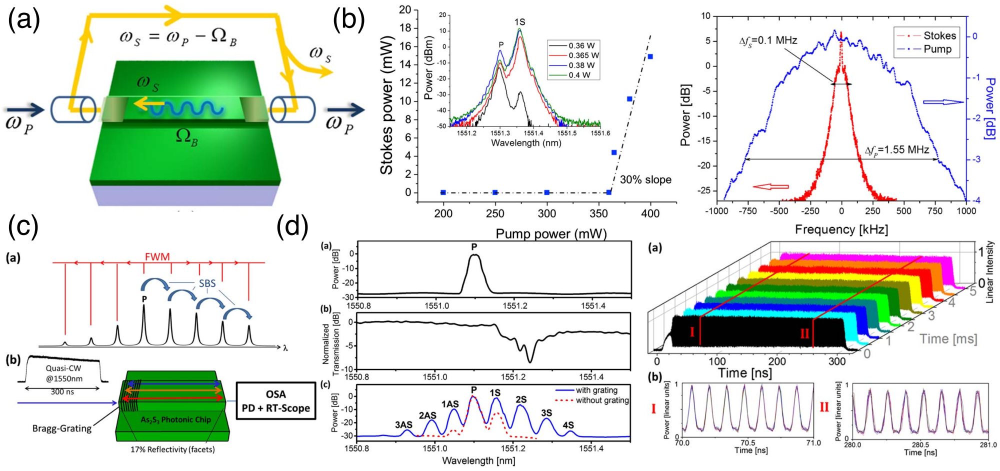

Figure 2.20: (a) Brillouin laser using fiber loop resonator and high gain As_2S_3 waveguide [126] (b) Slope efficiency and linewidth narrowing of the laser (c) Fabry-Perot configuration with internal grating [128] (d) Spectral and time domain measurements of generated frequency comb

Comments and List of Useful Resources

While researching the content for this chapter we came across, and utilised, a number of detailed references. For the benefit of the reader we itemise them below.

- Early history of optical fibers [130]
- History and context of SBS after the laser from a graduate student [131]
- Historical review of nonlinear optics using fibers [57]
- Discovery of Brillouin and Raman scattering from the Russian perspective [16]
- A detailed review of theory and experiment of SBS in single mode fibers up until 1983, including activities to suppress SBS [46]
- Recent reviews covering SBS in different systems [132–134]

Also while this chapter has covered a significant section of the literature it is by no means completely exhaustive. We have neglected to discuss a number of topics such as: phase conjugation using Brillouin scattering [135], spatial sensing using SBS [136, 137], Brillouin microscopy [138] or specific application areas using SBS within microwave photonics [139]. In general, starting with detailed review articles, and also different theses from students who worked in these areas, will provide sufficient detail for those with further interest into these points.

Chapter 3

Nonlinear Photonic Circuits

This chapter provides specific theory and background on optical waveguides and nonlinear optics in photonic circuits. We start with simple derivations of the optical wave equation, which then leads into a deeper discussion and understanding of optical waveguides and nonlinear optics. We then focus in further detail on the practical operation of photonic circuits comprising of linear and nonlinear components. The chapter finishes with a summary of the currently available foundry services, which allow external users to design devices.

3.1 Theory of Basic Concepts

In the first section of this chapter we explore the basic theory and concepts behind optical waveguides and nonlinear optics, after deriving the electromagnetic wave equation from Maxwell's equations.

3.1.1 Maxwell's Wave Equation

The propagation of electromagnetic waves is governed by Maxwell's equations, which can be represented in the following form

$$\boldsymbol{\nabla} \times \mathbf{E} = -\frac{\partial \mathbf{B}}{\partial t} \tag{3.1}$$

$$\boldsymbol{\nabla} \times \mathbf{H} = \mathbf{J} + \frac{\partial \mathbf{D}}{\partial t} \tag{3.2}$$

$$\boldsymbol{\nabla} \cdot \mathbf{D} = \rho_{\mathrm{f}} \tag{3.3}$$

$$\boldsymbol{\nabla} \cdot \mathbf{B} = 0 \tag{3.4}$$

where **E** and **B** are the electric and magnetic field vectors and **D** and **B** are corresponding electric and magnetic flux densities. The systems we explore in this thesis mostly contain no free charges, or free currents, such that ρ_{f} and **J** are both zero. Furthermore, we also assume that the device is non magnetic, such that

$$\mathbf{B} = \mu_0 \mathbf{H}$$

and have the constitutive relation for the flux density **D** as

$$\mathbf{D} = \epsilon_0 \mathbf{E} + \mathbf{P} \tag{3.5}$$

where ϵ_0 is the vacuum permittivity, μ_0 is the vacuum permeability and **P** is the induced electric polarisation.

Now if we take the curl of equation Equation (3.1) we have that

$$\boldsymbol{\nabla} \times \boldsymbol{\nabla} \times \mathbf{E} = -\boldsymbol{\nabla} \times \frac{\partial \mathbf{B}}{\partial t}$$

We now rearrange the right hand side and utilise Equation (3.2) to obtain

$$\boldsymbol{\nabla} \times \boldsymbol{\nabla} \times \mathbf{E} = -\mu_0 \frac{\partial^2}{\partial t^2} \mathbf{D}$$

with Equation (3.5), and by bringing the electric field terms to the left side we have

$$\boldsymbol{\nabla} \times \boldsymbol{\nabla} \times \mathbf{E} + \epsilon_0 \mu_0 \frac{\partial^2}{\partial t^2} \mathbf{E} = -\mu_0 \frac{\partial^2}{\partial t^2} \mathbf{P} \tag{3.6}$$

We can then use the relation from vector calculus

$$\boldsymbol{\nabla} \times \boldsymbol{\nabla} \times \mathbf{E} = \nabla(\boldsymbol{\nabla} \cdot \mathbf{E}) - \nabla^2 \mathbf{E}$$

If we now use the fact that $\nabla(\boldsymbol{\nabla} \cdot \mathbf{E}) = 0$, from Maxwell's equations, knowing the term is also small for nonlinear optics [140], to obtain the simplified wave equation

$$\nabla^2 \mathbf{E} - \epsilon_0 \mu_0 \frac{\partial^2}{\partial t^2} \mathbf{E} = \mu_0 \frac{\partial^2}{\partial t^2} \mathbf{P} \tag{3.7}$$

For linear optics the induced polarisation is described by the relation

$$\mathbf{P} = \epsilon_0 \chi^{(1)} \mathbf{E} \tag{3.8}$$

where $\chi^{(1)}$ is the linear susceptibility. To describe nonlinear optics we take a simple power expansion in $\mathbf{E}$ such that

$$\mathbf{P} = \epsilon_0 (\chi^{(1)} \mathbf{E}_1 + \chi^{(2)} \mathbf{E}_1 \mathbf{E}_2 + \chi^{(3)} \mathbf{E}_1 \mathbf{E}_2 \mathbf{E}_3 + \dots) \tag{3.9}$$

where $\chi^{(2)}$ and $\chi^{(3)}$ are the second and third-order nonlinear susceptibilities. We have separated the individual $\mathbf{E}$ terms for clarity. If we use the shorthand $\mathbf{P}_{\mathrm{NL}}$ for the higher order terms and we substitute the polarisation field back into Equation (3.7) we have that

$$\begin{aligned} \nabla^2 \mathbf{E} - \epsilon_0 \mu_0 \frac{\partial^2}{\partial t^2} \mathbf{E} &= \epsilon_0 \mu_0 \chi^{(1)} \frac{\partial^2}{\partial t^2} \mathbf{E} + \mu_0 \frac{\partial^2}{\partial t^2} \mathbf{P}_{\mathrm{NL}} \\ \Rightarrow \nabla^2 \mathbf{E} - \epsilon_0 \mu_0 (1 + \chi^{(1)}) \frac{\partial^2}{\partial t^2} \mathbf{E} &= \mu_0 \frac{\partial^2}{\partial t^2} \mathbf{P}_{\mathrm{NL}} \end{aligned}$$

Finally, using the fact that $n^2 = \epsilon/\epsilon_0 = 1 + \chi^{(1)}$ and that $\epsilon_0 \mu_0 = 1/c^2$ we arrive upon

$$\nabla^2 \mathbf{E} - \frac{n^2}{c^2} \frac{\partial^2}{\partial t^2} \mathbf{E} = \frac{1}{\epsilon_0 c^2} \frac{\partial^2}{\partial t^2} \mathbf{P}_{\mathrm{NL}} \tag{3.10}$$

which is the Maxwell's wave equation. Why is this equation known as the Maxwell's wave equation? If we recall the form of a generic wave equation in one spatial dimension, x, for some wave $u(x,t)$, we have that

$$\frac{\partial^2 u}{\partial x^2} = \frac{1}{v^2} \frac{\partial^2 u}{\partial t^2}$$

where v is the phase velocity of the wave $u(x,t)$. Let us now consider the case where the $\mathbf{P}_{\mathrm{NL}}$ term is zero, with simple rearranging of eq. (3.10) we have have

$$\nabla^2 \mathbf{E} = \frac{1}{c^2/n^2} \frac{\partial^2}{\partial t^2} \mathbf{E}$$

which is the form of the above wave equation, with the velocity now given by $v = c/n$, in a media with refractive index n. If we were in vacuum, then the electromagnetic wave would be moving at the speed of light c.

3.1.2 Optical Waveguides

To develop an understanding of the various properties of optical waveguides, we will begin by solving Maxwell's equations for a simple representative case, a dielectric slab waveguide. The working and process in this section follows the Guided-Wave Optics chapter of Saleh and Teich [141].

The slab waveguide, shown in fig. 3.1 consists of a high index material n_1, with thickness d, sandwiched between a lower index material n_2. Guidance in the slab waveguide is provided by total internal reflection (TIR) in the transverse direction, providing low loss propagation when the scattering angle $\bar{\theta}$ is beyond the critical angle θ_c, where $\theta_c = \sin^{-1}(n_2/n_1)$. For the sake of simplicity we assume that light travels in the $+z$ direction, that the problem is uniform in x and we define $y = 0$ along the centre of the waveguide.

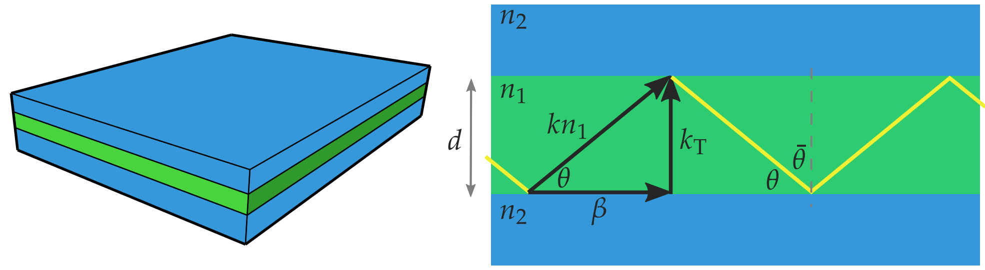

Figure 3.1: Geometry of a dielectric slab waveguide.

One set of solutions to the Maxwell's equations are expected to be plane waves of the form

$$e^{i(\mathbf{k}\cdot\mathbf{x}-\omega t)}$$

This is monochromatic light of frequency $\omega = ck_0$, travelling in direction $\mathbf{k}$, with wavelength λ where $k_0 = 2\pi/\lambda$ is the wavenumber. We will also assume that the field is polarised in the x-direction, with the reflections occurring in the y-z plane. We will first explore the properties of the propagation constant, and then move onto the modal fields of the waveguide.

Optical Propagation in Waveguides

For an electromagnetic wave to exist after any appreciably length, it needs to maintain constructive interference along the waveguide as it propagates. We implement this condition by starting with the requirement of standing waves across the core, which is the high index n_1 region, of the waveguide. This means that the phase accumulation on a single round trip is a multiple of 2π. Thus we have that

$$2dk_\mathrm{T} - 2\phi_\mathrm{R} = 2\pi m \tag{3.11}$$

where $k_\mathrm{T} \equiv k_{y,m}$ is the transverse wavevector, ϕ_R is the phase change on reflection and m is a positive integer. This condition means that, for a single wavelength, there will be discrete values of k_T. These discrete solutions determine the propagation constants of the waveguide *modes*. Modes are fields which will maintain the same transverse distribution and polarisation at all locations along the waveguide. We wish to determine the propagation constant β, which is k_z the wavenumber in the z direction, of the waveguide modes. From eq. (3.11) and simple trigonometry we have that

$$\beta_m^2 = (n_1 k_0)^2 - \left(\frac{\pi m + \phi_\mathrm{R}}{d}\right)^2 \tag{3.12}$$

The value of ϕ_R depends on the propagation angle θ in the following way [141]

$$\tan\left(\frac{\phi_\mathrm{R}}{2}\right) = \sqrt{\frac{\sin^2(\pi/2-\theta_\mathrm{c})}{\sin^2(\theta)} - 1} \tag{3.13}$$

Equation (3.13) can be combined with Equation (3.11) to form a transcendental equation in θ,

$$\tan\left(\frac{\pi d}{\lambda}\sin\theta - m\frac{\pi}{2}\right) = \sqrt{\frac{\sin^2(\pi/2-\theta_\mathrm{c})}{\sin^2(\theta)} - 1} \tag{3.14}$$

The left hand side of Equation (3.14) spans from zero to infinity and is periodic. The right hand side diverges at the origin and goes to zero at $\theta = \pi/2 - \theta_c$. The solutions of the equation, which can be solved graphically as shown in Figure 3.2a, determine the value of θ for the different modes m. With the value of theta in hand, we can solve for the propagation constant directly using

$$\beta_m = n_1 k_0 \cos\theta_m \tag{3.15}$$

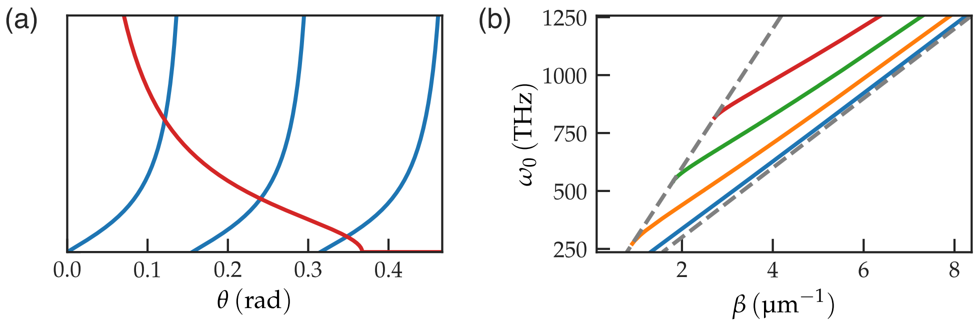

Figure 3.2: (a) Graphical representation of transcendental equation, solutions are found at the intercept points of the two curves. (b) Dispersion diagram of slab waveguide, showing first 4 modes only.

We can now consider some general features of this model. First of all, the number of modes will be determined by the number of intersections between the two curves. This is given directly by

$$M = \frac{\sin(\pi/2 - \theta_c)}{\lambda_0/2d} = \frac{2d}{\lambda_0}\sqrt{n_1^2 - n_2^2} \tag{3.16}$$

where M is rounded up to the nearest integer and $\sqrt{n_1^2 - n_2^2}$ is known as the numerical aperture, represented with NA. It is clear from the plots that, for any angle θ, there will *always* be at least one mode. For the higher order modes we have the concept of a cut-off frequency. For example, the $m = 1$ mode will be cut-off when at

$$\frac{2d}{\lambda_0} NA = 1$$

which corresponds to a cut-off frequency $\omega_{\text{cut},m}$ of

$$\omega_{\text{cut},m} = \frac{2\pi}{NA}\frac{c}{2d} m \tag{3.17}$$

Here we define a key parameter in optical waveguides, the effective refractive index, as

$$n_{\text{eff}} = \frac{\beta}{k_0} \tag{3.18}$$

When we consider the speed of light in a waveguide, the effective refractive index acts the same way as a normal refractive index in a bulk media. In other words, for the optical phase velocity we will have that

$$v_{\text{ph}} = \frac{c}{n_{\text{eff}}} \equiv \frac{\omega_0}{k_z} \tag{3.19}$$

This formulation brings about the question, how does the propagation constant vary with frequency? The fact that a glass prism can *disperse* a white light source, due to the change of refractive index with optical frequency within the material, is a well known and frequently taught topic. We can investigate the equivalence here by reformulating Equation (3.15) in terms of the optical frequency,

$$k_{z,m} = n_1 \frac{\omega_0}{c} \cos \theta_m \tag{3.20}$$

For a single frequency ω_0 we numerically solve Equation (3.14) to find θ, for the different modes m, and substitute this into Equation (3.20) to calculate the value of k_z. We have calculated the propagation constant for a range of frequencies and plotted the data in fig. 3.2b. Note that we have plotted this data with the k_z on the x-axis and ω_0 on the y-axis, which is a common convention. This result shows a number of interesting features. Firstly, that the calculated values are bound within two straight lines. These lines are the linear dispersion lines for the bulk refractive index of n_1 and n_2. When the guided modes approach cutoff, the n_{eff} approaches the index of the cladding. Secondly, that close to the cutoff frequency the slope of the curve can change significantly. This is an important observation, because while the phase of the electric field travels at the phase velocity, the energy of the wave travels at the *group* velocity. And this is given directly by the slope of the phase velocity

$$v_g = \frac{\mathrm{d}\omega}{\mathrm{d}k_z} \tag{3.21}$$

For the group velocity we also have a corresponding group index, which relates to the n_{eff} through the following,

$$v_g = \frac{c}{n_g} \qquad\qquad n_g = n_{\text{eff}} - \lambda \frac{\mathrm{d}}{\mathrm{d}\lambda}(n_{\text{eff}})$$

It is important to keep in mind that while we have assumed a constant refractive index for these materials, there is no *material* dispersion here. So, due to the simple guided nature of the waveguide modes, waveguides create significant differences to the propagation of light compared to a bulk medium made of the same material. The effects of dispersion, and the effective and group indices, are very important for the design and optimization of integrated components, linear *and* nonlinear. These effects will be explored throughout this chapter and the remainder of the thesis.

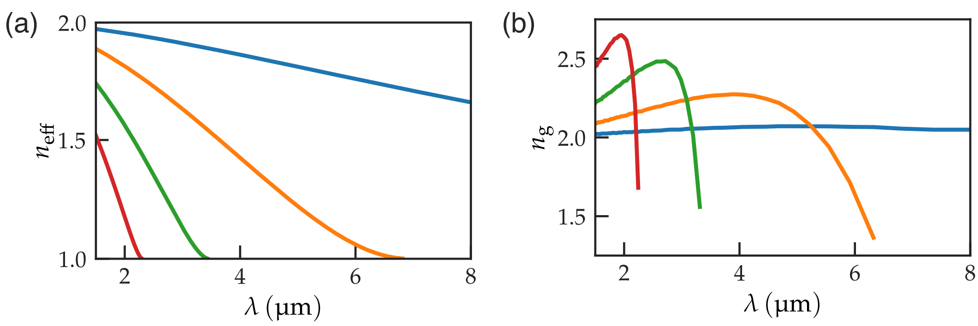

Figure 3.3: (a) Effective refractive indices and (b) group indices of modes calculated in fig. 3.2b.

Modal fields and polarisation

So far we have focused on the propagation properties of the modes of the waveguide. We will now discuss the electric field profiles of these waveguide modes. We return to the initial plane wave assumption for the solution to the Maxwell's equations in this structure. That is, that solutions will be of the form

$$e^{i(\mathbf{k}\cdot\mathbf{x}-\omega t)}$$

First of all, for the standing wave to form we require two plane waves in the y axis, with an $(m-1)\pi$ phase difference, such that the overall electric field has components like

$$e^{i(k_{y,\mathrm{m}}y+k_z z-\omega t)}+e^{i(-k_{y,\mathrm{m}}y+k_z z-\omega t)}e^{i(m-1)\pi}$$

thus for the x polarised field we will have

$$\mathbf{E}(x,y,z,t)=\hat{\mathbf{x}}u_{\mathrm{m}}(y)e^{i(k_z z-\omega t)} \tag{3.22}$$

where $u_{\mathrm{m}}(y)$ is the field component in the y direction which will be

$$u_{\mathrm{m}}(y)=\begin{cases} a_{\mathrm{m,e}}\cos(k_{\mathrm{y}}y)=a_{\mathrm{m,e}}\cos[n_1k_0\sin(\theta_{\mathrm{m}})y] & \text{for m even}\\ a_{\mathrm{m,o}}\sin(k_{\mathrm{y}}y)=a_{\mathrm{m,o}}\sin[n_1k_0\sin(\theta_{\mathrm{m}})y] & \text{for m odd}\end{cases}$$

where $a_{\mathrm{m,o}}$ and $a_{\mathrm{m,e}}$ are constants used for normalisation and maintaining that the field is real.

This covers the field in core, but the field can also extend into the cladding due to the boundary condition of tangential field components being continuous. Recalling our earlier requirement of monochromatic fields varying in time as $e^{-i\omega t}$, we can take Equation (3.10) and set the $\mathbf{P}_{\mathrm{NL}}$ term to zero as we are investigating the linear properties of the waveguide. This yields the Helmholtz equation

$$(\nabla^2-n^2k_0^2)\mathbf{E}=0 \tag{3.23}$$

For our general solutions $u_{\mathrm{m}}(y)$, in the cladding region this will then give

$$\frac{\mathrm{d}^2u_{\mathrm{m}}}{\mathrm{d}y^2}+((n_2k_0)^2-k_{\mathrm{z}}^2)u_{\mathrm{m}}=0$$

Making a simple substitution of γ^2, where $\gamma^2=k_{\mathrm{z}}^2-(n_2k_0)^2>0$, immediately yields

$$\frac{\mathrm{d}^2u_{\mathrm{m}}}{\mathrm{d}y^2}-\gamma^2u_{\mathrm{m}}=0$$

which has solutions of the form $e^{-\gamma y}$ or $e^{+\gamma y}$. For the sake of causality we require the fields to decay away from the core, and as such the appropriate solution is picked for the $+y$ plane or $-y$ plane. Using these requirements, and the matching of fields and continuity at the $y=\pm d/2$ boundaries, we can determine the solution of the field everywhere in the waveguide. We can now determine the components of the $\mathbf{H}$ field, using the calculated field $\mathbf{E}$ and Maxwell's equations.

We will finish this section with a discussion about the polarisation of the electric field. At the start of this section we made the assumption that the fields are polarised in the x axis. Was this an appropriate assumption? If we take the plane wave fields and put them into the divergence relations in Maxwell's equations, Equation (3.3) and Equation (3.4), we find that we require

$$\mathbf{E} \cdot \mathbf{k} = 0 \qquad \mathbf{H} \cdot \mathbf{k} = 0 \tag{3.24}$$

There are two ways to satisfy this condition, transverse electric (TE) modes and transverse magnetic (TM) modes, where the fields are related by

$$\text{TE:} \quad \mathbf{E} = (E_x, 0, 0) \quad \mathbf{H} = (0, H_y, H_z) \quad \text{TM:} \quad \mathbf{E} = (0, E_y, E_z) \quad \mathbf{H} = (H_x, 0, 0)$$

This means that for the x polarised field, which we have assume so far, we will indeed have

$$\mathbf{E} = E_x \hat{\mathbf{x}}$$

But we will also have another set of modes given by the TM polarisation where,

$$\mathbf{E} = E_y \hat{\mathbf{y}} + E_z \hat{\mathbf{z}}$$

The fields of these modes look very similar to Equation (3.22). The key difference is that the value of θ_{m} is distinct from the TE case due to the change in phase on reflection. The TM value is the same as Equation (3.13), but with an extra pre factor of $(-1/\sin^2(\theta))$. Thus for each value of m we will have two modes, a TE mode and TM mode.

3.1.3 Nonlinear Optics

At its most basic level, nonlinear optics Here we will give a brief introduction to nonlinear optics. In particular we will provide a few simple examples of nonlinear effects, the changes they cause in the system and the design requirements which need to be satisfied to induce strong interactions. We will explore the linear and quadratic electro-optic effects as well as four wave mixing (FWM).

As a brief reminder we can express the full electrical polarisation, including linear and nonlinear susceptibilities, as the following

$$\mathbf{P}(\omega) = \epsilon_0(\chi^{(1)}\mathbf{E}(\omega) + \chi^{(2)}\mathbf{E}(\omega_1)\mathbf{E}(\omega_2) + \chi^{(3)}\mathbf{E}(\omega_1)\mathbf{E}(\omega_2)\mathbf{E}(\omega_3) + \dots)$$

Here we have indicated the frequency of the different electric fields to highlight the fact that these nonlinear interactions can occur between waves with different frequencies, including constant fields, i.e zero frequency or DC fields. The possible number of permutations of such interactions is very high, in particular for the third order effects. For example, we can explicitly write out the *full* set of interactions for the $\chi^{(3)}$ as

$$\mathbf{P}_i(\omega_4) = \frac{1}{4}\epsilon_0 \sum_p \sum_{jkl} \chi^{(3)}_{ijkl}(\omega_4; \omega_1, \omega_2, \omega_3)\mathbf{E}_j(\omega_1)\mathbf{E}_k(\omega_2)\mathbf{E}_l(\omega_3) \tag{3.25}$$

where *ijkl* can each be x, y or z, polarised and $\sum_p$ indicates that we sum over all the distinct permutations of ω_1, ω_2 and ω_3. To satisfy energy conservation we must have that $\omega_4 = \omega_1 + \omega_2 + \omega_3$, though frequencies can be degenerate (i.e $\omega_1 = \omega_2$) or be constant in time (i.e $\omega_1 = 0$). One question which arises is, what stops these multiple sets of interactions from all occurring simultaneously? The answer is that for a specific interaction to build over appreciable length scales we must satisfy a *phase matching* condition. To help develop an intuition for this we will provide finer detail in the case of FWM later in this section.

The precise derivation of the effects discussed in this section are quite stringent and we will not go into them here. We refer the reader to a number of textbooks on nonlinear optics, in particular the work of Boyd [140] and Agrawal [142], with the text by Geoffrey New [143] providing a high level introduction to the area. Third order nonlinear optics using planar waveguides was considered in an early review of Stegeman [144].

Optical Kerr Effect

The optical Kerr effect is an important nonlinear effect where, through the $\chi^{(3)}$ non-linearity, a strong pump wave with frequency ω_2 and intensity $I(\omega_2)$ changes the refractive index of a weak probe at ω_1. To understand how strong this interaction is and how it relates to the physical parameters of a device we explore Equation (3.25) for this specific case. If the two frequencies have the same polarisation then we will have a term within the nonlinear polarisation

$$\mathbf{P}_x(\omega_1) = \frac{3}{2}\epsilon_0\chi^{(3)}_{xxxx}(\omega_1;\omega_2,-\omega_2,\omega_1)|\mathbf{E}_x(\omega_2)|^2\mathbf{E}_x(\omega_1) \tag{3.26}$$

We can first consider a more specific case where the frequencies are the same, $\omega_2 = \omega_1$, and the intense light changes its own index.

$$\mathbf{P}_x(\omega) = \frac{3}{4}\epsilon_0\chi^{(3)}_{xxxx}(\omega;\omega,-\omega,\omega)|\mathbf{E}_x(\omega)|^2\mathbf{E}_x(\omega) \tag{3.27}$$

If we now consider an electric field $\mathbf{E}(\omega) = E_0\cos(k_x x - \omega t)$ then the *total* polarisation will be given by

$$\mathbf{P}_x(\omega) = \epsilon_0\left(\chi^{(1)} + \frac{3}{4}\chi^{(3)}_{xxxx}|\mathbf{E}_x(\omega)|^2\right)\mathbf{E}_x(\omega)$$

If we recall the definition of the linear susceptibility, Equation (3.8), we find that this looks remarkably similar. In this case we can consider what will the *new* refractive index be, due to this nonlinear correction. We can define a corrected susceptibility $\Delta\chi$, which includes these two terms, such that

$$\Delta\chi = \chi^{(1)} + \frac{3}{4}\chi^{(3)}_{xxxx}|\mathbf{E}_x(\omega)|^2 \equiv \chi_{\mathrm{L}} + \chi_{\mathrm{NL}}$$

Now we use the fact that $n = (1+\chi)^{1/2}$ and that $\chi_{\mathrm{L}} \gg \chi_{\mathrm{NL}}$ to form a Taylor expansion around $1+\chi^{(1)}$ we will have

$$\begin{aligned}
n_{\mathrm{NL}} &= (1+\Delta\chi)^{1/2} \\
&= (1+\chi_{\mathrm{L}}+\chi_{\mathrm{NL}})^{1/2} \\
&\approx (1+\chi_{\mathrm{L}})^{1/2}\left(1+\frac{1}{2}\frac{\chi_{\mathrm{NL}}}{(1+\chi_{\mathrm{L}})}\right) \\
&= n(1+\frac{1}{2n^2}\frac{3}{4}\chi^{(3)}_{xxxx}|\mathbf{E}_x(\omega)|^2) \\
&= n(1+\frac{1}{2n^2}\frac{3}{4}\chi^{(3)}_{xxxx}\frac{2I}{\epsilon_0 nc}) \\
&= n + n_2 I
\end{aligned}$$

So we end up with an index change which is directly proportional to the intensity and the nonlinear index n_2 i.e $\Delta n = n_2 I$. The n_2 parameter is related to $\chi^{(3)}$ directly through the last line of the above,

$$n_2 = \frac{3}{4n^2\epsilon_0 c}\chi^{(3)} \tag{3.28}$$

The intensity dependent refractive index is unavoidable in most $\chi^{(3)}$ interactions. For the sake of phase matching, it is convenient to think about the additional phase shift generated from this change in index. The self induced phase shift is referred to as self phase modulation (SPM) and the phase shift from a strong pump onto a weak probe is known as cross phase modulation (XPM). It is standard to consider these effects in terms optical power instead of intensity. For example, the nonlinear phase shift induced by SPM from a pump power P_p, through a medium length L, is given by

$$\phi_{\mathrm{NL}} = \gamma_{\mathrm{K}} P_p L \tag{3.29}$$

where γ_{K} is referred to as the nonlinear coefficient and A_{eff} is the effective area of the propagating mode. For weakly guiding systems, like optical fiber or propagation through a bulk media, we have that

$$\gamma_{\mathrm{K}} = k_0 n_2 / A_{\mathrm{eff}} \qquad\qquad A_{\mathrm{eff}} = \frac{\left(\int_\infty |\mathbf{E}_t|^2 \,\mathrm{d}A\right)^2}{\int_\infty |\mathbf{E}_t|^4 \,\mathrm{d}A} \tag{3.30}$$

where $\mathbf{E}_t$ are the transverse electric field components of the mode [145, 146]. In typical experiments γ_{K} is readily measurable, the corresponding n_2 and $\chi^{(3)}$ can then be extracted if the other parameters are known to high enough accuracy.

Pockels effect

While $\chi^{(3)}$ effects are universal to all media, though the strength can vary considerably, the $\chi^{(2)}$ susceptibility is non-zero only in systems which *lack* a centre of inversion symmetry [140]. This means that all isotropic and amorphous glasses do not exhibit the effect, and in general different forms of crystals are required for experiments utilising the $\chi^{(2)}$. Even so, the $\chi^{(2)}$ nonlinearity is utilised in a wide variety of rich applications, and is very crucial to modern society enabling green laser pointers and, more seriously, modern telecommunications via external modulation [147]. We will now describe the linear electro-optic effect, or Pockels effect, which is commonly used in external modulators.

The electro-optic effect is the linear change in refractive index, arising from a constant external electric field. To keep the following derivation concise we will ignore the tensor nature of the nonlinear susceptibility and assume the fields are polarised in the same direction. We follow a similar argument to the optical Kerr effect, if we consider an electric field consisting of a DC component with amplitude E_0 and a component at frequency ω i.e $\mathbf{E} = E_0 + E_\omega \cos(k_x x - \omega t)$ we have

$$\begin{aligned}\mathbf{P}(\omega) &= \epsilon_0(\chi^{(1)}\mathbf{E} + \chi^{(2)}\mathbf{EE})\\ P(\omega) &= \epsilon_0\left(\chi^{(1)}(E_0 + E_\omega\cos(k_x x - \omega t)) + \chi^{(2)}(E_0 + E_\omega\cos(k_x x - \omega t))^2\right)\end{aligned}$$

Now, we are interested in terms varying at frequency ω, so factorisation will give

$$P(\omega) = \epsilon_0 \left(\chi^{(1)} + 2\chi^{(2)} E_0\right) E_\omega \cos(k_x x - \omega t) \tag{3.31}$$

It is clear from the previous section that this corresponds to a change in the original material index, and if we assume the same approximations as before, we should have a change in index Δn corresponding to

$$\Delta n = \frac{E_0}{n}\chi^{(2)} \equiv \frac{1}{2} r n^3 E_0 \tag{3.32}$$

where we have introduced the electro-optic coefficient r, which is proportional to the $\chi^{(2)}$ and can be negative. Thus, we can induce a proportional index change directly with a DC electric field.

We have been discussing modulation, but how does this occur? Imagine that, instead of our DC field, we now have a sinusoidally varying field with frequency ω_{RF}. As long as frequency of the ω_{RF} is much smaller than the optical frequency ω the above assumptions will all apply. A changing index will result in a changing phase, thus if we vary the electric field at ω_{RF} we will induce a *phase modulation* at this same frequency. By placing this modulation region within an interferometer, such as a Mach-Zehnder interferometer (MZI), the phase modulation can be converted into an *intensity* modulation. To maintain phase stability such components are typically required to be integrated.

Four Wave Mixing

Four wave mixing is a widely utilised nonlinear effect which can create new optical frequencies, conjugate optical signals and act as a phase sensitive amplifier [142]. A key aspect of FWM, unlike the electro-optic effects discussed prior, are the effects of phase matching. A thorough derivation of four wave mixing is beyond the focus of this work. Instead we will briefly cover the coupled wave equations and discuss important cases and outcomes of these.

We will also focus here on the specific case of degenerate four wave mixing (DFWM), where the optical inputs are a strong pump wave at ω_p and a co-propagating wave, often referred to as the signal, at frequency ω_s. The DFWM process will generate a new wave, the idler, at frequency ω_i. The frequency of ω_i is determined by energy conservation, such that $\omega_i = 2\omega_p - \omega_s$. The interactions between these multiple propagating waves are calculated from a set of coupled wave equations, derived from the Maxwell's equation [140, 142], which are the following for complex field amplitudes $E_p, E_s,$ and E_i:

$$\begin{aligned}
\frac{\mathrm{d}E_p}{\mathrm{d}z} &= -\frac{\alpha}{2}E_p + i\gamma_{\mathrm{K}}\left[(|E_p|^2 + 2(|E_s|^2 + |E_i|^2))E_p + 2E_s E_i E_p^* \exp(i\Delta k z)\right] \\
\frac{\mathrm{d}E_s}{\mathrm{d}z} &= -\frac{\alpha}{2}E_s + i\gamma_{\mathrm{K}}\left[(|E_s|^2 + 2(|E_i|^2 + |E_p|^2))E_s + E_i^* E_p^2 \exp(-i\Delta k z)\right] \\
\frac{\mathrm{d}E_i}{\mathrm{d}z} &= -\frac{\alpha}{2}E_i + i\gamma_{\mathrm{K}}\left[(|E_i|^2 + 2(|E_s|^2 + |E_p|^2))E_i + E_s^* E_p^2 \exp(-i\Delta k z)\right]
\end{aligned}$$

where α is the propagation loss and $\Delta k = k_s + k_i - 2k_p$ is the linear phase mismatch for the respective propagation constants $k_p, k_s,$ and k_i of the involved waves. The presence of the phase mismatch means that the phase of the driven nonlinear wave will become offset from the driving waves. To understand the length scale over which this occurs it is convenient to think of the coherence length: the distance at which the waves will be out of phase by 180°, which is given simply by

$$L_{\text{coh}} = \frac{2\pi}{\Delta k} \tag{3.33}$$

Returning to the coupled wave equations, the first set of terms in the square brackets are due to the SPM and XPM, and the second term is the phase mismatch, $\Delta k = 0$ for perfect phase matching. In this case we have that $2k_p = k_s + k_i$, and also from energy conservation $2\omega_p = \omega_s + \omega_i$. We can understand that two pump photons will become one idler photon and one signal photon, and that all of these photons need to travel in such a way that momentum is conserved. We discussed in section 3.1.2 how the propagation constant at a particular frequency can be tailored with the dimensions of a waveguide, by using this effect highly distinct frequencies can be used phasematched.

If we assume that the pump is significantly stronger than the other waves then the equations simplify to

$$\frac{\mathrm{d}E_p}{\mathrm{d}z} = -\frac{\alpha}{2}E_p + i\gamma_{\mathrm{K}}(|E_p|^2 E_p) \tag{3.34}$$

$$\frac{\mathrm{d}E_s}{\mathrm{d}z} = -\frac{\alpha}{2}E_s + 2i\gamma_{\mathrm{K}}|E_p|^2 E_s + \gamma_{\mathrm{K}} E_i^* E_p^2 \exp(i\Delta k z) \tag{3.35}$$

$$\frac{\mathrm{d}E_i}{\mathrm{d}z} = -\frac{\alpha}{2}E_i + 2i\gamma_{\mathrm{K}}|E_p|^2 E_i + \gamma_{\mathrm{K}} E_s^* E_p^2 \exp(i\Delta k z) \tag{3.36}$$

These equations can then, if desired, be further separated into the propagating optical powers and phases [148, 149].

The effects of SPM and XPM result in extra phase accumulation, creating a *nonlinear* phase matching condition. If the pump remains undepleted, i.e $P_p \gg P_s$, we can introduce the new phase mismatch parameter $\kappa = \Delta k + 2\gamma_{\mathrm{K}} P_p$. If we then assume that the idler power is zero at the input of the waveguide, the solutions of the above equations can be calculated analytically for the output power of the idler and signal [142]. For a device length L and pump input power P_p we have that

$$P_s(L) = \exp(-\alpha L) P_s(0) \left(1 + \left[\gamma_{\mathrm{K}} P_p \frac{\sinh(g L_{\text{eff}})}{g}\right]^2\right)$$

$$P_i(L) = \exp(-\alpha L) P_s(0) \left[\gamma_{\mathrm{K}} P_p \frac{\sinh(g L_{\text{eff}})}{g}\right]^2$$

where the parametric gain coefficient g is given by

$$g^2 = (\gamma_{\mathrm{K}} P_p)^2 - (\kappa/2)^2 \equiv -\Delta k\left(\frac{\Delta k}{4} + \gamma_{\mathrm{K}} P_p\right)$$

and L_{eff} is effective length, essentially correcting for the pump loss through the medium, and is given by

$$L_{\text{eff}} = \frac{1 - \exp(\alpha L)}{\alpha}$$

We can explore the FWM conversion efficiency, $\eta = P_i(L)/P_s(0)$ in two distinct limits by starting with the Taylor expansion of sinh,

$$\eta = \exp(-\alpha L)\left[\gamma_{\mathrm{K}} P_p \frac{\sinh(g L_{\mathrm{eff}})}{g}\right]^2$$
$$\eta = \exp(-\alpha L)(\gamma_{\mathrm{K}} P_p)^2 \left(\frac{g L_{\mathrm{eff}}}{g} + \frac{g^3 L_{\mathrm{eff}}^3}{3! g} + \dots\right)^2$$
$$\eta = \exp(-\alpha L)(\gamma_{\mathrm{K}} P_p L_{\mathrm{eff}})^2 \left(1 + \frac{g^2 L_{\mathrm{eff}}^2}{6} + \dots\right)^2$$

If the signal wavelength is close the pump, in the range of a few nm, then $\Delta k \approx 0$ and the higher order terms of the Taylor expansion will go to zero, resulting in

$$\eta = \exp(-\alpha L)(\gamma_{\mathrm{K}} P_p L_{\mathrm{eff}})^2 \tag{3.37}$$

In this limit the converted idler power increases with the square of the pump power. The conversion efficiency can be measured precisely with a typical optical spectrum analyser (OSA), enabling high accuracy measurements of γ_{K} directly, even for low pump powers. We adopt this technique for measuring γ_{K} in thick silicon waveguides in Chapter 7.

Finally we can consider the case of perfect phase matching, where $\kappa = 0$. In this case $g = \gamma_{\mathrm{K}} P_p$ and $\gamma_{\mathrm{K}} P_p L_{\mathrm{eff}} \gg 1$, and we can then approximate $\sinh(x) \approx \exp(x)/2$. Thus we will have exponential gain for the signal and idler, until the pump begins to deplete, with the conversion efficiency being given by

$$\eta = \frac{1}{4}\exp(-\alpha L)(\gamma_{\mathrm{K}} P_p)^2 \exp\left(2\gamma_{\mathrm{K}} P_p L_{\mathrm{eff}}\right) \tag{3.38}$$

Achieving the exponential gain condition over even a small wavelength region requires significant optimisation of system characteristics, including control of *higher* order dispersion terms. We will discuss the opportunities available in waveguides for tailoring dispersion in the next section.

Dispersion engineering and γ_{K} in waveguides

Waveguides provide a number of avenues to achieve phase matching. At the same time, sub-wavelength waveguides in high index materials, such as silicon or As_2S_3, possess geometries which greatly modify the modal features. These waveguides have properties which make the previous definition of γ_{K} inappropriate, needing corrections for multi material systems, slow light effects and changing modal field components. We will discuss these two points below.

Satisfying phase matching conditions for the desired nonlinear processes is critical. In early fibers phasematching could occur through the use of multiple *modes*, each with their own dispersion, either between the TE and TM fundamental modes or to higher order mode families [57, 150–153]. Techniques quickly developed to utilise modal dispersion of a single mode fiber mode, birefringence of a single fiber mode, and split pumps for phasematching different nonlinear processes [57, 154]. Key breakthroughs occurred with the development of small core highly nonlinear fibers, such as micro-structured fibers and PCFs [155], and the creation of a photonic band gap allowed for flexible tuning of the modal dispersion. With the development of low loss, high confinement integrated planar waveguides in the early 2000's, dispersion engineering with waveguide widths in Si nanowires [156–158] and As_2S_3 rib waveguides[159–161] proved highly effective. By taking into account the signs of the higher order dispersion terms when designing the waveguides, researches phasematched processes over exceedingly wide wavelengths, such as 1.5 µm and 3.5 µm simultaneously [162–164]. The choice of cladding material provides another degree of freedom for tuning the overall dispersion, with a range of dielectrics or air being used [162, 165–167]. Finally, as in the case of fibers, the use of photonic band gap guidance in photonic crystal waveguides provides significant freedom for tailoring dispersion, and can provide enhancement of nonlinear interactions through the increased group index [168–170].

3.2 Nonlinear Integrated Circuits

Integrated optics has existed for almost half a century, since the birth of the field following the publications by Miller and colleagues in volume 48 of *The Bell System Technical Journal* [171]. Modern integrated optical devices generally utilise lithographic processes to fabricate planar circuits. The flexibility of lithographic tools allows for a wide range of materials and geometries to be exploited, with the choice typically depending on the intended application. These systems can be categorised based on a number of different characteristics, which we will explore below. As well as the powerful flexibility of lithography, current fabrication techniques are capable of combining multiple sets of materials. This is known as hybrid integration and provides the opportunity to optimise individual components within an optical circuit, at the cost of added fabrication complexity. Integrated optical circuits can be simple, just a straight waveguide with external coupling is technically a circuit, or can combine multiple building blocks of linear, active and nonlinear components. We will commence with a discussion on design geometries and materials for linear and nonlinear components. This leads to a detailed discussion on the considerations for forming optical circuits, before finishing this section with a focus on fabless photonic platforms available to external users. To further place the following section in context, we have provided an overview of the early and pre-history of integrated optics in chapter B.

3.2.1 Linear and Nonlinear Waveguides: Materials and Geometries

Modern waveguide devices are exceptionally diverse, making comparisons between even basic systems not straightforward. To help guide our discussion we note that waveguides can be considered in three main classes, based on their use *within* a circuit; linear, nonlinear and active. Active waveguides are technically a subset of nonlinear waveguides, but as they require external connections with electronic devices the fabrication processes and materials which are used is more restrictive than a general circuit. The work in this thesis focuses on linear and nonlinear circuits, as such we will not go into fine detail on active waveguide components here. The characteristics of different waveguides are governed by the intrinsic materials, and the fabrication technologies the materials are compatible with. Some common technology platforms, with base materials and refractive index, used in integrated optics are

- Compound Semiconductors (or III-V): InP (3.2), $Al_xGa_{1-x}As$ (3.3)
- Semiconductors: Si (3.5)

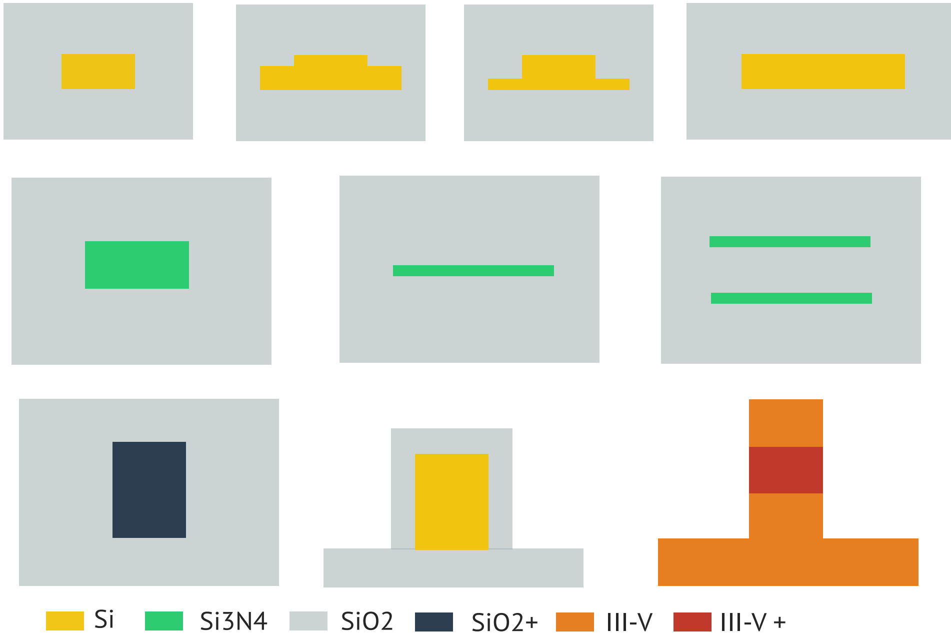

Figure 3.4: Representative geometries of waveguides found in different fabrication platforms. The + indicates a higher index than the base material.

- Dielectrics: Doped SiO_2 (1.5–1.9), Si_3N_4 (2.0), As_2S_3 (2.4)
- Nonlinear Crystals: Li_3NbO_3 (2.2), AlN (2.1)

It is highly desirable to utilise materials which are capable of being processed at the wafer scale, with preference to techniques which can be mapped directly to tools used for fabricating electrical semiconductor circuits, such as deep ultra violet (DUV) lithography and reactive ion etching (RIE) used in the complementary metal oxide (CMOS) electronics process. All of the above materials have device demonstrations using photolithography, in particular SOI has had extensive research on a number of CMOS pilot lines [172–178]. Here we will frame our discussions around features and tradoffs of fabricated waveguides, and limit discussions of fabrication processes except where critically required.

Linear Waveguides

Linear waveguides will generally form the basis of an optical circuit by being combined to form basic building blocks and being used for routing within the circuit. Waveguides can be formed out of a wide range of geometries, with typical geometries shown in fig. 3.4. For linear waveguides, which are building blocks of larger linear components and circuits, there are three key metrics

- Number of modes: Single mode operation desirable in circuits
- Compactness: Bending radius and device density
- Insertion Losses: Propagation Loss and coupling loss

These metrics are related to design and material/fabrication choices, however they are all related to one primary characteristic: the index contrast Δn between the waveguide core n_{core} and cladding n_{clad}, $\Delta n = n_{\text{core}} - n_{\text{clad}}$. For waveguides which are partially etched the index contrast is between the *effective* indexes from the core and the slab region [179]. In the following we will describe how the index contrast affects these three metrics.

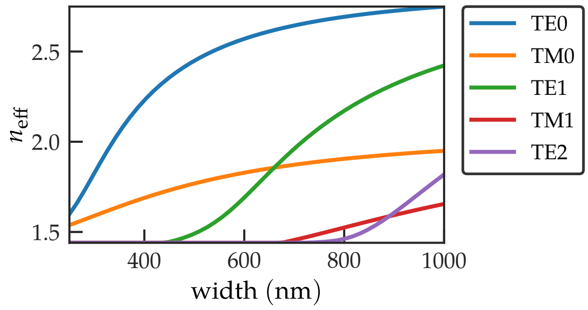

Figure 3.5: Increase in waveguide modes as width is increased.

Single mode operation within a circuit greatly simplifies design and simulation complexity, and the easiest way to achieve this is to use single mode optical waveguides. To understand this requirement we recall the condition for the number of modes within a slab waveguide, eq. (3.16), of thickness d and an optical wave with wavelength λ_0,

$$M = \frac{2d}{\lambda_0}\sqrt{n_{\text{core}}^2 - n_{\text{clad}}^2}$$

which is rounded up to the nearest integer, and there is a set of modes for each field polarisation. We can see immediately that as the index contrast is increased, generally through the use of a higher index core material, the thickness to achieve a single mode will be reduced, assuming a fixed wavelength. In very high index contrast regimes we need a thickness well below a µm, such as a slab thickness of 250 nm in the case of SOI. As the slab only confines light in the vertical direction, how small do we need to make a wire waveguide in SOI to achieve single mode guidance? In fig. 3.5 we sweep the width of a fully etched wire, embedded in SiO_2 and with a thickness of 220 nm, and plot the n_{eff} of the guided modes. We can see that for widths greater than 450 nm a second TE-like mode quickly becomes guided. We also note that the TE-like modes n_{eff} increases rapidly after cutoff, whereas the TM-like modes only vary slowly as the primary confinement is in the vertical direction, which remains unchanged.

Why do we call these waveguide modes TE-like, rather than just TE? In high confinement waveguides, especially when close to cutoff, the modes no longer *strictly* contain one field component, unlike the plane wave case described in section 3.1.2. To demonstrate this we plot the primary field components for the fundamental TE-like mode, in fig. 3.6a, for the silicon nanowire when the width is 450 nm. As well as the prevalent E_y and E_z components, a significant amount of the total field intensity exists outside of the waveguide core. The fundamental TM-like mode is similar, fig. 3.6b, but further expanded out of the core, which is understandable given that the mode is closer to cutoff. We also plot the absolute component of the the two modes at 450 nm, and the fundamental TE-like mode for a doubled width of 900 nm, demonstrating the varying profiles and confinement of the different modes (fig. 3.6c. The overall field distribution in all of these modes is altered by the significant E_z components, resulting in high field concentrations near the sidewalls of the waveguides. The presence of these multiple field components within a single mode is of great significance

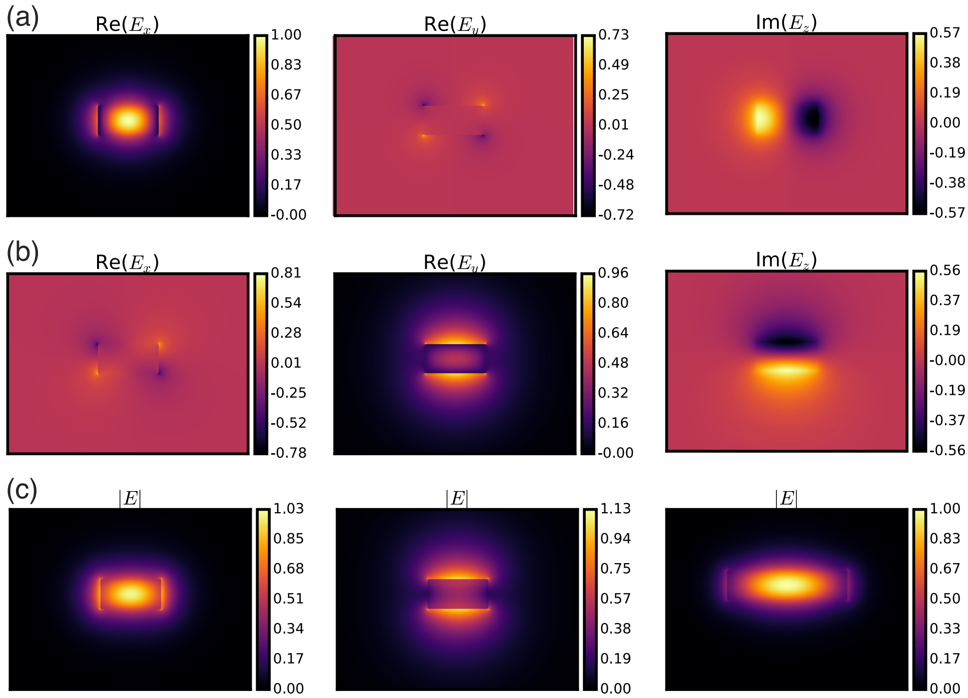

Figure 3.6: Fundamental TE-like (a) and TM-like (b) field components of a 450 nm × 220 nm Si waveguide embedded in SiO_2. (c) Absolute value of total field for the previous two modes, and the fundamental TE-like mode of a 900 nm wide waveguide.

for nonlinear optics, as well as the particular field distribution between the core and cladding, which we will discuss below. For those that wish to investigate the modal properties waveguides further, we mention the availability of a highly accessible, open source optical mode solver developed in our group.

Attaining bending radius below 100 µm is critical in achieving compact optical circuits, allowing for reduced costs (through number of devices per wafer) and improved functionality (by combining multiple compact components). A number of mechanisms may introduce losses during bends, which are discussed in further detail in the following section, however an upper limit is set by losses caused the *radiation* of light as the waveguide is bent. This was identified very early by Marcatili and Miller [180], with the new understanding that sufficiently high index contrast would lead to µm scale bends being one of the ideas behind the field of integrated optics [171]. Marcuse investigated the radiation for the case of slab waveguides [181], expressed in effective index form in [179], in which it was shown that the loss in the bend L_B was proportional to

$$L_B \propto R \exp\left(-R(\Delta n/n_{\text{eff}})^{3/2}\right)$$

where R is the radius of the bend. To demonstrate this dependence we have plotted the reduction in bend loss as the bending radii is increased for a waveguide with $\Delta n = 10^{-2}$, which is representative of waveguides used in silica planar lightwave circuits [182–184]. In this case the low index contrast requires bends with multiple mm radius to reduce radiation losses to a sufficient level. To show just how significantly the bending radii can be reduced, we calculate the bending radius to achieve 0.1 dB loss for increasing index contrast, with typical materials indicated. With just an index contrast of $\Delta n \approx 0.5$, satisfied by typical dielectrics with a SiO_2 cladding, bending radii in the 10s of µm range are attainable. If this is pushed even further to an index contrast of around 2, such as the case of SOI, low loss bends with radii of a *few* µm are possible [172, 185]. However, while significantly reducing the possible bend radii, the increasing of index contrast does have some trade-offs, in particular increasing the propagation loss of the waveguide.

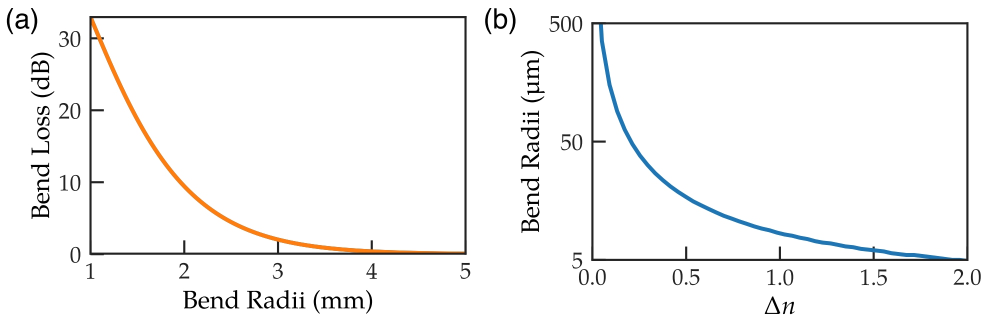

Figure 3.7: (a) Radiation losses from a 90° bend with index contrast $\Delta n = 10^{-2}$ (b) Bending radii required to reduce radiation losses below 0.1 dB level

So, how does the index contrast effect the propagation loss of a waveguide? While propagation losses in straight waveguides are the product of a number of mechanisms, material absorption and leakage to the substrate are possible issues, they are typically dominated by losses due to *scattering*. These scattering losses occur due to perturbations of the guided mode caused by the surface roughness existing at the core and cladding interface [186]. Work from Marcuse [187], Payne and Lacy [188], and Tien [189], described in the intro of [186], gives the magnitude of this loss mechanism as

$$\alpha_\mathrm{p} \propto \sigma^2 \frac{E_\mathrm{s}^2}{\int E^2 \, \mathrm{d}x} \Delta n^2 \tag{3.39}$$

where σ is the root mean square of the surface roughness and $E_s^2 / \int E^2 \, \mathrm{d}x$ is the normalised field intensity at the interface of the core and cladding. Reducing the surface roughness, through improvements and modifications to fabrication processes, is the primary consideration for minimising propagation losses and breakthroughs in this area have enabled modern integrated devices in high index contrast nanophotonic circuits [120, 177, 178, 190, 191]. Reducing the index contrast, typically by moving to lower index core materials, will reduce scattering but at the cost of compactness [192, 193]. Alternatively, waveguide geometries can be adopted which minimise the field *overlap* with the sidewalls of the waveguide, which generally have significantly higher surface roughness than the horizontal interfaces [190]. Rib waveguides, where the core is only partially etched, reducing the overlap region, can reduce losses significantly [194–197]. These designs can introduce some additional complexity, with coupling to leaky modes a possibility particularly in bends [198–201]. Alternatively, high aspect ratio designs can be adopted, pushing the field well out of the waveguide to minimize scattering [202–204]. These structures tend to have weak guiding and bending radii can suffer. However, tricks can be applied with the use of multiple high aspect layers, such as the Triplex dual stripe geometry [205]. By moving to very high confinement structures the interaction with the side wall is also diminished [206]. In fully etched nanowire geometries we can increase the width, which reduces losses dramatically $\alpha \propto 1/w^4$ [188], but this has the drawback of the waveguide becoming highly multimoded [190, 207]. Reducing scattering losses is beneficial to other aspects of circuit performance. In particular backscattering into the circuit is reduced, which can cause a number of issues when designing devices such as resonators [208–210].

Nonlinear Waveguides

The powerful functionality, enabled through the use of nonlinear optics and optical signal processing, has been of interest for integrated devices for a number of decades [144]. For nonlinear waveguide building blocks we wish to maximise the desired nonlinear interaction. This typically means having as large nonlinear coefficients as possible and minimising losses to keep pump and probe waves strong. In the case of phase matched processes we also need to maintain the appropriate dispersion and modal properties to induce the desired interaction. To frame the following discussion we will consider the example of how to maximise Kerr SPM. We will first describe the effect of the mixed field components on the nonlinear coefficient, γ_K. We will then discuss the effects of linear and nonlinear losses in the waveguides, how material choice affects the nonlinear performance and how to use circuit building blocks to enhance nonlinear interactions.

Modern subwavelength structures produce quasi-TE and quasi-TM modes, as we discussed in the previous section, which can result in a mix of E_x, E_y and E_z field components in a *single* mode. As such, the approximations made for defining the γ_K and A_{eff} in Equation (3.30) break down and new *vectorial* approaches are required to understand the nonlinear dynamics in these waveguides [211]. The importance of this understanding was quickly confirmed with experimental results in in small core bismuth fibers, with the measured γ_K a factor of 2 higher than the earlier scalar predictions [212]. It is also important to keep in mind that values of the n_2 determined with a scalar A_{eff} will be higher than the material value, which is likely the cause of the spread of n_2 in the silicon photonics literature. It is possible to formulate the vector form of γ_K a number of ways, the definitive work was published by Afshar in 2013 [213], where the authors separated the individual physical effects in an intuitive way. In particular, the most insightful formulation separates the group velocity from the other effects, such that

$$\gamma_K = k_0 \, n_g^2 \, \frac{n_2^{\text{avg}}}{A_{\text{eff}}} \tag{3.40}$$

where

$$n_2^{\text{avg}} = \frac{\int_\infty n^2 n_2 (2|\mathbf{E}|^4 + |\mathbf{E}^2|^2) \, \mathrm{d}A}{3 \int_\infty n^4 |\mathbf{E}|^4 \, \mathrm{d}A} \qquad A_{\text{eff}} = \frac{(\int_\infty n^2 |\mathbf{E}|^2 \, \mathrm{d}A)^2}{\int_\infty n^4 |\mathbf{E}|^4 \, \mathrm{d}A} \tag{3.41}$$

The n_2^{avg} is a weighted n_2 over the different materials in the waveguide, such as the core and cladding. For highly dispersive media a correction to above equations is needed [213]. The above integrals are performed to infinity, with calculations of the integrals being split over different materials to incorporate the n_2 and n of the constituents. This splitting has been effective in describing properties of multi-material slot waveguides [214, 215]. The work of Osgood follows a similar approach to that of Afshar [167], though the factorisation is not as clear, but also indicates the importance of calculating the n_2 based on the full vector mode profile, as different terms in the $\chi^{(3)}$ tensor may become significant for the different modes.

Suppose that we have a linear attenuation α through a waveguide with length L. Rather than incorporating the varying attenuation of a travelling pump or probe wave, we can instead lump the total attenuation into an effective length by considering the total loss along the structure, i.e $L_{\text{eff}} = \int_0^L e^{-\alpha z}\, \mathrm{d}z$ [216], which through direct integration yields

$$L_{\text{eff}} = \frac{1 - e^{-\alpha L}}{\alpha} \tag{3.42}$$

For large lengths the exponential will tend to zero and $L_{\text{eff}} \approx \alpha^{-1}$. We now recall the equation for the nonlinear phase shift from SPM eq. (3.29),

$$\phi_{\text{NL}} = \gamma_{\text{K}} P_p L_{\text{eff}}$$

We can see that to maximise the value of ϕ_{NL} we need to increase the pump power, γ_{K} and L_{eff} as much as possible. There generally exists an optimum waveguide width due to the fact that reducing the waveguide width reduces the A_{eff}, and increases n_g if close to cutoff, while increasing the width reduces propagation losses due to scattering at a high rate of $\alpha \propto 1/w^4$, as discussed above. For processes which are dependent on phasematching there is an extra constraint where the bandwidth is traded off with efficiency by varying the device length [154]. The primary method to improve γ_{K} is to use use materials which have higher nonlinear indexes n_2, however this is not a simple trade off either as such materials frequently have *nonlinear* losses, which we will discuss further below.

While investigating the linear and nonlinear coefficients of materials, researchers in the 1960s and 70s discovered an empirical relation between the linear and nonlinear susceptibilities, or equivalently, the linear and nonlinear indexes of materials. This is known as Miller's rule [217, 218] and, in general, it shows an *exponential* increase of n_2 with a linear increase of n. A typical plot of Miller's rule with different materials, glasses from [219] and integrated devices from [220], is shown in fig. 3.8.

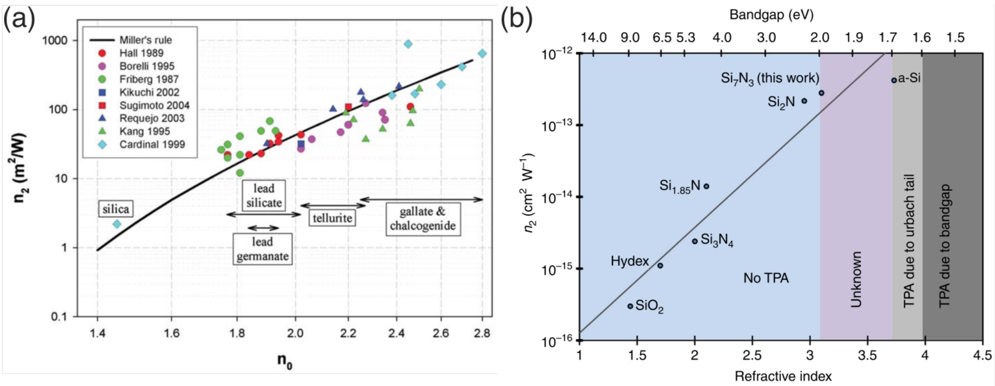

Figure 3.8: (a) Exponential increase in n_2 with increasing n, from [219]. A number of different glass groups are indicated. (b) Similar to (a), but focusing on integrated optics platforms and presence of two photon absorption, from [220].

There is thus a tremendous benefit to moving to higher index materials for nonlinear optics, however there is one downside, apart from the increased scattering losses. For many materials, moving to higher indexes, through varying composition, also means changing the size of the band gap. This introduces the issue of multiphoton absorption, a nonlinear loss mechanism where multiple photons can bridge the band gap. For many materials at the telecommunications band, 1550 nm, two photon absorption (TPA) becomes prevalent, and the new loss mechanism of β_{TPA} needs to be taken into account, especially when using high peak power pulses [221–226]. For the sake of explicitness, β_{TPA} will be non zero as soon as twice the photon energy is larger than the bandgap i.e $2\hbar\omega_p > E_g$, which is a band energy of $E_g = 1.6\,\text{eV}$ at 1550 nm. Depending on the precise shape of the bandgap this absorption may occur at higher energies.

The nonlinear loss due to TPA is exacerbated even further in semiconductor devices, such as SOI and III-V circuits [227], where the creation of free carriers due to the TPA process leads to excessive losses through further absorption, referred to as free carrier absorption (FCA) [145, 228]. FCA is so strong that a CW pump in SOI nanowires becomes completely saturated with powers over a few 10s of mW, for relatively short device lengths on the order of 1 cm. A significant amount of work has attempted to address this issue, primarily through the use of junctions which *sweep* the generated carriers out of the waveguide, reducing the carrier lifetime [229–232]. There is also the option of combining other materials with silicon, in particular highly nonlinear polymers [233], to achieve a large overall nonlinearity but smaller amounts of TPA, and thus FCA [214, 215, 234, 235]. This hybrid integration concept is discussed further in section 3.2.2. In some materials the composition can be varied to "bandgap engineer" the medium, enabling the highest n_2 before β_{TPA} becomes significant [220, 236], though higher order absorption such 3 photon absorption may still occur [221].

An alternative to increasing the n_2 directly is to use optimisation on the component level, with two examples being slow light waveguides or resonant enhancement, to increase the resulting strength of the nonlinearity. While a silicon nanowire is technically a slow light waveguide, with $n_g = 5.5$ significantly higher than the n_{eff} [237], photonic crystal (PhC) waveguides [169, 238] and coupled resonator optical waveguide (CROW) [239] are capable of large slowdown factors which enhance the nonlinearity [168, 240–243]. These enhancements, perhaps unsurprisingly at this point, do come with some caveats, linear effects such as absorption and dispersion are also increased with the slow down factor, but the nonlinear enhancement scales with the number of interacting fields such that three-wave and four-wave mixing see considerable enhancements even for modest slowdown factors [244]. PhC also have the capability of compressing the mode field significantly [245, 246], with conversion efficiencies in the range −20 dB being generated with modest pump powers in only a few 100 µm length [247, 248]. Resonant enhancement typically increases interaction strength by building up large circulating powers in compact mode volumes, and providing long effective lengths for spontaneous processes [249–251]. In resonant systems minimising losses is thus critical. For this reason lower index contrast systems, which have smaller n_2 values, are frequently used [252, 253]. Optical quality factors in integrated resonators can range from 10^4 to 10^{10}, with values in the range of 10^6 a typical upper limit for sub wavelength waveguides [120, 252, 254]. In the last decade optical microresonators have become of considerable interest for the generation of Kerr frequency combs, in particular stable frequency combs based on the generation of dissipative solitons [254–261].

3.2.2 Making a Circuit

So far we have explored some of the linear and nonlinear properties of integrated waveguides. However, a waveguide does not exist in isolation. Integrated waveguides form part of larger optical circuits, which are required to connect and exist in even larger photonic systems. Here we will discuss external coupling to optical circuits, waveguide designs for routing, what happens when you bend a waveguide, and techniques for combining multiple materials in a single circuit. A useful resource when researching this area is the Silicon Photonics Design textbook from Lukas Chrostowski and Michael Hochberg [262].

Coupling

Efficiently interfacing optical fibers with integrated devices is rather difficult due to the sheer size disparity between the different structures. The spatial overlap between the mode profile of a typical SMF fiber and a silicon nanowire is very low, resulting in coupling efficiencies on the order of −20 dB and large reflections. To increase this to a more feasible amount, two main techniques are adopted in the literature: the use of *gratings* to couple out of plane light into a waveguide, and end fire coupling from optical fiber into a mode matched waveguide.

Grating couplers have been used since the advent of integrated optics as a means of coupling light into optical circuits [263]. They provide additional momentum (i.e $\Delta\mathbf{k}$) which allows for phasematching between optical modes and, provided there is suitable optical overlap, produce efficient coupling between these modes [264]. In Si based high index contrast circuits, grating couplers provide typical insertion losses of 5 dB from close to vertically coupled cleaved single mode fiber, and bandwidths in the tens of nm range [265, 266]. Optimised designs have shown wide bandwidths [267], low optical back reflection [268, 269] or lower insertion losses [264, 270, 271], down to 1 dB if reflective elements below the waveguide are used. Grating couplers have also been demonstrated in lower index contrast materials such as Si_3N_4 [272, 273]. A key primary benefit of grating couplers is flexibility, as the ability to place coupling elements anywhere on a device enables highly dense circuits. An array of coupling fibers can be used to test, and package, compact multi port circuits, without requiring cleaving of samples [274, 275]. Finally, while µm scale gratings are not possible in thick waveguide structures, an alternative approach using vertical mirrors, metallic or TIR, can achieve similar functionality in these systems [276, 277].

Efficient end fire coupling can be performed a number of ways, which vary depending on the waveguide type. The most important aspect for efficient coupling is for the mode profiles to be as closely matched as possible, at the fiber to chip interface. For high index nano waveguides the waveguide widths are *reduced*, making the mode expand as the waveguide approaches cutoff. The mode can then be transferred to a large overlay waveguide, typically formed of polymer or SiONx, and then coupled to the external fiber [278]. If the end of the nano waveguide is within a few optical wavelengths of the device edge it can directly couple to an external fiber [279]. Advanced versions of these schemes have shown less than 1 dB loss [280–282]. Ultrahigh NA fibers with small mode fields, which can be spliced to SMF with low loss, or lensed fibers are typically used to achieve these overlap. A key benefit of end fire coupling schemes is much larger operational bandwidths than optical gratings. For larger micron scale waveguides, like silica circuits [184] or thick silicon waveguides [277], outward lateral tapers can be sufficient to produce low coupling losses in the range of 1 dB.

Routing: Bends

The desire to fabricate compact circuits imposes a number of constraints on waveguide designs used for routing. Ideal routing waveguides should have, low propagation losses, low cross-talk between adjacent structures and be capable of tight bends. We will discuss these conflicting requirements, and techniques to surpass them, with the specific example of silicon nanowaveguides.

As was mentioned in section 3.2.1, fully etched single mode nanowire waveguides have high propagation losses, with typical values in the range of 1 dB cm^{-1} to 2 dB cm^{-1}. The use of shallow etched rib waveguides can reduce these losses significantly, with a reduction from 1.4 dB cm^{-1} to 0.3 dB cm^{-1} demonstrated [194, 196]. Using multiple etch steps in a single fabrication process allows for both waveguide designs on a single wafer, and short linear tapers in the rib layer allows for low loss conversion between these geometries [194, 196, 283]. An alternative to rib waveguides is using multi µm wide deeply etched geometries, with losses below 0.1 dB /cm possible [207, 284]. Again tapers can be used to convert between the fundamental modes in each structure, care in the design process is required to prevent excitation of higher order modes. Depending on the final width, and the number of modes, low loss linear tapers can require long lengths in the range of 100 µm or above. Alternative designs, parabolic in particular, can be more efficient when designed correctly [184, 285].

So, while we can easily shift between different waveguide geometries, the question becomes, why wouldn't we just use a low loss geometry all the time? The answer to this is what happens when we *bend* a waveguide. As well as the radiation losses which we described earlier, there are two possible sources of loss due to waveguide bends, mismatch losses at the interface between the straight and bent waveguide, and mode conversion losses during the waveguide bend. To understand these effects it is informative to consider the modes of the bent waveguide [286], with an example shown in fig. 3.9a. Consider a bend with a constant radius of curvature, as the bending radii is reduced the mode is pushed outwards. This can be understand more intuitively using conformal optics, a bent waveguide can be shown to be equivalent to a straight waveguide with linearly increasing index along the cross section [287]. If this effect is sufficiently strong there will be a large mismatch between the modes of the straight and bent structure, and we will incur an insertion loss as the fundamental mode is coupled into the higher order modes, or leaky modes, of the bent waveguide [179, 286, 288]. One approach to this issue is simply to *offset* the interface of the bent and straight waveguides [179, 288]. While this is an improvement, a superior approach, in particular in terms of fabrication imperfections [289], is to slowly increase the curvature of the bent structure along the bend. Bezier or Clothoid based curves are used in the literature [192, 194, 207], ensuring that the overlap remains high along the entire bend region.

Even if we reduce the coupling at the bend and straight interface, it is not possible to completely suppress mode coupling during the bend. To further minimise losses due to mode conversion in the bends, we can design the bend to operate in a *matched* bend configuration [289]. In this case the length of the bend, which for a fixed bending angle will be given by the effective radius, is chosen such that it matches the *beat* length of the two bent modes, which is given by

$$L_B = \frac{2\pi}{k_{b1} - k_{b2}}$$

where k_{b1} and k_{b2} are the propagation constants of the two bent modes. This technique was proposed in a highly informative paper by Melloni et al in 2003 [289] and is commonly adopted when dealing with multi mode waveguides [291, 292]. The understanding also extends to waveguides with variable bending radii,

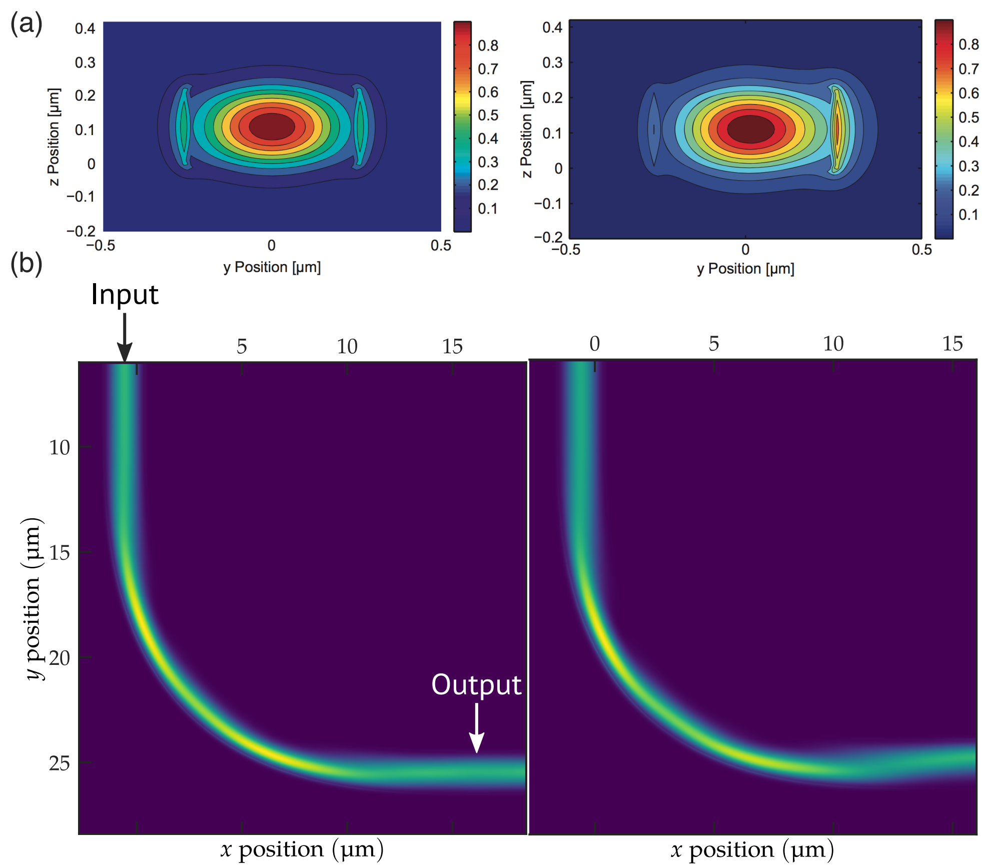

Figure 3.9: (a) Mode profile for Left: Silicon nanowire and Right: Silicon nanowire with 3 µm bend radii [290] (b) 3D FDTD Simulations of field propagation through a multimode waveguide. The left simulation is operating at the matched bend radii for the waveguide geometry. The right simulation is slightly offset (-10%) from the first simulation, distortion in the output of the bend is due to mode conversion.

in which case the matched bend will have a wider operational bandwidth than a typical circular arc [206, 293]. It is important to keep in mind that what may be considered "single mode waveguides" will often have leaky optical modes which can be coupled to in bends, which this technique can help avoid.

We have spent quite some time discussing mode coupling in waveguides, so you may be wondering, is it really this important? For a single bend only losing 1 % of power from the fundamental mode doesn't seem that bad. However at the circuit level, where there may be tens or hundreds of bends and mode sensitive components, this can be a crucial limiter of performance [294, 295]. Optical power which is coupled into higher order modes can, due to other bends or tapers in the circuit, couple *back* into the fundamental mode [296, 297]. This may result in destructive interference, which will be determined by the phase difference during propagation in other modes, and can result in significantly reduced performance in certain wavelength ranges [296]. It is important that simulations of circuit performance fully capture the effects of mode coupling, as well as backscatter from waveguides [209], to correctly inform the design process. A number of commercially available simulation tools utilise scattering matrix approaches to perform circuit simulations, in particular Caphe from Luceda Photonics, Interconnect from Lumerical Solutions and Aspic Design from Filarete.

Routing: Coupling and Cross-Talk

Minimising cross-talk between waveguides is an important consideration when designing dense circuits and compact spiral structures. So far we have considered a waveguide in isolation, what happens when we bring two waveguides in close proximity? The interaction between the waveguides causes them to *couple*, they no longer act independently from each other [298, 299]. The dynamics of this new system can be explored with coupled mode theory, in particular we can consider the new modes of the combined structure, which are referred to as *supermodes*. Each of the original modes of the single waveguide are now split into two modes, the symmetric and anti-symmetric super mode. In the case where the coupling waveguides are almost identical, the coupling coefficient can be calculated from the difference in effective index between the supermodes,

$$C = \frac{\pi \Delta n_{\mathrm{eff}}}{\lambda_0} \tag{3.43}$$

Now, if we assume that the optical power P_0 starts in a single waveguide then the fraction of power coupled to the other waveguide P_{cross} a length L, is given by

$$\kappa^2 = \frac{P_{\mathrm{cross}}}{P_0} = \sin^2(CL) \tag{3.44}$$

This means that the *all* power will be transferred after when $L_c = \pi/2C$, which is referred to as the coupling length. What is this length for a typical waveguide geometry? If we take two 500 nm $\times$ 220 nm silicon nanowires, embedded in SiO_2 and separated by a gap of 300 nm, then the coupling length is only 15 µm. This large amount of coupling is actually one of the reasons to actually *use* nanowires to begin with. We can make compact, micron scale, power splitters simply by bringing two nano waveguides close together. These highly coupled waveguides are actually a fundamental building block in integrated circuits, and are called directional couplers. Directional couplers frequently form the basis of more complex building blocks, such as coupled resonators and power splitters [300, 301].

We have just shown that two Si nanowires separated by a gap of 300 nm act as a *highly* effective optical coupler. How big of a gap do we need to reduce this coupling to a negligible, or tolerable, level? A calculation of the coupling parameter with varying gaps shows an exponential reduction in C, with increasing gap size [262]. Returning to eq. (3.44), and set a desired limit of the coupling, let us say 50 dB, occurring over a 1 cm interaction length. This will result in

$$\begin{aligned} &10^{-5} = \sin^2(0.01 \times C) \\ &\rightarrow C = 0.32 \end{aligned}$$

From the plot we find that this value occurs for a 3 µm gap, around ten times the width of the waveguide. It is important to note that the actual coupling may be even higher in waveguides with large amounts of surface roughness through radiative coupling [302]. How does this dependence change with the width of the waveguide? We can perform the same process as above for the 2 µm wide waveguide, looking just at supermodes formed from the fundamental waveguide mode. The required gap has reduced significantly, down to a value of only 500 nm. Qualitatively, we can see that as the field confinement is increased the expected coupling between two waveguides will be reduced, high confinement waveguides have been shown to provide highly dense circuits [294]. If further reductions in cross-talk are needed for nanowire waveguides a possible design route is the use of waveguides with different widths [303], or by using subwavelength metamaterials between the waveguides [304].

Hybrid Integration

We have seen that the geometries, and materials, which are suitable for strong nonlinear interactions in waveguides are not always suitable for forming linear circuits. From a design point of view it would be highly desirable to separate non-linear components into single building blocks which are used throughout a linear circuit. One approach to achieve this goal is hybrid integration, bringing multiple different materials onto a single circuit. Hybrid integration has been extensively explored to bring light sources and modulation components to integrated circuits [305]. Here we will focus on the design considerations, rather than the fabrication specifics, and look at a few examples from the literature.

The requirements for interfacing different hybrid waveguide geometries are very similar to those discussed earlier with external coupling to waveguides. To achieve low insertion losses we require a continuous transition of the mode profile along the structure, while avoiding coupling to undesired higher order or leaky modes. Milton and Burns explored this problem in detail, in the context of waveguide tapers, in their 1977 work [306]. This can be expressed more quantitatively by considering the overlap integral between two modes m and n, on either side of the interface between two waveguide geometries 0 and 1, which is given by

$$c_{mn} = \frac{\int_{-\infty}^{\infty}\int_{-\infty}^{\infty}\left[\left(\mathbf{E}_{m,0}\times\mathbf{H}^*_{n,1}\right)_z + \left(\mathbf{E}^*_{n,1}\times\mathbf{H}_{m,0}\right)_z\right]\mathrm{d}x\,\mathrm{d}y}{2\left(\int_{-\infty}^{\infty}\int_{-\infty}^{\infty}\left(\mathbf{E}_{m,0}\times\mathbf{H}^*_{m,0}\right)_z\mathrm{d}x\,\mathrm{d}y\int_{-\infty}^{\infty}\int_{-\infty}^{\infty}\left(\mathbf{E}_{n,1}\times\mathbf{H}^*_{n,1}\right)_z\mathrm{d}x\,\mathrm{d}y\right)^{1/2}}$$

An appropriately designed transition will maximise c_{mn} for the desired mode combination, and minimise any other cross terms, for the full length of the transition region. Adopting this process can enable low loss transitions between highly disparate waveguide geometries. For example, a 20 µm long transition from a Si nanowire to slot waveguide achieved losses below 0.1 dB [307].

There are two main schemes used for photonic circuits with hybrid integration. The first scheme comprises of a circuit where the separate waveguides are formed completely of the material, with tapers providing transitions between the multiple regions. Examples include Si and Si_3N_4 [296, 308, 309], Si and SiOx [310, 311] and InP and SiOx [312]. The second scheme involves hybrid waveguides formed of multiple materials, which generally are not etched, which interact evanescently. This scheme is very popular for integrating Si and III-V materials [313, 314], and was the basis of the first electrically pumped laser in a silicon circuit [305, 315]. Waveguide geometries of this form can generate strong interactions without needing to etch the hybrid material layer, such as the case for nonlinear polymer claddings [215, 235, 316, 317] and Li_3NbO_3 [318, 319]. It is worth mentioning that the flipped version of this scheme has gained attention recently, with glasses [320–322], Si_3N_4 [323, 324] and Si [325, 326] used so far, where the waveguide has been etched on *top* of a Li_3NbO_3 substrate. In these evanescent devices the interaction with the different layers is controlled by the waveguide widths, and tapers again need to be optimised to couple into the evanescent region from the passive/linear region of the circuit [327].

3.2.3 "Fabless" Photonic Platforms

The tools required to fabricate complex integrated photonic circuits can be prohibitively expensive, preventing the majority of academic groups, or small businesses, from accessing advanced multi step devices. To surpass this issue a number of institutions have adopted a sharing model from electronics, offering multi-project wafer (MPW) runs, also known as 'shuttle' services, to external users [328]. MPW services combine multiple device designs onto a single fabrication run, spreading the cost of specific tooling (like lithographic masks) between many users. This allows external users to access fabrication tools at significantly lower monetary cost than owning and running a facility, thus performing "fabless" research, without needing complex formal collaboration agreements. As the current state of MPW services is quite diverse, we will arrange discussions around base materials and emerging platforms, and also mention the brokers who provide access to the MPW foundries.

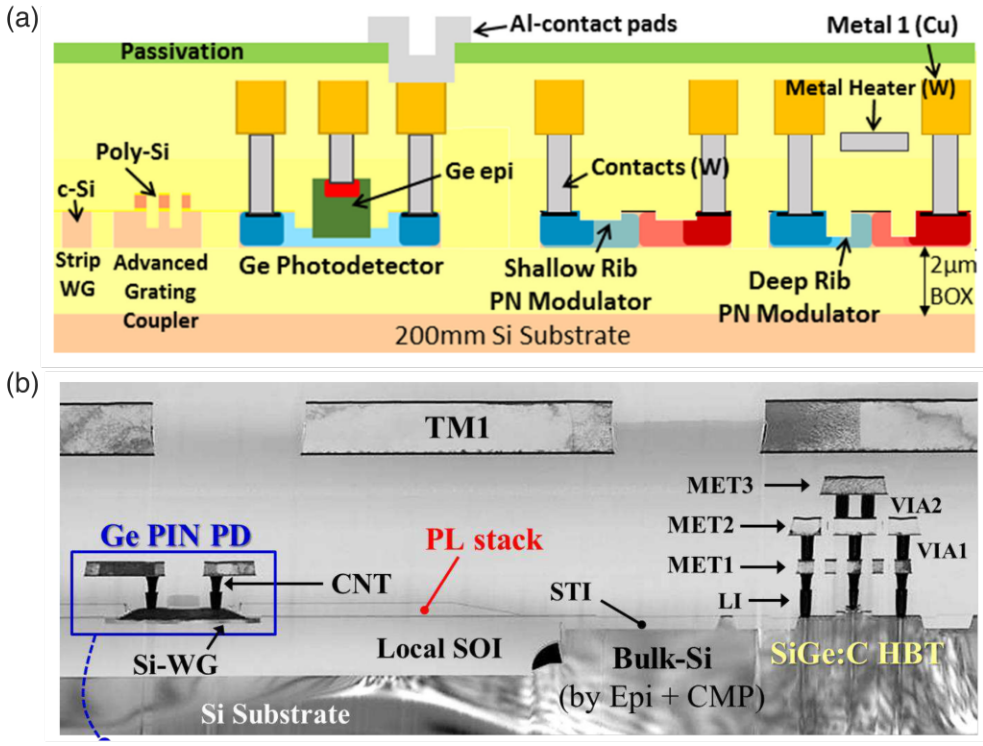

Figure 3.10: (a) Schematic of features of IMEC iSiPP50G platform [329] (b) SEM of cross section of IHP active device, showing SOI region and a BiCMOS Transistor in close proximity

Silicon on Insulator

In recent years, SOI has become *the* standard material platform for photonic integration. Sometimes termed more simply as 'Silicon Photonics', the lure of cheap material processing, supply and, in particular, ease of integration with silicon based electronics, has pushed research into SOI based devices into truly stratospheric levels with thousands of citations now occurring every year. This surge of research is partly due to the fact that MPW runs have been available, first through IMEC and LETI in Europe [330], for a number of years. The complexity of available devices varies between the foundries, from passive si nano-waveguides to active components with Si doping, metal layers and other materials such as germanium [331]. Foundries with active components generally offer cheaper passive only schemes, below we provide a list of MPW foundries available to external users.

- IMEC iSiPP50G: Active components with doped silicon modulators, Ge detectors and Ge-Si absorption modulators [329, 332]
- IHP SG25ePIC: Active optical components *and* co-integration of BiCMOS electronics [333, 334]
- IME SiPho: Active optical components. Was formally run through USA as the OPSIS foundry [335]. Multilayer Si_3N_4 also available [308]
- CEA-LETI Si310-PHMP2M: A 310 nm thick active platform available through CMP. Optimisations for 1300 nm applications. [336]

The above foundries all utilise deep UV photolithography to process 200 mm diameter Si wafers [175]. Moving to more advanced technology nodes can improve performance, through reduced surface roughness and wafer variability [177], but at added cost which is making this prospect currently out of bounds for MPW runs. MPW runs for IMEC, IHP and LETI are accessible through the Europractice broker service. IME services are accessible through IME directly or CMC Microsystems.

III-V Semiconductors

While silicon photonics has attracted significant attention in recent times, III-V based integrated photonic devices have existed for decades. A key advantage of III-V semiconductor systems is the ability to form quantum wells and engineer electronic bandgaps, while still on a monolithic substrate. This flexibility allows for truly diverse active circuits to be formed out of III-V materials, with electrically pumped lasers, semiconductor amplifiers, polarisation rotation elements and large bandwidth photodiodes all available in generic integration platforms [337]. The Jeppix broker service currently provides access to MPW runs in indium phosphide (InP) based circuits at Fraunhofer HHI and Smart Photonics [338].

Other Established Platforms

As well as the more standard SOI nanowires and InP structures, a few foundries provide access to unique materials and geometries. The most commonly accessed of these is the TriPleX platform [205], fabricated by LioNiX and accessible through the Jeppix broker. The TriPlex platform consists of alternating layers of SiO_2 and Si_3N_4, and can produce quite interesting waveguide geometries such as double strip structures, box shaped waveguides or more traditional high confinement Si_3N_4 structures [205]. Capable of providing low losses (<0.1 dB /cm) and tight bends, TriPlex is seen as highly complementary to other platforms, with active efforts to combine TriPlex and III-V structures, in both evanescent and end fire coupling schemes.

Another platform capable of very low loss routing is the thick Si platform provided by VTT [339]. The platform consists of 3 µm thick silicon waveguides, with half-etched rib waveguides providing access to single mode geometries and highly multi-moded fully etched wire waveguides enabling relatively tight bends (<100 µm), 100 µm long tapers enable low loss coupling between rib and wire waveguides. The large mode area of these waveguides enables end-fire coupling losses of around 1.5 dB with lensed fibers and reduced propagation losses in the range of 0.1 dB cm^{-1}. The fully etched waveguides are capable of very high density, with 1.9 µm wide waveguides able to be separated by only 2 µm, a 1.5 m long spiral was formed in less than 0.1 cm^2 [340]! Metallisation is also possible to enable thermo-optic phase shifters, higher speed active components are still currently under development. Access to MPW runs is available through VTT directly.

The previously described MPW services utilise photolithography to create tens to hundreds of optical circuits simultaneously. The development, and cost, of the lithographic masks required means that these services generally only run a few times a year, and lead times are typically in the range of a full year when the design deadlines are included. For rapid prototyping, and investigations of single components, multiple chips are not always required and a faster turnover would be highly ideal. This tradeoff is possible through the use of electron-beam lithography (EBL), and access to SOI based EBL chips is available through the Open EBL scheme or through applied nanotools. A similar scheme has been recently initiated in Australia. It is worth noting that these facilities are typically based within universities and fabrication tolerances are not necessarily as consistent as a private company based MPW run, such as with IMEC.

Emerging Platforms

The above MPW foundries have existed for a few years and are well established, with multiple fabrication runs and well developed basic components. A new emerging service is being developed by AIM photonics in the USA. More than just a single facility, AIM photonics is an end to end project focused on developing a photonic fabrication ecosystem within the USA. The final platform will be highly advanced, capable of featuring both Si and III-V devices for integrated lasers and high performance active components [341]. Due to the complexity of the process, the relative cost may be outside the range of academia for sometime, with the cheapest option currently at $25k USD for Si-based active devices.

Dispersion engineered Si_3N_4 has become a popular material for the generation of Kerr frequency combs using integrated micro resonators [253]. Si_3N_4 has also received interest as a passive, low loss, routing element in silicon photonics [308]. However the thickness of these waveguides is typically not suitable for dispersion engineering in the 1550 nm wavelength band. LIGENTEC has recently started providing thick Si_3N_4 structures, based on a photonic damascene fabrication process [342], suitable for use with nonlinear optics. Publications from external groups utilising this process has been limited, however there is on going effort to combine these structures with more traditional SOI systems [343].

Cornerstone is another recently commenced service, which is based in a number of universities in the UK. It is quite unique in that it provides three different thicknesses of SOI, 220 nm, 300 nm and 500 nm, with multiple etch depths. It also provides active components with different doping levels for silicon, and varies between the use of photolithography and electron-beam lithography. It is primarily aiming itself for establishing capability in the UK, though external users can submit designs. It is university funded, and the nature of the program after the end of the initial funding is not clear.

Chapter 4

Stimulated Brillouin Scattering in Waveguides

In this chapter we explore and develop a basic understanding of stimulated Brillouin scattering (SBS) in waveguides. We start with the traditional physical mechanisms behind SBS and the the operation of SBS in a bulk media. This leads into the remarkably different situation of SBS in systems with guided optical and acoustic waves, requiring a brief overview of acoustic waveguides, and the change of the phase matching conditions in these systems. Finally, the chapter closes with a description of the calculation of the Brillouin gain coefficient, in particular approaches which take into account the vectorial nature of the guided modes and forces due to interactions with the waveguide boundaries.

Comments and Resources

In 1922 Leon Brillouin introduced a theory to describe the scattering of electromagnetic waves, specifically X-rays, from acoustic vibrations within a media. Because of this, we now refer to the inelastic scattering of an optical wave from an acoustic wave as Brillouin scattering. For a historical overview of Brillouin scattering, and including details of state of the art devices during from the last decade, please refer to Chapter 2. *Spontaneous* Brillouin scattering occurs when the optical wave scatters from vibrations which are exist due to the thermal energy available at a given temperature. If a strong light source passes through the material it can further induce vibrations, phonons, in the material. *Stimulated* Brillouin scattering is the scattering of an optical wave from these *optically* induced acoustic waves. In this thesis we are focused on the effects of stimulated scattering, however spontaneous scattering is *always* present and should be considered when appropriate. The theses of Raphaël Van Laer, Johannes Köhler and Thomas Büttner are good starting points for additional resources in Brillouin scattering in waveguide systems.

4.1 Understanding Physical mechanisms behind SBS

On a fundamental level stimulated Brillouin scattering is a nonlinear interaction based around the coupling of optical waves with optically *induced* acoustic waves. In classical devices this interaction is generally mediated through the thermodynamically linked material properties of electrostriction and the photoelastic effect. Electrostriction is a property of a medium where a physical stress and strain can be created in the presence of an electric field, where the strength of the interaction scales with the field *intensity*. The photoelastic effect describes the change of dielectric properties of the medium in the presence of a strain. In this section we will begin with a high level description of SBS and provide more details on electrostriction and the photoelastic effect.

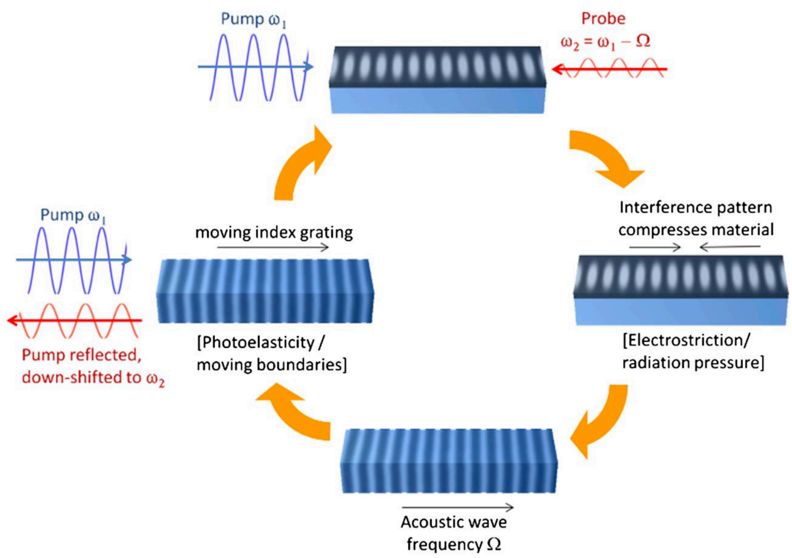

Figure 4.1: High level representation of stimulated Brillouin scattering [133]

4.1.1 High Level SBS Overview

The general interaction process of SBS is summarized in fig. 4.1. We start by considering a system with 1D propagation, with a pump wave, frequency ω_1, and a counter propagating probe wave, frequency ω_2, passing through the medium. The interference of the pump and probe will generate an intensity envelope, which has a wavelength determined by the frequency spacing of the waves $\Delta\omega = \omega_1 - \omega_2$. This intensity profile creates a moving density gradient, an acoustic wave, through the process of electrostriction. The density wave then creates a moving index perturbation, essentially an optical grating, through the photoelastic effect. If the frequency spacing $\Delta\omega$ is appropriate to satisfy the phase matching condition, a frequency known as the SBS shift, Ω_{SBS}, then the acoustic wave will be resonantly enhanced and the pump wave will *reflect* off the grating. As the grating is *moving*, then the pump frequency will be Doppler shifted by precisely the frequency spacing Ω_{SBS}, and result in an amplification of the probe wave at frequency $\omega_1 - \Omega_{\text{SBS}}$. This amplification is highly efficient and *exponentially* increases with the pump power and medium length. The spectral width of the response is determined by the phonon lifetime, generally on the order of 10 ns.

4.1.2 Electrostriction and Photoelasticity

Now that we have briefly given a high level overview of SBS we will go one step further and describe more quantitatively the physical mechanisms and dynamics of the SBS interaction. We will follow the general description given by Boyd [140] to understand the physical origin of the electrostrictive force, with a simple bulk example to elucidate the general physics.

As mentioned previously, electrostriction is an effect where materials become compressed, or expand, in the presence of an electric field. The origin of this force can be considered in the context of the stored energy of the system. Consider a dielectric slab placed between capacitive plates. The potential energy of a material located in an electric field with strength E is increased by the amount

$$u = \frac{1}{2}\epsilon\epsilon_0 E^2$$

The total energy of the system, integrating the potential energy over the volume (i.e $\int u \, \mathrm{d}V$), is maximised by the medium moving into the region where the electric field is the largest.

From a microscopic point of view we can consider the force produced on a molecule from an external electric field. Due to the presence of the field $\mathbf{E}$, the molecule will develop a dipole moment $\mathbf{p} = \epsilon_0 \alpha \mathbf{E}$ where α is the molecular polarizability. The energy stored in the polarisation field is given by

$$U = -\int_0^{\mathbf{E}} \mathbf{p} \cdot \mathrm{d}\mathbf{E}' = -\frac{1}{2}\epsilon_0 \alpha \mathbf{E} \cdot \mathbf{E} = -\frac{1}{2}\epsilon_0 \alpha E^2$$

and the corresponding force acting on the molecule from this potential is given by

$$\mathbf{F} = -\boldsymbol{\nabla} U = \frac{1}{2}\epsilon_0 \alpha \boldsymbol{\nabla}\left(E^2\right)$$

If we consider a macroscopic object there will be an accompanying change of material density due to this force, which will result in a change in the permittivity of the medium. This interaction is the photoelastic effect. This can be written as

$$\Delta\epsilon = \left(\frac{\partial \epsilon}{\partial \rho}\right) \Delta\rho \tag{4.1}$$

The change in permittivity will lead to a *further* change in the original potential energy, Δu. This change in energy must be equivalent to the work done in compressing the material, and thus we can define the *electrostrictive pressure* p_{st} as

$$p_{\mathrm{st}} = -\frac{1}{2}\epsilon_0 \left(\frac{\partial \epsilon}{\partial \rho}\right) \rho E^2 \equiv -\frac{1}{2}\epsilon_0 \gamma_e E^2 \tag{4.2}$$

where $\gamma_e = \left(\frac{\partial \epsilon}{\partial \rho}\right) \rho$ is known as the electrostrictive constant. The change in density $\Delta\rho$ due to small change in pressure Δp is given by

$$\Delta\rho = -\rho \left(\frac{1}{\rho}\frac{\partial \rho}{\partial p}\right) \Delta p \equiv -\rho\, C \Delta p$$

where $C = \rho^{-1}(\partial\rho/\partial p)$ is the compressibility of the medium. If we now insert the electrostrictive stress for Δp we will end up with

$$\Delta\rho = \frac{1}{2}\epsilon_0 \rho\, C \gamma_e E^2$$

The above equation describes the change in material density induced by an applied electric field, which can act as a source term in the acoustic wave equation. The derivation has been performed assuming a static electric field E. In the case of SBS the electric field should be replaced with an optical frequency which will yield

$$\Delta\rho = \frac{1}{2}\epsilon_0 \rho\, C \gamma_e \langle \tilde{\mathbf{E}} \cdot \tilde{\mathbf{E}} \rangle \tag{4.3}$$

where the angled brackets denote the time average over an optical period.

4.2 SBS in Bulk Media

In section 4.1.2 we have shown how an optical force, the electrostrictive pressure induced by an optical intensity, can create a density fluctuation in a medium. When satisfying the right conditions for the optical waves generating the optical force, the phase matching condition, this density fluctuation can generate strong acoustic waves which will couple all three waves. We will first discuss the phase matching condition and then introduce the standard coupled wave formalism used to describe SBS, for the case of bulk media.

4.2.1 Phase Matching

Consider an optical pump travelling in 1D within a bulk media with acoustic velocity v_{ac} and refractive index n. If this optical wave undergoes Brillouin scattering, it will either be down-shifted in frequency, Stokes scattering, or upshifted in frequency by the acoustic phonon, anti-Stokes scattering. The three waves have to satisfy energy conservation and momentum conservation, and for the case of

Stokes scattering we have that

$$\omega_{\mathrm{p}} = \omega_{\mathrm{s}} + \omega_{\mathrm{ac}} \qquad\qquad \mathbf{k}_{\mathrm{p}} = \mathbf{k}_{\mathrm{s}} + \mathbf{k}_{\mathrm{ac}}$$

In the case of backwards scattering it is typical to make the approximation that $\mathbf{k}_{\mathrm{s}} = -\mathbf{k}_{\mathrm{p}}$, which means that the acoustic wave is travelling in the forwards direction with a momentum of $\mathbf{k}_{\mathrm{ac}} \approx 2\mathbf{k}_{\mathrm{p}}$. If it is also assumed that only longitudinal acoustic waves are involved in the interaction, then the dispersion of the acoustic wave will be linear, and the acoustic frequency is given by

$$\omega_{\mathrm{ac}} = v_{\mathrm{ac}}|\mathbf{k}_{\mathrm{ac}}|$$

The optical wave vector in the medium is related to the vacuum wavelength simply through $|\mathbf{k}_{\mathrm{p}}| = 2\pi n/\lambda_{\mathrm{p}}$. Thus, if we combine all these relations, we will have that the SBS frequency shift is given by

$$\frac{\Omega_{\mathrm{SBS}}}{2\pi} = \frac{2nv_{\mathrm{ac}}}{\lambda_{\mathrm{p}}} \tag{4.4}$$

where $\Omega_{\mathrm{SBS}}/2\pi$ is the frequency shift expressed in Hz, i.e $\Omega_{\mathrm{SBS}}/2\pi \approx 11\,\mathrm{GHz}$ in typical SMF-28 fiber [344]. If we were to consider the case of forward scattering then the acoustic wavevector will approach zero, i.e $|\mathbf{k}_{\mathrm{ac}}| \to 0$, which implies that the acoustic frequency will also approach zero if assuming linear dispersion for longitudinal acoustic waves.

4.2.2 Coupled Wave Equations for Bulk

We will continue following the work of Boyd [140] in this section, keeping the description brief as we will focus on the formulation for waveguide systems later. The nonlinear coupling between the two optical waves and the acoustic wave can be treated within a coupled wave approach. For generality we will relabel the pump and counter propagating waves as E_1 and E_2 with frequencies ω_1 and ω_2. We can then treat the total optical field within the medium as $\tilde{E}(z,t) = \tilde{E}_1(z,t) + \tilde{E}_2(z,t)$, where

$$\tilde{E}_1(z,t) = A_1(z,t)e^{i(k_1 z - \omega_1 t)} + \mathrm{c.c}$$

and

$$\tilde{E}_2(z,t) = A_2(z,t)e^{i(-k_2 z - \omega_2 t)} + \mathrm{c.c}$$

where c.c denotes the complex conjugate of the adjacent term. The acoustic field can be described in terms fo the density distribution in the material in the following way

$$\tilde{\rho}(z,t) = \rho_0 + \left[\rho(z,t)e^{i(k_{\mathrm{ac}} z - \omega_{\mathrm{ac}} t)} + \mathrm{c.c}\right]$$

Now in the same way that the propagation of the electric field will obey Maxwell's Equations, the material density obeys the acoustic wave equation, which is given by

$$\frac{\partial^2 \tilde{\rho}}{\partial t^2} - \alpha_{\mathrm{ac}}\nabla^2 \frac{\partial \tilde{\rho}}{\partial t} - v_{\mathrm{ac}}\nabla^2 \tilde{\rho} = \boldsymbol{\nabla} \cdot \mathbf{f} \tag{4.5}$$

where α_{ac} is an acoustic damping parameter. The source term on the right hand side of the equation is given by the divergence of the force per unit volume $\mathbf{f}$, which in this case is driven *optically*, i.e light influencing sound, and is given by

$$\mathbf{f} = \boldsymbol{\nabla} p_{\mathrm{st}}$$

where p_{st} is the electrostrictive pressure as shown in eq. (4.2) and discussed in section 4.1.2. For the optical fields we have here the source term is given by

$$\boldsymbol{\nabla} \cdot \mathbf{f} = \epsilon_0 \gamma_e k_{\mathrm{ac}}^2 \left[A_1 A_2^* e^{i(k_{\mathrm{ac}} z - \omega_{\mathrm{ac}} t)} + \mathrm{c.c} \right] \tag{4.6}$$

If we now introduce the source term and the density field into the acoustic wave equation, and assume that the acoustic amplitude varies slowly in space and time, we will have that

$$-2i\omega_{\mathrm{ac}} \frac{\partial \rho}{\partial t} + ({\Omega_{\mathrm{SBS}}}^2 - \omega_{\mathrm{ac}}^2 - i\omega_{\mathrm{ac}}\Gamma_{\mathrm{B}})\rho - 2ik_{\mathrm{ac}} v_{\mathrm{ac}}^2 \frac{\partial \rho}{\partial z} = \epsilon_0 \gamma_e k_{\mathrm{ac}}^2 A_1 A_2^* \tag{4.7}$$

where the Brillouin linewidth has been introduced as

$$\Gamma_{\mathrm{B}} = k_{\mathrm{ac}}^2 \alpha_{\mathrm{ac}} \tag{4.8}$$

which is the reciprocal of the phonon lifetime, $\tau_p = \Gamma_{\mathrm{B}}^{-1}$. In the case where the phonon propagation distance is significantly less than the optical propagation length, which is quite typical but not always the case [345], then the term with $\partial \rho / \partial z$ can be removed. Similarly, if we assume the system is in steady-state then $\partial \rho / \partial t$ also vanishes, and the acoustic amplitude will be given by

$$\rho(z, t) = \epsilon_0 \gamma_e k_{\mathrm{ac}}^2 \frac{A_1 A_2^*}{{\Omega_{\mathrm{SBS}}}^2 - \omega_{\mathrm{ac}}^2 - i\omega_{\mathrm{ac}}\Gamma_{\mathrm{B}}} \tag{4.9}$$

Now we shift back to the optical waves. The spatial evolution of each of the optical waves will of course be given by the Maxwells wave equation, eq. (3.10),

$$\frac{\partial^2 \tilde{E}_i}{\partial z^2} - \frac{1}{(c/n)^2} \frac{\partial^2 \tilde{E}_i}{\partial t^2} = \frac{1}{\epsilon_0 c^2} \frac{\partial^2 \tilde{P}_{\mathrm{NL}}}{\partial t^2} \qquad i = 1, 2 \tag{4.10}$$

The total nonlinear polarization, which gives rise to the source term in this case, is given by

$$\tilde{P}_{\mathrm{NL}} = \epsilon_0 \Delta\chi \tilde{E} = \epsilon_0 \Delta\epsilon \tilde{E} = \epsilon_0 {\rho_0}^{-1} \gamma_e \tilde{\rho} \tilde{E} \tag{4.11}$$

where we have introduced the perturbation in the dielectric properties due to the presence of the acoustic wave, i.e sound influencing light, as discussed in section 4.1.2. Incorporating the appropriate nonlinear driving term for each amplitude, and making the slowly-varying envelope approximation, yields the coupled amplitude equations

$$\frac{\partial A_1}{\partial z} + \frac{1}{c/n} \frac{\partial A_1}{\partial t} = \frac{i\omega\gamma_e}{2nc\rho_0} \rho A_2$$
$$\frac{\partial A_2}{\partial z} + \frac{1}{c/n} \frac{\partial A_2}{\partial t} = \frac{i\omega\gamma_e}{2nc\rho_0} \rho^* A_1$$

where ρ is the derived amplitude for the density, eq. (4.9) and the distinction of ω_1 and ω_2 has been dropped for the prefactor as $\omega = \omega_1 \simeq \omega_2$ when close to the SBS shift. If we again consider steady state in time, dropping the $\partial A / \partial t$ terms, and insert the value for ρ then the coupled amplitude equations become

$$\frac{\mathrm{d}A_1}{\mathrm{d}z} = \frac{i\epsilon_0 \omega k_{\mathrm{ac}}^2 \gamma_e^2}{2nc\rho_0} \frac{|A_2|^2}{(\Omega_{\mathrm{SBS}}{}^2 - \omega_{\mathrm{ac}}^2 - i\omega_{\mathrm{ac}}\Gamma_{\mathrm{B}})} A_1 \tag{4.12}$$

$$\frac{\mathrm{d}A_2}{\mathrm{d}z} = \frac{-i\epsilon_0 \omega k_{\mathrm{ac}}^2 \gamma_e^2}{2nc\rho_0} \frac{|A_1|^2}{(\Omega_{\mathrm{SBS}}{}^2 - \omega_{\mathrm{ac}}^2 + i\omega_{\mathrm{ac}}\Gamma_{\mathrm{B}})} A_2 \tag{4.13}$$

There are no terms in the above amplitudes which depend on the relative phases of the fields E_1 and E_2. This means that the coupled amplitudes can be directly converted into coupled intensities, where the intensity is defined as $I_i = 2n\epsilon_0 c A_i A_i^*$, and which are more conveniently defined in terms of coupled *powers*, where we now also include the effect of linear loss α as given below

$$\frac{\mathrm{d}P_1}{\mathrm{d}z} = -\frac{g_B}{A_{\mathrm{eff}}} P_1 P_2 - \alpha P_1 \tag{4.14}$$

$$-\frac{\mathrm{d}P_2}{\mathrm{d}z} = +\frac{g_B}{A_{\mathrm{eff}}} P_1 P_2 - \alpha P_2 \tag{4.15}$$

where A_{eff} is the effective area, as has been discussed earlier, and g_B is known as the SBS gain factor, which is approximately given by

$$g_B = g_0 \frac{(\Delta v_{\mathrm{B}}/2)^2}{(\Omega_{\mathrm{SBS}} - \omega_{\mathrm{ac}})^2 + (\Delta v_{\mathrm{B}}/2)^2} \tag{4.16}$$

with the right term describing a Lorentzian with linewidth of Δv_{B}, where $\Delta v_{\mathrm{B}}/2\pi$ is the linewidth in Hz, centered around the SBS shift downwards from ω_1. The g_0 is the peak gain factor, and is given by

$$g_0 = \frac{2\pi\gamma_e^2\omega^2}{n v_{\mathrm{ac}} c^3 \rho_0 \Delta v_{\mathrm{B}}} \tag{4.17}$$

which can be used to determine the overall strength of the SBS interaction when incorporating the appropriate electrostrictive coefficient γ_e for the material.

These coupled equations can be solved to determine the power transfer between the two counter propagating optical waves throughout the medium. The stokes wave enters from the *end* of the medium, i.e $P_2(L)$ is the input Stokes power, whereas $P_1(0)$ is the input pump power. These equations can be solved numerically, more generally if the time dependant terms are included, or, in certain limits, analytically [132]. We will discuss these specific cases further later in this section, after introducing the dramatic changes brough about by moving to systems with guided optical and acoustic waves.

4.3 Brillouin Scattering in Waveguides: An Overview

As has been discussed in section 3.2.1, moving to guided wave systems provides a number of advantages, and additional complexities, to nonlinear optics. The guided nature of the optical wave provides diffraction free propagation, enabling long interaction lengths, which can be beyond kilometres in the case of optical fibres. Waveguides can tightly confine light, greatly increasing the field intensity and the nonlinear interaction strength, and control the optical dispersion, allowing for highly engineered phasematching of disparate frequencies. When approaching sub-wavelength scales, the optical modes of the structure can exhibit field components in all three spatial directions, requiring the full tensor nature of nonlinear coefficients to be implemented appropriately. These effects, and others, are also important for Brillouin scattering. However, Brillouin scattering has the added complexity of the acoustic interaction, bringing about another degree of freedom and design requirement. The three main ways in which waveguides alter the system compared to bulk are:

- Acoustic guidance introduces acoustic modes with unique dispersive properties and mode profiles, such as transverse and surface acoustic waves
- Optical guidance modifies phase matching, opening up the possibility of scattering between other optical modes
- Additional forces arise due to interactions at the boundaries of the structure. Depending on the material and the geometry these forces can interfere constructively or destructively with the bulk electrostriction

The interplay between these features can greatly change the strength and dynamics of the Brillouin process, resulting in interesting effects like cascading to multiple Stokes orders from a single pump, or self-cancellation of the Brillouin interaction. To develop our intuition we will briefly discuss the properties of acoustic waveguides, explain in detail the different Brillouin processes available in multimode optical waveguides, and how to incorporate the new boundary forces when we calculate the SBS gain coefficient.

4.3.1 Acoustic Waveguides

To focus on the dynamics of acoustic waveguides we re-introduce the equations of motion for the acoustic wave, this time formulating the problem in terms of the displacement $\mathbf{u}$ and using Voigt notation to increase the clarity of the formulation. For background on Voigt notation and stress and strain please refer to Chapter A. We start with the general equation of motion using Voigt notation,

$$\nabla \cdot \mathbf{T} + \mathbf{f}_{\text{body}} = \rho \frac{\partial^2 \mathbf{u}}{\partial t^2} \tag{4.18}$$

We recall that the strain tensor $\mathbf{S}$ is related to the displacement $\mathbf{u}$ through $\mathbf{S} = \nabla_S \mathbf{u}$, where ∇_S is the symmetrised gradient. The constitutive relation, and other required definitions are given by

$$\nabla \cdot = \begin{bmatrix} \partial_x & 0 & 0 & 0 & \partial_z & \partial_y \\ 0 & \partial_y & 0 & \partial_z & 0 & \partial_x \\ 0 & 0 & \partial_z & \partial_y & \partial_x & 0 \end{bmatrix} \quad \mathbf{T} = \mathbf{c} : \mathbf{S} \quad \nabla_S = \begin{bmatrix} \partial_x & 0 & 0 \\ 0 & \partial_y & 0 \\ 0 & 0 & \partial_z \\ 0 & \partial_z & \partial_y \\ \partial_z & 0 & \partial_x \\ \partial_y & \partial_x & 0 \end{bmatrix} \tag{4.19}$$

We will consider systems were we can neglect body forces, so the equation of motion to be solved is

$$\nabla \cdot [\mathbf{c} \nabla_S \mathbf{u}] = \rho \frac{\partial^2 \mathbf{u}}{\partial t^2} \tag{4.20}$$

To develop some understanding of the wave equation we can start by assuming a simple solution with no x or y dependence, and a plane wave solution in the form of $\mathbf{u} = \mathbf{u}e^{-i\omega t}$. The assumption puts all derivatives with x and y to zero, so the resulting equations will reduce to

$$\begin{bmatrix} c_{44}\partial_z^2 u_x \\ c_{44}\partial_z^2 u_y \\ c_{11}\partial_z^2 u_z \end{bmatrix} = \rho \begin{bmatrix} \partial_t^2 u_x \\ \partial_t^2 u_y \\ \partial_t^2 u_z \end{bmatrix}$$

Thus we have a set of equations for the transverse components, and a separate equation for the longitudinal component. These equations reduce to typical wave equations such that

$$\frac{\partial^2}{\partial z^2} u_x = \frac{1}{v_S^2}\frac{\partial^2}{\partial t^2} u_x \qquad\qquad \frac{\partial^2}{\partial z^2} u_z = \frac{1}{v_L^2}\frac{\partial^2}{\partial t^2} u_z \tag{4.21}$$

where we have the transverse acoustic velocity $v_S = \sqrt{c_{44}/\rho}$ and the longitudinal acoustic velocity $v_L = \sqrt{c_{11}/\rho}$. The transverse waves are referred to as shear waves, and involve oscillations in the transverse direction as the wave propagates. The longitudinal waves are also referred to as pressure, dilatational, or compression waves, as the medium is compressed in the direction of propagation. In isotropic media the pressure waves are always faster than the transverse waves due to the relationship between the elastic coefficients, as $c_{44} = (c_{11} - c_{12})/2$.

We can go one step further with the plane wave description and consider the dispersion of the different waves. If we assume a solution in the form of

$$u_z(z,t) = Ae^{i(\beta z - \omega t)}$$

then this can be directly substituted into eq. (4.21) and yield

$$-\beta^2 Ae^{i(\beta z-\omega t)} = \frac{1}{v_L^2}(-\omega^2)Ae^{i(\beta z-\omega t)}$$
$$\rightarrow \omega = v_L\beta$$

Thus, we will have two linear curves, starting from the origin, where the slope given by the acoustic velocity of the plane waves for the shear and longitudinal solutions. It is worth noting that this was the relation assumed when calculating the phasematching in the case of SBS in bulk in section 4.2.1.

While looking at plane wave solutions can be informative, the general solutions to the full equation of motion, eq. (4.20), need to be solved incorporating various material parameters and device boundaries. The existence of hard boundaries between different materials typically leads a to a mixing of the different field components, such that acoustic modes of waveguides consist of quasi longitudinal and shear modes. While some geometries are analytically solvable, such as cylinders, numerical solvers are typically required. To demonstrate the typical acoustic modes available in a small core waveguide we numerically calculate the eigenmode solutions to the problem, using an open source finite element method (FEM) solver. We calculate the acoustic dispersion diagram by varying the simulated wave vector from the band edge to slightly past the phasematching point for the case of SBS, discussed earlier as $2\mathbf{k}_\mathrm{p}$. The calculation is performed on a rectangular Si waveguide, with dimensions of 800 nm × 220 nm, suspended in air, with the results shown in fig. 4.2.

If we look at the dispersion diagram for the waveguide system we can see a

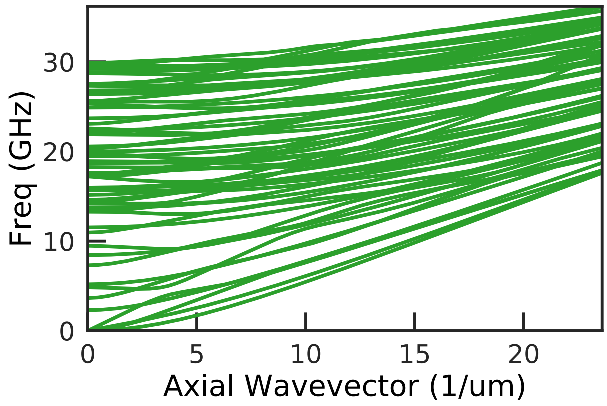

Figure 4.2: Calculated acoustic dispersion of a silicon nanowire suspended in air.

number of striking features. The majority of the curves are not linear, so assuming a linear dispersion from the offset is ineffective. The key differentiator in the case of acoustic guidance is that the majority of acoustic modes have a cutoff frequency, they do not approach zero frequency when **k** approaches zero. These modes are primarily shear waves, though they can possess a longitudinal component, and are typically flexural waves, which move horizontally or vertically, or torsional waves which twist the structure. The fact that these modes have a non-zero frequency as the wave vector approaches zero enables the possibility of strong forward Brillouin interactions. As the overall Brillouin interaction depends on the individual optical and modal fields, presence of both torsional and flexural modes is also interesting, particularly when considering the overlap with the optical fields, which we discuss in further detail in section 4.4.2.

4.4 Brillouin Processes in Multimode Waveguides

While the bulk of the work investigating and using Brillouin scattering in this thesis is based on traditional backwards SBS, with some experiments utilising forward scattering, it is incredibly useful to have an understanding of the available Brillouin interactions in waveguide systems. To that end we will provide a brief overview of the different interactions, show how phase matching is unique in the different cases and explore the dynamics of these processes. These different interactions are also discussed in detail in Chapter 2.

An optical waveguide with more than one optical mode is capable of 4 Brillouin interactions, depicted in fig. 4.3. These interactions can be categorized based on the *direction* of the scattered light, relative to the pump, and whether or not the scattered light is in the same optical *mode* as the pump. For the sake of the being explicit these are given below, with commonly used acronyms for these interactions also being specified.

- Backward intramodal scattering: SBS, BSBS
- Forward intramodal scattering: GAWBS, FBS, SRLS, FSBS, CBS
- Backward intermodal scattering: Intermodal SBS
- Forward intermodal scattering: FSBS, SIPS, SIMS

The multiple acronyms which have been used throughout the literature reflect the fact that these interactions have been investigated from a number of different perspectives, for a number of decades, and in different devices. We will provide some context for the origination of these terminologies. A frequent issue is the classification of interactions into stimulated vs spontaneous regimes, even though the dynamics are equivalent, and confusion about when one regime may transfer into the other.

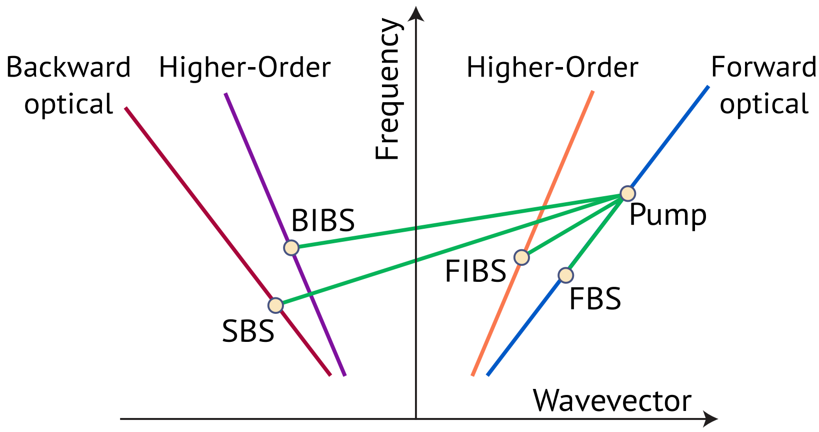

Figure 4.3: Schematic of brillouin interactions available in multimode optical waveguide

Backward intramodal scattering (SBS) This is the canonical Brillouin process in optical waveguides, first demonstrated in fibers in 1972 [45], and is simply referred to as stimulated Brillouin scattering (SBS). In some works discussing differing interactions the backwards propagating direction is sometimes clarified with the use of BSBS. When satisfying the phase matching condition, this process leads to exponential amplification of the Stokes wave, and corresponding build up of the acoustic wave, until the pump is depleted.

Forward intramodal scattering (FBS) The most controversial process, in terms of the number of acronyms, and is referred to as forward Brillouin scattering (FBS) in this thesis. The primary reason for this contention has been the distinction between the spontaneous process, typically referred to as guided acoustic wave Brillouin scattering (GAWBS), and the stimulated process, referred to as stimulated Raman-like scattering (SRLS) or forward SBS. This effect was first discovered in typical optical fibers by Shelby in 1985 [59, 60]. Shelby observed that the effect was purely a phase modulation, and could be polarised depending on the acoustic mode causing the scattering. Even though it is a phase modulation, this process can still be stimulated: an external pump and probe coherently generate a *constant* number of phonons through the medium, creating a phaselocked frequency comb akin to a strongly driven phase modulator [84, 104].

Backward intermodal scattering (BIBS) This process has received little attention in the literature, with a few publications investigating few-mode optical fibers [346–349]. This work has been primarily performed by a single group, which consistently used the naming convention intermodal SBS. The dynamics of the interaction are the same as SBS, with the gain coefficient being 1/2 to 1/3 lower for the fiber systems investigated so far. In this section we will refer to this process as backwards intermodal Brillouin scattering (BIBS).

Forward intermodal scattering (FIBS) First shown in 1990 by Russell [71, 72], in the MHz frequency range, this interaction is capable of exponential gain without cascading. In analogy with the backwards case, we refer to this process as forwards intermodal Brillouin scattering (FIBS). While the dynamics are quite distinct from FBS, it is possible for the same waveguide to host distinct acoustic modes capable of phasematching both processes [85, 86, 350]. This Brillouin process has recently been demonstrated in photonic circuits [109], utilising integrated mode-multiplexers to excite the distinct optical modes required for the interaction.

4.4.1 Phase-Matching with Guided Optical and Acoustic Modes

To understand why the dynamics of FBS is unique compared to the other processes we will start with the phase matching conditions for SBS, FBS and FIBS. Consider in an incoming pump wave, with frequency ω_p and wave vector $\mathbf{k}_\mathrm{p}$, which undergoes scattering from a phonon which exists in the medium. The scattered light can be frequency down shifted Ω_s, in which case a phonon with energy difference between the pump and the scattered wave is created, which is known as Stokes scattering. The scattered light can also be up shifted in frequency by Ω_as, absorbing a phonon from the medium, which is anti-Stokes scattering. The conservation of energy and momentum is given explicitly by

$$\hbar\omega_\mathrm{p} = \hbar\omega_\mathrm{s} + \hbar\Omega_\mathrm{s} \qquad \mathbf{k}_\mathrm{p} = \mathbf{k}_\mathrm{s} + \mathbf{q}_\mathrm{s} \qquad \text{(Stokes)}$$
$$\hbar\omega_\mathrm{p} + \hbar\Omega_\mathrm{as} = \hbar\omega_\mathrm{as} \qquad \mathbf{k}_\mathrm{p} + \mathbf{q}_\mathrm{as} = \mathbf{k}_\mathrm{as} \qquad \text{(anti-Stokes)}$$

For the sake of clarity, we now rearrange this for the acoustic frequencies and q values such that

$$\Omega_\mathrm{s} = \omega_\mathrm{p} - \omega_\mathrm{s} \qquad \mathbf{q}_\mathrm{s} = \mathbf{k}_\mathrm{p} - \mathbf{k}_\mathrm{s} \tag{4.22}$$
$$\Omega_\mathrm{as} = \omega_\mathrm{as} - \omega_\mathrm{p} \qquad \mathbf{q}_\mathrm{as} = \mathbf{k}_\mathrm{as} - \mathbf{k}_\mathrm{p} \tag{4.23}$$

The simultaneous solution of eq. (4.22), for the Stokes, and eq. (4.23), for the anti-Stokes, yields the phasematching conditions for the phonons involved in each case. Knowledge of the acoustic and optical dispersion of the waveguide is required to solve these relations in their generality. In the following we show this diagrammatically for each of the Brillouin processes of interest.

SBS We consider first the case of backwards intramodal scattering, typical SBS, where the optical wave is back scattered into the same mode as the pump, represented in fig. 4.4. From the optical dispersion diagram, fig. 4.4a, we can see that the $k_\mathrm{s,as} = -k_\mathrm{p} + \Delta k_\mathrm{s,as}$, where $\Delta k_\mathrm{s,as}$ is a small detuning around $-k_\mathrm{p}$. The slope of the optical band is given by, considering only first order dispersion terms, the optical group velocity at the frequency of interest i.e $\mathrm{d}\omega/\mathrm{d}k = c/n_{\mathrm{g(p)}}$, fig. 4.4b. If we recall that $k_z = n_\mathrm{eff}k_0$, we can express the relations for the k vectors of the scattered waves at a given acoustic frequency Ω, and thus the acoustic wave vectors $\mathbf{q}$ through

$$k_\mathrm{s} = -\frac{\omega_\mathrm{p} n_\mathrm{p}}{c} + \Omega_\mathrm{s}\frac{n_{\mathrm{g(p)}}}{c} \qquad k_\mathrm{as} = -\frac{\omega_\mathrm{p} n_\mathrm{p}}{c} - \Omega_\mathrm{as}\frac{n_{\mathrm{g(p)}}}{c}$$
$$\mathbf{q}_\mathrm{s} = 2\frac{\omega_\mathrm{p} n_\mathrm{p}}{c} - \Omega_\mathrm{s}\frac{n_{\mathrm{g(p)}}}{c} \qquad \mathbf{q}_\mathrm{as} = -\left(2\frac{\omega_\mathrm{p} n_\mathrm{p}}{c} + \Omega_\mathrm{as}\frac{n_{\mathrm{g(p)}}}{c}\right)$$

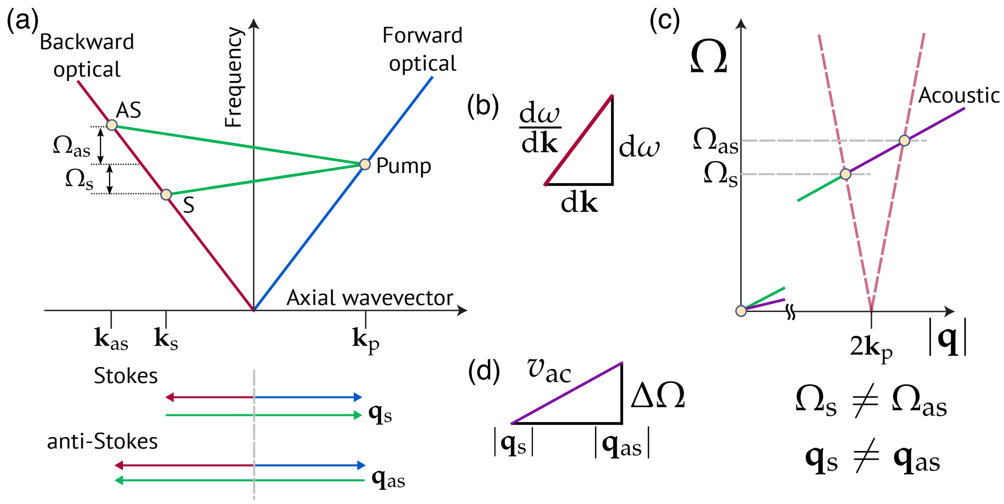

Figure 4.4: Phasematching of SBS (a) Optical dispersion diagram, with magnitude of wave vectors represented below (b) Small deltas of optical dispersion diagram (c) Acoustic dispersion diagram, with the phasematching conditions represented with the red dashed lines. From these distinct intercept points we can see that $\Omega_s \neq \Omega_{as}$ and $\mathbf{q}_s \neq \mathbf{q}_{as}$. (d) Small difference in frequency between Ω_s and Ω_{as}, typically on the order of 1 MHz.

This gives us the relations between the $|\mathbf{q}|$ values and Ω. As can be seen in the bottom of fig. 4.4a, the direction of the phonons is the same as the pump in Stokes scattering, and opposite to that of the pump in anti-Stokes scattering. By plotting these relations onto the acoustic dispersion, dashed red lines in fig. 4.4c, and looking at the intercept points, we can determine which acoustic modes phasematch at what frequencies. We also note that the values of acoustic wavevectors are quite large, with $|\mathbf{q}_s| = |\mathbf{q}_{as}| = +2|\mathbf{k}_p|$, when $\Omega = 0$.

For non-zero values of Ω, the length of the two acoustic wave vectors slightly differ. This may result in a frequency difference between Ω_s and Ω_{as} when phasematching to the same acoustic mode. Consider an acoustic wave with velocity v_{ac}, the difference between the two frequencies will be given by $\Delta\Omega \approx v_{ac} 2\Delta k$ where $\Delta k = \Omega n_g/c$, graphically shown in fig. 4.4d. If we consider the case of SiO_2, with $n_g = 1.44, v_{ac} = 5950\,\mathrm{m\,s^{-1}}$, and the difference around a frequency of $\Omega/2\pi = 10\,\mathrm{GHz}$, then $\Delta\Omega \approx 1\,\mathrm{MHz}$. As this value is small compared to the central frequency, it is typically neglected, however precise experiments recently measured this difference in a bulk TeO_2 crystal at cryogenic temperatures [351]. We can also consider the accuracy of typical SBS approximation that $k_s = -k_p$ as $\Delta k/k_p \approx 10^{-6}$, such that Δk can be safely neglected to first order.

FBS How does the phasematching change for the case of FBS? The scattered light is now along the same optical band as the pump, which means that the $\mathbf{q}$ values for Stokes and anti-Stokes phonons are given purely by the slope, and will thus be very small. For the sake of explicitness

$$k_s = \frac{\omega_p n_p}{c} - \Omega_s \frac{n_{g(p)}}{c} \qquad k_{as} = \frac{\omega_p n_p}{c} + \Omega_{as} \frac{n_{g(p)}}{c}$$
$$\mathbf{q}_s = \Omega_s \frac{n_{g(p)}}{c} \qquad \mathbf{q}_{as} = \Omega_{as} \frac{n_{g(p)}}{c}$$

As the $\mathbf{q}$ values are so small, this puts the phasematching curve right at the acoustic band edge. The acoustic modes facilitating the Brillouin interactions in this regime are typically transverse acoustic waves which are close to cutoff, such

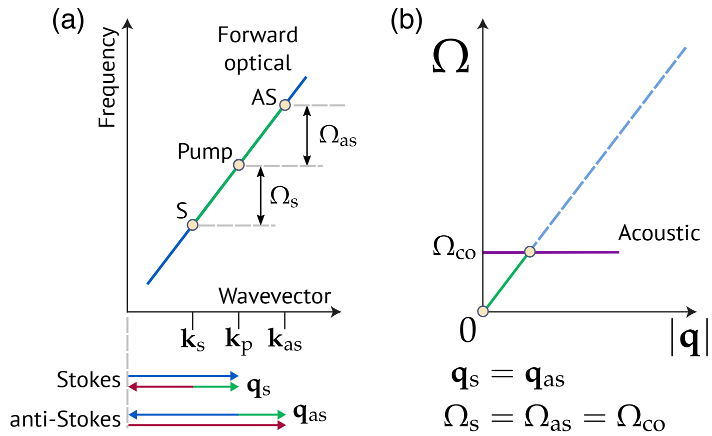

Figure 4.5: Phasematching of FBS (a) Optical scattering occurs within the same forward travelling mode. (b) Small values of $|\mathbf{q}|$ result in phasematching close to the acoustic band edge. Transverse acoustic mode families are close to cutoff and are practically flat, with $v_{ac} \approx 1\,\mathrm{m\,s^{-1}}$. This results in the unique situation that $\Omega_s = \Omega_{as} = \Omega_{co}$ and $\mathbf{q}_s \equiv \mathbf{q}_{as}$.

that $v_{ac} \approx 1\,\mathrm{m\,s^{-1}}$, making the frequency shift for the two scattering process now identical, i.e $\Omega_s = \Omega_{as} = \Omega_{co}$. This means that to first order $\mathbf{q}_s \equiv \mathbf{q}_{as}$. We can also consider the dephasing length of the two phonons, the distance over which they will accumulate a π phase difference. This is similar to the coherence length for the linear phase mismatch with FWM eq. (3.33). The dephasing length is be given by $\pi/\Delta\mathbf{q}$ where $\Delta\mathbf{q} = |\mathbf{q}_{as} - \mathbf{q}_s|$. As the Stokes and anti-Stokes frequencies are equal, the first order dispersion terms will cancel and the dephasing length will be primarily determined by the 2nd order dispersion at the pump wavelength, such that

$$L_{\text{phon}} = \frac{\pi}{\frac{\partial^2 k}{\partial \omega^2}\Omega_{co}^2}$$

For a silicon nanowire suspended in air, such the case of [103], the dephasing length is orders of magnitude beyond the cm length scale of the device.

What is the significance of the dephasing length being significantly longer than the device length? The phonons involved in the two scattering processes are practically identical; they act as the *same* phonons. If we enter the system with a single pump, as we spontaneously scatter light to Ω_s and Ω_{as}, we are *continuously* creating and annihilating phonons. The total amount of phonons will thus stay constant along the medium. If a pump and probe enters an FBS waveguide, with frequency spacing of Ω_0, a *constant* number of *stimulated* phonons will be generated. These phonons will efficiently scatter light to the Stokes and anti-Stokes frequencies, which will in turn continue to scatter to higher and lower frequencies, forming a *cascade* of phase-locked lines all driven from the *same* acoustic phonons. In contrast, in the case of SBS, as the pump is spontaneously scattered along the medium the Stokes phonons will increase, and the anti-Stokes phonons will *decrease*. The Stokes scattered light will quickly become amplified, generating even more phonons, facilitating *stimulated* scattering from noise. A more quantitative description of the dynamics will be given in section 4.4.3.

FIBS Forward scattering between two modes yields phasematching which is distinct from both SBS and FBS. Looking at the optical dispersion diagram for this case, fig. 4.6, we can see immediately that the acoustic phonons for the Stokes and anti-Stokes processes will not be equal, and that both k_s and k_{as} will be *smaller*

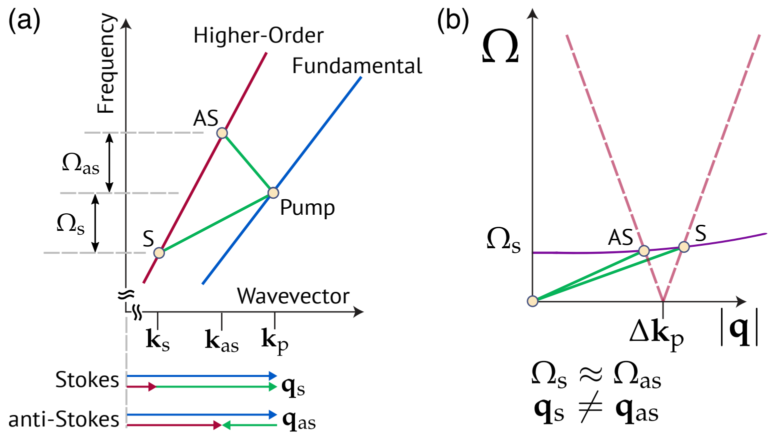

Figure 4.6: Phasematching of FIBS (a) Optical scattering occurs between two modes travelling the same direction, the n_g of the scattered mode provides the correction for $\mathbf{k}$ (b) Small values of $|\mathbf{q}|$ result in phasematching close to the acoustic band edge. Transverse acoustic mode families are close to cutoff and are practically flat, with $v_{ac} \approx 1\,\mathrm{m\,s^{-1}}$. This results in the unique situation that $\Omega_s = \Omega_{as} = \Omega_{co}$ and $\mathbf{q}_s \equiv \mathbf{q}_{as}$

than k_p, unlike in SBS. Following the previous two cases, the wavevectors for the optical and acoustic waves will be given by

$$k_s = \frac{\omega_p n_s}{c} - \Omega_s \frac{n_{g(s)}}{c} \qquad k_{as} = \frac{\omega_p n_s}{c} + \Omega_{as} \frac{n_{g(s)}}{c}$$
$$\mathbf{q}_s = \frac{\omega_p \Delta n}{c} + \Omega_s \frac{n_{g(s)}}{c} \qquad \mathbf{q}_{as} = -\left(\frac{\omega_p \Delta n}{c} - \Omega_{as} \frac{n_{g(s)}}{c}\right)$$

where n_s and $n_{g(s)}$ is the n_{eff} and n_g of the scattered optical mode, and $\Delta n = n_p - n_s$ at the pump frequency ω_p.

The form of the acoustic wave vectors is similar to that of SBS, with a forward and backwards travelling acoustic wave having slightly different lengths. However these are now centered around the difference in effective refractive index of the two modes i.e. Δn, rather than twice the pump n_{eff}. This puts the operating point closer to the acoustic band edge, but can shift higher if one of the modes is close to cutoff. For a typical small core waveguide we can expect $\Delta n > 0.1$, and the the term related to the slope of the scattered mode can be neglected. The acoustic waves of interest are generally relatively close to cutoff, such that $v_{ac} \approx 1\,\mathrm{m\,s^{-1}}$, and the acoustic frequency is primarily determined by the cutoff frequency of the acoustic mode such that $\Omega_{as} \approx \Omega_s$. However, because $|\mathbf{q}| \propto \omega_p$, there is likely to be some shift of Ω_s with the pump wavelength, quite distinct from the case of FBS. The dispersive symmetry braking of $\mathbf{q}_s$ and $\mathbf{q}_{as}$ results in exponential amplification at the Stokes shift, without further cascading, as in the case of SBS.

4.4.2 Mode Symmetry and Overlaps

We have been discussing the above phasematching conditions in the context of a single acoustic mode, but we know from the earlier discussions on acoustic waveguides that these can feature many modes, as shown in fig. 4.2. Does this mean that a single pump will couple, through the different Brillouin processes, to hundreds of acoustic modes? No, satisfying phase matching *alone* does not guarantee a strong interaction and large Brillouin gain coefficient. For non-negligible gain coefficients to be attained, the acoustic and optical mode profiles need to have a large overlap. We discuss the importance of the overlap in fine detail in

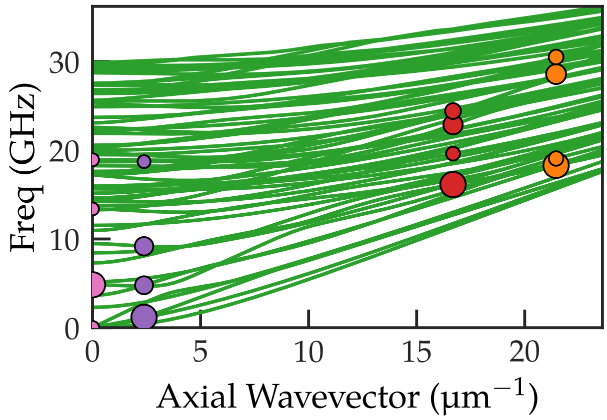

Figure 4.7: Representation of high Brillouin gain acoustic modes overlaid on the acoustic dispersion diagram. The 4 highest gain modes are shown for the case of FBS, FIBS and SBS, for the TE1 and TE0 (fundamental mode), respectively. The size of the circles are normalised to the maximum gain coefficient for each of the interactions. This result shows the highly disparate acoustic modes facilitating the various Brillouin processes.

section 4.5. A primary consideration is the symmetries of the various optical and acoustic modes, as described in [101] and in fine detail in [352], where the authors demonstrated selection rules for the different processes and general waveguide geometries.

To understand the importance of these symmetries in further detail we will explore the mode profiles of acoustic modes which yield large Brillouin gain coefficients for the different interactions. We investigate this in a single waveguide by showing the phasematching conditions, for SBS, FBS and FIBS, in a silicon nanowire with a geometry of 800 nm × 220 nm, suspended in air, fig. 4.7. For these calculations we use an internally developed tool, Numerical Brillouin Analysis Tool (NumBAT), to calculate the optical and acoustic modes, and the gain coefficient, assuming a pump wavelength of 1550 nm. This tool is discussed in section 4.5.3.

First of all, we plot the primary field components and intensity distribution of the fundamental TE-like mode, which has an $n_{\text{eff}} = 2.7$, and higher order TE-like mode, TE1 with $n_{\text{eff}} = 2.25$, in fig. 4.8a. We can see that the TE1 mode is less confined, unsurprisingly as the mode is closer to cutoff, and features large field intensities at the edges of the waveguide. Both the modes have a considerable E_z component, which affects the overall shape of the field intensity, $\|\mathbf{E}\|$. In fig. 4.8b we plot the field components of the acoustic modes yielding the highest gain for FBS and FIBS. While the norm of the acoustic modes $\|\mathbf{u}\|$ look similar, we can see that the symmetry of the components of the mode is highly distinct, as expected for the requirements for coupling distinct optical modes. Finally in fig. 4.8c we plot the field components for the acoustic modes which give the largest gain for SBS, for the TE0 and TE1 optical modes. The modes are longitudinal modes, identifiable due to the fact that the u_z component is dominant. The variations between the u_z profiles follow the mode profiles of the optical modes.

4.4.3 Dynamics: Cascading vs Non-Cascading

In the discussions of phase matching we found that in FBS, if the dispersion is low enough, Stokes and anti-Stokes scattering occur from the *same* phonons. These phonons are capable of further optical scattering to higher orders, producing a

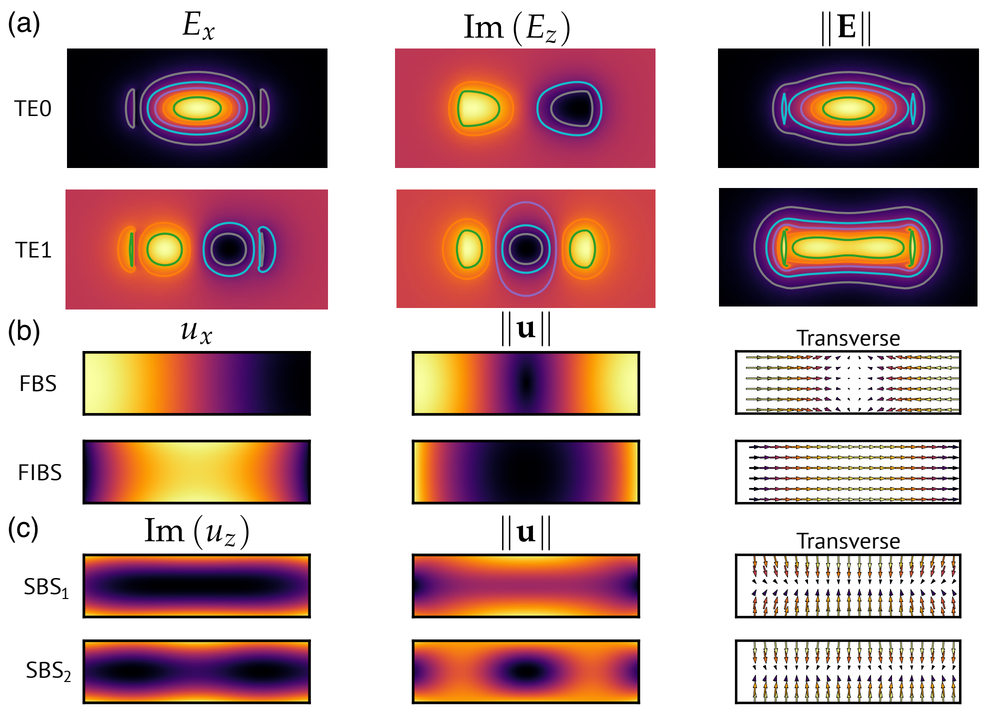

Figure 4.8: Mode profiles of optical and acoustic modes involved in Brillouin scattering (a) Plots of primary field components of TE0 and TE1 optical modes (b) Primary field components of acoustic modes yielding the highest gain coefficients for FBS and FIBS. The transverse plots show the flow the different modes. (c) The same as the prior but for SBS for the TE0 and TE1 modes respectively. The transverse field plot is primarily into the page.

cascade of scattered optical lines. Unsurprisingly this leads to a markedly unique set of dynamics compared to other Brillouin processes where this condition is not met. We will start with an overview of the case of non-cascaded systems, so SBS, FIBS and backwards intermodal Brillouin scattering (BIBS), and we can commence with the coupled wave formalism introduced in bulk, section 4.2.2. In particular the coupled wave equations for the pump and Stokes wave, eq. (4.15), were given by

$$\frac{\mathrm{d}P_\mathrm{p}}{\mathrm{d}z} = -G_\mathrm{B}(\Omega)P_\mathrm{p}P_\mathrm{s} - \alpha P_\mathrm{p}$$
$$-\frac{\mathrm{d}P_\mathrm{s}}{\mathrm{d}z} = +G_\mathrm{B}(\Omega)P_\mathrm{p}P_\mathrm{s} - \alpha P_\mathrm{s}$$

where G_B is the Brillouin gain coefficient. To solve these equations generally one needs to use numerical techniques, such as the shooting method [353, 354], however in certain limits they can be solved analytically. The most standard of these is the ”undepleted pump limit” [39, 355]. If we assume that the Stokes power is sufficiently low, and stays low enough through the medium, and that $P_\mathrm{p}P_\mathrm{s} \ll P_\mathrm{p}$, then the first term in the pump equation can be neglected. This allows for direct solution of the pump equation, as it is just simple attenuation, leading to $P_\mathrm{p}(z) = P_\mathrm{p}(0)\exp(-\alpha z)$ which can be substituted into the equation for the Stokes giving

$$-\frac{\mathrm{d}P_\mathrm{s}}{\mathrm{d}z} = \left(G_\mathrm{B}(\Omega)P_\mathrm{p}(0)\exp(-\alpha\, z) - \alpha\right) P_\mathrm{s}$$

and which leads to the well known exponential gain relation for the Stokes wave after a device length L,

$$P_{\mathrm{s}}(L) = P_0 \exp\left(G_{\mathrm{B}} P_{\mathrm{p}} L_{\mathrm{eff}}\right) \exp(-\alpha L) \tag{4.24}$$

where P_0 and P_{p} are the input Stokes and pump powers, and L_{eff} is the effective length as introduced in eq. (3.42), $L_{\mathrm{eff}} = (1 - \exp(\alpha L))/\alpha$. The range of parameters over which this assumption is valid has been explored in the case of linear operation for microwave photonic filters [355]. If $P_{\mathrm{s}} \approx P_{\mathrm{p}}$, then depletion occurs and the above approximations will be invalid. For waveguides with weak birefringence, such as typical SMF, the coupled equations should be tailored to account for the state of polarisation of the pump and probe light [356, 357].

How do these dynamics change in cascaded systems, such as FBS? First of all, if a coupled wave formalism is being implemented then it needs include an appropriate amount of coupled waves to start with. Here, we will follow the working of the supplementary of [84], which is similar to the supplementary of [103]. We consider a total electric field formed from the sum of n individual fields, each with frequency of $\omega_n = \omega_0 + n\Omega$, such that

$$E(z,t) = E_0 \sum_n a_n(z,t) e^{i(\beta_n z - \omega_n t)} + \text{c.c}$$

From here the approach is similar to Boyd [140], and section 4.2.2. Briefly summarising, we now consider the acoustic amplitude from the sum of all these fields, and the associated optical amplitude evolution in steady state,

$$b(z) = \epsilon_0 \gamma_e Q_1 \frac{\sum_n a_{n-1}^* a_n}{\omega^2 - \Omega_{\mathrm{SBS}}^2 + i\Omega\Gamma_{\mathrm{B}}} \tag{4.25}$$

$$\frac{\partial a_n}{\partial z} = \frac{i\omega_n \gamma_e Q_0}{2 n_{\mathrm{eff}} c \rho_0} (a_{n-1} b + a_{n+1} b^*) \tag{4.26}$$

As the spread of the comb of lines is quite small compared to the pump frequency ω_1, we can approximate the frequency and the propagation constant, for use in the prefactor, as $\omega_n \approx \omega_1$ and $\beta_n \approx \beta_1$ for all values of n. Inserting eq. (4.26) into eq. (4.25), and looking at the geometric series, yields the result that $\frac{\partial b(z)}{\partial z} = 0$, i.e that the phonon amplitude is *constant* along the medium, and depends on the initial input field amplitudes. If we now consider a dual frequency pump, which has spacing precisely matched to the frequency shift ($\Omega = \Omega_{\mathrm{SBS}}$) and optical powers of $P_1(0)$ and $P_2(0)$, the above equations simplify to

$$b(z) = b(0) = \frac{i\gamma_e |Q_1|}{2 n_{\mathrm{eff}} c \Omega_{\mathrm{SBS}} \Gamma_{\mathrm{B}}} \sqrt{P_1(0) P_2(0)} e^{i\phi_0} \tag{4.27}$$

$$\frac{\partial a_n}{\partial z} = \frac{1}{2} G_{\mathrm{B}} \sqrt{P_1(0) P_2(0)} \left(a_{n+1} e^{-i\phi_0} - a_{n-1} e^{i\phi_0} \right) \tag{4.28}$$

where ϕ_0 is the phase difference between the two pump fields at the input. Solutions to the field amplitudes are given by sets of Bessel's functions

$$a_n(\xi) = a_1(0) e^{i(n-1)(\phi_0 - \pi)} \mathrm{J}_{n-1}(\xi) + a_2(0) e^{i(n-2)(\phi_0 - \pi)} \mathrm{J}_{n-2}(\xi) \tag{4.29}$$

where $\xi \equiv G_{\mathrm{B}} z \sqrt{P_1(0) P_2(0)}$ is defined as the normalized propagation length. For $\xi > 2$, achieved by increasing G_{B}, device length or input power, 3rd and 4th order cascaded terms become significant. If we express this in terms of the pair of input electric fields we have that

$$E(z,t) = E_0\left(a_1(0)e^{i(\beta_1 z-\omega_1 t)} + a_2(0)e^{i(\beta_2 z-\omega_2 t)}\right)e^{-i\xi\,\sin[i(q_{\mathrm{ac}}z-\Omega_{\mathrm{SBS}}t)+\phi_0]} + \mathrm{c.c}$$

This equation is precisely, surprisingly, the form of a *phase modulation*. This is equivalent to an electro-optic modulator, where ξ would be a driving voltage at the acoustic frequency Ω_{SBS}. We also know that the acoustic waves which facilitate strong FBS are transverse acoustic waves close to cutoff, and with extremely slow acoustic velocities $v_{\mathrm{ac}} \approx 1\,\mathrm{m\,s^{-1}}$. Conceptually this means we can imagine the FBS process, with two strong input pumps, as coherently generating a constant number of standing acoustic waves along the waveguide, where each acoustic wave acts a localised oscillator modulating the phase of the pumping light, cascading the light to higher and higher frequencies in a phase locked frequency comb. This cascading has been demonstrated in small core PCFs [84] and si waveguides [104]. Note that the presence of the Kerr effect and optical dispersion will alter these equations. A rigorous derivation of the cascaded system, using envelopes to capture all the interacting waves automatically and based on a Hamiltonian approach, can be found in [358, 359].

If cascaded processes produce a phase modulation, does this prevent their use as a small signal amplifier? Not necessarily. In the supplementary of the work [103], Van Laer describes how the above reduces to the single sideband case in the appropriate limits. Following the argument in that work, if we look just at the evolution of the Stokes field amplitude, which corresponds to $n = 1$, we have that

$$a_{\mathrm{s}}(z) = a_{\mathrm{s}}(0) - \mathrm{J}_1(\xi)a_{\mathrm{p}}(0)e^{-i(\phi_0-\pi)}$$

converting this into a power, and approximating $\mathrm{J}_1(\xi) \approx \xi/2$ gives

$$P_{\mathrm{s}}(z) = P_{\mathrm{s}}(0)\left(1 + G_{\mathrm{B}}P_{\mathrm{p}}z\right) + \frac{\xi^2}{4}P_{\mathrm{p}}$$

For small values of ξ, the ξ^2 term is negligible compared to the others. Taking the derivative of z, and setting z to zero then results in

$$\frac{\mathrm{d}P_{\mathrm{s}}}{\mathrm{d}z} = G_{\mathrm{B}}P_{\mathrm{p}}P_{\mathrm{s}}$$

which is the same as the non-cascaded case, when neglecting linear loss and noting the forward travelling direction. Thus, in the case where cascading is minimal, i.e small values of ξ, FBS can be treated as a single sideband amplification, like non-cascaded systems. This limit is more stringent than the undepleted pump approximation, it strictly requires small input power values and amplification factors. However it does allow for the gain coefficient to be extracted using single sideband techniques, as experimentally demonstrated [103, 104, 360].

4.4.4 Spontaneous Scattering and Noise

So far we have assumed stimulated scattering, where the phonons are optically induced with a pump and probe or two pumps. However, we will also have spontaneous scattering from thermal phonons which exist due to the thermal energy available in the system. In terms of the dynamics, this adds an extra term, fluctuating in time, in the density equation used in the coupled wave equations

[361–366], and has been studied extensively in the literature. In effect this produces scattering from the pump, completely in the absence of any input Stokes wave, which will then act act as effective input to seed Brillouin scattering through the rest of the system. In the well cited work [44], Smith argued that this distributed scattering source could be summed and considered as an effective seed input into the fiber. This input will then be amplified through SBS and, at some *critical* power level, deplete the pump. Using the typical parameters for optical fiber at the time, in 1972, this critical power could be estimated analytically as

$$P_{\mathrm{crit}} \approx 21 \left(\frac{\alpha}{G_{\mathrm{B}}} \right)$$

and was found to be in the range 10 mW, clearly being a limitation for communications systems and nonlinear optics. The critical power is the pump power at which depletion is expected from a backwards travelling Stokes wave generated purely from noise. It is sometimes referred to the SBS "threshold" power, and has caused some confusion in the literature of its exact definition and use, with authors arbitrarily defining extra prefactors such as 1% [132]. If any accuracy is desired one should use the appropriate L_{eff} and Brillouin linewidth of their device, a thorough review of higher accuracy analytic calculations of the threshold are found in [132]. Because of this, caution must be placed on calculations on the G_{B} which use the critical power alone.

Even if we have a seeded configuration, with a pump and probe, the thermal phonons still exist and spontaneous scattering process will still occur. In this case the spontaneous scattering will act as a narrowband noise source, typically referred to as SBS amplified spontaneous emission (SBS ASE), within the Brillouin linewidth. This noise source was initially considered so large that Brillouin amplifiers would not be suitable for a range of applications [64, 66, 365]. Many experiments investigating Brillouin amplifiers used long lengths of fiber, operating close to P_{crit}, and did not correctly adopt techniques to measure the noise figure in a narrow band range [367]. Some more recent approaches adopting electronic techniques from communications, or producing highly stabilised pump and probe, have shown convincing results that the noise figure can be reasonable [368–370]. Brillouin amplifiers have been shown to be highly effective at amplifying extremely weak signals [371, 372], and the flexibility allows for complicated sources to self filter themselves [373]. There is also the possibility of reducing the noise figure by using FBS systems for amplification. Recent theoretical work found that the noise increases at a slower rate than the amplification factors, quite unlike typical SBS [359].

4.5 Calculating the Brillouin Gain Coefficient

The strength of the Brillouin interactions is governed by the Brillouin gain coefficient G_{B} and, as such, understanding and increasing G_{B} is highly desirable. The peak gain factor introduced in section 4.2.1 is only suitable for plane waves in bulk. We will show it is possible to extend this approach to fibers, however to correctly capture the interactions of boundary forces in subwavelength waveguides a new formulation is required. We will summarise the different techniques which have been introduced in the literature to calculate the gain coefficient, where they can be applied, and discuss the open source tool developed in our group for this purpose.

4.5.1 Optoacoustic Overlap and Optical Fibers

We recall the peak gain factor, eq. (4.17), derived from the coupled wave approach considering plane waves in bulk and the electrostrictive pressure term, as

$$g_0 = \frac{2\pi\gamma_e^2\omega^2}{nv_{\mathrm{ac}}c^3\rho_0\Delta v_{\mathrm{B}}}$$

For longitudinal waves in an isotropic medium the electrostrictive constant is $\gamma_e = n^4 p_{12}$, such that we will have

$$g_0 = \frac{2\pi n^7 p_{12}^2}{c\lambda^2\rho_0\Delta v_{\mathrm{B}}v_{\mathrm{ac}}} \tag{4.30}$$

It is immediately apparent that a material with high refractive index, and large photoelastic coefficient p_{12}, is critical to achieve large electrostrictive gain. We will now explain how this gain factor can be extended to the appropriate gain coefficient through the use of an overlap integral for the optical and acoustic wave.

Even before the 1980s, it had become clear that an understanding of the optical and acoustic modes of the fiber were required to accurately describe the Brillouin spectrum and peak gain factor [55]. With the advent of high resolution measurement techniques, based on electrical equipment such as RF spectrum analysers [60, 374] or lock-in amplifiers [78], the complex features due to the various overlaps between distinct acoustic modes could be fully captured. From these measurements the theory was appropriately further developed and the optoacoustic overlap was introduced [76, 375]. With this the Brillouin gain coefficient, for a given acoustic mode m, is given by

$$G_{\mathrm{B}} = g_0\eta_m/A_{\mathrm{eff}} \qquad\qquad \eta_m = \frac{|\int ||\mathbf{E}||^2\tilde{\rho}_m\,\mathrm{d}A\,|^2}{\int ||\mathbf{E}||^2\,\mathrm{d}A\int|\tilde{\rho}_m|^2\,\mathrm{d}A} \tag{4.31}$$

where η_m is the optoacoustic overlap, and where $||\mathbf{E}||^2$ is the intensity profile of the optical mode and $\tilde{\rho}_m$ is the acoustic mode field, the density fluctuation away from equilibrium. The optoacoustic overlap is normalised in such a way that it is dimensionless and varies between 0 and 1. Thus upon calculation of the optical and acoustic mode profiles, typically with a FEM solver, η_m can be calculated and combined with the peak gain factor to determine the Brillouin gain coefficient. It is important to note that this calculation is a purely scalar overlap, based on the intensities of the fields and not the directions of individual components. As such it is only appropriate for large waveguides away from cutoff, such that the E_z component of the optical mode is minimised and the optical and acoustic fields are well confined within the core.

Numerical calculations of the overlap integral are capable of accurate and informative results, provided that appropriate acoustic modal solvers are available [376–380]. Analytic calculations can also be highly informative, and typically allow for more straightforward dis-entangling of different components, and significant effort has been put into developing analytic models for optical fiber geometries [381, 382]. To this end McCurdy developed a set of equations capable of solving for the acoustic modes of a fiber for any arbitrary radial index profile [383]. This was expanded further by Dong, with the formulation of a *complex* mode solver, capable of solving for leaky acoustic waves of an arbitrary waveguide and providing detailed comparison with experiment [384, 385]. Adopting a combination of analytic, or semi-analytic, and numerical approaches is overall highly desirable and should be attempted if possible.

4.5.2 Small Core Devices and Boundary Interactions

Moving to small core waveguides brings a number of new challenges for calculating the gain coefficient. The optical and acoustic modes both become highly hybridised, with a single mode capable of containing field components of all three axis. This requires an appropriate vector overlap integral, needing a full vectorial solution of the acoustic mode, and was initially performed for small core PCFs devices using an acoustic eigenmode solver [82, 85, 86]. Perhaps more crucially, forces arising due to interactions with the boundary of the waveguide can significantly alter the gain coefficient. In this section we will summarise the development of approaches incorporating these affects, while outlining key equations of the different approaches.

The fact that photons carry momentum, which gives rise to the force of radiation pressure, was first postulated by Kepler in the 17th century. In the last decade the harnessing of radiation pressure in subwavelength optical cavities has recieved tremendous attention, in particular as a new means of investigating quantum systems [98, 386]. In this context Peter Rakich explored the addition of electrostrictive forces to those of radiation pressure, for high index dielectric waveguides surrounded by air [100]. It was found that appropriate tailoring of the geometry could significantly enhance the overall interaction, or depending on the signs of the particular medium, the two sets of forces could destructively interfere. While further exploring how these forces change with geometry, it was shown that the force due to radiation pressure scales precisely with the magnitude of the dispersion of the guided mode [387].

With this understanding Rakich then determined the Brillouin gain in these subwavelength waveguides, with values above $10^4\,\mathrm{m}^{-1}\,\mathrm{W}^{-1}$ for SBS, and, quite extraordinarily, coefficients beyond $10^5\,\mathrm{m}^{-1}\,\mathrm{W}^{-1}$ for FBS in Si nanowires surrounded by air [95]. The precise formulation recast the Brillouin coupling based on a particle flux argument, considering the generated particles in the time and spatial domains, and the resulting force densities. To improve the understanding and calculation of the resulting gain coefficient, Wenjun Qiu, working with Rakich, developed a calculation framework purely on the basis of overlaps of the optical and acoustic modes [101], extending the particle flux approach. For a single acoustic mode m with frequency Ω_m and linewidth Γ_m the gain coefficient G_B is given by

$$G_\mathrm{B} = \frac{2\omega}{\Omega_m \Gamma_m v_\mathrm{g}^2} \frac{|\langle \mathbf{f}, \mathbf{u}_m \rangle|^2}{\langle \mathbf{E}_p, \epsilon \mathbf{E}_p \rangle \langle \mathbf{E}_s, \epsilon \mathbf{E}_s \rangle \langle \mathbf{u}_m, \rho \mathbf{u}_m \rangle} \tag{4.32}$$

where v_g is the optical group velocity and the 3 terms in the denominator on the right are required for normalisation of the optical and acoustic mode fields. The angled brackets represent an overlap integral across the waveguide cross section, and it is key to note that the force integral can be represented as a sum over individual forces

$$\langle \mathbf{A}, \mathbf{B} \rangle = \int \mathbf{A}^* \cdot \mathbf{B}\, \mathrm{d}s \qquad\qquad \langle \mathbf{f}, \mathbf{u}_m \rangle = \sum_n \langle \mathbf{f}_n, \mathbf{u}_m \rangle \tag{4.33}$$

The force of electrostriction is derived from the electrostriction tensor, which is given by

$$\sigma_{ij} = -\frac{1}{2}\epsilon_0 n^4 p_{ijkl} E_k E_l$$

where n is the refractive index, and p_{ijkl} is the photoelastic tensor. As the total electric field is given by the sum of the pump and stokes waves, which are separated in frequency by Ω, the resultant terms of interest at Ω are given by

$$\sigma_{ij} = -\frac{1}{4}\epsilon_0 n^4 p_{ijkl}(E_{pk}E_{sl}^* + E_{pl}E_{sk}^*) \tag{4.34}$$

where E_{pk} denotes the k-th component of the pump field etc. The divergence of all the six components represented in eq. (4.34) yields the electrostrictive force. The radiation pressure contribution of the forces is found by looking at the difference in the Maxwell stress tensor on either side of a material boundary, formed between two materials ϵ_1 and ϵ_2. If this is decomposed into the appropriate values, again considering the total electric field of the pump and Stokes at frequency Ω, the resulting force due to radiation pressure is

$$\mathbf{F}^{\text{RP}} = -\frac{1}{2}\epsilon_0 E_{pt}E_{st}^*(\epsilon_2 - \epsilon_1)\mathbf{n} + \frac{1}{2}\epsilon_0^{-1} D_{pn}D_{sn}^*(\epsilon_2^{-1} - \epsilon_1^{-1})\mathbf{n} \tag{4.35}$$

where the fields have been deconvolved into tangential components, such as E_{pt}, and normal components such as D_{pn}. D_n are determined from the boundary conditions, such that $D_n = \epsilon_1 E_{1n} = \epsilon_2 E_{2n}$. The force of radiation pressure is normal to the surface and points from the high index medium to the low index medium, i.e outwards for a dielectric surrounded by air. The paper of Qiu then looks specifically at the cases of SBS and FBS in a silicon waveguide surrounded by air, and how the individual forces scale [101]. There are also discussions of what *symmetries* of acoustic modes facilitate the different Brillouin interactions, which was given more focus in a work of Wolff which applied group theory to the problem [352].

While being wholly comprehensive, and being applied with good matching between simulation and experiment [103, 104], the work of Rakich and Qiu is not totally without contention. In particular, the divergence of the electrostrictive stress, eq. (4.34), introduces boundary terms due to electrostriction which are not immediately understood. This point is addressed in the highly detailed work of Wolff [388], which avoids this issue by describing the system not with forces and particle fluxes, but instead from the direction of perturbation theory. The resulting framework is similar to the above, utilising overlap integrals of optical and acoustic modes. The exact implementation within our group has lead to the development of an open source tool, using internal expertise for the optical and acoustic FEM solvers, which will be discussed further in the next section. This perturbation approach has been applied with great success to tapered silica fibers, with the remarkable experimental demonstration of perfect cancellation of SBS through destructive interference of radiation pressure and electrostriction [389]. The electrostrictive force found from the perturbation approach has also been used previously in PCFs [85, 86].

So far we have focused on calculations utilising overlap integrals of the optical and acoustic modes. It is not always straightforward to calculate acoustic modes of structures, particularly in the case of PCFs which may simultaneously have may high frequency acoustic modes, inside the PCFs core, and low frequency acoustic modes which exist over the entire fiber structure. An alternative to overlap integrals is performing calculations based on elastodynamics [390–392]. This approach entails looking at the phonon distribution which is *directly* generated due to the optical mode of the pump, taking into account the boundaries, and then determining the scattered light from this perturbation. This technique has been applied to a number of devices including PCFs [393], hybrid and surface acoustic waves in a tapered silica fiber [394], and slowly tapered PCFs with spatial measurements [395], among others. The main drawback of this technique is the focus on phonon energy density and scattered optical power, preventing quantitative comparisons of the gain coefficient.

4.5.3 The Numerical Brillouin Analysis Tool

As discussed in the previous section, calculations utilising overlap integrals to determine the Brillouin gain coefficient G_{B} require the optical and acoustic modes of the waveguide structure. While a number of tools exist for calculation of the optical modes, for the acoustic problem researchers typically utilise Comsol Multiphysics, with the mode field then exported to Matlab for the final overlap calculation. While being highly accessible, commercial tools limit the available reach of research and can inhibit reproducibility with various separate implementations of essentially the same calculation. Building on previous experience with an open-source optical simulation package, EMUstack, members of our extended group have developed a new open-source tool, termed the Numerical Brillouin Analysis Tool (NumBAT), which is available on github.

The gain coefficient calculated by NumBAT is quite similar to the forces approach of eq. (4.32). The key difference is the use of the perturbation factors for the photoelastic term and the moving boundary, which are summed to give the total term [388, 389]. We also utilise the acoustic energy density for normalisation, instead of the acoustic modal power, as the modal power becomes undefined for small $\mathbf{q}$ values like with FBS [396]. With this approach the G_{B} is given by

$$G_{\mathrm{B}} = \frac{2\omega |Q|^2}{P_{\mathrm{P}} P_{\mathrm{S}} \mathcal{E}_{\mathrm{A}}} \frac{\Omega}{\hat{\alpha}} \tag{4.36}$$

where $P_{\mathrm{P}}, P_{\mathrm{S}}$ are normalisation terms for the optical powers, $\mathcal{E}_{\mathrm{A}}$ is the acoustic energy density, $\hat{\alpha}$ is the acoustic attenuation in units of s^{-1} and $Q = Q_{\mathrm{PE}} + Q_{\mathrm{MB}}$ is the total interaction due to electrostriction and radiation pressure. The normalisation terms are given by the following overlap integrals

$$P_{\mathrm{P}} = 2 \int \mathrm{d}^2 r \, \hat{\mathbf{z}} \cdot (\mathbf{E}_{\mathrm{P}}^* \times \mathbf{H}_{\mathrm{P}}) \qquad \mathcal{E}_{\mathrm{A}} = 2\Omega^2 \int \mathrm{d}^2 r \, \rho |\mathbf{u}|^2 \tag{4.37}$$

$$\hat{\alpha} = -\frac{\Omega^2}{\mathcal{E}_{\mathrm{A}}} \int \mathrm{d}^2 \mathbf{r} \sum_{ijkl} \partial_j u_i^* \eta_{ijkl} \partial_k u_l \tag{4.38}$$

where η_{ijkl} is the dissipation tensor. If the dissipation is not known, a fixed mechanical quality factor of $Q_{\mathrm{m}} = \Omega / \hat{\alpha}$ can be utilised instead. The electrostriction and radiation pressure terms are given by

$$Q_{\mathrm{PE}} = \epsilon_0 \int \mathbf{E}_s^* \cdot (-n^4 \mathbf{p} \cdot \boldsymbol{\nabla}_{\mathrm{S}} \mathbf{u})^* \cdot \mathbf{E}_p \, \mathrm{d}A \tag{4.39}$$

$$\begin{aligned} Q_{\mathrm{MB}} = &\int_C (\mathbf{u}^* \cdot \hat{\mathbf{n}}) \Big[(\epsilon_a - \epsilon_b)\epsilon_0 (\hat{\mathbf{n}} \times \mathbf{E}_s)^* \cdot (\hat{\mathbf{n}} \times \mathbf{E}_p) \\ &- (\epsilon_a^{-1} - \epsilon_b^{-1})\epsilon_0^{-1} (\hat{\mathbf{n}} \cdot \mathbf{D}_s)^* \cdot (\hat{\mathbf{n}} \cdot \mathbf{D}_p) \Big] \, \mathrm{d}\mathbf{r} \end{aligned} \tag{4.40}$$

where $\mathbf{p}$ is the photoelastic tensor and $\boldsymbol{\nabla}_{\mathrm{S}}$ is the symmetrised gradient from section 4.3.1, and the Q_{MB} term consists of a contour integral performed along the interface between the two dielectric media.

NumBAT provides an accessible python interface to the calculation of the Brillouin gain coefficient. The most intensive calculations, the optical and acoustic FEM and the overlap integrals, are implemented in Fortran for efficiency, and called from a simple python script. Standardised plotting routines, for the field profiles and Brillouin frequency spectrum, are also implemented as pre defined functions. To accompany the software a materials database has also been created with values from various parts of the literature. With only tens of lines of python code it is possible to define a geometry, simulate the modes of the structure, and determine the gain coefficient. NumBAT is used throughout this thesis for simulations of the Brillouin gain coefficient, and optical and acoustic modes.

Part II

Brillouin Scattering in Circuits

Chapter 5

Giant Brillouin Gain in Photonic Circuits

Chalcogenide glasses have been investigated widely in photonics since the 1950s. These materials are frequently of interest due to their low material processing temperatures, optical transmission into the mid and far infrared, and large optical nonlinearity. They are also have excellent acousto-optic properties, and can be found within certain acousto-optic devices. In this chapter we explore Brillouin scattering within chalcogenide glass waveguides, with a specific focus on As_2S_3. After overviewing work on Brillouin scattering in chalcogenide fibers, we will discuss the extra complications of acoustic confinement which can arise when using these soft glasses in waveguide form factors. We will describe typical experimental setups used for measuring Brillouin scattering in the literature and provide measured data on numerous waveguide devices, characterised throughout the duration of this thesis.

General Resources

Chalcogenide glasses, sometimes referred to as glassy semiconductors, are amorphous materials which contain one or more chalcogen elements (sulfur, selenium or tellurium). In this chapter we are focused solely on SBS, and the characterisation of such scattering, in waveguides formed of these materials. For the use of the reader, please find the following resources and references therein on chalcogenide materials and their applications [225, 397–405]. There is also considerable detail on the fabrication and characterisation of chalcogenide photonic devices in the following PhD theses: Viveck Singh, Juejun Hu, Mark Hughes, Yifeng Zhou.

5.1 Brillouin Scattering in Chalcogenide Fibers

In this section we briefly highlight the first demonstrations of Brillouin scattering in chalcogenide glass fibers, and the context in which these measurements were made. We provide a summary table of measured parameters at the end of the section.

Since the early work of Smith [44], Brillouin scattering was expected to be a significant issue in optical communication systems, limiting the amount of light transmitted through long optical fibers. In the early 2000s, the emergence of wavelength division multiplexing in fiber communications led to significant interest in all-optical wavelength conversion and switching, utilising the $\chi^{(3)}$ optical nonlinearity [216]. This uncovered a particular problem: that SBS could saturate the pump and limit the desired nonlinearity. The search began for highly nonlinear glasses which could be prepared into optical fibers, which would have a large Brillouin threshold. One set of investigated materials were chalcogenide glasses. It was known that chalcogenide glasses were highly nonlinear materials [226, 406], and they had been used for acousto optics [407–410], however Brillouin scattering had not been observed in these glasses. To estimate the Brillouin gain coefficient in As_2S_3 and As_2Se_3 [411], Ogusu made the connection between the Brillouin peak gain factor g_0 [142] (eq. (4.30)) and the acousto optic figure of merit M_1 [412, 413], enabling the estimation of the peak gain factor for a wide range of materials previously characterised for acousto optics [412, 414]. This connection is given by

$$g_0 = \frac{2\pi n^7 p_{12}^2}{c\lambda^2 \rho_0 \Delta v_B v_{ac}} \qquad M_1 = \frac{n^7 p_{12}^2}{\rho v_{ac}} \qquad \Longrightarrow \; g_0 = \frac{2\pi}{c\lambda^2 \Delta v_B} M_1 \tag{5.1}$$

Utilising material parameters from the literature, and estimating the linewidth by estimating the phonon lifetime from estimated attenuation parameters (a likely source of uncertainty), it was found that that the g_0 values of both glasses was around *25 times higher* than SiO_2 [411]. It is worth pointing out that Smith used the M_2 figure of merit for calculating g_0 in his paper [44], re-framing the earlier equations from Tang [39].

The first experimental demonstration of SBS in chalcogenide fibers was performed in the 2005 work of Abedin [415], following quickly the paper from Ogusu. Abedin investigated a single mode As_2Se_3 fiber, with a core of $As_{39}Se_{61}$ and cladding of $As_{38}Se_{62}$ [416], and observed a strong Brillouin interaction with a critical power of only 85 mW in a 5 m long fiber. The measured gain coefficient of 6×10^{-9} m W^{-1} was about *130 times* that of SiO_2. Abedin followed this work with further experiments demonstrating large amounts of Brillouin amplification and low threshold lasing [417]. Song, working with Abedin, used the large gain factors to demonstrate highly efficient SBS slow light [418, 419].

Interest in Brillouin based slow light [419] led to further investigations of different chalcogenide glasses in the following years. Florea measured Brillouin scattering in As_2S_3 and As_2Se_3 fibers, finding values similar to Abedin for the As_2Se_3 and $3.5 \times 10^{-9}\,\mathrm{m\,W^{-1}}$ for As_2S_3 [91]. Abedin measured the gain coefficient of an Erbium doped tellurite (TeO_2), fiber with three different techniques [420]. A peak gain coefficient of $1.5 \times 10^{-10}\,\mathrm{m\,W^{-1}}$ was found using a pump-probe technique. Further experiments on pure TeO_2 fiber determined a gain coefficient of $1.7 \times 10^{-10}\,\mathrm{m\,W^{-1}}$. Fortier investigated another glass composition based on a germanium sulfide glass, $Ge_{15}Sb_{20}S_{65}$, which was micro structured to guide light within the core [421, 422]. The peak gain coefficient was smaller than As_2S_3, $8 \times 10^{-10}\,\mathrm{m\,W^{-1}}$, initially surprising considering the small difference in the material indexes of 2.3 and 2.4. Sanghera performed further experiments on As_2S_3 and As_2Se_3, and measured the linewidth of As_2S_3 as 31 MHz [423]. Finally, Tow investigated Brillouin lasers for the purpose of linewidth reduction in microstructured fibers formed of $Ge_{10}As_{22}Se_{68}$ [424] and $As_{38}Se_{62}$ [425, 426], with fabrication details in [427], finding gain values in the range of previous measurements. From these various studies it is clear that chalcogenide glasses are highly effective materials for inducing Brillouin interactions, for reference we have summarised the results in table 5.1.

Here, we should point out that some suspicion should be given to Brillouin parameters determined from experiments utilising the critical power, which is the majority of the results in table 5.1. Due to issues with prefactors, and a high likelihood of cavity effects in these high index fibers [428], pump probe results are generally much more reliable, as we will discuss in section 5.3. Care also needs to taken with linewidth values quoted from spectral measurements with large Stokes powers, linewidth narrowing during amplification can lead to large reductions below the spontaneous, natural, linewidth [80].

Table 5.1: Brillouin scattering parameters of various chalcogenide based optical fibers

Ref	Material	n	$g_0(\mathrm{m\,W^{-1}})$	$\Delta\upsilon_B(\mathrm{MHz})$	$\Omega_{SBS}(\mathrm{GHz})$
Abedin[415]	As_2Se_3	2.8	6.08×10^{-9}	13	7.8
Florea[91]	As_2S_3	2.4	3.9×10^{-9}	–	–
Abedin[420]	Er^+-TeO_2	2	1.5×10^{-10}	24	7.87
Qin[429]	TeO_2	2	1.70×10^{-10}	21	7.97
Fortier[421]	$Ge_{15}Sb_{20}S_{65}$	2.3	8×10^{-10}	9.5	8.2
Sanghera[423]	As_2S_3	2.4	5.70×10^{-9}	30	7.9
Tow[424]	$Ge_{10}As_{22}Se_{68}$	2.6	4.4×10^{-9}	17	7.25
Tow[425]	$As_{38}Se_{62}$	2.8	5.5×10^{-9}	14	7.95

5.2 Acoustic Confinement and the Opto-Acoustic Overlap

Researchers based in the University of Sydney and Australian National University, as part of the CUDOS program, had been utilising chalcogenide waveguides for all optical signal processing from the mid 2000s, with a focus on telecommunications applications [430]. However, it wasn't until 2011 that Brillouin scattering was demonstrated in an As_2S_3 waveguide by members of these groups, in the work of Pant [124]. Considering the exceptionally large peak gain factors in As_2S_3, it is reasonable to wonder why this observation was not made earlier. One factor is that the signals involved in telecommunications are typically much shorter than the acoustic lifetime, on the order of a few ns, which will inhibit the build up of acoustic waves and reduce the effective gain coefficient [40, 80, 431]. Another key factor was likely the use of polymer claddings, utilised for dispersion engineering purposes [159], which will affect the opto-acoustic overlap and the acoustic confinement. The importance of this is addressed thoroughly in the detailed work of Poulton [432], who's general arguments we will follow here.

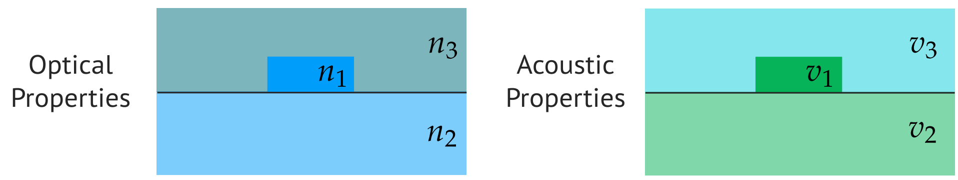

Figure 5.1: Schematic of waveguide geometry with material parameters indicated

Opto-Acoustic Overlap We will initially focus on the opto-acoustic overlap. To do so we shall assume we have an appropriate waveguide geometry and material such that the lifetime of the acoustic wave is dominated by material properties alone, not acoustic leakage. For the core material we will assume the material properties of As_2S_3, ($n = 2.44$ and $v = 2400\,\mathrm{m\,s^{-1}}$), but the arguments being made can be considered more generally.

Let us first consider a wire waveguide as shown in fig. 5.1, with a substrate and cladding which are the *same* material, i.e $n_1 > n_2 = n_3$ and $v_2 = v_3$. We set the refractive index of the cladding to silica ($n = 1.44$), and sweep the acoustic velocity of the cladding from above As_2S_3, $v = 3500\,\mathrm{m\,s^{-1}}$, down to well below that of the core, $v = 1500\,\mathrm{m\,s^{-1}}$, which is in the range of typical polymers. Unfortunately, NumBAT (section 4.5.3) is not currently capable of calculating the gain coefficient (G_B) in systems with leaky acoustic problems, so we will refer to the work of Poulton [432] for our present discussion.

The results from the work of Poulton are shown in fig. 5.2, with fig. 5.2a showing the change in peak gain coefficient as the velocity is swept, with the acoustic mode profiles in the insets, and fig. 5.2b looking at the Brillouin spectrum for the three cladding velocity regimes. We can see that as the v_2 is reduced and approaches that of the core the acoustic field begins to expand, very rapidly, which will significantly reduce the overlap of the optical and acoustic modes, reducing the peak gain factor. In the situation where $v_2 \approx v_1$, the core is indistinguishable from the cladding, so the acoustic system is essentially that of the bulk material, however the gain coefficient is non negligible. Poulton looks at this case in fine detail [432] and finds that this is due to coupling to acoustic radiation modes, which produce a significantly broadened spectra consisting of multiple sets of peaks. Now, as the cladding velocity is decreased even further, such that $v_2 < v_1$, the acoustic wave seems to become guided once again and the gain coefficient increases. This is due to the fact that the impedance mismatch between the materials becomes so large that the reflection at the interface increases to a sufficient level to provide guidance, with sufficiently low loss over certain length scales. This is highly analogous to the case of leaky or anti-guiding optical systems [433], such as hollow core fibers. It is important to note that because the geometry was chosen such that the effects

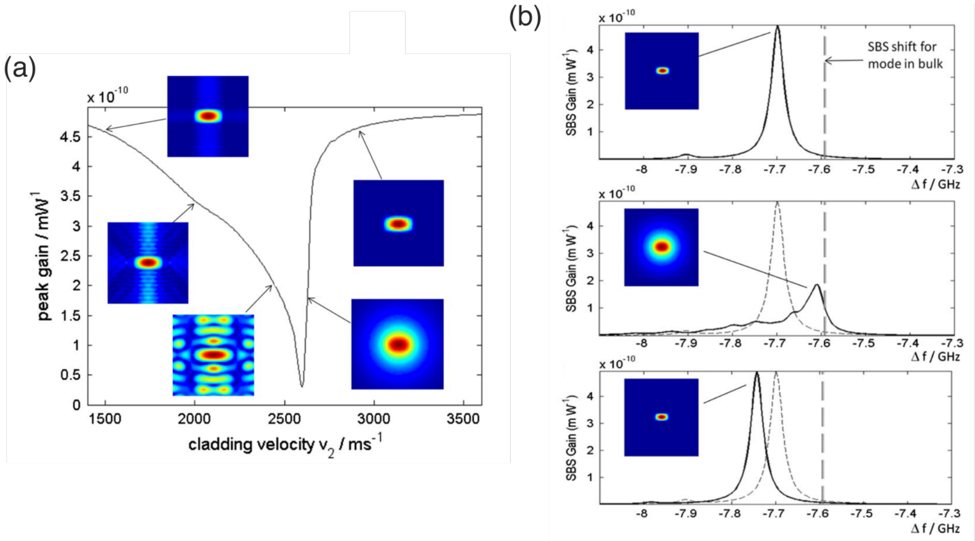

Figure 5.2: Figures from the work of Poulton [432] (a) Change in peak gain factor as the velocity of cladding (and substrate) is swept around the core. (b) Brillouin spectra for cases where, from top to bottom, $v_2 > v_1$, $v_2 \approx v_1$ and $v_2 < v_1$.

of acoustic leakage were negligible, the change in gain factor is due to overlap alone.

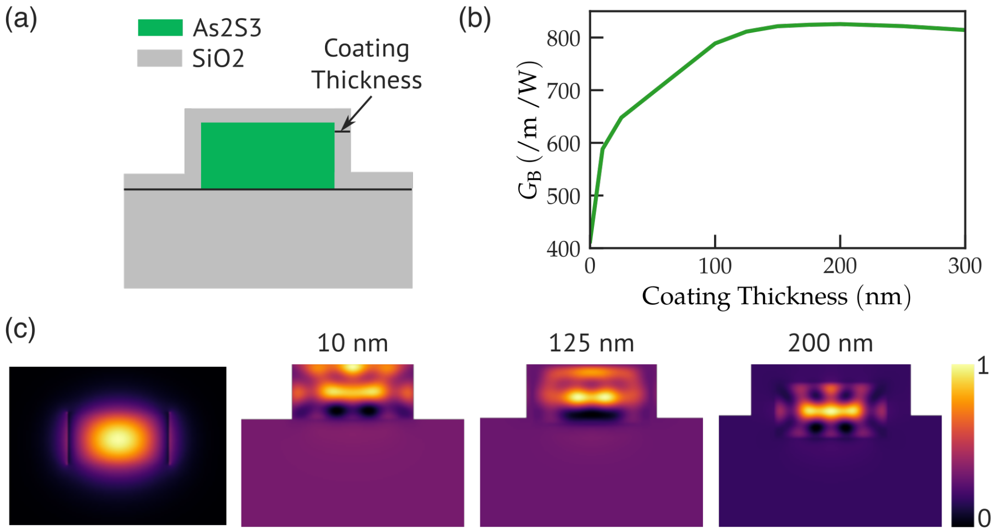

Figure 5.3: (a) Schematic of geometry for coating thickness variation (b) Increase in Brillouin gain coefficient as the thickness of the coating is increased (c) Fundamental optical mode, and u_z component of acoustic mode profiles for cladding thickness 10 nm, 125 nm and 200 nm. As the thickness is increased the acoustic mode becomes symmetric.

So far we have considered a waveguide where the core is embedded in a uniform medium. However, the standard fabrication processes of lithographic waveguides quite frequently utilise a substrate, onto which the high refractive index waveguide is formed, followed by a cladding. This cladding can have properties that can vary considerably, such as dielectrics deposited at a range of temperatures and pressures to spun coat polymers, or even air. To investigate how a change of the cladding alone affects the opto-acoustic overlap, in fig. 5.3 we compare an air-clad waveguide to an embedded waveguide by slowly increasing the thickness of silica over the waveguide. As the thickness increases beyond

200 nm, the gain coefficient becomes constant. The cause of this can be observed by comparing the field profiles of the optical and acoustic waves in fig. 5.3c. For geometries where the thickness is less than 150 nm, the u_z component of the acoustic mode is asymmetric, due to the different boundary conditions of the SiO_2 substrate and air cladding. As the thickness of the coating increases, the acoustic mode becomes symmetric and will have have the highest overlap with the optical mode, which was only slightly perturbed by the different cladding conditions. As the cladding increases further there is a slight reduction in the gain coefficient, possibly caused by the optical mode becoming less confined in the waveguide core. In general, we should expect the highest overlaps to occur in geometries where the optical and acoustic properties ensure symmetric mode profiles.

Acoustic Confinement and Leakage We have just seen that it is possible to achieve a reasonable opto-acoustic overlap in situations where the cladding has lower acoustic velocity than the core. The other issue that arises in this situation is, how significant is the acoustic loss due to the leakage which is occurring? In cases where this leakage is smaller than that of the material attenuation, there will be no observable reduction to the Brillouin gain coefficient. If an acoustic mode solver with a perfectly matched layer is used, the degree of leakage can be determined directly, which can be converted into a phonon lifetime. This was performed in the work of Van Laer [103], when investigating FBS in a partially underetched silicon nanowire, where even a 15 nm pillar exhibited sufficient leakage to reduce the optical quality factor to 400, well bellow the 1000 observed in fully suspended systems [104, 105]. In the work of Poulton the leaky acoustic mode lifetime was also determined analytically for cylindrical waveguide systems, and a few different material systems were investigated [432] (fig. 5.4). It was found that the lifetime was proportional to the cube of the radius, $\tau \propto a^3$, and inversely proportional to the acoustic V parameter.

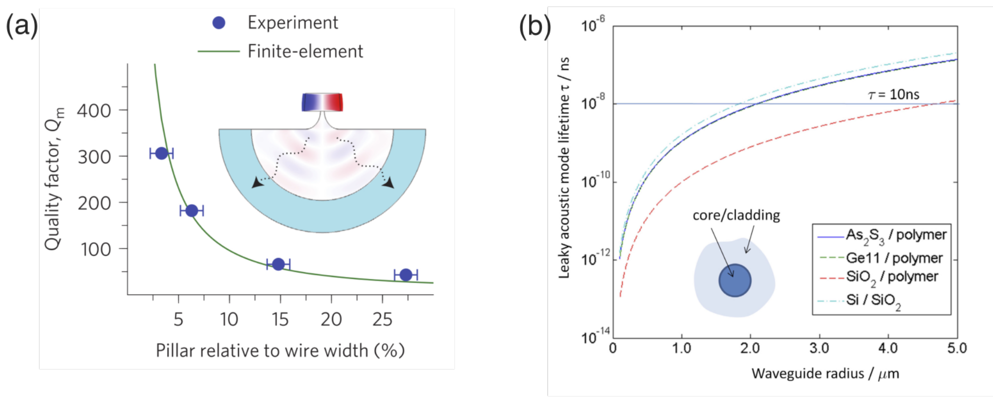

Figure 5.4: (a) Calculations, and measurements, of acoustic leakage through a small SiO_2 pillar in the work of Van Laer [103] (b) Analytically calculated acoustic lifetimes in leaky acoustic waveguides, from the work of Poulton [432]

In general, for typical material combinations, the calculations of Poulton showed that for waveguide widths less than 4 μm leakage can quickly become significant and dominate the material lifetime. We will observe this later on in experimental measurements of linewidths of chalcogenide glass systems with polymer claddings, confirming the importance of acoustic optimisation even in these soft glass based waveguides.

5.3 Measuring Brillouin Scattering

Accurately measuring Brillouin scattering is critical to the design and optimisation of waveguides for use in different applications. While a traditional grating based OSA is capable of resolving Raman scattering, the multi-GHz resolution bandwidth is barely sufficient for resolving typical Brillouin shifts, let alone the natural linewidth on the order of 10s of MHz. Advances in scanning etalon techniques lead to impressive results in the late 70s [55, 56], however the use of an electrical spectrum analyser by Tkach [374] greatly improved the resolution far beyond previous optical based measurement techniques. For applications wishing to avoid Brillouin scattering, usually the critical power and frequency shift are the properties of interest. In general, the most important parameters required to be measured are the

- Brillouin Gain Coefficient (G_B)
- Natural Linewidth (Γ_B)
- Brillouin Shift (Ω_{SBS})

We will summarise the self-heterodyne and threshold techniques which are frequently used in the literature, and describe the pump probe technique which we use to measure all 3 of these parameters simultaneously with high accuracy. Before moving further, it is important to point out that the first step of any measurement of the nonlinear properties, in this case Brillouin scattering, is accurate measurements of the *linear* properties of the waveguide. Thus, appropriate measurements should be taken to characterise the transmission response, preferably over a reasonable wavelength range, and determine the coupling and propagation losses of the device under test [434]. It is advisable to use reference components, with the same geometry as the nonlinear waveguide, to determine the n_{eff}, dispersion and n_g of the structure [435, 436]. For consistent measurements it is also highly desirable to automate the acquisition and data processing stages of the experiment. Python code used for interfacing and processing measurements, using the PyVISA package and VISA command libraries, are available from the author.

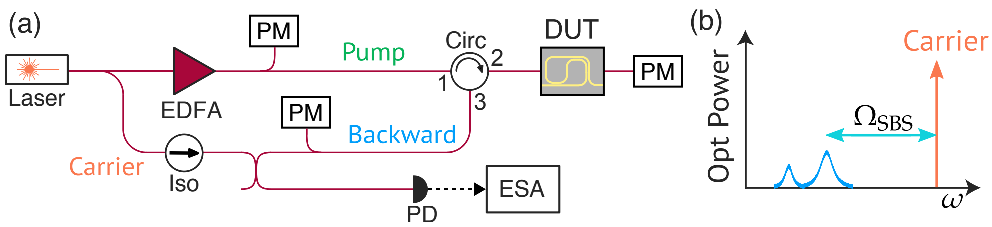

Figure 5.5: (a) Schematic of self-heterodyne and threshold setup (b) The optical spectrum of the signal which is received at the photodetector. The beat-note between the carrier and the backscattered light is measured on the ESA.

5.3.1 Self-Heterodyne and Threshold

The self-heterodyne technique measures the RF beat-note formed between spontaneously initiated backwards scattering and the initial pump signal, to extract the Brillouin spectrum with high resolution. By monitoring the optical power of the input pump, backscattered wave and transmitted pump the critical power can be measured, from which the Brillouin gain coefficient can be estimated. A typical schematic capable of performing both these measurements simultaneously is shown in fig. 5.5a. A CW laser is split into a pump and carrier, which acts as the reference for the heterodyne measurement. The pump is amplified with an EDFA, passes through the circulator (ports 1 $\rightarrow$ 2) and enters the device under test, generating Brillouin scattering in the backwards travelling direction. The backscattered light is directed through the circulator (ports 2 $\rightarrow$ 3), combined with the carrier and is measured on the highspeed photodetector. As the laser and the carrier have the same frequency the measured beat-note on the electrical spectrum analyser (ESA) is at precisely the Brillouin shift, and the Brillouin spectrum is retrieved, allowing for measurements of the linewidth and frequency shift. Optical power meters (PM) monitoring the pump power, backscattered power and transmitted power are used to determine the critical power for the device under test.

The critical power can be used to determine the gain coefficient, provided that the effective length, Brillouin shift and linewidth are also known. While it is common to utilise the approximated prefactor from the original work of Smith [44], the transcendental expression derived in Smith's paper should instead to be used [437]. Among the possible issues with the critical power approach is the fact that this power level is going to be very high in short devices or systems with weak gain coefficients, meaning that it is possible to not reach the critical power *at all*. Conceptually it is also a somewhat indirect measurement, utilising the amplification of a randomly scattered spontaneous signal, at the point the amplification is high enough for the Stokes to approach the pump power. Because of this, this technique is generally inadequate to characterise the devices investigated in this thesis, and we instead utilised a pump probe-approach.

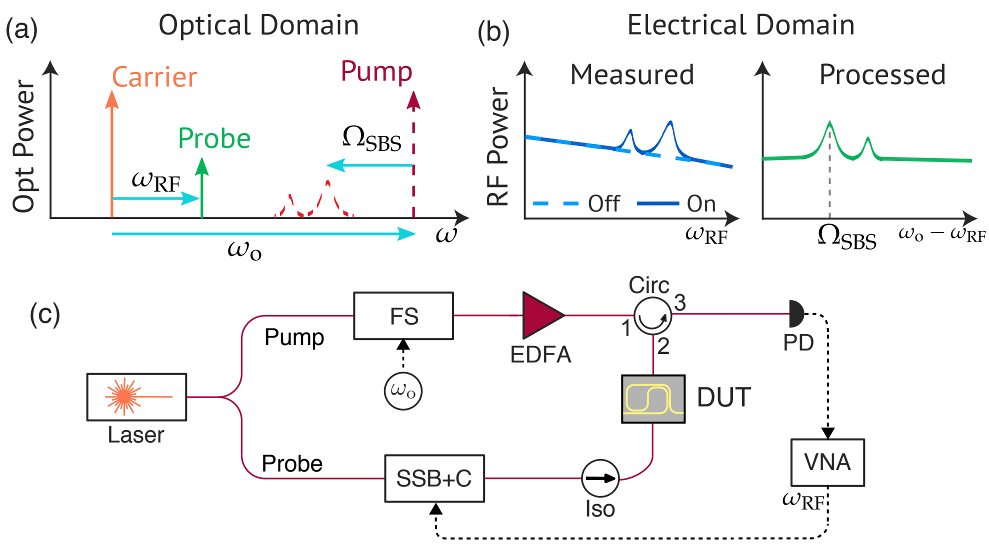

Figure 5.6: General operation of pump-probe characterisation (a) In the optical domain, the upshifted pump wave generates SBS at $\omega_{RF} = \omega_o - \Omega_{SBS}$. The carrier and amplified probe will then beat on the photodetector, generating a tone at ω_{RF}. (b) The RF beatnote is measured on the electrical network analyser. By performing a measurement with the pump off the response of the RF system is characterised. The measured signal with a pump on is then calibrated, and flipped in frequency, resulting in the processed spectrum which is the Brillouin spectrum.

5.3.2 Pump-Probe Technique

The use of an electro-optic modulator based pump-probe technique for characterising SBS was introduced in the 1997 work of Nikles [438]. We use a modified version of this scheme, utilising single sideband optical modulation to accurately map the Brillouin response as demonstrated by Loayssa [439]. An overview of the operation of a generic pump probe setup is shown in fig. 5.6. In the experimental setup, fig. 5.6c, we start with a CW laser which is split into two arms. In the pump arm the laser is frequency up-shifted by some known frequency ω_o, which is larger than the SBS shift, then amplified to a high power level. Suitable frequency shifters include a dual-parallel Mach-Zhender modulator (operating in single sideband suppressed carrier bias conditions [440]), an intensity modulator combined with an optical filter to keep one sideband only or a high frequency acousto-optic shifter. The amplified pump traverses a circulator, from ports $1 \rightarrow 2$, and then passes through the device under test, before being removed by an isolator.

In the probe arm an optical probe is generated using single sideband modulation, driven by the network analyser, with the original laser frequency now becoming the optical carrier. The carrier and the probe then pass through the device under test, where the probe will undergo Brillouin amplification at an RF frequency $\omega_{RF} = \omega_o - \Omega_{SBS}$, fig. 5.6a. The two waves will then exit the device under test, pass through the circulator, ports $2 \rightarrow 3$, to be detected upon the high-speed photodetector. The sideband frequency, ω_{RF}, is swept with a high resolution, over the desired frequency range. To correctly retrieve the Brillouin spectrum, due to the fact we are mapping around the *carrier* instead of the pump, the measured response needs to be *reversed* and subtracted by the pump frequency shift ω_o, as shown in fig. 5.6b. When appropriately calibrated, the retrieved beatnote at ω_{RF} will map the SBS response in a 1 to 1 fashion, including amplitude and phase, enabling very high resolution measurement of Ω_{SBS}, the Brillouin spectrum and the peak amplification.

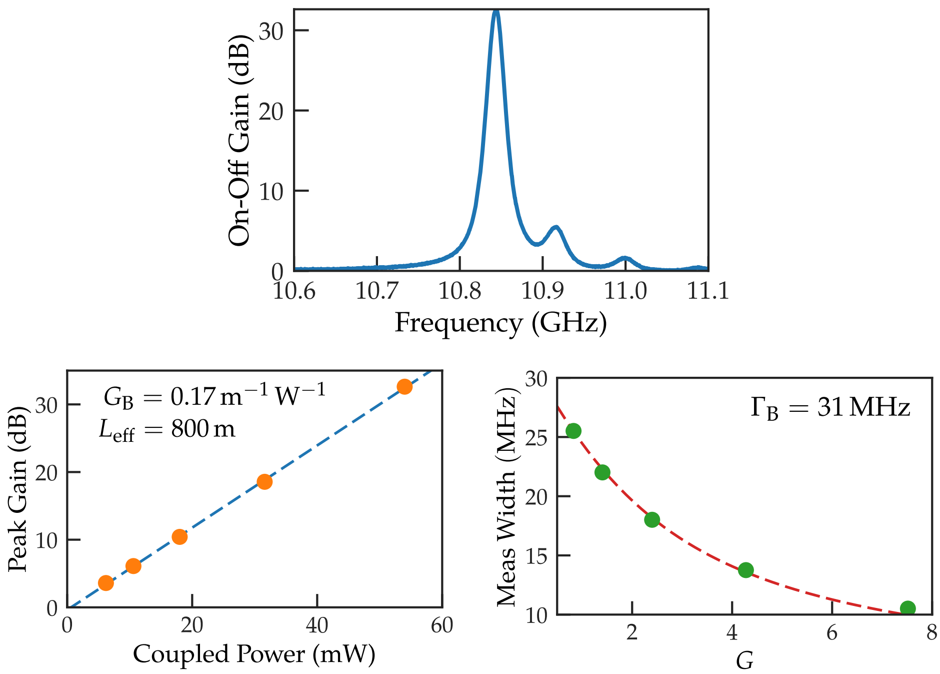

Figure 5.7: Pump-Probe measurements of a 1 km single mode fiber

While this technique was initially proposed as a robust way of extracting the Brillouin spectrum and frequency shift, we can take it slightly further to determine the gain coefficient and natural linewidth. We know that in the small signal regime (eq. (4.24)), the amplified stokes wave is exponentially dependant on G where $G = G_{\mathrm{B}} P_{\mathrm{p}} L_{\mathrm{eff}}$. Thus, by performing multiple spectral measurements with different pump powers, we can extract the G_{B} from the slope of the peak gain,

$$\mathrm{dB} = 4.34 \times (G_{\mathrm{B}} P_{\mathrm{p}} L_{\mathrm{eff}}) \qquad\qquad L_{\mathrm{eff}} = \frac{1 - e^{-\alpha L}}{\alpha}$$

where dB is the peak on-off amplification in decibels and we have used the fact that $10 \log_{10}(\exp(1)) = 4.34$. After accurate measurements of the coupling and propagation losses, the L_{eff} and coupled pump power can be determined with high certainty. Fitting the slope of the on-off gain for various pump powers then allows the G_{B} value to be determined. Care must be taken to avoid nonlinearities, in particular pump depletion effects in systems with high amplification. As the optical probe power is directly controlled by the modulation strength, the RF output power of the network analyser can be adjusted as appropriate.

Now, we can determine the G_{B}, so what about the natural linewidth? It is important to recall that even though the Brillouin linewidth of a single peak is given by a Lorentzian, in a pump probe measurement the measured linewidth of the RF response is squashed by the exponential amplification (or broadened by the attenuation). This leads to the general expression for the RF 3-dB linewidth [80], in terms of the G value, as

$$\Delta\nu_{\mathrm{RF}} = \Gamma_{\mathrm{B}} \sqrt{\frac{G}{\ln(e^G + 1) - \ln 2} - 1}$$

As the G value is directly proportional the on-off gain ($G = \mathrm{dB}/4.34$), sweeping the pump power will allow for the relation to be fitted. It is interesting to note that the linewidth is a prefactor for the main trend, essentially moving the y-intercept without affecting the trend shape. If higher accuracy is desired the use of Brillouin attenuation, where the G values are now negative, can provide further data points for reduced pump powers. Again care must be given to avoid pump depletion, and the RF photonic link without SBS needs to be accurately calibrated. Thus, with the pump-probe technique, and an electrical network analyser, we can determine the critical parameters of interest to high accuracy. Measurements of the properties of a single mode fiber (1 km coil from General Photonics) is shown in fig. 5.7. The high resolution spectra allows clear identification of the central shift and also higher order Brillouin peaks. The peak gain and linewidth narrowing measurements are also shown for varying pump power, along with the extracted G_{B} of $0.17\,\mathrm{m}^{-1}\,\mathrm{W}^{-1}$ and Γ_{B} of 31 MHz.

Pulsed Techniques

In device systems where the gain is very weak, pulsed pumps are sometimes used to measure the Brillouin spectrum [441]. The pulses should be longer than the Brillouin lifetime, so are generally referred to as quasi-CW, and will typically consist of pulse widths on the order 100s of nanoseconds. A pump-probe configuration can be formed using a lock-in amplifier, where the electrical signal used for generating the pump pulses is the lock-in frequency, then the amplified probe can be extracted at low optical powers, improving sensitivity and avoiding depletion effects [442]. Such a system can efficiently measure the Brillouin spectrum, by sweeping the probe frequency around the Brillouin frequency shift while monitoring the response on a synchronized oscilloscope [442]. The use of a lock-in amplifier can be a viable alternative to methods utilising electrical spectrum and network analysers, and is capable of achieving high resolution as demonstrated in the early and informative work of Shibata [78].

5.4 Characterisation of Soft Glass Waveguides

Chalcogenide rib waveguides were the basis of multiple investigations performed throughout this thesis. Here we will collate a range of device properties, measured between 2013 and 2016, for concise reference and comparison. Due to observations of device performance at the start of 2015, a shift in device design lead to the current utilised paradigm within the group. We will start with a general overview of fabrication processes for soft glass waveguides and summarise different measurements of devices before 2015. We will provide further detail of the improved gain coefficient waveguide devices developed at this time, and a wider exploration of designs and materials performed during 2016. We will close with measurements on two additional chalcogenide glasses, $Ge_{11.5}As_{24}Se_{64.5}$ and TeO_2.

5.4.1 Waveguide Fabrication and Design

While waveguide fabrication was not directly performed in this thesis, samples were fabricated through the collaboration with researchers in the Nonlinear Physics Centre at the Australian National University. We provide an overview of the fabrication procedure for reference, and a schematic of the fabrication process is shown in fig. 5.8.

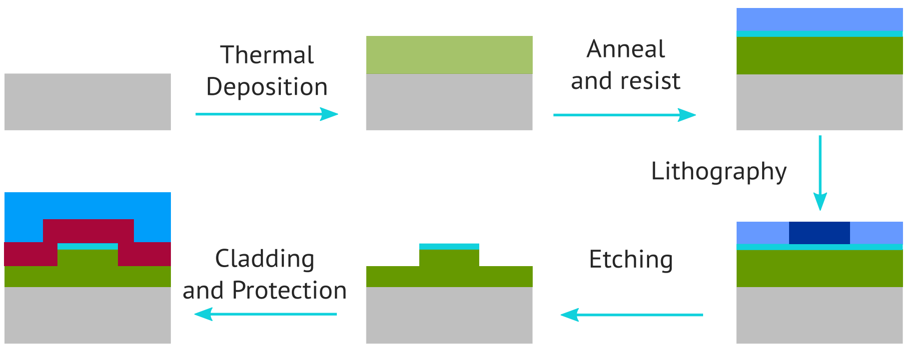

Figure 5.8: Reduced schematic of fabrication process for As_2S_3 waveguides

The majority of the waveguides characterised in this chapter consist of partially etched As_2S_3 rib waveguides. The fabrication process starts with thin film deposition of As_2S_3 via thermal evaporation. Raw As_2S_3 material (Amorphous Materials, Garland, Texas, USA) was placed in an electrically heated Tungsten boat in a chamber at low base pressure of 3×10^{-7} Torr. The thin film was deposited on <100> oriented 100 mm diameter thermal oxide silicon wafer. The wafers were mounted on a carousel which was rotated during the deposition process, resulting in a thickness variation less than 1%. The deposition parameters were was controlled to result in a constant rate of 0.1 nm/s. The total film thickness and etch depth varied between devices. An ≈100 nm SU8 polymer layer was spin-coated on the wafer before the films were annealed in vacuum at 130°C for 24 h, to improve the stability and increase the refractive index from deposited values of 2.31 to bulk-like values of 2.42 at 1550 nm [443]. The waveguide pattern was typically printed using a 1:1 projection photolithography system. Afterwards, plasma dry etching was performed in an Oxford Plasmalab 100 ICP RIE system using a mixture of CHF_3, O_2 and Ar gases [444, 445]. This was followed by a cladding layer which was varied between different samples, with the use of SiO_2 or different polymers, and will be indicated when appropriate. When SiO_2 was used, it was deposited via a sputtering process and followed by a 10 µm thick UV-cure polymer layer (Ormocore) to coat the wafer for protection during handling. After cleaving the wafers into the individual chips of the correct dimension, 270 nm of SiO_2 was sputtered to the end facets of the waveguide to act as anti-reflection coating and for passivation of As_2S_3 from the external environment.

Lithographic Masks Two sets of masks were used for devices. The first is referred to as the ”snake mask”, which contained a number of different device designs. Generally, straight waveguides of 6.5 cm length, with widths of 4 µm were used from this mask. Fabricated chips utilising mode matched polymer tapers were also used with these designs [127]. The second mask is referred to as the ”die mask”, this design is significantly more space efficient, featuring nested spirals of 5 waveguides in different sets of loops. A single die consists of a set of straight structures which are 2 cm long, and then sets of 2, 3 and 6 loops corresponding to 8.6 cm, 11.7 cm and 23.7 cm respectively. This is repeated for 3 sets of waveguide widths, nominally 2.2 µm, 2.4 µm and 2.6 µm, with the 2.4 µm waveguides generally used in the experiments. The designs are connected in the wafer, allowing for multiple dies to be connected and enabling very long lengths in relatively compact form factors. Images of the GDS file of the die mask and photographs of some fabricated chips are shown in fig. 5.9. The die mask and snake mask design were prepared by our collaborators at the ANU.

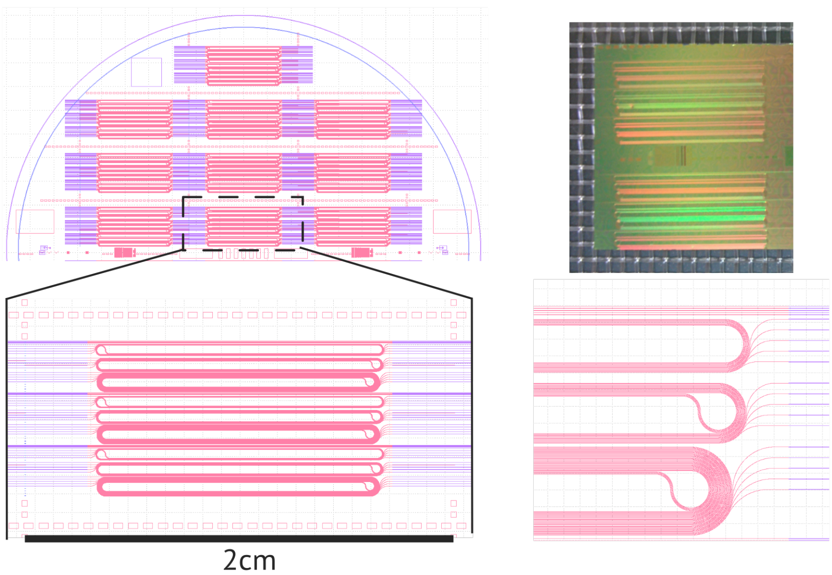

Figure 5.9: Images of die mask file and photo of a fabricated chip.

Bends The spiral structures from the die masks consist of a mix of bent and straight waveguides. One concern this brings to light is the effect of bends on Brillouin scattering. In devices with large gain coefficients, such as small mode area integrated devices, the localised amplification approaches the same length scale as the buildup of the acoustic wave. In this situation, modifying the acoustic properties will inhibit the buildup of a single acoustic mode and reduce the effective gain. This effect has been explored in detail for suspended structures [345], and effects FBS differently as the acoustic wave is stationary in this case. Bends may also result in additional issues in crystalline materials, such as silicon, as the optical and acoustic properties can depend on the orientation of propagation through the medium. Additional distortion due to the changing acoustic velocity in bend regions has been characterised in Silicon nanowires (supplementary of Van Laer [446]). Very tight bends will also alter the n_{eff} of the optical mode. For these reasons bends are generally minimised in long structures designed for single-pass Brillouin amplification.

5.4.2 Early Devices (2013-2015)

After the initial demonstration of Brillouin scattering in soft glass waveguides [124], a quick flurry of activity explored multiple applications of SBS with this new platform, as described in section 2.4.2 and [133]. In August of 2013 we were performing measurements utilising Brillouin scattering in As_2S_3 waveguides for the purpose of creating high suppression microwave notch filters [447]; this work will be described in section 8.4. The waveguides used for these experiments were 850 nm thick, 4 µm wide and 6.5 cm long half etched structures based on the snake mask. Typical insertion losses of 9.5 dB were obtained at the time for the measurements, with coupling losses estimated at 4 dB per chip facet through optical overlap simulations. Peak gain measurements yield a gain coefficient of 350 $\mathrm{m^{-1}\,W^{-1}}$, shown in fig. 5.10a, similar to those in the work of Pant [124]. While performing these experiments comparisons were also made with a similar device, which had lower insertion losses of 2 dB per facet through the use of vertical tapers and an SU8 overlay waveguide [127]. This device had Ormocore polymer cladding, required due to the mode conditions of the SU8 taper [127], and yielded a gain coefficient of only 170 $\mathrm{m^{-1}\,W^{-1}}$ fig. 5.10b (though this was not calculated at the time).

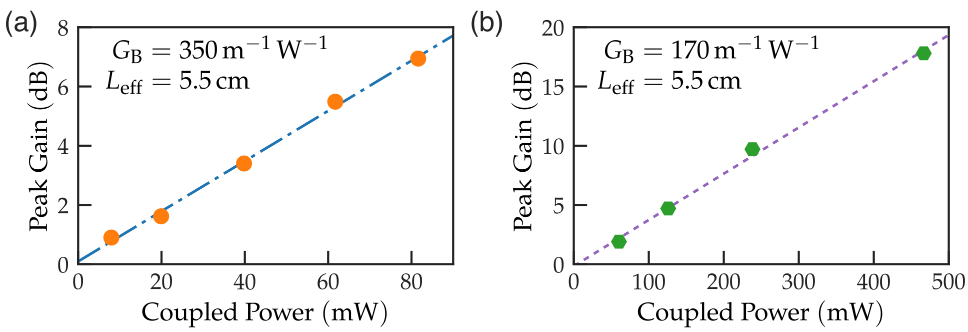

Figure 5.10: Peak gain measurements, correcting for insertion losses, of (a) IPG clad chip (b) Ormocore clad chip with SU8 tapers

During March of 2015, we performed experiments with the opto-electronics group in the department of physics within the Thales Research and Technology campus based in Palaiseau, France. The purpose of the trip was to demonstrate the stabilisation of a dual frequency laser [448, 449] with injection locking, utilising a Brillouin laser generated by the photonic chip. For these experiments we utilised another chip with SU8 tapers, and also brought a backup chip, with a set of 8 dies, fabricated with the die mask. The configuration used for the Brillouin laser was the same as the earlier work of Kabakova [126], which had a threshold for laser oscillation of 350 mW coupled pump power. Unfortunately in this case, it was quickly found that the power handling of the SU8 tapered chip was insufficient for the planned experiments, with the SU8 waveguides igniting with moderate CW powers of a few 100 mW. It was later found that a higher thermal load, in the form of a vacuum chuck the full width of the chip, was utilised in previous systems [127].

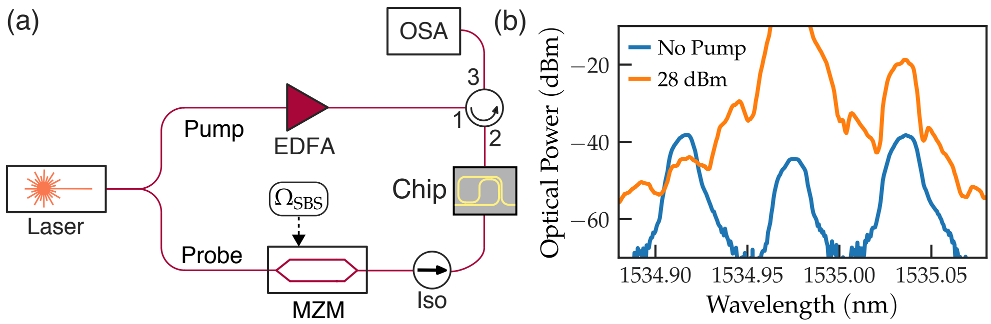

Figure 5.11: Measurements from Thales visit.

To proceed with experiments at Thales, we turned our attention to the backup chip based on the die mask. We explored the losses in the different widths and lengths, and typically measured low insertion losses around 13 dB for the 2.4 um wide and 11.7 cm long waveguides. To characterise SBS in these structures we performed a quick optical pump-probe measurement to measure the on-off amplification and estimate the gain coefficient. Up to 20 dB of amplification was measured with 600 mW of coupled pump power. This was unexpected as this waveguide has almost twice the length, and half the width, of the original waveguides in the work of Pant [124], which demonstrated 16 dB of amplification for similar pump power levels. Fitting the measured pump-probe values yielded a gain coefficient in the range of 200 $\mathrm{m^{-1}\,W^{-1}}$, below that of the original work of Pant ($G_B = 300\,\mathrm{m^{-1}W^{-1}}$). While Brillouin lasing could be observed at close to 1 W of pump power, the stability was quite poor, and ultimately the experiments could not move forward due to the performance of the As_2S_3 waveguides.

The primary question which arose from the issues found during the Thales experiments was, why was the G_B lower than expected? Upon investigating the previous publications using As_2S_3 chips, it was observed that in the first on-chip SBS paper a thin 140 nm layer of SiO_2 was used as the top cladding, with no other materials. All of the follow up samples had been utilising polymers, typically Ormocore in the latest devices formed from the die mask. The linewidths for Ormocore based devices was on the order 90 MHz, and chips based on IPG polymer had linewidths of around 60 MHz (for 4 µm width waveguides), both higher than the originally quoted 34 MHz from the original on-chip SBS work. The decreased gain measured in the Thales experiments was thus likely the result of a reduced phonon lifetime and partially due to a varied opto-acoustic overlap [432], as discussed in section 5.2.

5.4.3 Giant Gain Devices and Design Optimisation (2015+)

With the importance of cladding material further understood, new devices were fabricated with a SiO_2 cladding with around 500 nm thickness, followed by a thick protection layer of polymer for handling purposes. The shift to a SiO_2 cladding led to orders of magnitude improvement in amplification over previous Brillouin integrated devices. The waveguide geometry and SBS measurements for these structures is shown in fig. 5.12. In the 12 cm waveguides, with an insertion loss of 13 dB, almost 40 dB of amplification was initially measured. Furthermore, in the longer, and higher loss, 24 cm structures greater than 50 dB of on-gain was observed for coupled powers less than 300 mW. The amplification was so high that there was initially confusion during the measurement process, due to a large amount of pump depletion, requiring the probe power to be significantly reduced to correctly monitor the extremely large gains. The Brillouin gain coefficient for these new devices was on the order of 500 $m^{-1}\,W^{-1}$, fig. 5.12c, in line with the reduced A_{eff}. This significantly improved amplification efficiency enables a new paradigm of experiments, not previously possible in chip integrated devices. These waveguides were recently used in a photonic-phonic memory [450] and were also applied to microwave photonic systems, enabling a number of new configurations due to the large amount of amplification available [89]. One example was the improvement to the Brillouin laser: a lasing threshold of 80 mW coupled power was observed with a 12 cm chip, a factor of 5 improvement compared to the Thales experiments. Follow up batches of chips in 2016, fig. 5.12d, showed slightly improved performance with 550 $m^{-1}\,W^{-1}$.

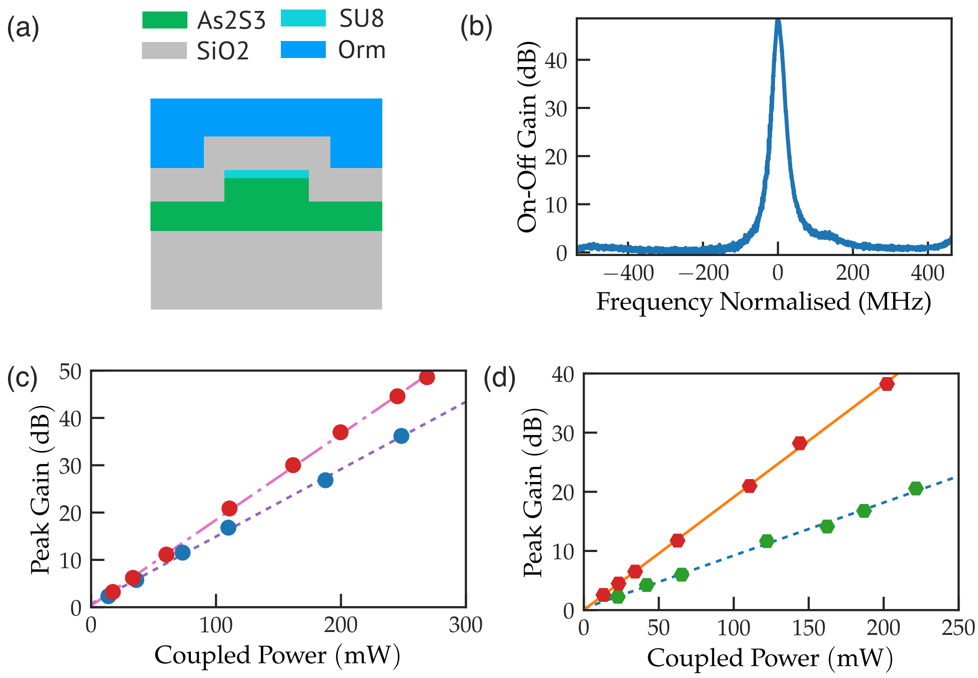

Figure 5.12: Brillouin scattering in half-etched designs (a) Schematic of waveguide cross-section (b) Brillouin spectrum of 48 dB peak (c) Peak gain measurements for 23 cm and 12 cm waveguides (d) Peak gain measurements for 16 cm and 4 cm waveguides, fabricated in 2016.

While the G_B was considerably improved in these devices, the insertion loss was slightly worse than the previous 4 μm width waveguides due to the larger propagation losses, typically varying between 0.5 dB/cm to 0.7 dB/cm, arising from the increased surface roughness scattering in the half etched geometry. For many applications, in particular microwave photonics, the optical insertion loss is critical to system performance. To reduce the propagation loss, we implemented an alternative design with a shallower 1/3 etch depth, combined with an increased thickness of 930 nm. The measured propagation loss ranged between 0.2 dB/cm to 0.3 dB/cm. The slight increase in A_{eff} was expected to impact the G_{B}, but this should be compensated through the improved L_{eff}. Peak gain measurements are shown in fig. 5.13a, along with a Brillouin spectrum fig. 5.13b, from which we determine a G_{B} of 500 m^{-1} W^{-1}. With a coupled power of only 150 mW, 30 dB of amplification was generated in a 16 cm long waveguide, for a device insertion loss of just 11 dB. This amount of gain is slightly higher than the 1/2 etched device for the same power, and is obtained with 3 dB lower insertion loss. These waveguides were recently used in a microwave photonic processor [451].

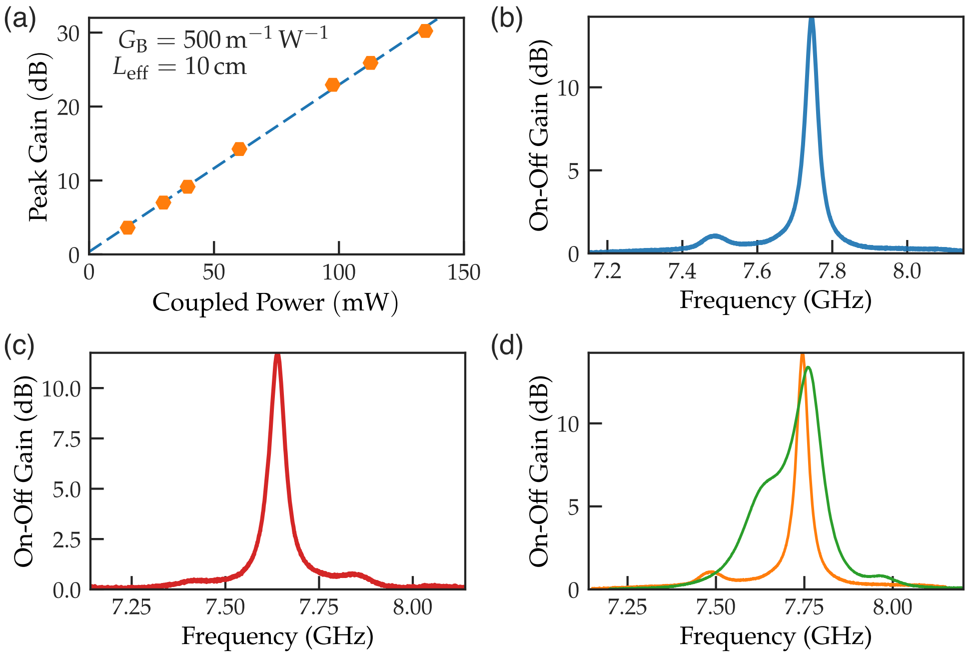

Figure 5.13: (a) Peak gain measurements of 16 cm 1/3 etched As_2S_3 SiO_2 clad waveguide (b) Brillouin spectrum of SiO_2 clad 1/3 etched waveguide (c) Spectrum of 1/2 etched waveguide (d) Comparing spectra of 1/3 etched waveguides with SiO_2 and ZPU polymer cladding. The polymer clad waveguide has a significantly broadened peak.

The overall amplification of the 1/2 and 1/3 etched devices is similar, so are there any other differentiating factors, apart from loss, which might influence the application choice? Well, the acoustic modes of the waveguide are highly dependant on the final geometry, and will have an impact the Brillouin spectrum. This can be explored by comparing the measured pump-probe spectrum for these two different waveguide structures, as shown in fig. 5.13b and fig. 5.13c. The difference between the two spectra is primarily the central frequency shift, due to a slight difference in n_{eff}, and the prevalence of higher order gain peaks due to additional acoustic modes. We can also show the effect of acoustic confinement by replacing the silica cladding with a soft polymer, in this case ZPU (an acrylate polymer from ChemOptics). The central peak of the polymer clad waveguide is significantly wider than the silica clad devices, and a large tail also seems to exist, reminiscent of coupling to radiation modes mentioned in the work of Poulton [432]. These high resolution measurements indicate the importance of geometry tailoring for optimisation of the acoustic spectrum, but a detailed study on the effect of etch-depth changes to the acoustic confinement is yet to be performed.

5.4.4 Non As_2S_3 chalcogenide waveguides

As_2S_3 is just one material within broad range of chalcogenide glasses which have been investigated for optical waveguides, and acousto-optic devices, in the literature. Here we will present measurements of waveguides based on two other glasses, $Ge_{11.5}As_{24}Se_{64.5}$ and TeO_2.

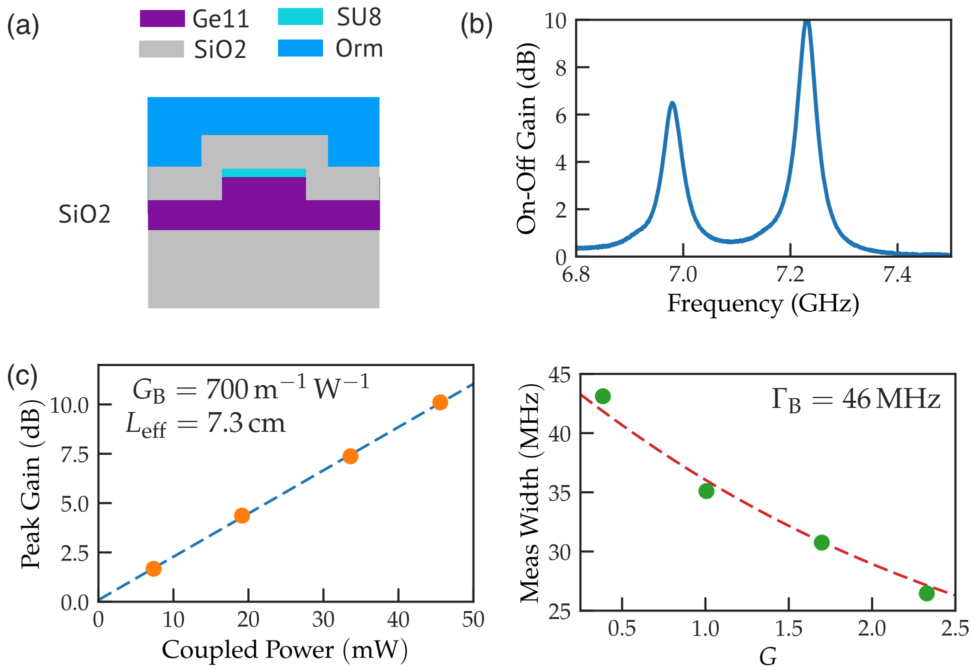

Figure 5.14: (a) Schematic of waveguide geometry (b) Brillouin Spectrum showing shift around 7 GHz and two distinct peaks (c) Peak gain and linewidth narrowing for increasing pump power.

$Ge_{11.5}As_{24}Se_{64.5}$ GeAsSe based glasses are generally of interest due to their high nonlinearity and increased stability, compared to pure AsSe glass [452]. Certain compositions are available commercially (AMTIR-1 from Amorphous Materials and Umicore GASIR family), and this chalcogenide glass family was the focus of research into acousto-optic devices in the early 70s, due to its low acoustic loss and figures of merit [408, 410]. The composition we investigated, $Ge_{11.5}As_{24}Se_{64.5}$, is capable of supercontinuum generation in waveguides [453] and posses stable glass forming properties [454, 455]. The geometry of the waveguides was similar to the 1/2 etch As_2S_3 devices with the die mask utilised, however the thickness was reduced to 660 nm due to the higher refractive index of 2.6, a cross-section is shown in fig. 5.14a. The extracted gain coefficient is higher than the As_2S_3 samples, in part due to the reduced A_{eff}, however the spectra is quite different, showing two strong distinct peaks. The cause of the distinct spectra is likely the particular geometry used and the mechanical properties. Similar spectra can be observed in simulations of As_2S_3 waveguides. Considering that waveguides with effective areas $< 0.5\,\mu m^2$ have been demonstrated with propagation losses of $1.5\,dB\,cm^{-1}$ [398], $G_B > 2000\,m^{-1}W^{-1}$ could be expected with further optimisation. This makes this material quite promising for future single-pass devices, provided that issues with thermal power handling can be overcome [398].

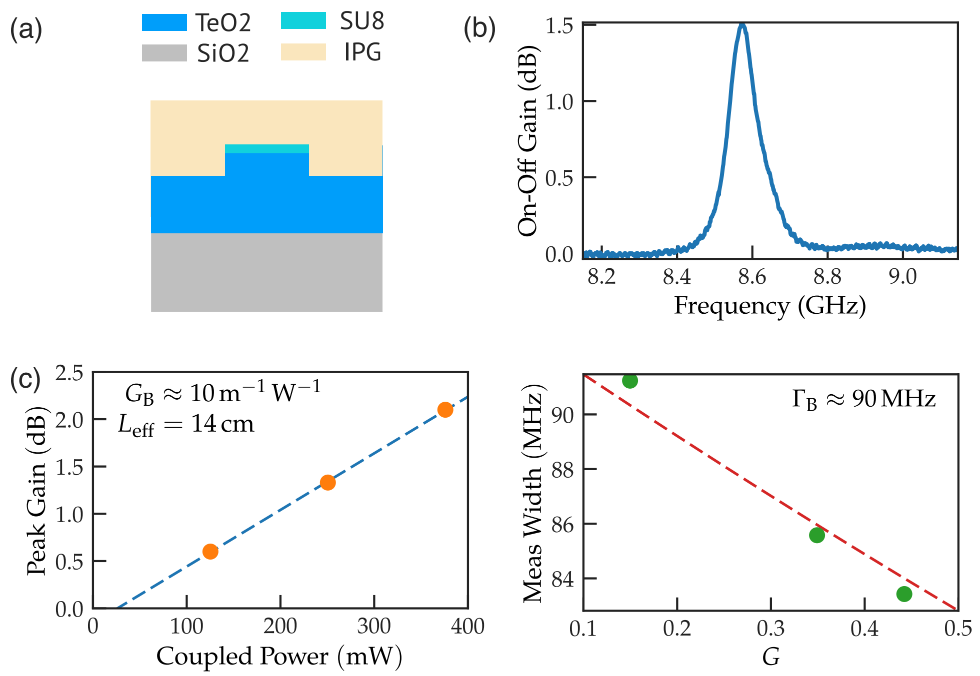

Figure 5.15: (a) Schematic of waveguide geometry (b) Brillouin Spectrum, with a high central freq of 8.6 GHz (c) Peak gain and measured linewidths for increasing pump power.

TeO_2 For many applications, propagation losses are critical to device and system operation. As discussed in section 3.2.1, reducing index contrast is one means of minimising scattering losses. Tellurite glass (TeO_2) is another chalcogenide which was investigated in the early 70s for acousto-optics [409]. It has a index of 2.1, at 1550 nm, and thus a lower index contrast than As_2S_3. It is capable of being fabricated into low loss waveguides, with sputtering possible for film deposition [456], is suitable for nonlinear optics [404, 456–458], and can also be doped [459]. SBS has been previously demonstrated in TeO_2 fibers as mentioned in section 5.1. The samples characterised here were old devices, optimised for Kerr nonlinear effects and utilised an IPG polymer cladding. The linear loss was very low, with propagation losses around 0.1 dB/cm in a 17 cm long meandering waveguide from the snake mask. These waveguides have a thickness of 1.8 µm, and measured widths of 3.5 µm, much larger than the previous rib waveguides. Measurements of SBS, using a different network analyser which yielded higher uncertainty than the other measurements, are in fig. 5.15.

The measured gain coefficient of the TeO_2 waveguide was on the order of $10\,\mathrm{m^{-1}\,W^{-1}}$, with a linewidth of ~ 90 MHz. This G_B is quite low, and is even lower than expected from the A_{eff} of $4\,\mu\mathrm{m}^2$ which corresponds to a peak gain factor of $4 \times 10^{-11}\,\mathrm{m\,W^{-1}}$, around 4 times lower than fiber value. This most likely arises from a combination of reduced overlap integral and lifetime, due to the polymer cladding, with the measured linewidth also around 4 times *higher* than the fiber value. The higher frequency shift of 8.6 GHz is due to the acoustic velocity of $3400\,\mathrm{m\,s^{-1}}$, much higher than As_2S_3 at $2400\,\mathrm{m\,s^{-1}}$. If a silica cladding was used, bringing the G_B closer to the bulk material, then a G_B beyond $100\,\mathrm{m^{-1}\,W^{-1}}$ is expected for an optimised geometry. It is also worth mentioning that the device was very stable during the measurements, even for coupled powers approaching approaching 1 W CW power. Thus, this material is highly suitable for applications requiring low loss and high power handling, such as Brillouin lasers generated from high-Q resonators.

Conclusion

In this chapter we have provided an overview of Brillouin scattering in soft glass waveguides. After discussing the literature of Brillouin scattering in chalcogenide fibers, we focused on the issue of acoustic confinement and the opto-acoustic overlap. We then provided a detailed description of measurement techniques for Brillouin scattering, and why pump-probe processes are generally the preferred option. The remainder of the chapter explored Brillouin scattering in chalcogenide waveguides, providing an overview of measurements and context for investigated devices throughout this thesis. We demonstrated record Brillouin amplification, with an improvement of 3 orders of magnitude over previous planar waveguide devices.

Chapter 6

Hybrid Integration of As_2S_3 and Silicon

In the last chapter we found that waveguides based on chalcogenide glasses, As_2S_3 in particular, are capable of strong Brillouin interactions. To develop and extend current functionalities, Brillouin processing elements need to be combined with integrated photonic components and circuits. The low processing temperatures required for As_2S_3 waveguides precludes its use as a front-end optical material platform, preventing integration with highspeed modulators and photodetectors. In this chapter we explore the back-end integration of As_2S_3 onto traditional silicon on insulator (SOI) circuits, and find this hybrid platform to be a compelling and promising step forward for Brillouin scattering in photonic integrated circuits. We demonstrate record Brillouin amplification for a silicon-based circuit and present the first results of Brillouin lasing in a planar integrated circuit.

This chapter has sections based on the following publications:

6.2-6.4 **B. Morrison**, A. Casas-Bedoya, G. Ren, K. Vu, Y. Liu, A. Zarifi, T. G. Nguyen, D.-Y. Choi, D. Marpaung, S. J. Madden, A. Mitchell, B. J. Eggleton, "Compact Brillouin devices through hybrid integration on silicon", Optica **4**, 847 (2017)

General Resources

This chapter builds upon all of the concepts covered so far in the thesis. For a detailed overview of nonlinear circuits and integration technologies refer to Chapter 3. Background material on Brillouin scattering in waveguides is found in Chapter 4, with experiments of chalcogenide glasses found in Chapter 5. In the following section we provide a description of waveguide ring resonators and Brillouin lasers, before leading to the published work.

6.1 Brillouin Lasers in Waveguide Resonators

Optical resonators are capable of greatly enhancing nonlinear effects through increased circulating powers, and are critical in the creation of lasers. In section 6.2.5 we experimentally demonstrate Brillouin lasing in a planar integrated resonator for the first time. Here we will provide a very brief overview of optical resonators and how they can be used to enhance nonlinear effects, with a focus on Brillouin scattering and Brillouin lasers.

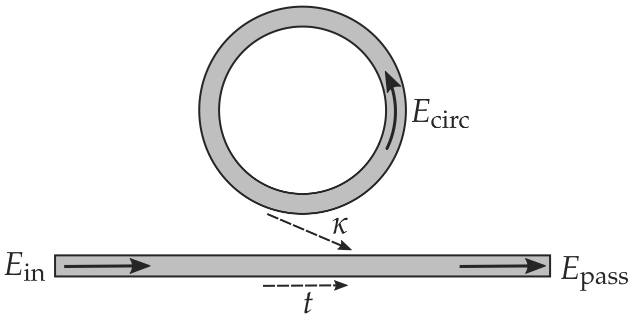

Figure 6.1: Schematic of an all-pass ring resonator

6.1.1 Optical Waveguide Resonators

Optical resonators can be created out of a vast number of schemes and materials, and find use in equally diverse sets of applications. For the work here we shall concern ourselves with the canonical example of a single dielectric waveguide coupled to a resonator [460–462], as shown in fig. 6.1. The relationship between the input and output waves, referred to as E_{in} and E_{pass}, and the waves inside the resonator $E_{r,in}$ and E_{circ}, immediately after and before the coupler, can be given in matrix form as

$$\begin{pmatrix} E_{pass} \\ E_{r,in} \end{pmatrix} = \begin{pmatrix} t & \kappa \\ -\kappa^* & t^* \end{pmatrix} \begin{pmatrix} E_{in} \\ E_{circ} \end{pmatrix}$$

where t and κ are the coupling parameters, and $|\kappa|^2 + |t|^2 = 1$ in the case of zero loss in the coupling element. After a single round trip of the resonator the field will accumulate phase, and be attenuated such that,

$$E_{circ} = ae^{i\theta} E_{r,in}$$

where in the case of a lossless resonator $a = 1$, and the round trip phase is given by $\theta = k_z L$, where k_z is the propagation constant of the waveguide mode and L is the roundtrip length. Using the above relations we can reframe the transmitted and circulating fields, in terms of the input field, as

$$\frac{E_{\text{pass}}}{E_{\text{in}}} = \frac{-a + te^{-i\theta}}{-at^* + e^{-i\theta}} \qquad \frac{E_{\text{circ}}}{E_{\text{in}}} = \frac{-a\kappa^*}{-at^* + e^{-i\theta}}$$

Let us consider the transmitted response of the ring. To simplify the discussion we will assume that t is not complex, meaning that $t^* = t$. We square the equation for E_{pass} and have that

$$T = \frac{I_{\text{pass}}}{I_{\text{in}}} = \frac{a^2 - 2at\cos\theta + t^2}{1 - 2at\cos\theta + (at)^2} \tag{6.1}$$

Now, the ring is "on resonance" when the roundtrip phase is a multiple of 2π, such that $2\pi m = k_z L$. This is equivalent to the wavelength of the laser being such that it is an integer multiple of the length of the ring and "fitting" in the resonator. Recalling that $k_z = n_{\text{eff}} k_0$, where k_0 is the vacuum wavenumber, then the wavelength on resonance will be given by

$$\lambda_{\text{res}} = \frac{n_{\text{eff}}(\lambda)L}{m}$$

On the resonance, setting $\cos\theta = 1$, the transmitted power will be given simply by

$$T_{\text{R}} = \frac{(a-t)^2}{(1-at)^2}$$

What becomes immediately apparent is that, when $t = a$, then $T = 0$ and there will be no power transmitting past the ring. This is known as critical coupling, and can be understood by considering the destructive interference of the initially transmitted field, with that of the out coupled circulating field. The other limits for coupling, $t < a$ and $t > a$, are referred to as overcoupling and undercoupling respectively. These different coupling conditions result in modified spectral responses, which we will show below.

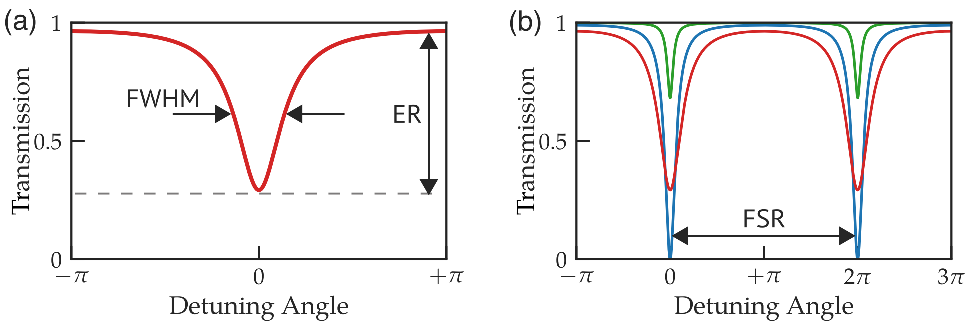

Figure 6.2: (a) Response of a single resonance in an overcoupled peak (b) Responses of three coupling conditions, including a full FSR.

Spectral Response and Key Features

The overall transmission response of the coupled resonator can be described using eq. (6.1), however it is common to reduce the response to more fundamental and key features to ease comparisons and understandings with other systems. In fig. 6.2 we indicate the standard features of the resonator response, particularly the free spectral range (FSR), extinction ratio (ER) and the linewidth or full width half maximum (FWHM). The free spectral range is the mode spacing between two adjacent resonances, and due to the optical dispersion this is related to the n_g rather than the n_{eff}, such that

$$\text{FSR} = \frac{\lambda^2}{n_g L} \quad [\text{m}] \qquad\qquad \text{FSR} = \frac{c}{n_g L} \quad [\text{Hz}] \tag{6.2}$$

These spectral features relate to two very important parameters of the resonator: the optical quality factor (Q) and the finesse ($\mathcal{F}$). Both of these parameters are a measure of how well light stays in the resonator. The Q is proportional to the number of oscillations the electric field takes before the circulating energy drops by $1/e$. This can be determined directly in the time domain by measuring the leaked output power of the resonator, or can be inferred from the spectral width, which can be related to the ring parameters through the following

$$Q = \frac{\lambda_{\text{res}}}{\text{FWHM}} = \frac{\pi n_g L \sqrt{ta}}{\lambda_{\text{res}}(1 - ta)} \tag{6.3}$$

It can be common to refer to the loaded and unloaded Q factor. The unloaded Q is the Q if we were to neglect any losses due to the coupling of the resonator, such that the Q is determined solely due to the cavity losses. In general, we can see that reducing losses and increasing the cavity length is the primary means to achieving a large Q. In planar circuits, modern microring resonators can attain Qs on the order of a 10^6, with extremely optimised devices able to reach in the tens of million. The coupling coefficients can be conveniently tuned with a Mach-Zehnder coupler configuration, rather than a single directional coupler [461].

Similarly to the Q, the finesse is related to the loss of the resonator. The subtle difference is that the finesse is a measure of the total number of *round trips* the light takes of the resonator, before the energy decreases by $1/e$. It is thus directly related to the *buildup* of the circulating field, and can be determined from the spectral and physical properties of the resonator through

$$\mathcal{F} = \frac{\text{FSR}}{\text{FWHM}} = \frac{\pi\sqrt{ta}}{1 - ta} \tag{6.4}$$

We now return to the original field relations, and consider the circulating field intensity, which we describe as a magnification factor relative to the input field, as

$$M = \frac{a^2(1 - t^2)}{1 - 2at\cos\theta + (at)^2}$$

If we are on resonance, and at critical coupling such that $t = a$, then the field enhancement is related to the finesse through

$$M = \mathcal{F}\frac{a}{\pi}$$

High finesse resonators are thus clearly of great use to nonlinear optics, as each interacting wave circulating in the resonator receives an enhancement proportional to $\mathcal{F}$ in power. This is very effective for four wave mixing in particular, which will receive $\mathcal{F}^4$ enhancement [463], with rings of a few 10s of µm circumference attaining performance comparable to cm length nonlinear waveguides, or km of optical fiber [464].

6.1.2 Brillouin lasers

So far in this thesis we have primarily been investigating SBS in the context of a pump and amplified probe wave, which is typically referred to as an SBS amplifier. Another class of devices utilises the spontaneously scattered optical, in the absence of input probe. By placing the Brillouin medium within a resonator, with the correct spectral properties, the spontaneously scattered light can build up and be amplified above the round-trip loss of the cavity, resulting in net gain and oscillation. This is referred to in the literature as a Brillouin *laser*, though oscillator is probably a less divisive term. There are also some subtleties of the dynamics of the system above oscillation [465], which can change depending on the ratio of the cavity linewidth to the acoustic linewidth [466]. We have summarised demonstrations of Brillouin lasing in modern waveguide and resonator systems in section 2.4.3.

Brillouin lasers have been receiving interest in the wider literature due to their unique noise properties. If the optical damping is smaller than the acoustic damping then the noise from the pump is transferred to the acoustic wave [465, 467–469], narrowing the scattered Stokes relative to the pump. In highly optimised cases this spectrally purified Stokes wave can reach sub-Hz Schawlow Townes limited linewidths, after starting with typical KHz sources [121], and be used to generate spectrally pure microwaves [122]. In the following we will briefly mention standard schemes for creating Brillouin lasers in the literature, with the focus here on fiber schemes, and how using a resonator results in low threshold operation.

Brillouin lasing in a full fiber resonator was first demonstrated by Stokes in 1982 [50]. The scheme used by Stokes was highly effective, consisting of a *tunable* directional coupler where two ports were connected to each other to close the loop [49, 470]. This allowed for sub-mW thresholds in a 10 m fiber loop. Keeping the fiber loop relatively short is crucial to prevent mode-hopping between multiple cavity modes [471, 472]. Placing a stretchable piece of fiber, SMF wrapped around a piezoelectric crystal for example, into the resonator can enable active stabilisation [473]. Stable operation can also be achieved through the use of an optical circulator, instead of a directional coupler, to circulate either the pump or Stokes wave around the fiber loop in a non resonant manner [425, 474]. This is at the cost of an increased threshold, as only one optical wave is circulating. Another alternative scheme is to embed a broadband gain medium, such as an erbium doped fiber and pump, within the resonator to create a hybrid Brillouin/erbium laser [475], though the noise and dynamics of these systems is different to a typical Brillouin laser.

What is the typical threshold for Brillouin lasing in a waveguide ring resonator? This has been discussed for Raman scattering in whispering gallery mode resonators [476] and in the presence of nonlinear losses in [477, 478]. To summarise, we require a net amplification of the Stokes wave, after a round trip. While we are generating the Stokes from noise, we can assume there will be sufficient spontaneous scattering that the system will experience amplification as if in the presence of an external seed. If we apply the standard small signal approximation [132], considering the *circulating* power of the pump wave, it can be shown that the threshold, in the case that the loss is low and the cavity is at critical coupling, is given by

$$P_{\mathrm{th}} = \frac{\pi^2 {n_{\mathrm{g}}}^2}{\lambda_{\mathrm{p}}^2} \frac{L}{G_B Q_{\mathrm{L}}^2} \equiv \frac{\pi^2}{G_B \mathcal{F}^2 L}$$

For the Stokes and pump to both be circulating in the resonator, if generating lasing between two longitudinal cavity modes, we require that the cavity length be sufficient such that $\Omega_{SBS}/FSR = m$ where m is an integer. To minimise the threshold we can choose a waveguide geometry which maximises $G_B\mathcal{F}^2$, which we will discuss in further detail in the next section. If we consider a 1 cm long device, with the parameters of the ribs in the previous chapter, $G_B = 500\,m^{-1}W^{-1}$ and propagation loss of 0.3 dB/cm, which yields a $Q = 7 \times 10^5$ or $\mathcal{F} = 22$, we have a threshold power of just 4 mW. If we prioritise the propagation loss, by, for example, making a larger effective area device with loss of 0.1 dB/cm but a $G_B = 250\,m^{-1}W^{-1}$, then we can achieve sub-mW oscillation. This is an orders of magnitude reduction in threshold, compared to the Watt level peak powers required for multi-cm Fabry-Perot As_2S_3 resonators previously explored [125], and significantly more compact than hybrid fiber loop systems [126].

6.2 Compact Brillouin devices through hybrid integration on silicon

Stimulated Brillouin Scattering (SBS) has recently emerged as a flexible tool for optical processing and radio-frequency (RF) photonics [139][1]. SBS is one of the strongest nonlinearities known to optics, hundreds of times larger than Raman scattering in SMF-28 fiber [480], and is capable of providing exponential gain over narrow bandwidths of the order of tens of megahertz. This narrowband amplitude response is accompanied with a strong dispersive response, capable of tailoring the phase or group delay of a counter propagating optical signal. In light of these effects a rich body of applications have been explored such as slow light [419], stored light [481], narrowband RF photonic filters [482–484], dynamic optical gratings [485, 486], narrowband spectrometers [487], optical amplifiers [371, 372] and RF sources [488] among others. When pumped in a resonator configuration, a narrow linewidth spectrally pure SBS laser can be generated [467, 489, 490]. Highly coherent lasers are used in optical communication, LIDAR and producing pure microwave sources [491] among other applications. While the majority of previous works have traditionally utilised SBS in optical fiber, a number of these applications have been demonstrated in integrated form factors [92, 121, 122, 139, 360]. Most recently, the demonstration of 52 dB Brillouin gain [89] in centimeter length scale As_2S_3 rib waveguides proves that performance equivalent to kilometers of optical fiber is achievable in integrated devices.

The capability to embed SBS as a functional component in active photonic circuits will enable the creation of a new class of opto-electronic devices, in particular for integrated microwave photonics [492]. The desire to harness SBS optical processing in CMOS (Complementary metal-oxide-semiconductor) compatible platforms has recently culminated in demonstrations of SBS in various silicon on insulator (SOI) device architectures [103–105, 493]. Underetching of different waveguide geometries is performed to create guided acoustic modes, generating strong SBS from the high opto-acoustic overlap. Initial works have demonstrated large Brillouin gain coefficients [103, 105, 493] in excess of $10^3\,m^{-1}\,W^{-1}$, 10^4 times higher than single mode optical fiber, made possible due to boundary forces which exist in these subwavelength structures [95]. More recent work has focused on reducing propagation losses to improve amplification factors to more than

[1]Parts of the following section have been published in Optica: B. Morrison et al., "Compact Brillouin devices through hybrid integration on silicon", Optica 4, 847 (2017)

5 dB [104]. But in general, higher gains in SOI devices have been prevented due to nonlinear losses in silicon [107, 108] and linewidth broadening due to small dimension fluctuations introduced during device fabrication [106].

In this work we introduce a hybrid integration approach to generate large Brillouin gain in a silicon-based device, free from nonlinear losses. We embed a compact 5.8 cm As_2S_3 spiral waveguide into a silicon circuit, enabling record Brillouin gain of 22.5 dB (18.5 dB net gain) on a silicon-based chip. Traditional silicon grating couplers are used for coupling in and out of the chip, with silicon tapers providing low loss transitions between the Si and As_2S_3 sections of the circuit. To further explore the flexibility of this approach we fabricate precisely designed As_2S_3 ring resonators, enabling the first demonstration of Brillouin lasing in a planar integrated circuit. This work marks a significant step towards the realisation of fully integrated active SBS devices, such as integrated opto-electronic oscillators [494], lossless microwave photonic filters [495] and compact optical gyroscopes [123] in the near future.

6.2.1 Silicon interfaced As_2S_3 spiral waveguide

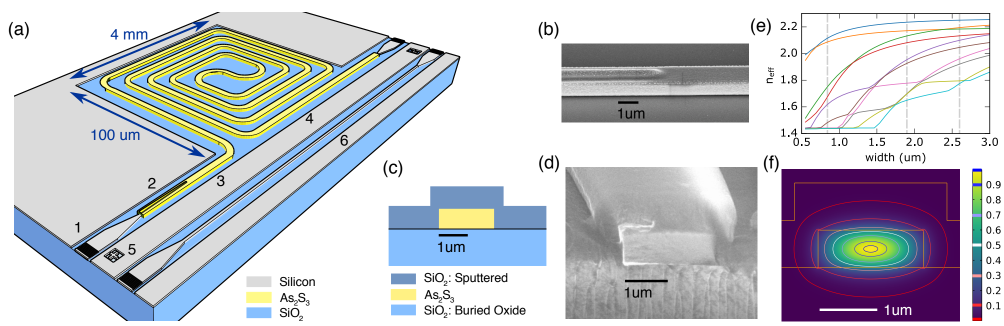

Figure 6.3: An As_2S_3 silicon hybrid circuit (a) A schematic of the hybrid circuit with a number of components indicated 1. Silicon grating couplers with tapers to 450 nm × 220 nm nanowires 2. Silicon nanowire taper region with As_2S_3 overlay waveguide 3. As_2S_3 waveguide lead into the hybrid structure 4. Spiral waveguide formed out of As_2S_3 5. Alignment markers formed in the silicon layer for patterning the As_2S_3 structures 6. Reference silicon structures existing on the same chip (b) An SEM image of the end of silicon taper before cladding deposition (c) Schematic cross section of waveguide in chalcogenide only region (d) An SEM image of chalcogenide region cross section with silica cladding (e) Calculated effective indexes for 10 waveguide modes with increasing waveguide width. Waveguide widths used throughout the work, 1.9 µm in the spiral, 2.6 µm in the resonator and 0.85 µm in the coupler, are indicated with dashed vertical lines) (f) Optical mode simulation of fundamental TE mode of 1.9 µm wide As_2S_3 waveguide

Figure 6.3a shows the schematic of the fabricated hybrid circuit. The circuit consists of a base silicon section and an As_2S_3 SBS active section. Silicon grating couplers are used for chip coupling [266], followed by 2 mm long a silicon waveguide. The nanowire waveguide (450 nm × 220 nm cross section) then linearly tapers, over a length of 100 µm, to a width of 150 nm and ends in a open silicon region of 0.1 mm × 4 mm. Amorphous As_2S_3 was deposited in the open region, with a thickness of 680 nm, completely covering the silicon tapers. Overlay waveguides were processed over the silicon taper before proceeding to the rest of the circuit, an SEM of the end of the taper region before cladding deposition is shown in fig. 6.3b. Optical propagation simulations, discussed in the supplementary, indicate a total insertion loss on the order of 0.1 dB for transmission into the fundamental mode of the As_2S_3 waveguide. Silica cladding of 1 µm thickness was sputtered over the sample after As_2S_3 etching, with care taken to keep processing temperatures suitable for optimum losses [443]. A schematic of a typical waveguide geometry is shown in fig. 6.3c, along with a cross sectional SEM fig. 6.3d and optical mode simulation of the fundamental mode of a 1.9 µm wide waveguide (fig. 6.3f). Further details of the fabrication process is provided in the supplementary. The As_2S_3 region of the circuit is confined to within a small region of 0.4 mm^2 requiring significant design optimisation to achieve high performance.

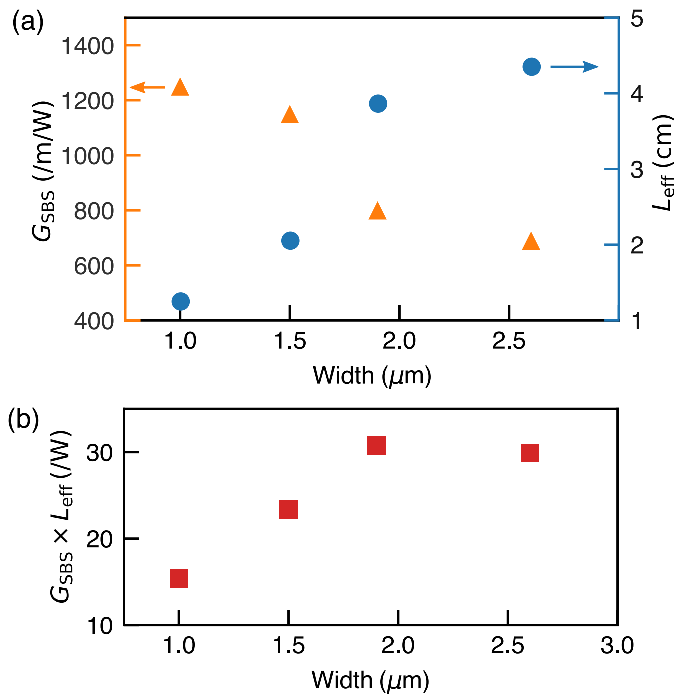

Figure 6.4: (a) Peak SBS gain coefficient and effective lengths for varying waveguide width (b) Corresponding $G_{SBS} \times L_{eff}$ values.

To maximise the physical waveguide length in the available device area (0.1 mm × 4 mm) we employ a folded spiral design with a rectangular shape and identical bends for each loop. As we will explain in further detail, the device geometry was chosen to give the highest Brillouin amplification in this confined area. The expected gain of a weak probe, P_o, for a coupled pump power, P_P, in the small signal gain regime of backwards SBS is given by

$$P_S = P_o \exp(G_{SBS} L_{eff} P_P) \tag{6.5}$$

where G_{SBS} is the Brillouin gain coefficient and L_{eff} is the effective length which is related to the physical device length L by $L_{eff} = (1 - \exp\{(-\alpha L\}))/\alpha$ where α is the linear loss. To achieve the largest gain for a given pump power we thus need to maximise $L_{eff} \times G_{SBS}$. The Brillouin gain coefficient is inversely proportional to the effective optical mode area, A_{eff}, so that the trade off becomes whether to reduce the waveguide width, w, to decrease A_{eff} or increase the waveguide width to reduce α, while maintaining long physical device lengths. The propagation loss is dominated by scattering losses from the rough sidewalls [186], which has a quartic reduction with waveguide width (i.e $\alpha \propto 1/w^4$). Larger widths lead to the waveguide becoming heavily multimoded, effective index values for the first ten guided modes are calculated for increasing widths in fig. 6.3e. Adiabatic bends based on the Euler spiral [206], in a matched bend configuration [289], are used in the design to minimise mode conversion, preventing extra loss throughout the structure.

To explore these trade-offs more quantitatively propagation losses for a number of waveguide widths were measured, and simulations calculating G_{SBS} were performed for corresponding geometries. The effective lengths, assuming a 6 cm long device, and the peak gains are shown in fig. 6.4a. The resulting $L_{\mathrm{eff}} \times G_{\mathrm{SBS}}$ is plotted in fig. 6.4b, while widths greater than 2 µm provide further improvement, the required bend radii prevents use in the compact spiral. From this comparison we determined an optimum waveguide width of 1.9 µm, with effective bend radii of 16.5 µm calculated through FDTD simulations, further data is provided in the supplementary. A total device length of 5.8 cm consisted of 8 loops (36 bends including external connections) with a very compact structure achieved through a small waveguide spacing of 1.4 µm. We measured a total propagation loss of 4 dB through the spiral when correcting for the coupling losses from the grating couplers and $Si - As_2S_3$ transitions. An estimated propagation loss of 0.7 dB /cm resulted in an L_{eff} of 3.9 cm for the nonlinear interaction. The overall formfactor of this spiral represents orders of magnitude reduction compared to that of previous As_2S_3 waveguides used for SBS [89]. The typical half-etch rib geometries with multi micron widths, used for the low losses <0.5 dB cm^{-1}, require bend radii of more than 100 µm and are incapable of high density due to the significant cross-talk introduced from the partial waveguide etch. Similarly, under etched devices require an appropriate spacing between adjacent waveguides to prevent acoustic interactions and maintain structural support, $\sim$ 20 µm width was used for a single underetched membrane structure [104].

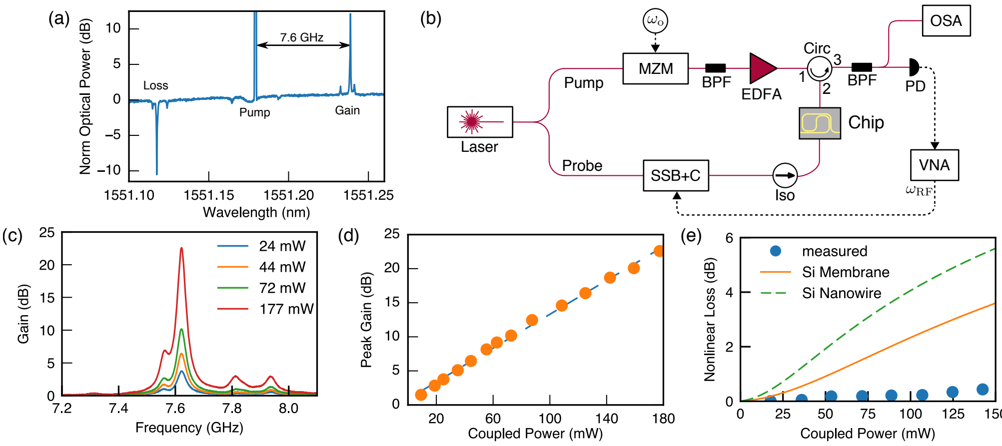

Figure 6.5: Backwards SBS in As_2S_3 spiral waveguide. (a) Optical spectrum measurement of SBS gain and loss. (b) Setup schematic for high resolution pump probe (c) High resolution SBS spectrum for various pump powers. (d) Peak gain values up to 180 mW coupled pump power with fit. (e) Nonlinear loss comparison of this work, silicon nanowire and silicon membrane

6.2.2 Backwards SBS in As_2S_3 spiral waveguide

To experimentally investigate the behaviour of different devices we performed two sets of pump-probe SBS measurements, a coarse measurement using an optical spectrum analyser (OSA) and a high resolution setup with an electrical vector network analyser (VNA). In the optical spectrum analyser measurement, a high resolution OSA (0.8 pm) was used to measure the transmission of a weak probe while an amplified pump laser was counter-propagated through the sample. A schematic of the setup is provided in the supplementary material. This measurement allowed for a rough estimate of the Brillouin frequency shift in the device and enabled simultaneous monitoring of the gain and loss response. An on-off gain of >10 dB was observed at 80 mW coupled power, as shown in fig. 6.5a. A Brillouin shift of ~ 7.6 GHz was measured relative to the residual back-reflected pump (centered at 1551.18 nm) and symmetric gain and loss spectra were measured.

To measure the SBS response in further detail we implemented a high resolution (<1 MHz) pump-probe experiment through the use of a radio frequency vector network analyser (VNA) [439]. A laser, frequency ω_c, is split into two arms to create the pump and the probe wave. The pump is upshifted in frequency by ω_o from the carrier through the use of a Mach-Zehnder intensity modulator (MZM) and optical bandpass filter (BPF). The pump was then amplified with a high power EDFA, passes through ports $1 \rightarrow 2$ of an optical circulator and coupled with TE polarisation silicon grating couplers into the hybrid circuit. In the probe arm the laser undergoes single sideband with carrier modulation (SSB+C) to produce a weak probe upshifted by frequency ω_{RF}. The carrier and probe were both coupled to the device and pass through the hybrid circuit. After coupling at the output, the transmitted waves were routed from ports $2 \rightarrow 3$ of an optical circulator and then a bandpass filter was used to remove any residual back reflected pump. The remaining optical waves beat on a highspeed photodetector and the change in RF power at frequency ω_{RF} is measured by the VNA. In the frequency region of the Brillouin shift from the pump $(\omega_{\mathrm{RF}} \approx \omega_o - \Omega_{\mathrm{SBS}})$, the modulated sideband will experience Brillouin amplification as shown in fig. 6.5c. Further details of the measurement process can be found in the supplementary. We measured the frequency spectrum for increasing pump powers up to 180 mW coupled power, as shown in fig. 6.5d. Net amplification was achieved above 25 mW on-chip power, overcoming the 4 dB of propagation losses, with a maximum on-off gain of 22.5 dB and a net gain of 18.5 dB. This represents a $> 20\times$ improvement of net gain gain compared to recent demonstrations for forward Brillouin scattering (FBS) [104] and forwards intermodal Brillouin scattering (FIBS) [496] in suspended silicon membrane waveguides. Fitting the slope of the measured peak gain data from fig. 6.5d obtains a Brillouin gain coefficient of $G_{\mathrm{SBS}} = 750 \pm 50\,\mathrm{m}^{-1}\,\mathrm{W}^{-1}$, a 50 % increase over previous chalcogenide waveguides [89]. This increase is primarily due to the reduction of A_{eff} compared to the previous partially etched rib structures.

Here we compare the effects of pump attenuation through nonlinear losses in the devices in this work with simulated silicon geometries (fig. 6.5e). Nonlinear losses are a key limiting factor in integrated silicon waveguide devices at telecommunications wavelengths [228, 497]. For silicon-based Brillouin systems the effect is two-fold, a direct reduction in pump power from two-photon absorption (TPA) and free carrier absorption (FCA) leading to a power dependent L_{eff} for the pump and also the direct attenuation of the probe wave through cross-photon absorption and free carriers which are generated *by* the pump. We experimentally measured the transmission through a 2 mm reference hybrid waveguide, maximising the optical power through the silicon leads of 3 mm on either side of the hybrid structure. This is a worst-case scenario, with negligible linear losses in the hybrid region, with 6 mm of silicon waveguide contributing to nonlinear losses. Even so, at high coupled powers of 150 mW only 0.5 dB was measured. This is in stark contrast to pure silicon structures, with close to 4 dB of pump attenuation expected for a simulated silicon membrane and almost 6 dB for a nanowire geometry, effectively saturating the input pump power and preventing any further gain [103]. Careful theoretical analysis [107, 108] has indicated that reducing linear losses and increasing device lengths may enable higher Brillouin amplification at low pump powers, but this can be hampered by dimensional broadening as explored below.

6.2.3 Dimensional Broadening

Dimensional broadening has been identified as a key issue which reduces the expected gain, particularly in nanoscale waveguides reliant on transverse acoustic waves such as forward SBS structures [105, 106]. The effect manifests in changing Brillouin lineshapes as device lengths are modified, measured mechanical quality factors were reduced by almost half when moving from millimeter to centimeter scales in suspended membrane structures [104]. We explore dimensional broadening in As_2S_3 waveguides by measuring the SBS response of a number of different waveguide widths and lengths, including straight and spiral structures.

To determine if there are any issues from dimensional broadening in the As_2S_3 hybrid chip we measure the natural linewidth of a number of different waveguide geometries. The natural linewidth can be directly measured from the spontaneous Brillouin or inferred from pump probe measurements [80]. Due to the high sensitivity available with the pump probe system we used this technique for measuring the natural linewidth. The natural SBS spectrum is a Lorentzian with width Γ_B, which becomes compressed under high gain and approaches a Gaussian shape. The measured linewidth in a pump probe measurement is related to the gain through the G coefficient by the following,

$$\Delta\nu_{RF} = \Gamma_B \sqrt{\frac{G}{\ln(e^G + 1) - \ln 2} - 1} \tag{6.6}$$

where G is the term in the exponential of the small signal gain equation ($G = G_{SBS} L_{eff} P_P$). The G parameter can be directly determined by the on-off gain only, making linewidth measurements robust against changes in pump power and coupling loss. Experimental measurements of linewidths with different gain values of the 5.8 cm spiral waveguide described in the body text is shown in fig. 6.6a. The fitted data is also shown and the best fit yields $\Gamma_B = 42$ MHz.

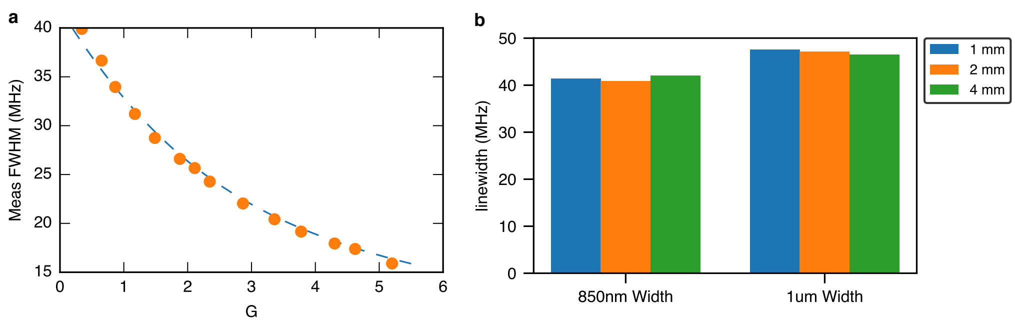

Figure 6.6: (a) Measured linewidth narrowing with increasing gain in 5.8 cm spiral waveguide b) Fitted natural linewidths of different waveguides

Figure 6.6b shows the calculated linewidths for two sets of waveguides. The waveguides with widths of 850 nm and 1 µm had Γ_B of $\sim$ 41 MHz and 47 MHz respectively. A spiral structure (from another batch of samples) with 1 µm width and length of 4 cm had a $\Gamma_B =\sim 45$ MHz. The changes of natural linewidth over the lengths here are within the uncertainty range of these measurements. This is in stark contrast to forward Brillouin scattering structures which are highly sensitive to fluctuations in dimensions [105], a 30 % reduction of quality factor (directly proportional to linewidth) was observed when increasing length from 1 mm to 4 mm in silicon membranes [104] (data in supplementary material). The lack of dimensional broadening with increasing length makes propagation loss and compactness the only difficulties for As_2S_3 devices if long SBS structures are desired.

The significant increase in available gain, and negligible effects of nonlinear losses, will enable a number of new applications beyond the limited Brillouin signal processing currently demonstrated in silicon [360], including Brillouin lasing as explored in the next section.

6.2.4 Compact ring resonator

Brillouin lasers are capable of spectrally narrowing laser sources and, if cascaded, can produce pure microwave frequencies. Achieving Brillouin lasing in micro resonators is challenging due to the requirement for the cavity free spectral range (FSR) to closely match the Brillouin shift. Initial demonstrations used highly overmoded resonators such that two resonances between different mode families were aligned [115, 116]. More recently, precise matching of the cavity FSR and the SBS shift was achieved in lithographically processed silica wedge resonators [120]. These previous devices have extremely low losses, enabling low threshold oscillation, but require external coupling via tapered optical fibers or free space optics. To show a further application of the combined As_2S_3 and Si platform, we fabricate high Q ring resonators designed for Brillouin lasing and achieve the first demonstration of Brillouin lasing in a planar integrated circuit.

A schematic of the ring design is shown in fig. 6.7a. To achieve low threshold lasing in the sample we must satisfy three competing challenges; the FSR must match the Brillouin shift, the loss throughout the cavity must be minimal and the whole structure must be as compact as possible. The SBS shift scales (Ω_{SBS}) with effective index (n_{eff}) of the optical mode and acoustic velocity of the acoustic mode (v_{ac}), such that $\Omega_{\mathrm{SBS}} = 2\, n_{\mathrm{eff}}\, v_{\mathrm{ac}}/\lambda_{\mathrm{p}}$. The FSR of a resonator depends upon the total roundtrip time of the cavity, and is related to the length (L) and group index (n_{g}) such that FSR $= c/(L \times n_{\mathrm{g}})$. Thus we need to take into account the change of n_{eff} and n_{g} with waveguide width when determining the appropriate length of the resonator, as represented in fig. 6.7b. The threshold for a Brillouin laser in a resonator with an FSR matching the Brillouin shift is given by [476]

$$P_{\mathrm{th}} = \frac{\pi^2 n^2}{\lambda_{\mathrm{p}}^2} \frac{L_{\mathrm{Trip}}}{G_B Q_{\mathrm{tot}}^2} \frac{(1+K)^3}{K} \tag{6.7}$$

$$P_{\mathrm{th}} \propto \frac{L_{\mathrm{Trip}}}{G_B Q^2} \tag{6.8}$$

where G_{SBS} is the SBS gain coefficient as above, Q_{tot} is the loaded Q of the resonator, λ_{p} is the pump wavelength, L_{Trip} is the roundtrip length of the resonator and K is the coupling parameter which is related to the transmission (T) such that $T = ((1-K)/(1+K))^2$. To reduce propagation losses we increase the width of the waveguides up to 2.6 µm, increasing the required bend radii to 22.5 µm. Finally, to maintain a compact structure we utilised a number of individual components within the circuit. Short adiabatic couplers, based on the Milton and Burns criterion [285], were used to transition from the heavily multimoded waveguides with widths of 2.6 µm down to few mode structures with widths 850 nm. These narrow waveguides were used in the directional coupler to provide coupling to the ring with as short length as possible. A nested spiral design, again with Euler bends, was used to minimise the footprint of the resonator and enabled the required roundtrip length (~1.5 cm) to fit within the required area. Further details on individual component design, including microscope images of the fabricated sample, are provided in the next section.

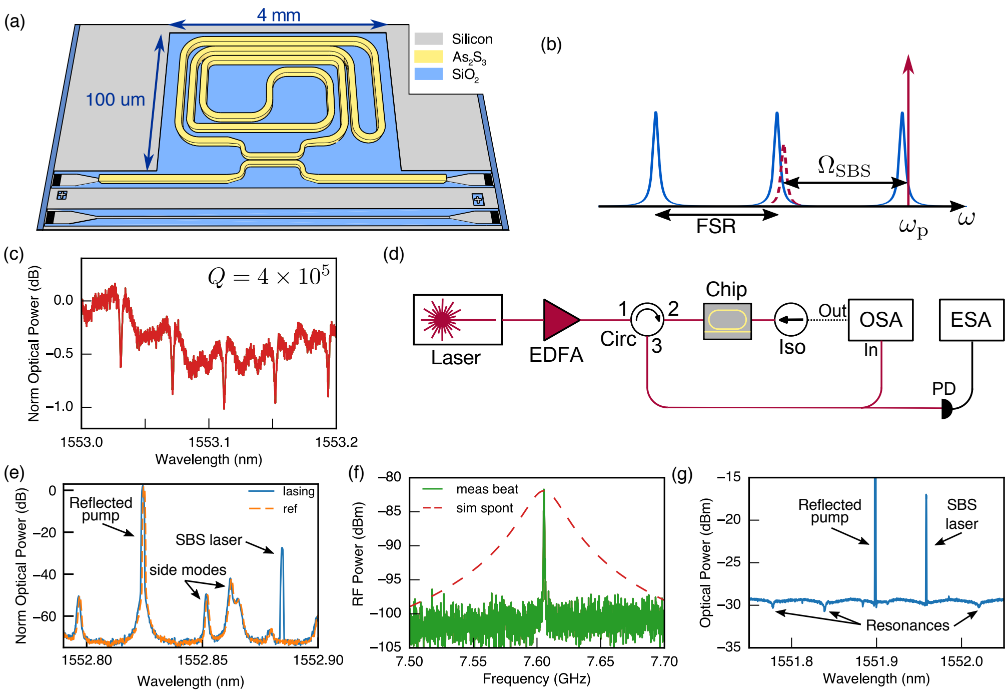

Figure 6.7: Brillouin lasing in planar As_2S_3 resonator (a) Schematic of the hybrid ring resonator structure. (b) A concept figure for the lasing conditions. The cavity free spectral range needs to precisely match the Brillouin shift (c) Typical optical transmission of ring resonator (d) The setup used for measuring the laser and resonator (e) Lasing signal measured on OSA. The Brillouin lasing signal is observed in blue solid trace. The tunable laser is shifted slightly and the lasing no longer occurs. A number of peaks due to the modes of the laser are observable in the orange dashed trace (f) RF beat of the backreflected pump and lasing signal. The measured linewidth was less than 5 MHz, significantly narrower than the natural lifetime of 40 MHz confirming that we are above the lasing threshold (g) Brillouin lasing while monitoring the resonance position. Both the pump and generated Stokes are aligned to cavity resonances

Optical transmission measurements were performed on the fabricated device with the same high resolution OSA used in the pump-probe measurements (fig. 6.7c). From these measurements we observed a FSR of 7.62 GHz at 1553 nm and an extinction ratio of around 0.65 dB or, equivalently, a transmission of 85 %, which corresponded to $K = 0.04$. The measured resonance linewidth was 4.5 pm corresponding to a Q_{tot} of 4×10^5. The measured Q factor was limited by the propagation losses in the 2.6 µm waveguide, estimated as 0.5 dB/cm, and losses due to the ring coupler, on the order of 0.2 dB. This value compares favourably to previous demonstrations of planar centimeter length scale As_2S_3 ring resonators with 3.5×10^5 in As_2S_3 on Lithium Niobate [498] and 1.5×10^5 for directly written As_2S_3 waveguides [499]. From Equation (6.7) we determine an expected threshold of 80 mW for the fabricated sample, assuming optimum matching of the SBS shift to the cavity FSR.

6.2.5 Brillouin lasing

To demonstrate Brillouin lasing in the fabricated resonator we seamlessly tuned a pump onto the resonance for a range of power levels, while monitoring the back reflected optical waves (fig. 6.7d). The pump light source was an external cavity laser (ECL), capable of fine resolution tuning with a continuous step size of 10 MHz, allowing for accurate alignment to the center of the resonance. The pump was amplified before passing through a circulator (ports $1 \rightarrow 2$) and coupling to the chip through silicon grating couplers. Back-scattered light from SBS, and the back-reflected pump wave, then passed through the circulator (ports $2 \rightarrow 3$) and was monitored on a high resolution OSA while the RF beat was measured on an electrical spectrum analyser (ESA). A weak reference output of the OSA was also used as a probe to measure the transmission of the resonator when desired.

For coupled powers above 50 mW Brillouin lasing was observed on the OSA and ESA. Figure 6.7e shows a Brillouin lasing signal on the OSA, along with a reference signal at the same power level with the pump shifted just past the resonance. A single lasing signal is observed at a power level in the range of –30 dBm. A strong signal close to 0 dBm, at the pump wavelength, was also measured due to the $\sim 1\,\%$ backreflection of pump from the chip grating couplers. A number of cavity side modes from the backreflected pump were also observed, these are around 50 dB below the pump signal in line with the pump laser specifications. To confirm that the measured signal was not due to spontaneous scattering we measured the electrical beatnote above threshold on the ESA (fig. 6.7f). The measured beatnote was significantly narrower than the SBS natural linewidth of 40 MHz [89], plotted with a dashed line in fig. 6.7f. The frequency of the beatnote was at 7.60 ± 0.005 GHz and slow drifts on the order of 5 MHz were observable on the ESA over minute time scales. The lack of active locking of the pump to the resonator prevented the measurement of a slope efficiency of the Brillouin laser above the threshold level. For the weak coupling case that we have ($K = 0.04$) a low slope efficiency of 4 % is expected [476], improving the coupling to the ring would drastically improve this and also reduce the lasing threshold. Finally, to confirm that the Brillouin lasing is indeed occurring on the resonances of the ring, we perform an OSA measurement while sweeping a weak probe signal to measure the resonator transmission. In this case the coupled pump power was 75 mW, fig. 6.7g shows that the lasing signal and pump are both aligned to cavity resonances.

6.3 Further Technical Details

6.3.1 Additional Experimental Details

Figure 6.8 is the schematic of the optical pump probe setup which is used in the main text. An optical "network analyser" is formed using the swept source from an OSA (http://www.apex-t.com). The pump (frequency ω_p) is amplified and counterpropagated through the sample, generating SBS amplification/attenuation at the Stokes/anti-Stokes ($\omega_p - \Omega_{SBS}$, $\omega_p + \Omega_{SBS}$) shifts from the pump. This measurement technique enables simultaneous measurements of the gain and loss response over a broadband frequency range (i.e. 0 GHz to 100 GHz), difficult for techniques utilising radio-frequency equipment.

A general schematic for the high resolution setup was provided in the previous section. Here we also provide, fig. 6.9, a more detailed schematic outlining the

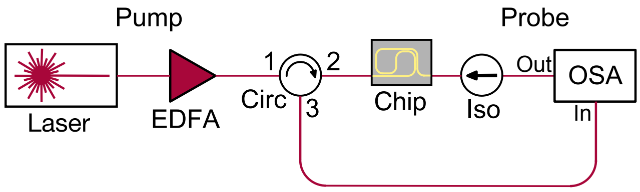

Figure 6.8: The schematic of the optical pump probe setup.

overall setup. A 100 mW laser (with 50 KHz linewidth) is split into two arms which form the pump and the probe. About 1 mW enters the pump arm, is amplified with an Erbium doped fibre amplifier (EDFA) to 100 mW and enters a Mach-Zehnder modulator (MZM). The modulator is biased with a DC voltage to suppress the original laser tone and modulated at ω_o generating two sidebands. The upper sideband is selected using a narrow ($\sim$ 10 GHz) bandpass filter and is amplified with another EDFA and sent to the chip through ports $1 \rightarrow 2$ of an optical circulator. The input to the chip is weakly tapped at 1 % to monitor the power, with an optical power meter (PM), and device insertion losses throughout the experiments. After transmission through the chip the remaining pump is removed with an optical isolator. In the probe arm close to 100 mW enters a dual parallel Mach-Zehnder modulator (DPMZM). A DPMZM consists of two nested MZM and a phase shifter in one arm [500]. The DPMZM is modulated at ω_{RF}, with a hybrid coupler splitting and phase shifting the ω_{RF} input, from the vector network analyser (VNA) and biased with 3 DC voltages to suppress only the lower sideband (equivalent modulation can also be achieved with a dual drive MZM [501]).

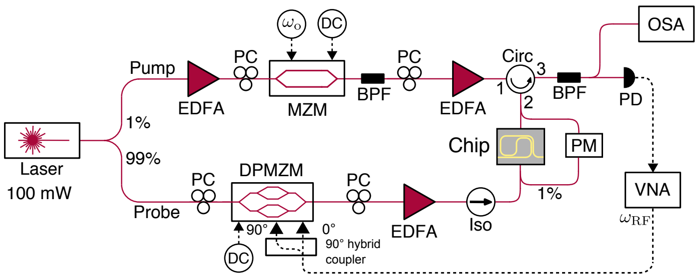

Figure 6.9: The schematic of the full high resolution pump probe setup

Polarisation controllers (PC) are required in the setup to align to the correct polarisation axis of the modulators and the silicon grating couplers. The carrier and probe couple to the chip and will undergo SBS in the frequency region of the Brillouin shift from the pump ($\omega_{RF} \approx \Omega_B - \omega_o$). After transmission through the chip the carrier and probe pass through a bandpass filter to remove any residual back reflected pump, back reflection of the order of 1 % is expected from the grating coupler and cleaved SMF fibre. The carrier and probe will then beat at the highspeed photodetector (PD), producing a microwave beatnote at the original ω_{RF} frequency produced by the VNA. The VNA directly measures the change in RF power as ω_{RF} is swept in the region of interest. By turning off the pump the system response, which includes conversion from optical to microwave domain, optical transmission and also RF loss in components and cables, can be normalised and corrected directly. When the pump is turned on the SBS spectrum can be accurately extracted.

6.3.2 Fabrication, Design and Simulation Details

The base silicon devices were fabricated in a multi project wafer run at Imec, obtained through the europractice shuttle service. The silicon chips were cleaned with acetone and isopropanol solution to remove protective polymer layer before thermal deposition of As_2S_3 680 nm thickness in a local region using a shadow mask process. Optical and thermal annealing stabilised the index in the range of $n = 2.44$ at 1550 nm, measured material dispersion numbers are provided below. Electron beam lithography was used to pattern a spun coat ZEP resist on the As_2S_3. Alignment markers used for EBL were formed in the original silicon design. ICP etching was used to form the nanowires before the remaining resist was removed. Finally, sputtered SiO_2 of approximately 1 µm thickness was deposited as a cladding layer.

Waveguide mode simulations for calculating n_{eff} and n_g, required for mask design, were performed in Comsol Multiphysics 5.0 (https://www.comsol.com), utilising measured material dispersion. The Mask design and layout of both the silicon and chalcogenide devices were performed using Ipkiss 3.1 from Luceda Photonics (http://www.lucedaphotonics.com). Multimode chalcogenide components were optimised through 3D-FDTD simulations using FDTD Solutions 2016a from Lumerical (https://www.lumerical.com). FDTD simulations incorporated material dispersion and the appropriate device cross-section. Due to the long length of silicon tapers, 3D-BPM simulations were performed using RSoft's (https://optics.synopsys.com/rsoft/) BeamProp software. Microscope images of a fabricated ring resonator are shown in fig. 6.10.

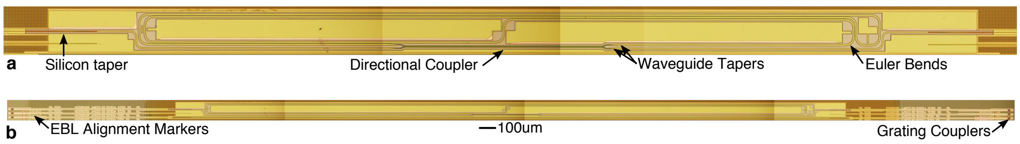

Figure 6.10: a) Microscope images (not to scale) highlighting key device components b) To scale image of entire circuit with silicon grating couplers and EBL alignment markers highlighted

When performing mode simulations in Comsol and propagation simulations in Lumerical the measured As_2S_3 refractive index was used. The measured material dispersion (for the as deposited thin film) was fit with a general Sellmeier equation in the following form with Mathematica,

$$n(\lambda) = B_0 + \frac{B_1\lambda^2}{\lambda^2 - C_1} + \frac{B_2\lambda^2}{\lambda^2 - C_2} + \frac{B_3\lambda^2}{\lambda^2 - C_3} + \frac{B_4\lambda^2}{\lambda^2 - C_4} \tag{6.9}$$

to allow for ease of use in Comsol. The fit values, with λ in units of µm, were

$$\begin{aligned} &[B_0, B_1, C_1, B_2, C_2, B_3, C_3, B_4, C_4] \\ \mathrm{As_2S_3}: &[3.801238, 2.229502, 0.120952, 1.205326, -1.864329, \\ &-0.148652, -1.029330, -1.142527, -1.743148] \\ \mathrm{SiO_2}: &[2.6461, 2.0750, 0.07762, 0.88840, 0.09802, \\ &0.10101, 0.208958, 0.0029796, 10.1777] \end{aligned}$$

As discussed in the previous section, the ring resonator and spiral waveguide required a number of individual components to be implemented in Ipkiss. The Euler bends were created in parametric fashion, following the description in Ref [206], using the first 5 terms of the exponential expansion for x and y components.

The bending algorithm was implemented to be compatible with the rest of the Ipkiss library, enabling the bend to simply replace circular bends (or other bend shapes) where desired. This allowed the same algorithm to be used for the spiral waveguides, ring resonator and also S bends in the directional coupler. The bends were designed to operate in a matched bend configuration to maintain low losses for all bends. For the 1.9 µm width waveguides in the spiral the optimum bend radius was determined to be 16.5 µm, FDTD simulation data for transmission through a single bend, at a wavelength of 1550 nm, is provided in table 6.1. The wider waveguides in the ring, 2.6 µm, had a larger bending radius of 22.5 µm. The scripts developed for generation of the Euler bend have since been incorporated into Ipkiss, please contact Luceda Photonics or the author for more information.

Table 6.1: Simulated Bend losses for 1.9 µm wide waveguide

Bend Radius (µm)	Single Bend Transmission	36 Bends
14.0	0.942	0.11
16.5	0.999	0.96
18.5	0.983	0.53
20.0	0.962	0.24

The significantly wider waveguides in the ring, 2.6 µm, compared to the directional coupler, 0.85 µm, required tapers for efficient mode conversion. To reduce the taper length and minimise mode conversion as much as possible, we implemented adiabatic tapers based on the Milton and Burns condition as described in Ref [285]. To implement this component in Ipkiss the effective index for waveguide widths from 0.5 µm to 4.0 µm was calculated, to determine the local tapering angle for a given position. The optimised designs were determined through 3D FDTD simulations in lumerical solutions, $\alpha = 0.225$ for the 2.6 µm $\rightarrow$ 0.85 µm taper resulted in $<$ 0.01 dB loss over a 20 µm length. For the bus waveguide, $\alpha = 0.125$ for the 1.9 µm $\rightarrow$ 0.85 µm resulted in similar losses over 16.5 µm length. The directional coupler consisted of 400 µm long coupling region with 850 nm gap, and s bends with a radius of 16 µm and bend angle of 25.0°. A single round trip consisted of the coupler region and 14.9 mm of 2.6 µm wide waveguide.

For consistent simulations while varying device parameters (bend radius for example) we implemented a number of scripts in Ipkiss and also Lumerical FDTD (based on scripts available with Ref [290]). The scripts would import the GDS layout as created in Ipkiss, create the appropriate cross section with material dispersion for core and cladding and define the simulation region. A simulation would propagate power in a specified waveguide mode and record the relative transmitted and backreflected power in the desired (typically first 10) waveguide modes. The simulated powers were monitored in a region from 1525 nm to 1575 nm, when desired the simulated field profile at 1550 nm was also recorded for reference. The scripts used to perform these calculations are available from the author.

6.4 Discussion

To provide further details on how the $As_2S_3 - Si$ hybrid circuit results compared with previous demonstrations of SBS in integrated waveguides, we prepared a comparison summary in Table 6.2. Initial silicon devices focused on achieving the highest gain coefficients possible, using highly sub wavelength structures which harnessed radiation pressure [103, 105, 493]. Issues arising from high scattering

Table 6.2: Comparison of SBS performance in different integrated devices

Device	Type	on-off Gain	net Gain	G_{SBS}	A_{eff}	FOM	NL Loss
Si/Si_3N_4 Membrane [493]	F	0.4	–	2500	0.1	3	Y
Si nanowire pillar [103]	F	4.4	–	3200	0.1	50	Y
Si nanowire suspended [105]	F	2.0	0.5	6500	0.1	12	Y
Si membrane [104]	F	6.9	5	1150	0.25	31	Y
Si membrane [496]	F_{SIMS}	3.5	2.3	470	0.35	10	Y
As_2S_3 Rib [92]	B	22	16.5	320	2.3	13	N
As_2S_3 Rib spiral [89]	B	52	40	500	1.5	40	N
This work	B	22.5	18.5	750	0.9	30	N

F, forward SBS; F_{SIMS}, forward stimulated intermodal scattering; B, backwards SBS; G_{SBS}, Brillouin gain coefficient; A_{eff}, effective mode area; NL, nonlinear loss; Y, Yes; N, No

losses, dimensional broadening and nonlinear losses, resulted in low net gain values of below 1 dB. More recent work has shifted to larger device geometries, resulting in interactions produced almost entirely through electrostriction. High sensitivity to local wafer conditions prevented the membrane structure from being folded, resulting in reduced compactness with straight waveguides up to 3 cm long. However, the reduced propagation losses enabled significantly higher net gain, up to 5 dB [104], than previous silicon demonstrations. In comparison it is clear that, being free from nonlinear losses, the As_2S_3 devices are capable of significantly higher on-off gain (greater than 50 dB) compared to full silicon devices. In this work we address the compactness limitations of previous As_2S_3 demonstrations, through the high density and tight bends of fully etched structures, while maintaining large net gain. Finally, to understand the relative efficiency of different devices, we introduce a simple figure of merit (FOM) $G_{SBS} \times L_{eff}$, which is from the exponential term in eq. (6.5). To achieve 20 dB of gain, sufficient for many microwave photonics applications [139], with 50 mW coupled pump power requires an FOM $\sim$ 100. None of the currently demonstrated devices have approached this regime, equivalent to half a km of SMF optical fiber, further improvements to the G_{SBS} and L_{eff} are expected to accomplish this goal in the near future.

One of the most desirable characteristics of Brillouin lasers is a significant linewidth narrowing of lasing Stokes lines. The key requirement to enter this regime is for the optical damping to be less than the acoustic damping or, in terms of linewidths, the cavity linewidth to be narrower than the natural linewidth of the acoustic mode [467]. If this regime is achieved then the Stokes spectrum will narrow and the fullwidth at half maximum will be given by

$$\Delta v_s = \frac{\Delta v_p}{(1 + \gamma_A/\Gamma_c)^2} \tag{6.10}$$

where γ_A represents the damping rate of the acoustic wave and Γ_c is the cavity loss rate. Thus to achieve a $100\times$ narrowing factor of the pump wave would require a cavity with $10\times$ narrower linewidth than the acoustic wave. For As_2S_3 waveguides with a Brillouin linewidth of 40 MHz an optical cavity linewidth of 4 MHz is required, corresponding to a Q factor in the range of 5×10^7. Improvements in our current fabrication processes have led to losses down to 0.2 dB/cm being measured in similar structures as those used in this work, leading to Q factors of a few million and linewidths less than 200 MHz. An alternative to improving the optical Q is to instead reduce the acoustic lifetime, thus broadening the natural linewidth. This is possible by replacing the silica cladding with a softer cladding with acoustic velocity lower than As_2S_3, such as the many polymers used for lithography resists like PMMA. Simulations have shown that orders of magnitude reduction can occur in appropriate waveguide geometries [432] and experimental measurements of polymer clad As_2Se_3 fibers saw an increase of $10\times$ the natural linewidth [502]. These approaches would allow for spectral purifiers and pure microwave sources based on SBS to be implemented in fully integrated planar devices, with thresholds of a few mW, for the first time.

In this chapter we have introduced a hybrid integration approach to generating large Brillouin gain in a silicon-based device. We embedded a compact 5.8 cm As_2S_3 spiral waveguide into a silicon circuit, enabling a record Brillouin gain of 22.5 dB (18.5 dB net gain) on a silicon-based chip. Fabrication of a compact ring resonator enabled the first demonstration of Brillouin lasing in a planar integrated circuit. Combining active photonic devices, such as modulators and detectors, with the work shown here will enable the creation of compact, high performance devices with capabilities beyond traditional RF systems.

Chapter 7

Nonlinear Circuits in Thick Silicon

In this chapter we explore the nonlinear properties of the 3 µm thick silicon platform provided by VTT in Finland. While not suitable for Brillouin scattering, we found that the linear properties of the platform enable long effective lengths, suitable for efficient Kerr four wave mixing. The high nonlinear loss thresholds enabled the generation of strong idler waves, a critical requirement for applications such as instantaneous frequency measurement.

This chapter has sections based on the following publications:

7.2 **B. Morrison**, Y. Zhang, M. Pagani, B. J. Eggleton, D. Marpaung, ”Four-wave mixing and nonlinear losses in thick silicon waveguides”, Optics Letters **41**, 2418 (2016)

7.1 Thick Silicon Waveguides

If you were to look at the vast majority of silicon photonics publications, and form factors available from MPW foundries, you would see that the typical device geometry consists of a 100 nm to 300 nm thick waveguide. These sub micron structures only moved into focus in the literature in the mid-2000s due to improvements in fabrication techniques enabling low losses in these geometries. Before this was the case, the standard geometry for silicon photonics was a multimicron thick rib waveguide, as outlined in the following informative review articles and references therein [503–506]. While the focus of the literature has shifted to sub micron waveguides, primarily due to a focus on compact bends, some interest still exists in waveguides of these large geometries. For example, it was shown quite recently that high confinement waveguides with multi micron geometries are a suitable platform in the 2 µm to 4 µm mid infrared region, due to the reduced SiO_2 absorption, even with a SiO_2 substrate [507]. In the following we will briefly provide details on the silicon photonics devices used by Kotura, and the MPW thick silicon platform provided by VTT in Finland.

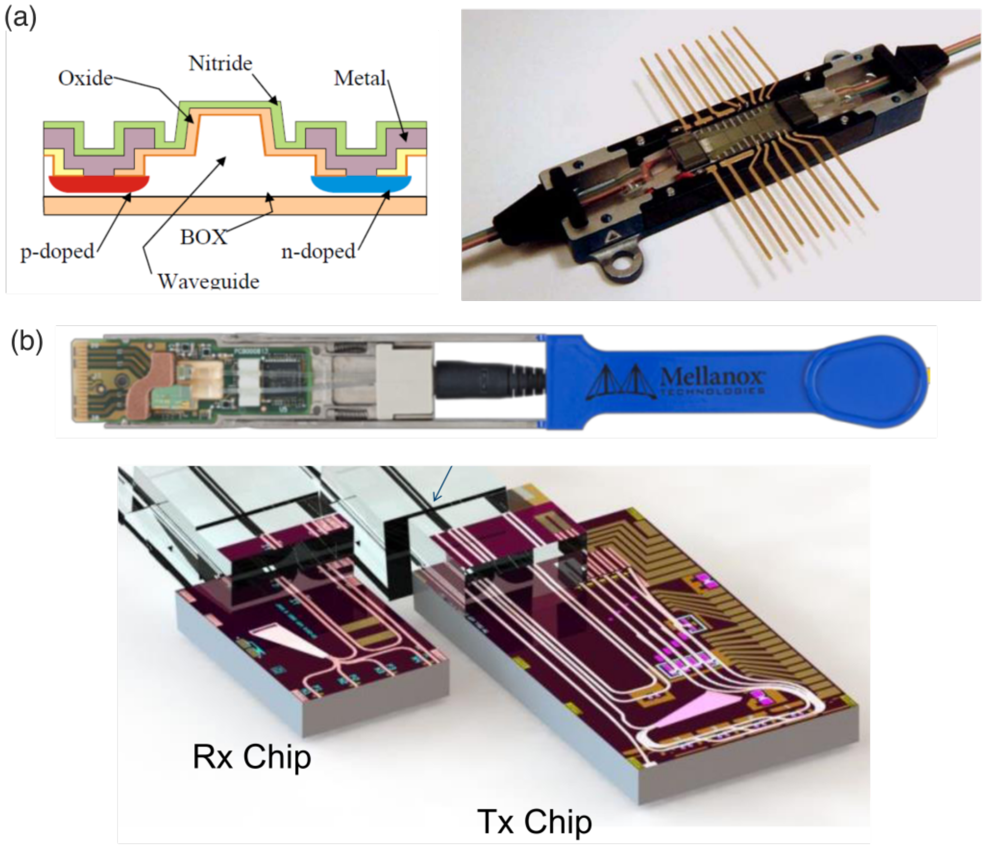

Figure 7.1: (a) Cross section and image of VOA chip (b) Images of packaged transceiver and the emitter and receiver chips. Notice the clear Echelle gratings. [506, 508, 509]

Kotura One of the first commercial silicon photonics products was a tunable variable optical attenuator (VOA) sold by Kotura in 2004 [506, 508], as shown in fig. 7.1a. This device utilised carrier injection to attenuate signals at MHz speeds, with an 8 fiber packaged device standard, for the purpose of channel equalisation in the telecommunications market. The early history leading to the development of this VOA device can be found in [510]. Over the following years Kotura, which was acquired by Mellanox in 2013, added a number of passive and high speed active components to their 3 µm platform; Si-Ge electro absorption modulators, Ge Photodetectors, Echelle gratings and flip chip lasers [511–513]. These combined developments, and the experience of shipping hundreds of thousands of the VOA devices, have enabled Mellanox to release 100 Gb/s transceivers, with wavelength division multiplexing and multi fiber devices available. The choice of a 3 µm waveguide platform was a key enabler for these products, and in presentations researchers stress the robustness of their devices and the fact that no hermetic seals are required [509], unlike standard solutions. From this, it is clear that submicron geometries are not required to achieve performance in critical industry environments, images of these transceiver components are shown in fig. 7.1b.

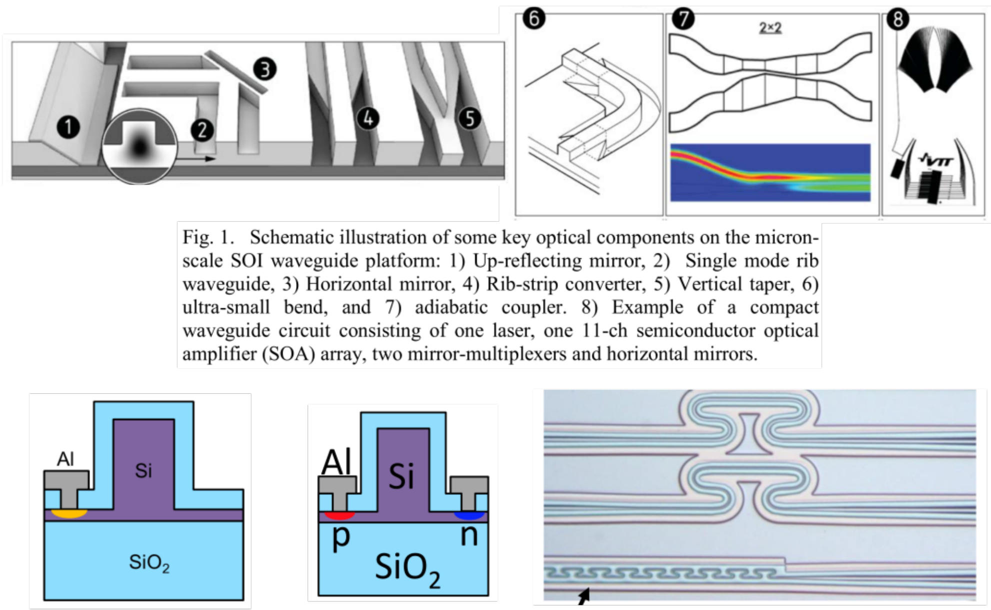

Figure 7.2: Top: Components from VTT's MPW platform. Bottom Left: Cross section of active waveguides for thermo-optic and electro-optic tuning. Bottom Right: Microscope images of bent waveguides, including 1 µm bend radii

VTT VTT have provided MPW services for 3 µm thick Si waveguides since the start of 2014 [339], based upon more than a decade of research into thick silicon devices [514, 515]. Originally this platform was planned to act as an interposer, to assist with packaging and coupling to typical sub micron SOI chips available through EpixFab. This changed with the realisation that the heavily multimode devices could achieve bend radii in the 10s of µm range, sufficient for high density photonic integration [206]. It was shown that devices based on the 3 µm thick platform were indeed capable of very dense integration, with up to a 1.5 m long spirals in a few mm^2 area [340]. The current platform available from VTT (as of 2017) provides some active components, with metallisation for heaters and doping available. There is ongoing work developing high speed germanium integration, in the style of Kotura, and flip chip bonding with III-V devices has also been demonstrated [516]. Images of the components and geometries from the VTT platform are shown in fig. 7.2.

From the work of Mellanox and VTT it is quite evident that the linear device performance of these thick Si waveguides is very high. In the following section we investigate the *nonlinear* performance, characterising FWM and nonlinear losses in these waveguides. We thank Timo Aalto from VTT for sending us the samples upon which these experiments were performed. These devices were used in experiments in our group as the nonlinear building block in an instantaneous microwave frequency measurement system [517].

7.2 Four-Wave Mixing and Nonlinear Losses in Thick Silicon Waveguides

The choice of material platforms is crucial for the diverse range of applications found in integrated photonics ranging from sensing [518], telecommunications [430], radio frequency signal processing [492], nonlinear optics [228], and many others [1]. While to date there is no consensus on the ideal platform for these various applications, certain device characteristics are highly desired including low insertion loss, compact circuits and compatibility with mass produced fabrication techniques such as complementary metal-oxide semiconductor (CMOS) processes. Silicon on insulator (SOI) [506] is becoming the key technology which has found the widest spread of applications to date. Silicon photonics has a deep library of devices available through multiple foundries focused around single-mode nanowire geometries of typically 450×220nm [331]. Such devices have been exploited for the applications above, nevertheless there are still drawbacks related to the small size in particular high linear losses resulting from scattering due to surface roughness and nonlinear losses from multiphoton absorption at 1550nm. To overcome this issue recent activities have been focused on alternative platforms which are free from nonlinear losses but with properties which still allow low linear losses and compact bending radii, such as silicon nitride and hydex [253]. Alternatively, by moving to larger silicon geometries linear losses are reduced and lower intensities can mitigate nonlinear losses.

A recent development that specific bend designs can enable micron scale bend radii in heavily multimoded silicon strip waveguides [206], has enabled the creation of compact low loss circuits in large silicon waveguides [340], breaking the previous paradigm in μm thick silicon of mm bend radii rib waveguides [520]. While the linear properties of these waveguides have been explored [339, 340], nonlinearity and in particular nonlinear losses are yet to be investigated in detail. In this work we report on four-wave mixing (FWM) and nonlinear losses in 3μm thick waveguides fabricated by VTT Finland, available through the epixfab multiwafer shuttle service.

7.2.1 Devices and Linear Characterisation

The waveguide geometries investigated consisted of 3μm thick silicon waveguides with half etched ribs (2.4μm width) or fully etched strips (1.875μm width), with a 0.25μm thick silica cladding as shown in Fig. 7.3. The ability to locally change the etch depth enables devices based on rib and strip waveguides in the same circuit, with low loss coupling < 0.01 dB between the fundamental modes in the different geometries. Due to the high confinement, scattering losses are very low with typical propagation losses of $\sim$0.15 dB/cm for rib waveguides. Comparable losses are possible in nanowire geometries with the use of advanced lithography techniques, such as immersion lithography, not yet widely available [177]. At the

[1] Work in this section has been published in Optics Letters: B. Morrison et al., "Four-wave mixing and nonlinear losses in thick silicon waveguides", Opt. Lett. **41**, 2418 (2016)

facets, single mode rib waveguides with anti reflection coatings enable low loss coupling of 0.5dB/facet with 3µm lensed fibers into the fundamental mode of the rib [339]. What separates this platform from earlier works with thick silicon rib waveguides [520] is the use of fully etched strip waveguides with bends having continuously varying curvature (Euler bends) to minimize higher order mode (HOM) coupling [206], which is the primary loss mechanism in these multimode geometries. The Euler bends consist of mirror symmetric sections with linearly increasing curvature which minimizes coherent coupling to HOM along the length of the bend, while maintaining mode overlap to straight waveguides at the interface, producing exceptionally low loss bends of < 0.01 dB/90° for 13µm bend radius in a 2µm wide waveguide. As well as enabling routing for dense circuits, these bends provide the ability to form compact spirals with lengths over 1m in mm^2 area [340]. Combining the long lengths with low propagation losses enable low loss delay lines and long effective lengths suitable for nonlinear interactions which are explored in this work.

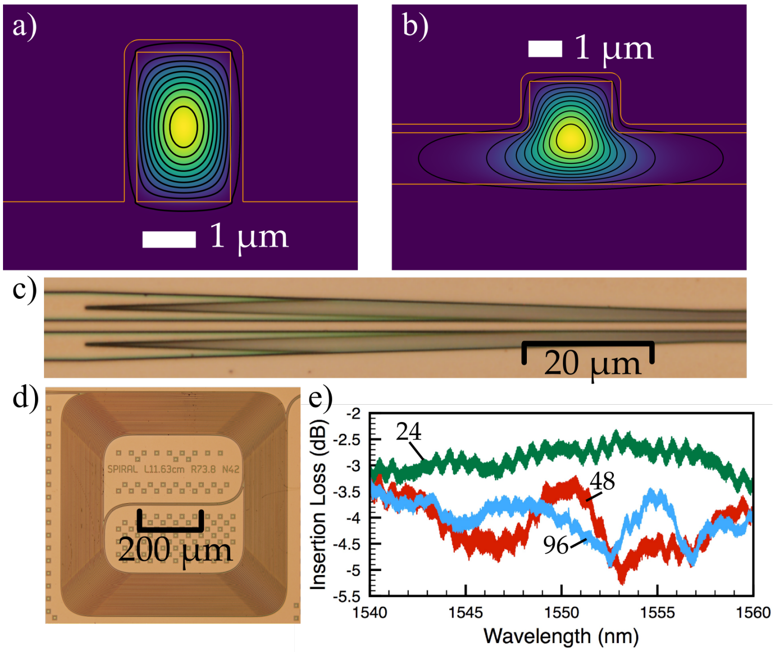

Figure 7.3: Fundamental mode profiles with 10% contour lines for strip (a) and rib (b) waveguides. Microscope images of of rib to strip taper (c) and 11.6cm spiral structure (d). (e) Transmission measurement of three waveguides with 24 (green) 48 (red) and 96 (blue) 180° bends.

To characterise the linear losses of the platform we measured transmission losses in multiple structures on a test chip, consisting of short waveguides (up to 1.3 cm long) with different numbers of tight bends and also performed reflectometry measurements on a 35cm waveguide which consisted of 3 compact spirals. These devices had coupling losses of ∼1.5dB/facet, with the 2µm lensed fibers used in the experiments. The fundamental mode of the rib waveguide is then tapered into the fundamental mode of a strip waveguide, allowing for tight bends and compact low loss routing, before finally converting back into a rib waveguide and coupling out of the chip. Any HOM coupling will result in loss at the output as the HOM are stripped out of the exit rib waveguide and taper. The first set of measurements consisted of transmission measurements of three waveguides with 24, 48 and 96, 180° bends with effective bend radii of 13µm. The swept source of an APEX Optical Spectrum Analyser (OSA) was coupled through the chip and the output power was measured in the range of 1540 to 1560nm with 1.5pm resolution. The transmitted power was maximised with a polarization controller for a fixed wavelength of 1550.05nm and a reference measurement was performed by bypassing the coupling setup with a short SMF fiber. The results, plotted in Fig. 7.3e, show that the waveguides with 48 and 96 bends have fluctuation of $\sim$1dB over the 20nm range and that the insertion loss at 1550.05nm was 2.9, 3.5 and 4 ± 0.1 dB respectively. This indicates that even with 96 bends coherent HOM coupling and other bend related losses can be minimal.

In the case of the 35cm spiral, Euler bends with an effective radius of 74µm are utilized in 3 square shaped spirals (one spiral shown in Fig. 7.3d), a total loss of 9 dB is measured through the spiral at a wavelength of 1550nm. Reflectometry measurements where performed using a Luna optical frequency domain reflectometer, enabling accurate measurements of device length and propagation loss. The roundtrip time of the waveguide was 8.5ns, corresponding to a device length of 35cm using group index determined by modal simulations. The propagation loss was estimated by determining the slope of the background in the region of the waveguide and is 0.17 dB/cm, in agreement with previous measurements [340]. These low losses demonstrate the suitability of the Euler bend design with heavily multimoded strip waveguides, allowing for new circuits with functionality not possible in previous implementations with rib waveguides requiring mm bend radii.

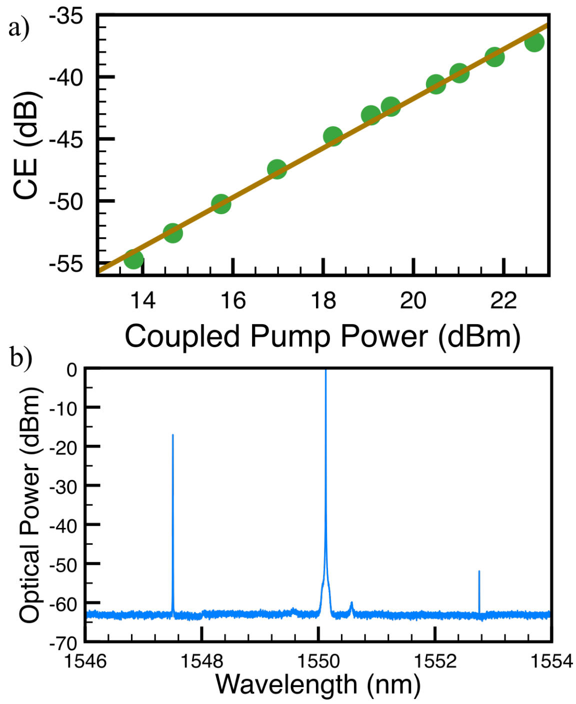

Figure 7.4: a) Conversion Efficiency in a 1.3cm waveguide with fit (solid line) b) High resolution OSA measurement of generated idler with 22dBm pump power.

7.2.2 FWM Experiments

We begin the investigation of the nonlinear properties of the platform with experiments to characterise the nonlinear coefficient γ, using four wave mixing.

The strength of the third order nonlinearity in a given device is represented by the nonlinear coefficient γ given by $\gamma = k n_2 / A_{\text{eff}}$ where k is the wavevector, n_2 is the nonlinear index and A_{eff} is the effective mode area. Degenerate FWM

Table 7.1: Comparison of some platforms for linear and nonlinear integrated optics

Platform	γ ($m^{-1}W^{-1}$)	α (dB cm^{-1})	Bend radii (µm)
Si nanowire [167]	550	2.5	5
This Work	5.5	0.17	75
Si_3N_4 [522]	1.2	0.5	20
Si_3N_4/SiO_2 [523]	0.3	0.06	1000
Hydex [524]	0.2	<0.06	50

occurs when a high power pump passes through a third order nonlinear medium with a signal wave, generating an idler. The conversion efficiency (CE) is defined as $P_{\mathrm{idler}}^{\mathrm{out}}/P_{\mathrm{signal}}^{\mathrm{in}}$, relating the output idler power to the input signal power. If the pump is much stronger than the signal, assuming no nonlinear losses and that the effects of dispersion can be neglected, the CE is related to γ by the expression $\mathrm{CE} = \exp\left[-\alpha L\right]\left(\gamma P_{\mathrm{in}} L_{\mathrm{eff}}\right)^2$ [166], where α is the linear loss coefficient, L is the length, P_{in} is the coupled pump power and L_{eff} is the effective length. This relationship allows the γ to be experimentally determined by measuring the CE for various coupled pump powers. A high power pump at 1550.18 nm and a tunable signal laser with 7.9dBm power at 1547nm were coupled into the 1.3cm waveguide measured earlier with 2µm lensed fibers. The generated idler wave was measured on a high resolution OSA (Finisar Waveanalyzer) with bandwidth resolution of 1.5pm allowing for accurate calculations of the absolute idler power due to the reduced effect of noise from the optical amplifier in the measurement bandwidth. To prevent damaging the OSA a variable optical attenuator (VOA) and tunable filter with 0.5nm bandwidth is used to remove the pump and signal such that only the generated idler is measured. As shown in Fig. 7.4a, a maximum CE of -37dB is measured at a coupled power of almost 200mW. Figure 7.4b shows a measurement of the optical spectrum bypassing the bandpass filter for the same pump power. Numerically fitting the experimental data gives a γ of $6.5 \pm 1.0\ \mathrm{m^{-1}W^{-1}}$ which, from the equation above, corresponds to an n_2 of $4.5 \pm 1 \times 10^{-18}\ \mathrm{m^2W^{-1}}$, which is in the expected range for silicon [228]. The changing orientation through the 96 bends will result in a varying n_2 through the structure, this is expected to only reduce the γ by $\sim$5% compared to a straight waveguide [521]. The γ value is expectedly lower than for nanowires due to the increased A_{eff} (2.75 µm^2) of these waveguides, yet is still in the range of other platforms while also maintaining very low propagation and coupling losses along with compact bends, as summarised in Table 7.1.

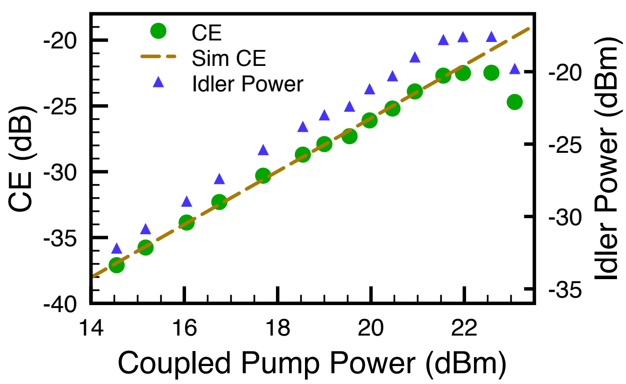

Figure 7.5: Conversion Efficiency of 35cm waveguide for various coupled pump powers (left) and the optical power of the generated idler (right)

High idler powers are key for a number of applications utilising FWM, such as multicasting [525] and instantaneous microwave frequency measurement [517]. Generating high absolute idler powers in silicon nanowires is difficult due to linear losses from scattering at the silicon interface [209] and nonlinear losses from two photon absorption (TPA) and free carrier absorption (FCA) from TPA generated carriers [526]. One solution to this issue is the use of materials with reduced nonlinear losses [253], unfortunately this is often accompanied with reduced nonlinearity. Low propagation losses can compensate the reduced nonlinearity, allowing for long effective lengths for nonlinear interaction even in devices with reduced γ compared to silicon nanowires. This approach was adopted in recent work using hybrid Si_3N_4/SiO_2 devices [523], where waveguides with a length of 1m and a γ of 0.3 $m^{-1}W^{-1}$ generated idler powers of -20dBm for 1W of coupled pump power. Here we explore the possibility of high idler generation using the 35cm spiral waveguide.

We perform CE measurements with the spiral waveguide with the same setup as for the short waveguides. The signal laser was shifted to 1549.5nm, closer to the pump, to limit the effects of dispersion during propagation and the VOA was set at a fixed attenuation of 20dB for the measurements. The resulting output CEs were almost 20dB higher than in the case of the 1.3cm waveguide, with a maximum CE of -23dB and a maximum idler power of -18dBm measured, as seen in Fig. 7.5. For coupled pump powers less than 140mW, the CE increases at constant slope of 2, as expected from the fact that CE $\propto P_{\text{in}}^2$. Above 140mW the increased loss due to TPA and FCA attenuates the idler and reduces the CE. Determining the γ from numerical fits on these measurements yields a value of 5.5 $m^{-1}W^{-1}$, which is a slight reduction from the short waveguides. Considering that there are >500 bends in the structure, the impact of mode coupling to the FWM dynamics [527] is low, implying that the Euler bend design is compatible with high power nonlinear optics. When combined with the fact that the spiral structures fit within an area of $\sim$mm^2, compared to $\sim$cm^2 for low loss low index contrast waveguides [523], this platform seems suitable for applications which may require low loss delay lines, nonlinearity and compact circuits, such as microwave photonics [492] or telecommunications [528].

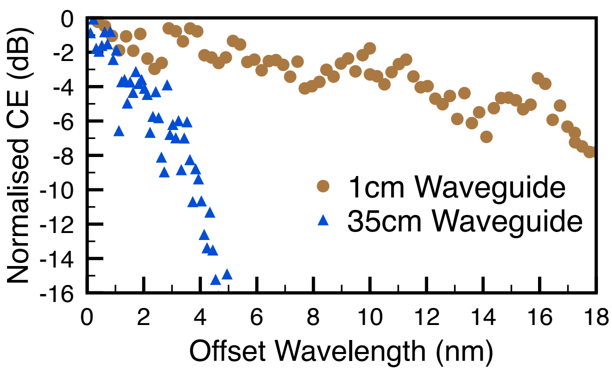

Figure 7.6: Normalised CE rollof for increasing wavelength away from pump for 1cm and 35cm waveguide

Silicon exhibits strong normal dispersion in the telecommunications band at 1550nm. While it is possible to tailor the modal dispersion in sub micron waveguides, the high confinement of the thick silicon waveguides prevents sizeable engineering of the total dispersion, resulting in normal group velocity dispersion [529]. To characterise the effect of the dispersion on the FWM bandwidth we maintain a fixed pump at 1550.18nm while stepping the signal laser from 1530 to 1550nm in 0.25nm steps, monitoring the output on the OSA. The results for the measurements of the two waveguides are shown in Fig. 7.6 and are plotted for the relative drop in CE from the maximum value. For the 1cm waveguide the CE falls continuously by 7 dB over the 20nm measurement range. The CE of the 35cm sample falls much faster, by 16dB within 5nm. Mode simulations using a commercial finite element solver (COMSOL Multiphysics 5.1) determine a group velocity dispersion of 0.88 ps^2m^{-1} at 1550nm, in line with calculated values determined from the experimental measurements. This bandwidth is small compared to dispersion engineered nanowires, however it is more than sufficient for applications in RF photonics as 1nm corresponds to 125 GHz of radiofrequency bandwidth.

The optimal waveguide length for idler generation was calculated based on simulations using the generalized nonlinear Schrödinger equation [526]. This involved monitoring the generated CE through the structure while incorporating the effects of linear loss, TPA, FCA and dispersion in the simulation to determine the most suitable length. It was found that for a device lengths of $\sim$30cm an improvement of 2dB higher CE than in the experiment could be obtained. The fact that such long lengths are needed to achieve high idler generation opens up the possibility of length engineering for both linear and nonlinear signal processing. The nonlinear cross talk due to FWM in short nanowires has been identified as a possible issue for linear devices since early works [156]. For example, a 1.5cm long nanowire with the typical single mode geometry of 450 $\times$ 220nm, which has a $\gamma \sim 550\ m^{-1}W^{-1}$, would generate a CE of -20dB for only 20mW coupled pump power. In contrast, with the requirement of long lengths for FWM in the thick silicon it becomes possible to separate the nonlinear generation in building blocks of compact spirals while linear devices exist without nonlinear degradation in the same circuit.

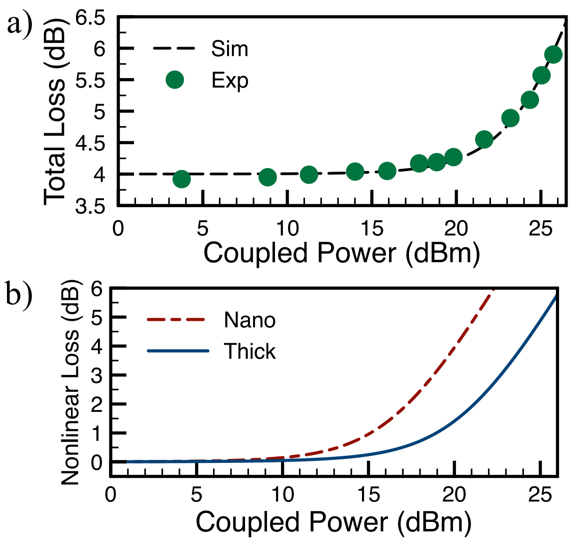

Figure 7.7: a) Total loss in 1.3cm thick silicon waveguide with simulated result (dashed curve) b) Simulated nonlinear loss comparison of Thick Si 35cm spiral waveguide (blue, solid, ”Thick”) and a 1.5cm silicon nanowire (red, dashed, ”Nano”)

7.2.3 Nonlinear loss characterisation

Finally the effects of nonlinear loss were investigated by performing a power dependent transmission measurement through the 1.3cm waveguide. The transmitted pump power at 1550nm was monitored for pump powers up to 500mW on the front of the waveguide. The loss begins to increase at 100mW coupled power, as shown in Fig. 7.7a. If a steady state carrier distribution is assumed, which is valid due to the continuous wave pump, the carrier lifetime can be determined through numerical fitting simple models to the transmitted power [530]. The best fit for the experimental data yields a carrier lifetime of 40ns, around 10 times higher than nanowires using current photolithography techniques. This value is in the typical range for larger waveguides which suffer from slower carrier diffusion times than sub micron structures [531]. Knowing these numbers allows for a comparison between nanowires and the thick silicon spiral waveguide. We performed simulations for a 1.5cm long nanowire with A_{eff} of 0.1μm^2 and the 35cm spiral waveguide (A_{eff} 2.75μm^2). Comparing the simulated structures we find that the difference in saturation power is ∼4dB, that is that the thick silicon structure saturates out an output power of 100mW compared to 40mW for the nanowire, as shown in Fig. 7.7b. For systems which are dependent on the square of the transmitted power, such as the CE in FWM or link gain in microwave photonic links [492], this results in an 8dB difference which is almost an order of magnitude. This higher threshold, along with the long effective length, is what allows for modest CE's to be obtained in the low γ structures and CE's which can be comparable to nanowires when linear and nonlinear losses are appropriately incorporated as discussed in [532]. As such the thick silicon platform is most suitable for applications where the combination of high output optical powers and Kerr nonlinearity is required, such as instantaneous frequency measurement [517].

7.3 SBS in Thick Silicon Waveguides

One of the requirements for strong Brillouin interactions in waveguides is a large opto-acoustic overlap, which implies a guidance of both the optical and acoustic wave in the same region. Silicon suffers from acoustic leakage into the SiO_2 substrate, however the work of Poulton [432] indicates that in sufficiently large waveguides the acoustic mode lifetime will be dominated by material properties, rather than acoustic losses from leakage.. Additionally, the long effective lengths and higher power handling, due to the large A_{eff}, might have meant that measurable Brillouin scattering could occur. This chip was used for the work in section 7.2 and the instantaneous frequency measurement experiments [517]. While FWM clearly worked reasonably well, repeated experiments were unable to show any signatures of Brillouin scattering, in the forward or backward directions.

The following outlines the possible reasons why we did not observe Brillouin scattering. It is possible that the acoustic leakage was quite high, suppressing the gain. However, let us assume that is not the case, and go through a rough calculation to estimate how much gain we should expect. These waveguides are rather large, and embedded in SiO_2, so we can assume that effects due to moving boundaries are negligible and that electrostriction is the sole contribution to the gain coefficient. We can then recall the standard equation for the peak gain factor, eq. (4.30)

$$g_0 = \frac{2\pi n^7 p_{12}^2}{c\lambda^2 \rho_0 \Delta v_B v_{ac}}$$

If we utilise typical parameters for silicon [103], with $n = 3.44$, $p_{12} = 0.017$, $v_{ac} = 8400\,\mathrm{m\,s^{-1}}$ and assume the linewidth is 50 MHz (an estimate from figure 5 of [432]), then we have that

$$g_0 = 1.5 \times 10^{-11}\,\mathrm{m\,W^{-1}} \qquad G_B = \frac{g_0}{A_{\mathrm{eff}}} \approx 5\,\mathrm{m^{-1}W^{-1}} \tag{7.1}$$

The estimated peak gain coefficient is comparable to that of silica fiber, but the relatively small effective area results in Brillouin gain coefficient of around $5\,\mathrm{m^{-1}\,W^{-1}}$. This number is significantly lower than the typical As_2S_3 devices, but is only around half that of the TeO_2 chip which was successfully measured in chapter 5.

Considering the estimated gain coefficient of $5\,\mathrm{m^{-1}\,W^{-1}}$, we can determine the expected amplification from the spiral waveguide. We have a propagation loss of 0.17 dB /cm, and physical length of 35 cm, which leads to an L_{eff} of 19 cm. With an upper limit of 100 mW coupled power, the on-off gain is 0.4 dB, about half a decibel. This is low, but well within our measurement systems sensitivity, which means that the gain me be lower due to unconsidered effects.

A possible issue reducing the gain, on top of the leakage already considered, could be the additional *stress* induced in the fabrication process. Residual stresses are known to affect the acoustic properties and alter SBS response in waveguides [533]. Silica cladding is also known to induce intrinsic stresses within a silicon waveguide, and can used to control waveguide birefringence [534, 535]. It is possible that a combination of residual stress and a excess leakage inhibited the Brillouin gain. Ultimately, the low photoelastic coefficient, acoustic leakage and nonlinear losses, prevent thick silicon from being a highly desirable material for Brillouin scattering in the telecommunications band. In under etched submicron structures, the significantly reduced A_{eff} can be sufficient to achieve reasonable Brillouin amplification with electrostriction [104, 110].

To conclude, in this chapter wave explored the nonlinear properties of highly multimode thick silicon waveguides, available through a MPW program from VTT. We have found that reasonably high output idler powers can be generated, due to the low coupling and propagation losses in the device. This platform is thus placed the platform between highly nonlinear devices such as SOI nanowires and more linear platforms like Hydex, while maintaining low propagation and coupling losses. Considering the effectiveness of thick silicon waveguides in commercial devices, which are actively developed by Mellanox for communications applications, these results may enable extensions of current applications to include Kerr based nonlinear functions, such as all-optical frequency multicasting [525].

Part III

Microwave Notch Filters using Photonic Devices

Chapter 8

Microwave Notch Filters Using Brillouin Scattering

Microwave photonic signal processing, and in particular the use of stimulated Brillouin scattering (SBS) based optical processors, has seen a renewed focus in recent years, due to its unique capabilities beyond those of traditional electronic devices. In this chapter, we discuss microwave photonic signal processing, and in particular microwave photonic notch filters. We introduce a technique which enables the capability to achieve high suppression microwave filters, independently of the depth of the initial optical response. We apply this technique in integrated devices utilising Brillouin scattering, and explore the benefits in different systems.

This chapter has sections based on the following publications:

8.2 **B. Morrison**, D. Marpaung, R. Pant, E. Li, D-Y. Choi, S. Madden, B. Luther-Davies, B. J. Eggleton, "Tunable microwave photonic notch filter using on-chip stimulated Brillouin scattering", Optics Communications **313**, 85-89 (2014)

8.3 D. Marpaung, **B. Morrison**, R. Pant, B. J. Eggleton, "Frequency agile microwave photonic notch filter with anomalously high stopband rejection", Optics Letters **38**, 4300 (2013)

8.4 D. Marpaung, **B. Morrison**, M. Pagani, R. Pant, D-Y. Choi, B. Luther-Davies, S. Madden, B. J. Eggleton "Low-power, chip-based stimulated Brillouin scattering microwave photonic filter with ultrahigh selectivity", Optica **2**, 76 (2015)

8.1 Background: Microwave Photonic Signal Processing

Microwave photonics encompasses the use of photonic techniques and devices in microwave systems. As such, microwave photonics is very a broad field comprising of different implementations, requirements and applications. This thesis focuses on microwave photonic notch filters, a type of microwave photonic signal processor [536, 537]. To build an understanding we will give a description of photonic links and optical modulators. For general information on the history, applications, and development of microwave photonics please refer to the following review papers [492, 538–543] and theses: Mattia Pagani, David Marpaung, Javier Fandino.

8.1.1 A photonic link

A microwave photonic link is the simplest form of a microwave photonic system. Seemingly straightforward, the system is highly suitable for studying performance and understanding the balancing of various tradeoffs in basic photonic processing implementations. An overview of photonic link properties can be found in [544], with an extremely detailed investigation found in the thesis of Marpaung [545].

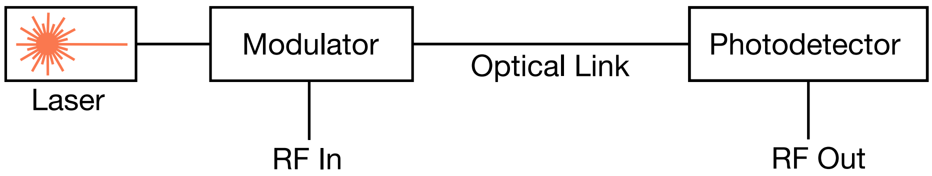

Figure 8.1: A typical microwave photonic link

As represented in fig. 8.1, a photonic link consists of the following components

(A) A laser, the carrier for the microwave signal

(B) An electro-optic modulator for bringing the microwave signal into the optical domain

(C) A transmission system and/or processing system

(D) A detection system for retrieving the microwave signal

These individual elements can vary considerably in complexity and can also be combined in some instances, such as in the case of directly modulated lasers [544]. In this thesis we utilise a simple, and typical, photonic link architecture consisting of an externally modulated laser, with measurement on a single high-speed photodiode. In the following section, we will work through a basic example of optical modulation and detection in order to understand how this effects the properties of a photonic link.

Optical Modulation

Consider the electric field of a single frequency optical wave,

$$E(t) = \mathbf{x}E_0 \sin(\omega t + \phi)$$

Optical modulation is the perturbation an electric field, typically referred to as the carrier, by some external time varying signal. This can be performed on the amplitude, frequency, phase or polarisation of the carrier wave, i.e

$$E(t) = \mathbf{x}(t)E_0(t)\sin(\omega(t)t + \phi(t))$$

The modulation in these bases can be induced by a number of different physical effects. However the most common is the use of physical mechanisms which alter the real or imaginary part, i.e absorption, of the refractive index of the propagation medium. In waveguide systems the most frequently used of these is the Pockel's effect, also known as the electro-optic effect, to alter the phase of the light through the $\chi^{(2)}$ nonlinearity, as discussed in section 3.1.3. By placing this phase modulation component within an optical circuit, more complex forms of modulation can be created.

Phase Modulation Let us consider the case of an initial optical wave at some carrier frequency ω_c passing through a phase modulator. We will have that

$$E_{\text{pm}} = E_0 e^{i\omega_c t} e^{i\theta(t)}$$

where E_0 is the real part of the electric field amplitude and $\theta(t)$ is the phase change induced due to the phase modulator, which can be time varying. We are interested in a sinusoidal varying phase change, with a frequency ω_{RF}, this will be mapped to the phase such that

$$E_{\text{pm}} = E_0 e^{i\omega_c t} e^{im\sin(\omega_{\text{RF}})t}$$

To simplify this further, we invoke the well known Jacobi-Anger expansion

$$e^{iz\sin(\theta)} = \sum_{n=-\infty}^{\infty} J_n(z)e^{in\theta}$$
$$e^{iz\cos(\theta)} = \sum_{n=-\infty}^{\infty} i^n J_n(z)e^{in\theta}$$

and note that for Bessels functions of the first kind $J_{-n}(z) = (-1)^n J_n(z)$, and that $e^{i\pi} = -1$. Using these relations we now expand to first order $(n = 0, \pm 1)$ and simplify such that

$$E_{\text{pm}} = E_0 e^{i\omega_c t}\left(J_0(m) + J_1(m)e^{i\omega_{\text{RF}}t} + J_1(m)e^{-i\omega_{\text{RF}}t}e^{i\pi}\right) \tag{8.1}$$

The modulation depth, m, is typically given in terms of the applied voltage, V_{RF}, required to reach π phase shift in the physical device,

$$m = \frac{\pi V_{\text{RF}}}{V_{\pi,\text{RF}}}$$

where $V_{\pi,\text{RF}}$ depends upon the physical construction of the modulator as well as material properties. From eq. (8.1) it is clear that after under going sinusoidal phase modulation, for small modulation depths, the electric field is now composed of three components in the frequency domain: the original optical carrier and two new tones spaced above and below the carrier by the modulation frequency ω_{RF}. The amplitude is dependant on the modulation strength m and the sidebands have a π phase difference.

Intensity Modulation Intensity modulation is the next simplest form of modulation after phase modulation. A basic intensity modulator is also quite simple to implement, placing a phase modulator within an optical interferometer will convert the phase modulation to an intensity modulation in the optical domain. This leads to the canonical Mach-Zhender interferometer configuration, as shown in fig. 8.2. As well as the radio-frequency (RF) bias, a DC bias is applied to the modulator, enabling modulation operation at a number of points, such as suppressed carrier or at the quadrature point. In the following we show the transfer function of a Mach-Zhender modulator (MZM), designed to operate in a push-pull configuration.

We start with an electric field, with amplitude E_0, which is split by a 50:50 power splitter into two equal length arms of the interferometer. In each arm the transmitted field will undergo phase modulation, such that in the upper arm we have

$$E_{\text{upper}} = \frac{E_0}{\sqrt{2}} e^{i\omega_c t} e^{im\sin(\omega_{\text{RF}})t} e^{i\theta_{\text{B}}}$$

which is similar to the previously discussed phase modulation except we now include an extra phase term $e^{i\theta_{\text{B}}}$, which is constant in time. In the lower arm the voltage is applied such that a negative phase is induced,

$$E_{\text{lower}} = \frac{E_0}{\sqrt{2}} e^{i\omega_c t} e^{-im\sin(\omega_{\text{RF}})t} e^{-i\theta_{\text{B}}}$$

At the output of the interferometer these components interfere depending on their phase *difference* such that

$$\begin{aligned}
E_{\text{im}} &= \frac{1}{\sqrt{2}} \left(E_{\text{upper}} + E_{\text{lower}}\right) \\
E_{\text{im}} &= \frac{E_c}{2} e^{i\omega_c t} \left(e^{im\sin(\omega_{\text{RF}})t} e^{i\theta_{\text{B}}} + e^{-im\sin(\omega_{\text{RF}})t} e^{-i\theta_{\text{B}}}\right) \\
E_{\text{im}} &= \frac{E_c}{2} \sum_{n=-\infty}^{\infty} J_n(m) e^{i\omega_c t} \left(e^{in\omega_{\text{RF}}t} e^{i\theta_{\text{B}}} + e^{-in\omega_{\text{RF}}t} e^{-i\theta_{\text{B}}}\right)
\end{aligned}$$

where we have again invoked the Jacobi-Anger relations and the fact that $-\sin(\theta) = \sin(-\theta)$. If we now take these terms to first order, as for the phase modulation case, we have

$$\begin{aligned}
E_{\text{im}} = \frac{E_c}{2} e^{i\omega_c t} \Big[& J_0(m)(e^{i\theta_{\text{B}}} + e^{-i\theta_{\text{B}}}) + J_1(m)(e^{i\omega_{\text{RF}}t} e^{i\theta_{\text{B}}} + e^{-i\omega_{\text{RF}}t} e^{-i\theta_{\text{B}}}) \\
& + J_{-1}(m)(e^{-i\omega_{\text{RF}}t} e^{i\theta_{\text{B}}} + e^{i\omega_{\text{RF}}t} e^{-i\theta_{\text{B}}}) \Big] \\
= \frac{E_c}{2} e^{i\omega_c t} \Big[& J_0(m)(e^{i\theta_{\text{B}}} + e^{-i\theta_{\text{B}}}) + J_1(m) e^{i\omega_{\text{RF}}t}(e^{i\theta_{\text{B}}} - e^{-i\theta_{\text{B}}}) \\
& - J_1(m) e^{-i\omega_{\text{RF}}t}(e^{i\theta_{\text{B}}} - e^{-i\theta_{\text{B}}}) \Big] \\
= \frac{E_c}{2} e^{i\omega_c t} \Big[& 2J_0(m)\cos\theta_{\text{B}} + 2J_1(m)\sin\theta_{\text{B}} \left(ie^{i\omega_{\text{RF}}t} - ie^{-i\omega_{\text{RF}}t}\right) \Big]
\end{aligned}$$

where we have used the standard hyperbolic identities. Factorising the above finally yields

$$E_{\text{im}} = E_c e^{i\omega_c t} \left[J_0(m)\cos\theta_{\text{B}} + J_1(m)\sin\theta_{\text{B}} \left(e^{i\omega_{\text{RF}}t} e^{i\pi/2} + e^{-i\omega_{\text{RF}}t} e^{-i\pi/2}\right) \right] \tag{8.2}$$

Thus intensity modulation through a Mach-Zhender interferometer has a few key differences to pure phase modulation. The first order sidebands have phase differences of $\pm\pi/2$ with the carrier, and the amplitude of the modulation sidebands and carrier can be controlled with the DC bias which governs the strength of θ_B. Intensity modulators are typically operated in either the *quadrature* bias point $\left(\cos\theta_B = \sin\theta_B = 1/\sqrt{2}\right)$ or the *null* point, represented in fig. 8.2c, where the carrier is suppressed $(\cos\theta_B = 0)$.

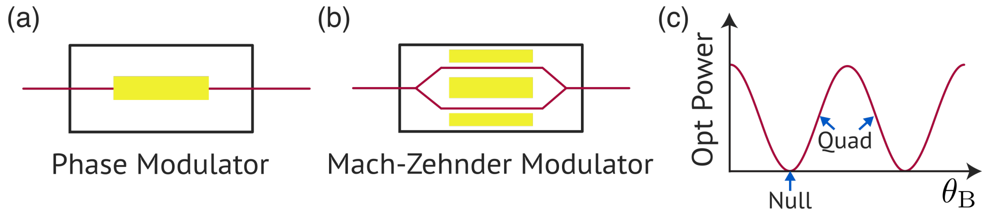

Figure 8.2: (a) Schematic of a phase modulator (b) Schematic of Mach-Zehnder modulator (c) MZM carrier transmission with changing bias phase

Detection

The microwave signal is retrieved after propagating through a link via the use of a high speed photodetector. Let us look at a simple example. Suppose that we have an electrical field consisting of two frequency components:

$$E = a_c e^{i\omega_c t} + a_s e^{i(\omega_c+\Delta\omega)t}$$

where a_c and a_s are the *complex* amplitudes of the two fields. The detected photo current is proportional to the optical power, $I_{RF} = r_{PD}P = r_{PD}EE^*$, such that

$$\begin{aligned} P &= \left(a_c e^{i\omega_c t} + a_s e^{i(\omega_c+\Delta\omega)t}\right)\left(a_c^* e^{-i\omega_c t} + a_s^* e^{-i(\omega_c+\Delta\omega)t}\right) \\ &= |a_c|^2 + |a_s|^2 + a_c a_s^* e^{-i\Delta\omega t} + a_s a_c^* e^{i\Delta\omega t} \\ &= |a_c|^2 + |a_s|^2 + 2\,\mathrm{Re}\left(a_c^* a_s e^{i\Delta\omega t}\right) \end{aligned}$$

If we split the complex amplitudes into magnitude and phase components, i.e $a_c = E_c e^{i\theta_c}$ and $a_s = E_s e^{i\theta_s}$, and focus only on the terms involving $\Delta\omega$, then the above will reduce to

$$\begin{aligned} P(\Delta\omega) &= 2\,\mathrm{Re}\left(E_c E_s e^{i(\Delta\omega t+\theta_s-\theta_c)}\right) \\ &= 2E_c E_s \cos(\Delta\omega t + \Delta\theta) \end{aligned}$$

where $\Delta\theta = \theta_s - \theta_c$ is the phase difference between the two fields. Thus, if we have two fields separated by a frequency $\Delta\omega$, their detection upon a photodiode will generate DC terms for each field and a time varying signal $\cos(\Delta\omega t)$, which is proportional to their amplitudes. This time varying signal is generally referred to as the *beat-note* of the two waves, and can be a method for the generation of high frequency microwaves.

How does the generation of the beat-note change if we have three fields, such as in the cases of intensity modulation and phase modulation previously discussed? Starting again with the field, where we represent the carrier and waves at $\omega_c \pm \omega_{RF}$

as the following

$$E = a_c e^{i\omega_c t} + a_+ e^{i(\omega_c+\omega_{RF})t} + a_- e^{i(\omega_c-\omega_{RF})t}$$

The optical power in this case will be given by

$$\begin{aligned}
P = & \left(a_c e^{i\omega_c t} + a_+ e^{i(\omega_c+\omega_{RF})t} + a_- e^{i(\omega_c-\omega_{RF})t}\right) \\
& \times \left(a_c^* e^{-i\omega_c t} + a_+^* e^{-i(\omega_c+\omega_{RF})t} + a_-^* e^{-i(\omega_c-\omega_{RF})t}\right) \\
= & |a_c|^2 + |a_+|^2 + |a_-|^2 + a_+ a_-^* e^{i2\omega_{RF}t} + a_- a_+^* e^{-i2\omega_{RF}t} \\
& + a_c a_+^* e^{-i\omega_{RF}t} + a_+ a_c^* e^{i\omega_{RF}t} + a_c a_-^* e^{i\omega_{RF}t} + a_- a_c^* e^{-i\omega_{RF}t}
\end{aligned}$$

which is similar to the previous case, but we have now picked up some extra terms, which depend on $2\omega_{RF}$. Focusing again on the terms at ω_{RF} we find that,

$$\begin{aligned}
P(\omega_{RF}) &= a_c a_+^* e^{-i\omega_{RF}t} + a_+ a_c^* e^{i\omega_{RF}t} + a_c a_-^* e^{i\omega_{RF}t} + a_- a_c^* e^{-i\omega_{RF}t} \\
&= 2\,\mathrm{Re}\left(a_+ a_c^* e^{i\omega_{RF}t}\right) + 2\,\mathrm{Re}\left(a_c a_-^* e^{i\omega_{RF}t}\right) \\
&= 2\,\mathrm{Re}\left(E_+ E_c e^{i(\omega_{RF}t+\theta_+-\theta_c)}\right) + 2\,\mathrm{Re}\left(E_c E_- e^{i(\omega_{RF}t-\theta_-+\theta_c)}\right) \\
&= 2E_c E_+ \cos(\omega_{RF}t + \theta_+ - \theta_c) + 2E_c E_- \cos(\omega_{RF}t - \theta_- + \theta_c)
\end{aligned}$$

If we further factorise and re arrange we will finally have that the current

$$I_{RF}(\omega_{RF}) = 2E_c r_{PD}\left[E_+ \cos(\omega_{RF}t + \theta_+ - \theta_c) + E_- \cos(\omega_{RF}t - (\theta_- - \theta_c))\right] \tag{8.3}$$

We now have two beat-notes, which are occurring at the *same* frequency, meaning that these two beat-notes can interfere with each other. For the case of phase modulation we have that the amplitudes of the waves are $E_c = E_0 J_0(m), E_+ = E_0 J_1(m), E_- = E_0 J_1(m)$, and the phases are $\theta_c = 0, \theta_+ = 0, \theta_- = \pi$. Substituting this in yields

$$\begin{aligned}
I_{pm}(\omega_{RF}) &= 2P_0 J_0(m) J_1(m) r_{PD}\left[\cos(\omega_{RF}t) + \cos(\omega_{RF}t - \pi)\right] \\
&= 2P_0 J_0(m) J_1(m) r_{PD}\left[\cos(\omega_{RF}t) - \cos(\omega_{RF}t)\right] \\
&= 0
\end{aligned}$$

where $P_0 = E_0^2$ is the input optical power. Thus with phase modulation the two beat-notes at ω_{RF} *cancel*, leaving zero current at ω_{RF}. Unsurprisingly, this means that phase modulation is unsuitable for use in a direct-detection photonic link.

What about intensity modulation? The amplitudes of the fields are given by $E_c = E_0 J_0(m)\cos\theta_B, E_+ = E_- = E_0 J_1(m)\sin\theta_B$, and the phases are $\theta_c = 0, \theta_+ = \pi/2, \theta_- = -\pi/2$. Substituting these parameters into eq. (8.3) yields

$$\begin{aligned}
I_{im}(\omega_{RF}) &= 2P_0 J_0(m) J_1(m) r_{PD} \sin\theta_B \cos\theta_B \left[\cos(\omega_{RF}t + \pi/2) + \cos(\omega_{RF}t - (-\pi/2))\right] \\
&= -4P_0 J_0(m) J_1(m) \sin\theta_B \cos\theta_B r_{PD} \sin(\omega_{RF}t)
\end{aligned}$$

Thus, after starting with a modulation of $m\sin(\omega_{RF}t)$, upon detection intensity modulation returns a signal component at $\sin(\omega_{RF}t)$, with pre-factors determined by the modulator and link properties. This current is proportional to the optical power of the carrier-wave, meaning that a large optical carrier may result in a *higher* RF power than on the input. This can be understood further by looking at the link gain.

Link Gain How efficient is the transport of some initial RF signal through the photonic link? This can be investigated simply by looking at the ratio of the source RF power, P_S, to the output link RF power, P_L, and is known as the link gain

$$g = \frac{P_\mathrm{L}}{P_\mathrm{S}} \qquad P_\mathrm{L} = \langle I_\mathrm{L}^2(t)\rangle R_\mathrm{L} \qquad P_\mathrm{S} = \frac{\langle V_\mathrm{S}^2(t)\rangle}{4R_\mathrm{S}}$$

where R_S and R_L are the source and load resistances and the angled brackets denote time averages. To consider this for the case of intensity modulation we will make a number of simplifications. Firstly, we assume that the modulation strength is weak, which means if we Taylor expand out the Bessell's functions we will have $J_0(m) = 1, J_1(m) = m/2$. We also include a term L_T which covers any insertion losses found in the link, apart from the detector efficiency and recast $2\theta_\mathrm{B} = \phi_\mathrm{B}$, following standard conventions. This means that the detected current for the intensity modulation can be approximated as

$$I_\mathrm{im}(\omega_\mathrm{RF}) = \frac{-P_0 \sin\phi_\mathrm{B} r_\mathrm{PD}}{L_\mathrm{T}} \frac{\pi V_\mathrm{RF}}{V_{\pi,\mathrm{RF}}} \sin(\omega_\mathrm{RF} t)$$

Now, due to intricacies of biasing [545], the load current will be half of the above, upon making the assumption that the load resistance is equal to the source resistance. Plugging all these relations together gives the well known result for link gain with an intensity modulation signal

$$g_\mathrm{link} = \left(\frac{\pi P_0 R_\mathrm{L} r_\mathrm{PD}}{4L_\mathrm{T} V_{\pi\mathrm{RF}}}\right)^2 \tag{8.4}$$

While referred to as the link *gain*, due to the inefficiency of the electro-optic conversion steps, a typical photonic link will have values on the order of -20 to -30 dB. This is not sufficient for stringent applications involving low loss transmission and thus amplification steps, in the optical or electrical domains, are required to improve this level, with corresponding trade-offs to noise being added to the system. Research is still ongoing in developing components which can improve the various properties of the conversion processes, such as lower V_π modulators and photodetectors capable of handling large optical powers.

However, it turns out that intensity modulation is not necessarily the best modulation scheme in long fiber links. As the carrier and sidebands travel through a fiber, they will accumulate a relative phase shift due to the dispersion of the fiber medium. If this phase shift begins to approach π, then the intensity modulation will be converted into phase modulation and large nulls will occur in the RF spectrum. This can be avoided through the use of single sideband modulation [546].

8.1.2 A photonic Processor

Building on a microwave photonic link, a microwave photonic processor performs an operation in the optical domain, modifying the original electrical signal. Microwave photonic processing has been of interest in the literature for many decades [542, 547] due to the inherently wideband frequency operation available in the photonic domain. Signal processing at frequencies in 10s to 100s of GHz becomes possible, if the required modulators and detectors are available. Photonic processing exists in many forms. In this thesis we focus on coherent signal processing involving optical carriers and modulated sidebands. To understand how to build a photonic processor, we discuss the mapping of optical to frequency domain.

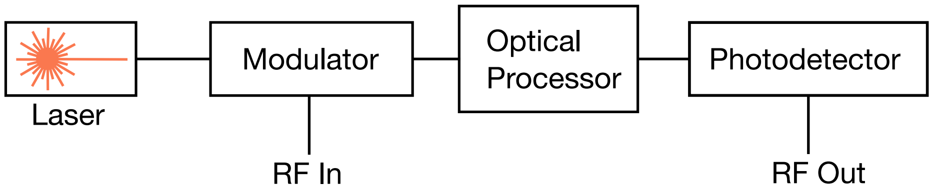

Figure 8.3: A typical microwave photonic processor

Let us again consider the case of single sideband modulation, as discussed in section 8.1.1,

$$E = a_c e^{i\omega_c t} + a_+ e^{i(\omega_c + \omega_{RF})t}$$

where again a_c and a_+ are the *complex* amplitudes of the two fields. As we pass through the link, the fields will be altered by the optical processor, which we assume interacts only with the sideband as unity in the region of the carrier, such that the field becomes

$$E = a_c e^{i\omega_c t} + a_+ |H(\omega)| e^{i\phi(\omega)} e^{i(\omega_c + \omega_{RF})t}$$

Now, from the previous discussion we know that this will map *directly* to the measured beatnote at ω_{RF}, i.e

$$\begin{aligned} I_{RF}(\omega_{RF}) &= 2\,\mathrm{Re}\left(E_c E_+ |H(\omega)| e^{i(\omega_{RF}t + \theta_+ - \theta_c + \phi(\omega))}\right) \\ &\propto |H(\omega)| \sin(\omega_{RF}t + \Delta\theta + \phi(\omega)) \end{aligned}$$

So with this single sideband configuration, the *amplitude* and *phase* of the optical processor is mapped onto the measured RF signal. This leads to a couple of interesting observations. Firstly, this allows for a very precise characterisation of the optical device after an appropriate calibration to measure the initial link response, albeit over a limited bandwidth. This scheme is typically referred to as optical vector network analysis [548–551], and is particularly useful for determining coupling parameters of resonators due to the phase sensitivity of the measurement. Secondly, that the formation of a high extinction electrical filter can be performed simply through the use of a high suppression *optical* filter. Thirdly, optical processing with this scheme is *inherently* tunable. Changing the carrier frequency, i.e the laser, will change the central RF frequency at which the sideband overlaps with the optical response. This frequency tuning can be performed completely independently of the optical processor, which will thus consistently maintain its properties while the central frequency is tuned. This is in stark contrast to resonant RF filters, where frequency tuning will affect other device parameters such as bandwidth and suppression.

8.1.3 Integrated Microwave Photonic Processing

Microwave Photonic processors are capable of providing significant advantages over typical microwave devices, in particular for wideband operation at frequency ranges above 10's of GHz. To enable widespread adoption, there is a need to compete with traditional electrical processing elements, such as surface acoustic wave filters, at a system level. Depending on the application, the requirements of features such as size, weight, power and cost can be critical. Photonic integration provides the capability to meet these requirements, and also opens up new processing functionalities and paradigms, possible due to the integration of multiple building blocks in a single circuit [552, 553]. A highly detailed overview of integrated microwave photonics is provided in [492]. Moving to integrated devices also significantly increases the optical intensity, opening up the possibility of efficiently harnessing nonlinear optical processing [554, 555]. In the following sections we utilise integrated optical elements, both linear and nonlinear, for optical processing in microwave photonic signal processors.

8.1.4 Radio-frequency Notch Filters

Highly selective microwave filters are of great importance in radio-frequency signal processing. In particular, modern applications have increased the desire for *reconfigurable* systems, which can adjust operational frequencies in real-time. Dealing with dynamic interfering signals has thus become critical for applications utilising and interacting with these shifting frequencies such as cognitive radio [556, 557] and jamming systems [558], and wideband RF systems such as ultra-wideband radio [559] and modern radar. These systems would benefit hugely from RF filters that can be tuned over many gigahertz whilst keeping MHz-scale resolution and high selectivity to prevent severe interference due to spectrum-sharing. To understand the requirements of such filters further, we represent the operation and key properties of an RF notch filter in fig. 8.4. State-of-the-art RF notch filters [560–562] [3-5] are capable of a high peak attenuation (>50 dB) and high selectivity (<10 MHz bandwidths) but have a limited notch frequency tuning range, of the order of a GHz [562].

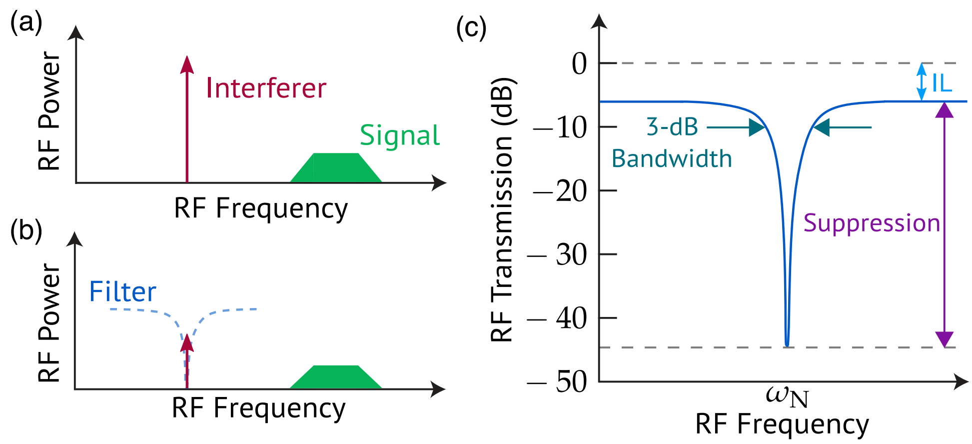

Figure 8.4: (a) RF spectrum showing signal of interest and an interferer (b) Spectrum after passing through an RF Notch filter. Interferer is highly attenuated, with the signal power being slightly lowered due to the insertion loss, but shape is preserved (c) Features of notch filter showing the 3-dB bandwidth, the filter suppression and insertion loss (IL).

Microwave photonic (MWP) notch filters, on the other hand, are capable of tens of gigahertz tuning and have advanced in terms of performance. These filters can generally be implemented in two ways: via a multitap filter approach [536, 563–565], in which multiple replicas of RF modulated signals are delayed, weighted, and combined to generate nulls in the RF frequency response, or via sideband filtering using an optical filter (OF) [566–568], as described in section 8.1.2. A multitap approach can generate a notch filter with a narrow bandwidth and relatively high rejection but exhibits a periodic transfer function, which is undesirable for wideband applications. Particularly from this filter class, a very narrow notch response (≈15 MHz) with a relatively wide passband was demonstrated in [563], but without any tuning capability. The sideband filtering approach requires a high-Q optical resonance to generate the RF notch filter response. Optical cavities, such as silicon ring resonators [566, 567] or $LiTaO_3$ whispering gallery mode resonators [568] have been considered, with isolation bandwidths ranging from 6 GHz [567] down to 10 MHz [568]. But to attain high rejection these devices require precise control over coupling parameters, and strict requirements are placed on fabrication to attain low losses to enable narrow bandwidths.

To bypass the issues associated with resonators, in the following work we instead utilise the narrow optical response of Brillouin scattering as an optical filter. To enable compatibility with integrated microwave photonic devices, we harness SBS in a highly nonlinear waveguide on a photonic chip, demonstrating competitive performance to previous filters based on optical resonators.

8.2 RF Notch filter with on-chip SBS

In the last two decades it has been repeatedly demonstrated that SBS can be controlled and harnessed for a wide range of RF signal processing applications [482, 569–574]. Several applications such as wideband phase shifting [570], tunable true time delay [571, 572], separate carrier tuning [573], and microwave photonic filtering [482, 484, 574], among others, have been demonstrated. The 2011 demonstration of on-chip SBS [88] has enabled implementation of chip-based SBS RF signal processing, which was traditionally reserved to optical fibers. This has led to a remarkable advantage in terms of size and weight and is well in line with the current trend of integrated microwave photonics [492]. Key RF signal processing functionalities such as tunable delay lines [92] and tunable bandpass filtering [94] have been demonstrated with this new technology.

Recently, SBS has also been explored for RF notch filtering with ultrawide frequency tunability [484], which featured a single notch (instead of periodic notches in the case of multi-tap filters [536]) in a frequency range of 1-20 GHz with a narrow 3-dB bandwidth of 82 MHz. This was demonstrated in 1 km of dispersion-shifted fiber.

Here we demonstrate a continuously tunable microwave photonic notch filter (MPNF) using on-chip SBS. To the best of our knowledge, chip based MPNFs reported to date are only capable of showing a periodic response (i.e. not a single notch) [564, 566, 575, 576] and are currently limited to a large 3-dB bandwidth (for example 910 MHz as reported in [566]). We show photonic chip-based MPNF with a 3-dB bandwidth of 126 MHz, a notch depth of 20 dB and frequency tunability in the range of 2-8 GHz, which is limited only by the measurement equipment. [1]

8.2.1 Operational Principle

The tunable MPNF proposed here uses the loss that occurs at the anti-Stokes frequency of SBS to remove a portion from a single sideband with carrier (SSB+C) signal spectrum. The MPNF notch frequency is tunable by modulating the SSB+C

[1] Work in this section has been published in Optics Communications: B. Morrison et al., "Tunable microwave photonic notch filter using on-chip stimulated Brillouin scattering", Opt. Commun. **313**, 85–89 (2014)

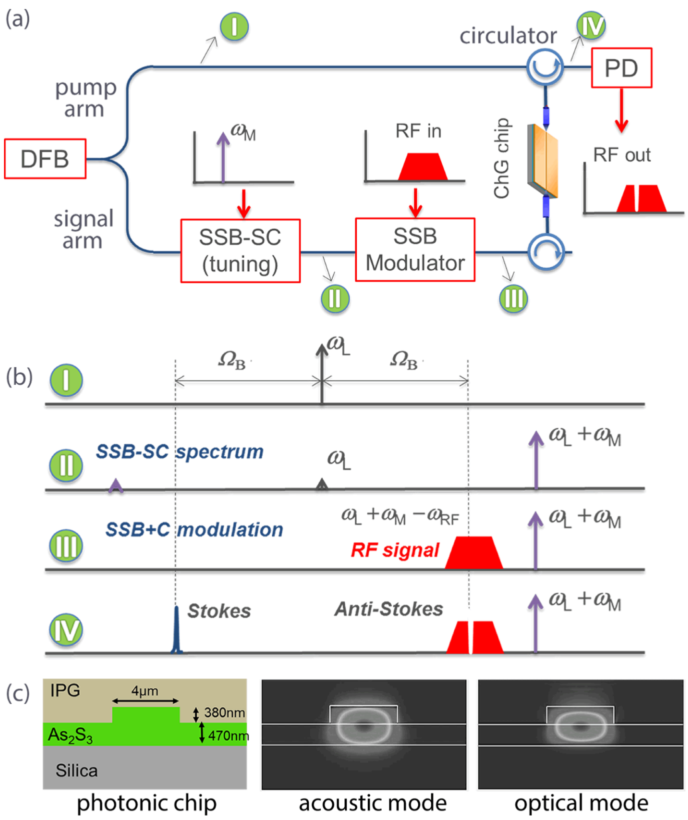

Figure 8.5: (**a**) Schematic diagram of the proposed continuously tunable MPNF (**b**) Optical spectra at various points of the scheme. (**c**) As2S3 waveguide showing confinement of acoustic and optical modes.

signal onto a tunable carrier, which is generated by means of SSB suppressed-carrier (SSB-SC) modulation from a DPMZM. This configuration prevents drift between the pump and the carrier wave, a possible issue if two lasers are instead used.

A schematic of principle of the the MPNF appears in fig. 8.5a. Light from a DFB laser with frequency ω_L is split into two arms: the upper one is called the pump arm and the lower one the signal arm. In the signal arm, the light is modulated with an RF tone at frequency ω_M generating the SSB-SC spectrum depicted in fig. 8.5b line II. This creates the tunable carrier frequency necessary for the filter tuning. This carrier is then modulated by the RF signal which is to be filtered, using an SSB+C modulator. In this case, the lower sideband of the RF signal is retained while the upper sideband is suppressed (fig. 8.5b line III). The light from the signal arm is then counter-propagated with the pump wave inside the photonic chip using circulators.

The SBS pump generates gain and loss responses at frequencies $\omega_L - \Omega_B$ (anti-Stokes) and $\omega_L + \Omega_B$ (Stokes), respectively (fig. 8.5b positions I,IV). The SBS shift, Ω_B, has been measured to be 7.7 GHz for the photonic chip that we used in these experiments. By adjusting ω_M, a portion of the RF signal can be made to overlap with the anti-Stokes loss spectrum (fig. 8.5b line IV), thereby generating a notch at the RF spectrum after photo-detection (right-side of fig. 8.5a). The notch will appear at RF angular frequency ω_N, which follows the relation:

$$\omega_N = \omega_M - \Omega_B \tag{8.5}$$

Thus, it is clear from eq. (8.5) that the notch frequency is continuously tunable by changing the drive frequency, ω_M.

8.2.2 Experiments

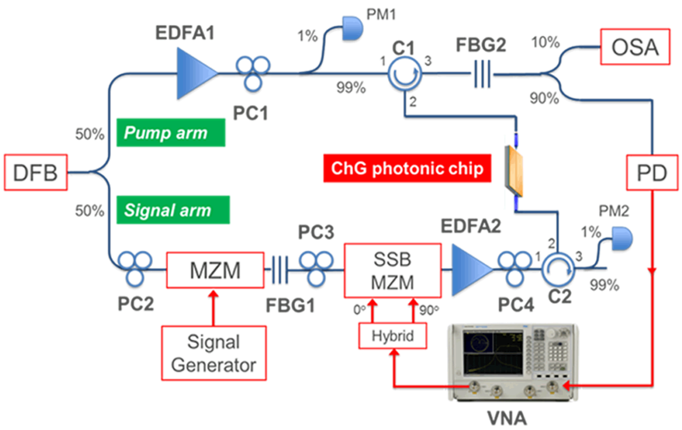

Figure 8.6: The experimental setup to realize the continuously tunable MWP notch filter using on-chip SBS. Key component acronyms; PC: polarization controller, MZM: Mach-Zehnder modulator, SSB: single sideband, FBG: fiber Bragg-grating, PM: power meter, C: circulator, PD: photodetector, VNA:vector network analyzer, OSA: optical spectrum analyzer

Figure 8.6 shows the experimental setup. Light from a DFB laser diode (Teraxion Pure Spectrum) at $\omega_L = 1550$ nm with an output power of +13 dBm was split using a 50:50 coupler. The signal arm comprised a Mach-Zehnder modulator (MZM, Covega Mach-40) biased at the minimum transmission point and driven by an RF tone from a signal generator to generate a double-sideband suppressed-carrier (DSB-SC) spectrum. The MZM was followed by a fiber Bragg-grating in transmission mode to filter out the lower sideband. This combination formed the SSB-SC modulator used for tuning the frequency of the notch filter. The response of the fiber Bragg-grating (FBG1) was wide enough that the lower sideband was suppressed over the entire tuning range of the experiment. A dual parallel MZM (DPMZ, Covega Mach 40-086) driven through a 2-18 GHz quadrature hybrid coupler was used as the SSB+C modulator. The modulator was driven with an RF frequency sweep from port 1 of a vector network analyser (VNA) to measure the filter response. The output of the modulator was then amplified using a low noise erbium-doped fiber amplifier (EDFA2). Two polarization controllers (PC2 and PC3) were used to adjust the light polarization to the modulators to optimize the modulation depths and the suppression of the unwanted carrier and sideband.

The 50% portion in the pump arm was amplified using a high power (2W) EDFA1. A 99:1 coupler was placed in the pump arm to monitor the insertion loss of the photonic chip. The 1% output was monitored with an optical power meter (PM1) while the remaining 99% of the pump light was launched into the photonic chip via an optical circulator (C1) and lensed-tip fiber. Since SBS is a polarization-sensitive process [357, 578], PC1 and PC4 were used to optimize the SBS gain (loss) during measurements. Another power meter (PM2) was placed at output port 3 of C2 via a 99:1 coupler to measure the pump power after propagation through the chip. The photonic chip contained a 6.5 cm long As_2S_3 optical waveguide with a cross-section of 4 um $\times$ 850 nm. The waveguide has an effective mode area of 2.3 um^2 and a large SBS gain coefficient ($g_0 \sim 7.15 \times 10^{-10}$ mW^{-1} [88]). The total waveguide insertion loss, monitored by comparing the pump power measured in

PM1 and PM2, was around 9.8 dB. The loss was typically comprised of around 4.2 dB of coupling loss per facet and a propagation loss of around 0.2 dB/cm.

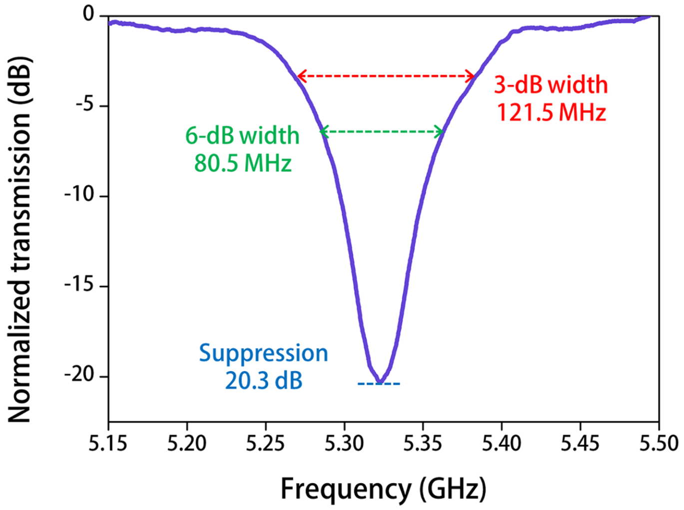

Figure 8.7: Measured normalized frequency response of an MPNF centered at 5.32 GHz and with a 3-dB width of 121.5 MHz, a 6-dB width of 80.5 MHz and a suppression of 20.3 dB.

The desired filtered signal was available at port 3 of C1. Due to reflections at the ends of the chip, the injected counter-propagating pump generates a parasitic pump co-propagating with the signal, which may lead to degradation in the filter response [94]. For this reason, we removed the parasitic pump signal at the output using FBG2. The signal after pump removal was then split with a 90:10 coupler, of which the 10% port lead to an OSA and the other to a 50 GHz photo detector (PD, u2t XPDV2120) connected to port 2 of the VNA, to measure the RF response.

8.2.3 Results and Discussions

Figure 8.7 shows the frequency response of the MPNF at a notch frequency of 5.32 GHz. We deliberately used a frequency sweep with a small range (350 MHz) to resolve the profile of the notch. The 3-dB bandwidth, measured from the pass band of the filter, was measured to be 121.5 MHz while the 6-dB bandwidth is 80.5 MHz.

Figure 8.8 shows the measured normalized frequency response for the tunable MPNF when the carrier frequency ω_m, was tuned. Continuous tuning of the notch frequency was achieved when the carrier frequency was changed from 10 GHz up to 15 GHz in steps of 500 MHz. For a Brillouin frequency shift of 7.7 GHz, the variation of the notch frequency is from 2.3 GHz to 7.3 GHz, as expected from eq. (8.5). A notch suppression of larger than 17 dB was achieved for virtually all the filter responses. Note that in these measurements, the lowest frequency range of the sweep was limited to 2 GHz by the quadrature hybrid coupler. For frequencies lower than 2 GHz, the coupler did not maintain the amplitude-balance and the quadrature phase relation between the output ports, which will lead to an optical spectrum with insufficient sideband suppression from the modulator. The highest notch frequency, on the other hand, was limited by the highest frequency of our signal generator, which was 15 GHz.

The amplitude and bandwidth fluctuations in the filter response over the tuning range were also inspected. The results are shown in Figure 8.9. Over the entire range, high notch suppression (-19 ± 2 dB) and bandwidths (3 dB: 126 ± 7 MHz, 6 dB: 78 ± 4 MHz) were achieved.

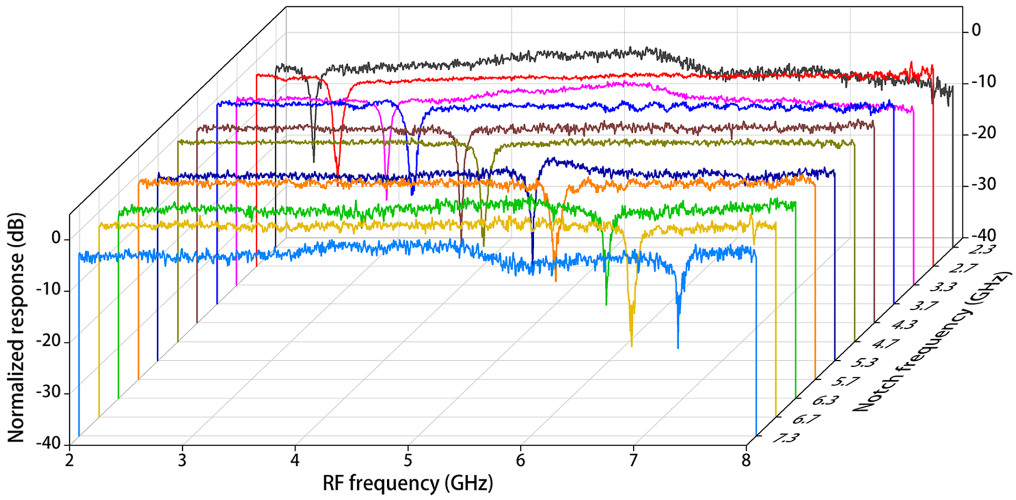

Figure 8.8: Normalized MPNF responses demonstrating the tunability of the notch frequency in the frequency range of 2-8 GHz.

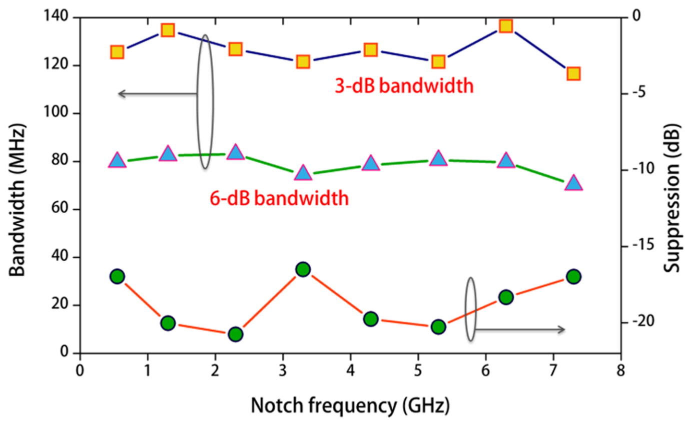

Figure 8.9: Notch suppression and 3-dB and 6-dB bandwidths of MPNF for different center RF frequencies.

The measured filter responses can be improved in several ways. The notch depth was limited by the peak SBS absorption and the sideband suppression from the SSB modulator. The power handling capabilities of the waveguide set an upper limit on maximum pump power, and subsequently the maximum achievable gain. A waveguide with lower loss would enable higher gain for the same pump power levels. For a given SBS gain, limited sideband suppression will lead to a reduction in the notch contrast due to the presence of extra RF signal power at the notch frequency. In our experiments we observed typically 25 dB sideband suppression ratio from our modulator. Bias drifts will reduce this value to 20 dB after approximately 15 minutes of operation. Using an SSB modulator with higher sideband suppression ratio, in conjunction with a bias control circuitry will lead to an improvement in the notch contrast.

The flatness of MPNF pass-band (around 5 dB maximum variation in current experiments), on the other hand, was limited by the presence of the FBGs in the setup. These FBGs introduced non-flat frequency response as the notch frequency was tuned. Replacing the MZM and FBG1 combination with a second SSB modulator will improve the flatness of the MPNF pass-band. The FBG2 can be removed if the reflections from the chip interfaces are small. This can be achieved by improving the coupling to the optical waveguide for example by using on-chip tapers [127].

The noise figure is another important parameter of RF filters; it is the measure of the degradation of the signal to noise ratio of an RF signal through a system. In microwave photonics the transmission of the RF signal through the different components is given by the link gain. It is well known that in a lossy microwave device, the noise figure is dominated by losses in the system, and becomes proportional to the inverse of the link gain for large losses [544]. If we recall the link gain equation, Equation (8.4), one can conclude that the link gain of this filter can be significantly improved by mitigating the optical losses, notably in the signal arm and in the chip. The losses in the signal arm are due to the insertion losses ($L_{\mathrm{MZM}} > 4$ dB) and the relatively high RF half-wave voltages ($V_{\pi,\mathrm{RF}} > 5$ V) of the RF modulators, the insertion loss of the FBG (L_{FBG} 2 dB) and the loss of the chip ($L_{\mathrm{WG}}{\approx}10$ dB). Using ultra-low V_π modulators will give quadratic improvement to the MWP link gain of the filter and subsequently a quadratic reduction of the noise figure [544]. Reducing the losses associated with the insertion of the photonic chip (coupling loss and propagation loss) will also see a dramatic improvement in terms of the noise figure and possibly enable the removal of the EDFA in the signal arm.

8.3 Cancellation Technique for Ultra Deep RF Notch Filters

In the previous section we have shown that the use of SBS as on optical filter allows for notch bandwidths in the range of a 100 MHz, comparable to that of high-Q optical resonators. The use of an integrated device based on a photonic chip is highly desirable, opening up possibilities for further functionality and compactness. However, this introduces a new complexity, the the depth of the notch filter is directly related to the strength of the SBS attenuation. Achieving large attenuation beyond 20 dB requires strong optical pumps beyond 100s of mW, which is not conducive for compact, low power and efficient systems. Under the standard operating conditions this is clearly a significant problem, and could prove to be an issue with any implementation in practical devices. However, in the following we will show that the introduction of a *second* optical sideband allows for the creation of a high attenuation filter, and provides a number of advantages over the single sideband processing discussed so far.[2]

8.3.1 The Cancellation Technique

The key idea behind the new concept is the use of a frequency localised RF cancellation, essentially phase modulation at a single frequency ω_{N}, to generate an anomalously deep microwave filter. To attain this condition we need to adapt the typical techniques for generating and processing the optical sidebands. Instead of processing single-sideband (SSB) (fig. 8.10a) or conventional dual-sideband (DSB) signals, i.e., equal amplitude and equal phase (intensity modulation) or equal amplitude and opposite phase (phase modulation), as in traditional MWP filters, here we utilise DSB signals with tunable amplitudes and phases. The RF signal is encoded in the optical sidebands with unequal amplitudes and a phase difference, $\Delta\phi$. We then exploit *both* the amplitude and phase responses of an optical filter to equalize these sideband amplitudes and to produce an antiphase

[2]Parts of the following section have been published in *Optics Letters*: D. Marpaung et al., "Frequency agile microwave photonic notch filter with anomalously high stopband rejection", Opt. Lett. **38**, 4300 (2013)

relation between them, $\Delta\phi = \pi$, in only a selected frequency region within the optical filter response (fig. 8.10b). Upon photodetection, the beat signals generated from the mixing of the optical carrier and the two sidebands perfectly cancel at a specific microwave frequency, forming a notch with an anomalously high stopband rejection (fig. 8.10d). We believe that this concept is a photonic implementation of the "bridged-T" notch filter concept in microwaves proposed by Bode in 1936 [579]. He exploited the concepts of attenuation balance and phase cancellation in a lumped-element RF circuit to achieve a notch filter with quasi-infinite rejection [580].

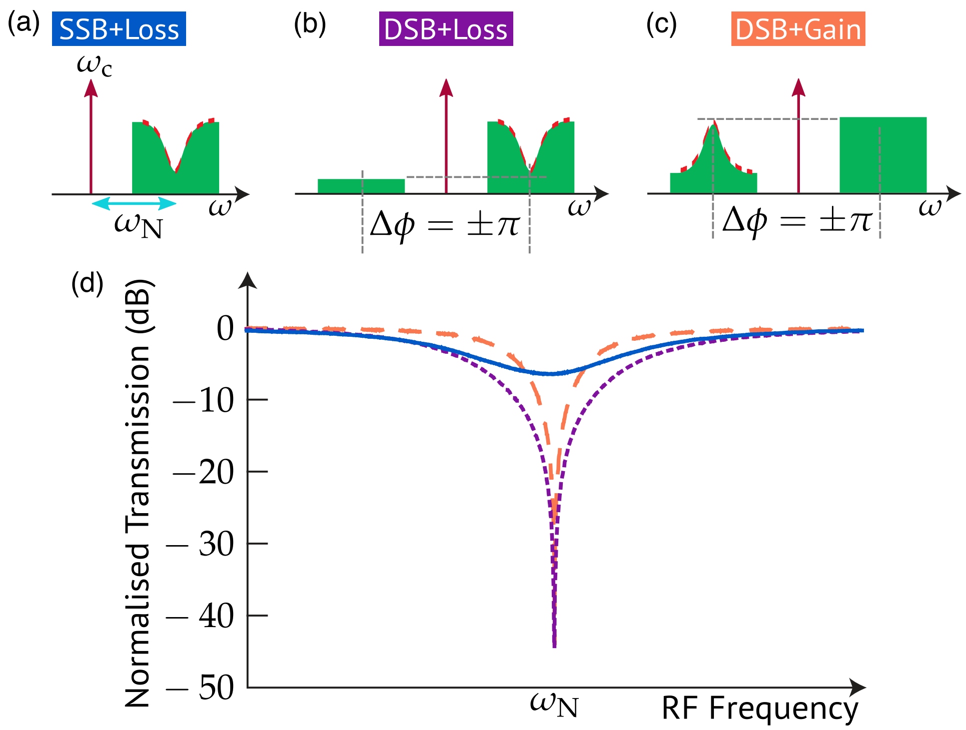

Figure 8.10: Principle of operation of notch filter. (a) Conventional SSB scheme, (b) scheme using DSB modulation utilizing loss, and (c) scheme utilizing gain. (d) RF filter responses for the three architectures using SBS (gain = 7 dB) as an optical filter.

To understand the conditions required for cancellation further we can consider a simple example case of a phase modulation, where the amplitudes of the sidebands are controlled arbitrarily. If we recall eq. (8.3), we know that we will have a separate beatnote for each sideband, which are out of phase, such that the magnitude of the current at ω_{RF} will be

$$I_{RF}(\omega_{RF}) = 2E_c r_{PD} \left(E_+ - E_-\right)$$

Thus for frequencies away from the optical filter, the passband level of the RF response will be set by the difference of the amplitudes of the two sidebands. Now, assuming that $E_- < E_+$, we place a narrowband optical loss filter on the upper sideband, centred at a frequency ω_N above the carrier. This means that the current at this particular RF frequency will now be given by

$$I_{RF}(\omega_{RF} = \omega_N) = 2E_c r_{PD} \left(E_+ A_N - E_-\right)$$

where A_N is the optical filter amplitude at $\omega_{RF} = \omega_N$ and we have assumed that the phase response of the optical filter is zero at this point. By choosing the appropriate value of A_{N}, or altering E_+ or E_-, the current will go to zero, at this frequency alone, creating a filter with extremely high suppression. Elsewhere the amplitude of the optical filter will be unitary ($A = 1$) and the passband current will be set by the above.

It is important to stress that the tailored spectrum required for the filter operation is very different from spectra generated and used in conventional MWP signal processing so far, such as intensity modulation (IM), phase modulation (PM), or SSB modulation. Ideally, the spectrum should contain an optical carrier and sidebands that can be tailored independently in amplitude and phase. A good approximation of this ideal spectrum can be generated using a dual-parallel Mach-Zehnder modulator (DPMZM). In the small signal approximation this electro-optic modulator can create an optical carrier with two sidebands whose relative amplitude and phase difference can be sufficiently tunable [581, 582]. We describe, in further detail, the conditions required to achieve cancellation using such a modulator with a range of optical responses in [583].

The cancellation concept leads to two key advantages. First, the microwave filter peak attenuation is no longer limited by the optical filter peak attenuation because the RF notch is formed by signal cancellation. Second, the optical filter is no longer restricted to producing a notch response, but instead can have a bandpass/gain response, as shown in fig. 8.10c. Instead of attenuating the stronger sideband with loss from the optical filter (fig. 8.10b), one can amplify the weaker sideband with gain, to achieve the amplitude equalization required for signal cancellation. SBS gain is an ideal candidate for such an active optical filter, and it has long been considered for MWP signal processing, due to the fine spectral width of its gain spectrum [94, 570, 574]. The cancellation concept will enable a new direction in exploiting the SBS gain spectrum as a high-performance *notch* filter. The fact that a high suppression RF filter can be created through the use of a small amount of optical amplification is quite surprising and not immediately intuitive.

8.4 Ultrahigh Attenuation, On-Chip SBS Notch Filter

In section 8.2 we required a large SBS gain and high pump power to achieve moderate filter suppression. From a broader perspective, this need for high power is unattractive for on-chip signal processing with particularly stringent requirements for energy efficiency. More importantly, this prevents implementation of integrated RF signal processing in low gain SBS devices, such as the ones recently reported in CMOS-compatible platforms [96, 103]. By harnessing SBS in silicon, these devices are highly attractive due to the potential to integrate RF signal processing in a single compact monolithic chip [581]. Nevertheless, they currently exhibit very low gain, of the order of 1 dB to 4 dB, which is far from sufficient for any MWP signal processing if one relies on conventional techniques.

Here, we utilise the cancellation technique (section 8.3.1) to demonstrate experimentally a highly selective SBS IMWP bandstop filter in a cm-scale chalcogenide glass waveguide that operates with a low pump power (8 mW to 12 mW) and a low SBS gain (1 dB to 4 dB). This is possible while also maintaining high, reconfigurable resolution (32 MHz to 88 MHz) and high stop-band rejection of >55 dB. We show that the filter can be tuned over a wide frequency range of 0 GHz to 30 GHz, leading to a unique performance combination difficult to match with any existing filter technology. We also show that for a given SBS gain, this approach allows the

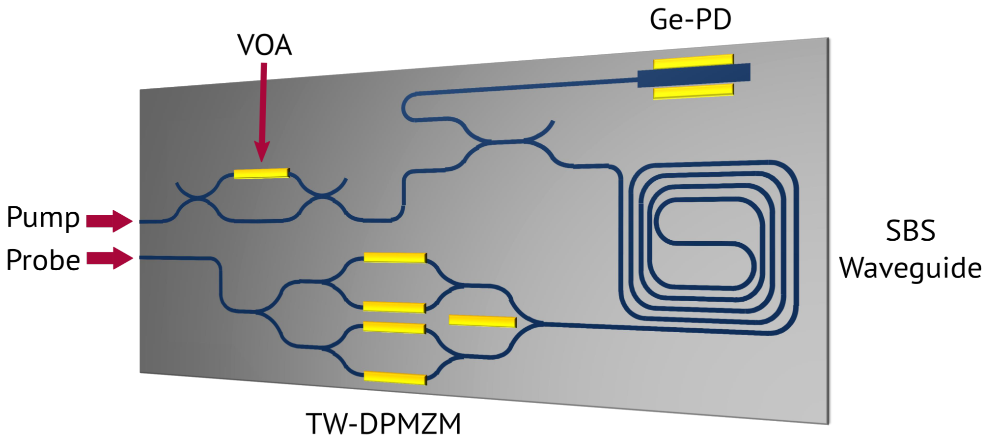

Figure 8.11: Artist's impression of a future monolithic-integrated high suppression and reconfigurable SBS MWP filter in a silicon chip. VOA: variable optical attenuator, TW-DPMZM: travelling wave dual-parallel Mach-Zehnder modulator, Ge-PD: germanium high speed photodetector.

flexibility to re-distribute the pump optical power into modulated optical power, thereby reducing the filter insertion loss. The results presented here point to new possibilities for creating high performance SBS-based reconfigurable MWP filters that will play a key role in modern RF systems for next generation radar [584] and high data rate wireless communication [585], with a potential for monolithic integration in silicon chips (fig. 8.11). [3]

8.4.1 On-Chip Filter Experiments

Figure 8.12a depicts the experimental setup used to demonstrate the filter operation. An SBS pump at 1550 nm was generated, amplified and injected into a 6.5 cm-long As_2S_3 rib optical waveguide via a lens-tipped optical fiber. A frequency-detuned RF-modulated probe generated using a DPMZM was launched from the opposite end. The typical insertion loss of the photonic chip was measured to be 9.5 dB, including coupling and propagation losses. The rib waveguide has a cross-sectional area of $4\,\mu\text{m} \times 0.85\,\mu\text{m}$, with a partial etch of 30 %, and it exhibited a large Brillouin gain coefficient ($G_B \approx 300\,\text{m}^{-1}\text{W}^{-1}$) due to its high acoustic confinement, small effective area and large photoelastic response [124].

For the SBS pump we used a DFB laser (Teraxion Pure Spectrum ($\lambda = 1550\,\text{nm}$) with 100 mW of optical power, connected to an electronically-controlled variable optical attenuator (VOA, Kotura), and an EDFA (Amonics) with maximum output power of 1 W. The VOA was used to control the pump power, and subsequently the SBS gain, with a high precision of 0.5 dB. For the SBS probe we used a DFB laser (Teraxion) to generate the optical carrier which was modulated using a DPMZM (EOSPACE IQ-0D6V-35). The half-wave voltage, insertion loss, and 3 dB bandwidth of the modulator were 5 V, 5 dB, and 35 GHz, respectively. The RF input ports of the DPMZM were driven by an RF signal through a quadrature hybrid coupler with frequency range of 1.7 GHz to 36 GHz (Krytar). The three bias voltages of the DPMZM were adjusted using a programmable multi-channel voltage supply with 1 mV voltage accuracy (Hameg HM7044G). The signal was detected using a high-speed photodetector (PD, u2t XPDV2120) with 0.6 A/W

[3]Parts of the following section have been published in *Optica*: D. Marpaung et al., "Low-power, chip-based stimulated Brillouin scattering microwave photonic filter with ultrahigh selectivity", Optica **2**, 76 (2015)

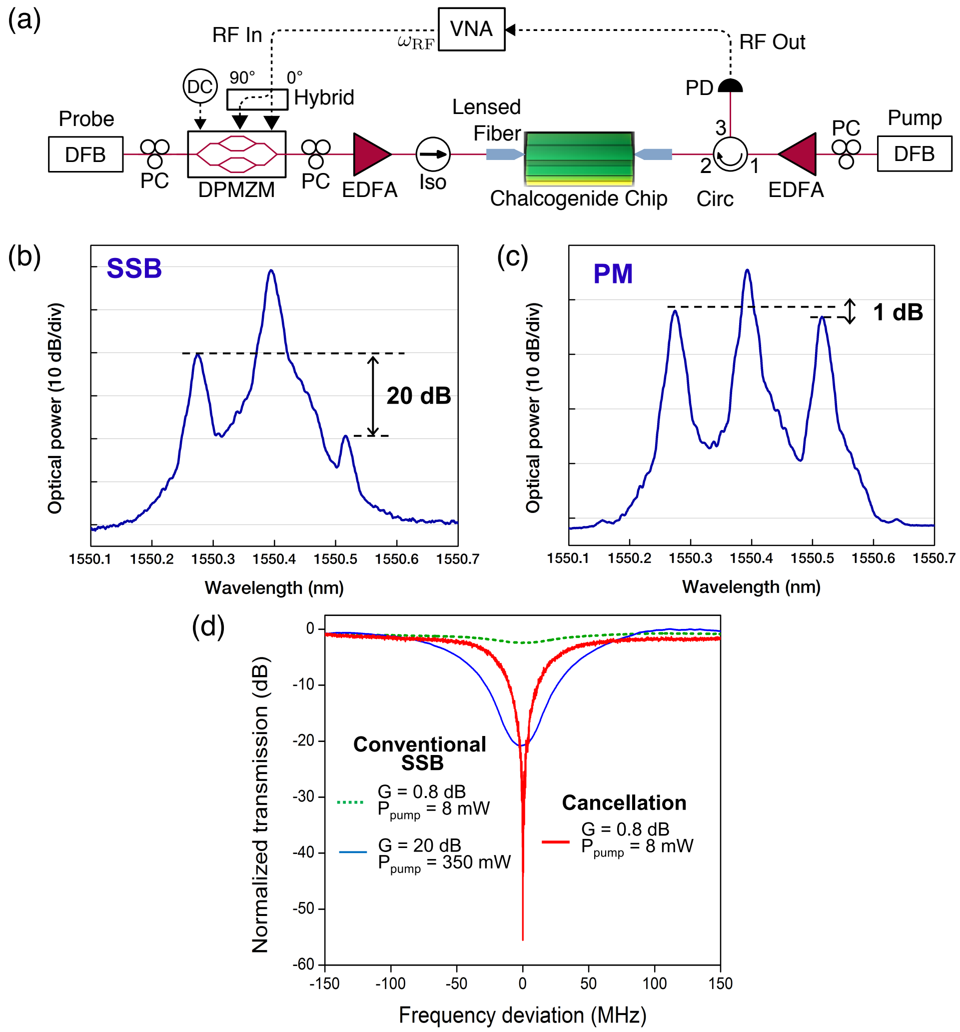

Figure 8.12: Microwave photonic filter experiments. (a) Pump-probe experimental setup for filter performance evaluation, including distributed feedback laser (DFB), 90° RF hybrid coupler (Hybrid), dual-parallel Mach-Zehnder modulator (DPMZM), erbium-doped fiber amplifier (EDFA), polarization controller (PC), photodetector (PD), and vector network analyser (VNA). (b) Optical spectrum measurement of input RF-modulated signal for the conventional single-sideband (SSB) filter. (c) Optical spectrum input for the cancellation filter, yielding near-phase modulation with unequal-amplitude sidebands. (d) Corresponding VNA traces depicting filter responses for the conventional SSB and cancellation filters. For the same low pump power (8 mW), the SSB filter yields 0.8 dB suppression, while the cancellation filter yields 55 dB suppression.

responsivity and 50 GHz RF bandwidth. For filter response measurements, a frequency-swept RF signal with 0 dBm power was supplied from and measured on a 43.5 GHz vector network analyzer (VNA, Agilent PNA 5224A).

With the experiment setup we demonstrated and compared the filtering performance of the conventional SSB approach and the cancellation-based filter. The conventional filter generated a SSB RF modulated optical spectrum as the input to the optical filter. Typically, the measured extinction ratio of the suppressed optical sideband with respect to the unsuppressed sideband was a minimum of 20 dB (fig. 8.12b). The cancellation filter requires a near phase modulation signal as input. The measured optical spectrum of the generated sidebands with opposite phase and 1 dB amplitude difference is shown fig. 8.12c.

Figure 8.12d shows the measured RF magnitude responses of both the conventional and the cancellation approaches. In the conventional approach, a bandstop filter with moderately high suppression (20 dB) can only be achieved by pumping the optical waveguide with a high pump power (350 mW), as shown as the blue trace of fig. 8.12d. When very low pump power, in the order of 8 mW, was used instead, the filter suppression was very shallow, of the order of 0.8 dB (green dashed trace). On the other hand, with the same low pump power, and a sub-1 dB SBS gain, the cancellation filter can achieve 55 dB of suppression and a higher resolution compared to the conventional filter (thick red trace). This result illustrates the superiority of the cancellation filter, which exhibited impressive peak suppression and a high resolution whilst using only low SBS gain and very low pump power. This massive 43-fold reduction in required pump power (8 mW versus 350 mW) highlights the energy efficiency enhancement of the cancellation based RF filter.

8.4.2 Frequency Tuning and Bandwidth Reconfigurability

We demonstrate the frequency agility of the MWP filter by tuning the central frequency of the RF bandstop response and its 3-dB bandwidth. Central frequency tuning with a resolution of 12.5 MHz was achieved by adjusting the frequency difference between the pump and the probe waves by temperature tuning the probe DFB laser. For all measurements, the pump wavelength and power at the facet of the photonic chip were kept at 1550.43 nm and 24 dBm, respectively. The chip insertion loss was 8.5 dB. The result is depicted in fig. 8.13a, where central frequency tuning from 1 GHz to 30 GHz was achieved. Critically, the filter suppression was maintained above 51 dB for the entire tuning range.

Reconfiguration of the filter bandwidth was achieved by switching between SBS gain and loss responses, and the variation of pump power for each case. The RF bandwidth of the bandstop filter is equivalent to that of the SBS process, given by [80]

$$\Delta\nu_{\mathrm{RF}} = \Gamma_{\mathrm{B}}\sqrt{\frac{G}{\ln(e^{G}+1)-\ln 2}-1} \tag{8.6}$$

where Γ_{B} is the Brillouin linewidth, and the G parameter is proportional to the SBS pump power. Here, $G > 0$ corresponds to SBS gain, while $G < 0$ corresponds to SBS loss. Figure 8.13b shows the calculated filter bandwidth as a function of G, for $\Gamma_{\mathrm{B}} = 58$ MHz, together with the experimental data. For the SBS gain, we tuned the SBS pump to achieve gain variation from 0.8 dB to 11.6 dB and obtained increase in filter resolution from 56 MHz down to 32 MHz. As for the SBS loss, we tuned the peak absorption from –0.8 dB to –8.1 dB to expand the filter

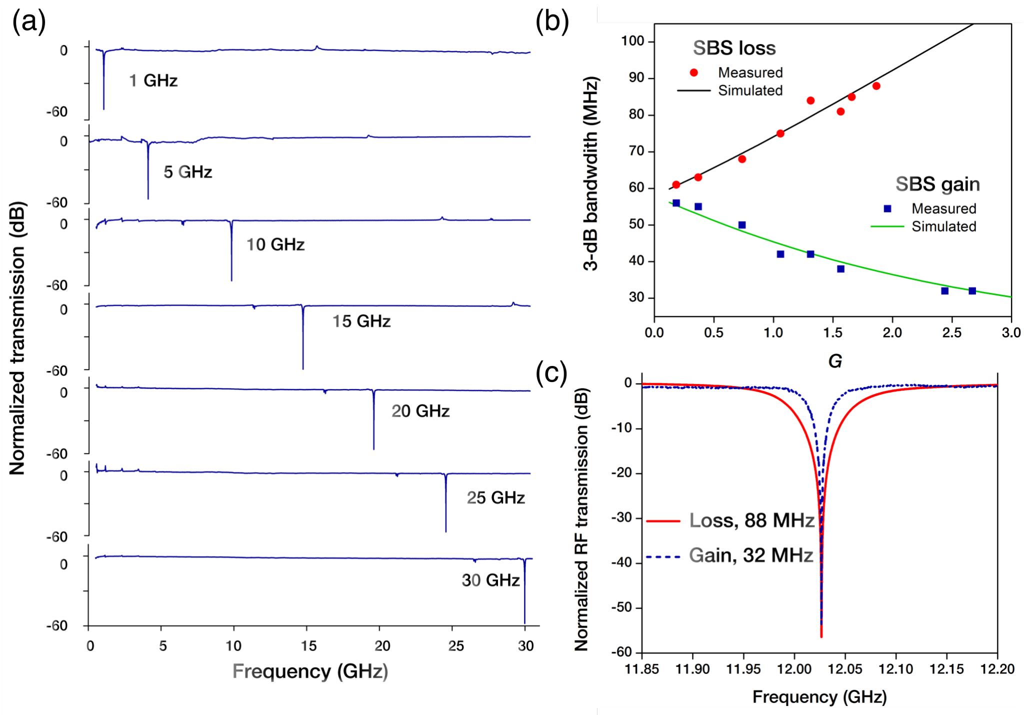

Figure 8.13: Frequency agility of the filter (a) Stopband center frequency tuning. Filter suppression was kept above 51 dB in all measurements. (b) Bandwidth tuning from 32 MHz to 88 MHz was achieved by means of tuning the pump power to vary SBS gain and loss. (c) Filter response at the extremes of the bandwidth tuning range.

bandwidth from 61 MHz to 88 MHz. In total, we achieved 56 MHz tuning range in the experiment. For each measurement we kept the stopband suppression beyond 50 dB by changing the balance between the sidebands, simply by varying the DC voltage supplied to the DPMZM, to maintain cancellation at the center of the SBS resonance. The normalized frequency response of the filter at the extreme points of the bandwidth tuning range is shown in fig. 8.13c.

8.4.3 Demonstration of RF Filtering

Here we demonstrate what is to our knowledge the *first* high resolution RF filtering experiment using a chip-based MWP filter. We consider a scenario where two RF signals, one of interest and the other an unwanted interferer, were supplied to the input of an optical modulator (see fig. 8.14). The signal of interest was band-limited with a width of 1 MHz, whilst the unwanted interfering signal was a single frequency tone. These were separated in frequency by 20 MHz, and the power of the unwanted signal was 21 dB higher than the signal of interest. To generate the signal of interest, we created a frequency modulated signal with unity modulation index from an RF tone with a frequency of 11.982 GHz and power of –9 dBm. The modulation signal was a triangular waveform with 30 kHz frequency and 1 V peak-to-peak amplitude generated using an arbitrary waveform generator (Tabor Electronics WW5061). This created a band-limited signal with 1 MHz width and peak power of –21 dBm. The unwanted tone at 12.002 GHz and power of 0 dBm was generated using the signal source of an Agilent Fieldfox N9918A microwave handheld combination analyzer. The two RF signals were combined and supplied to an electro-optic modulator using a 1.7 GHz to 36 GHz microwave combiner (Krytar). We analyzed the filter output RF spectrum using the N9918A microwave combination analyzer with a span of 50 MHz and 100 Hz resolution bandwidth.

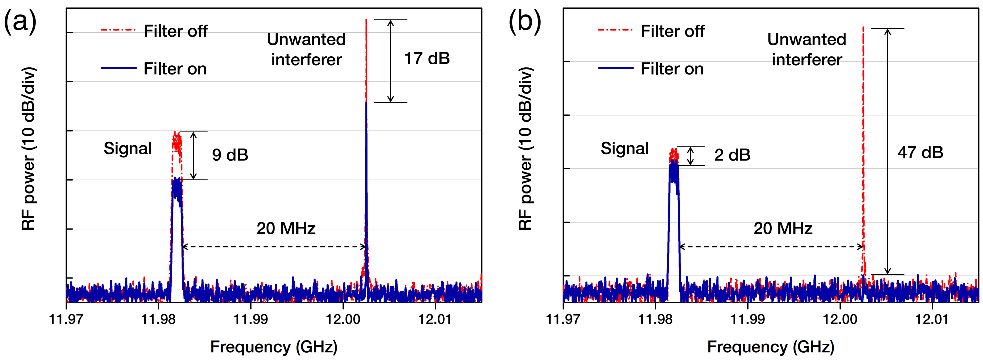

Figure 8.14: High resolution RF filtering experiment. Two RF signals with 20 MHz frequency separation were used at the filter input. (a) Filtering with conventional single-sideband scheme with 17 dB SBS loss as optical filter. Peak attenuation at the unwanted interferer tone was 17 dB, and signal attenuation was 9 dB. (b) Filtering with the cancellation filter using 4 dB of SBS gain. Complete reduction of unwanted interferer was observed with low attenuation of the desired signal (2 dB).

We compare the filtering performance of this input spectrum between a conventional SSB filter and the cancellation filter. The SSB filter was generated using SBS loss with 28 dBm pump power at the chip facet creating 17 dB of peak suppression. The cancellation filter was created using 4 dB of SBS gain from 21 dBm of pump power at the chip facet. The chip insertion loss in these measurements was 8.8 dB. In both measurements the filter response was aligned to have maximum suppression at the unwanted tone frequency of 12.002 GHz.

The measured output RF spectra with and without the SBS pump in the conventional SSB filter are depicted in fig. 8.14a. As expected the unwanted tone power was reduced by 17 dB, but the signal attenuation was as high as 9 dB, which indicated that the conventional filter resolution was below 20 MHz. This clearly demonstrates the limitation of the conventional approach which cannot simultaneously achieve high resolution and high suppression filtering. In contrast, this can be achieved using the cancellation filter, as shown in fig. 8.14b. The measured interferer suppression in this case was 47 dB, limited by the noise floor of the measurements. The signal underwent a low attenuation of 2 dB, indicating that the half-width at half-maximum of the filter was below 20 MHz.

8.4.4 Insertion Loss Reduction Experiment

For various reasons, such as photosensitivity [400], heating [94], or intensity-dependent losses [103], many on chip devices are not suited to handle high optical power. These devices are thus expected to work with a stringent optical power budget. Here, we investigate and compare the overall performance of the conventional SSB filter and the cancellation filter under a total optical power budget of the order of 400 mW at the facets of the chip. Such a power was chosen to optimise long term operation and stability of the chip based filter. We quantify the filter performance in terms of peak suppression, resolution, and RF-to-RF filter insertion loss.

In the case of the conventional SSB filter we distributed the optical power as follows: 25 dBm (316 mW) as the SBS pump and 20 dBm (100 mW) as the (probe) modulated optical carrier power. Higher pump power was chosen to maximise

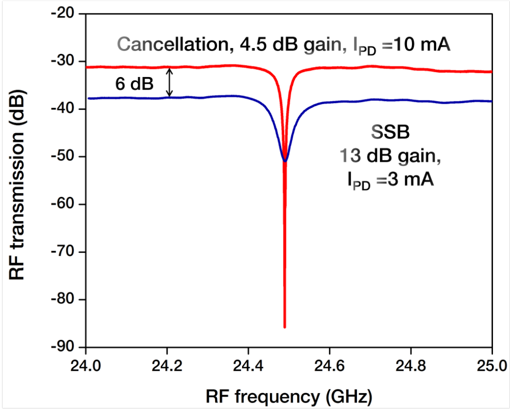

Figure 8.15: Filter insertion loss reduction. Experiments for an optical power budget of 400 mW at the facets of the optical chip. Blue trace: Conventional single sideband approach with 25 dBm of input pump power and 20 dBm of probe power. Red trace: Cancellation approach with 20 dBm of pump power and 25 dBm of probe power. I_{PD} : detected photocurrent.

the suppression of this filter. The insertion loss of the photonic chip in these experiments was 9.3 dB. We generated an RF filter with 13 dB suppression and a resolution of 100 MHz. The measured RF insertion loss was –37.7 dB, obtained using 3 mA of detected photocurrent. The measured response centered at frequency of 24.5 GHz is shown in fig. 8.15 (blue trace). We then reversed the optical power distribution between the pump and the probe in the case of the cancellation filter. With 100 mW of pump power we generated 4 dB of SBS gain. The filter response exhibited 55 dB of peak suppression and a resolution of 40 MHz. The detected photocurrent increased to 10 mA due to higher optical carrier power,and an RF filter insertion loss of –31.3 dB was measured which is a 6.3 dB improvement compared to the case of the conventional SSB filter.

The results of these experiments demonstrate that in the case of limited power budget, the cancellation filter allows re-distribution of optical power from pump to probe waves, thereby reducing the insertion loss of the filter, with improved peak suppression and resolution compared to the conventional filtering approach. Combined with a higher power handling photonic chip and a photodetector that can handle higher photocurrent, the cancellation filter can potentially achieve very low insertion loss in addition to the high suppression, high resolution, and wide frequency range - a combination very difficult to achieve using any existing RF or MWP filtering approach. Using such an approach, and with an advanced version of the cancellation scheme, researchers have recently created a lossless RF photonic filter [495].

8.4.5 Discussion of As_2S_3 Chip Filter Results

We compared the overall performance of the SBS-on-chip cancellation filter to other state-of-the-art integrated filter technologies. This is summarized in Table 8.1. First, the SBS-based filter uniquely combines salient features of two different MWP filter classes; high rejection levels typical of a multi-tap filter, and wide frequency tuning typical of resonance-based filters. In terms of linewidth, our filter is unmatched by any other integrated MWP approach, achieving nearly two orders of magnitude higher resolution. In fact, such a high resolution is more akin to low-loss electronic filters [560, 562, 588, 589]. However, for the same resolution and rejection level, the SBS filter achieves 36 times wider tuning range compared

Table 8.1: Performance comparison of state-of-the-art microwave band-stop filter technologies

Technology	Class	Size	Line-width (MHz)	Depth (dB)	IL (dB)	Max Q	Tuning Range (GHz)	(%)
This Work	MWP	cm	33-88	>55	-30	375	1-30	2900
Photonic Crystal[564]	MWP	mm	1000	>50	-45	NA	10-30	200
Frequency Comb[565]	MWP	km	170	>60	-40	NA	0-12	NA
Si_3N_4 ring[586]	MWP	mm	250-850	>60	-30	28	2-8	300
Silicon Ring[566]	MWP	mm	910	>30	NA	16	2-15	650
Silicon Ring[567]	MWP	mm	6000	>40	NA	1.84	2.5-17.5	600
MEMS-absorptive[587]	Elec	cm	35/306	>35	-2	128	4-6/6-11	80
MEMS-resonator[588]	Elec	cm	77	>24	-0.8	90	8.9-11.3	27
RF resonator[562]	Elec	µm	710	>50	-2	6	2.9-4.3	48
MEMS-absorptive[560]	Elec	cm	9.7	>30	-0.3	345	3.4-3.8	11

to the best performing electronic RF filter reported very recently [587]. Overall, our filter showed the highest quality factor ($Q = 375$) and the fractional tuning range (2900%) compared to any integrated filter technology to date. Here, the Q-factor is defined as the ratio of the filter 3-dB bandwidth to the central frequency of the resonance, while the fractional tuning range is defined as the ratio of the frequency tuning range to the lowest center frequency of the stopband. Note that this measured Q value is higher than previously reported values ($Q = 134$) in fiber-based SBS MWP filter [484].

The lowest insertion loss measured in our filter was –30 dB, which is lower than typical losses in integrated MWP filters [564, 565] but is high compared to electronics solutions. This loss can be recuperated using two approaches: reducing chip-coupling loss and reducing the loss in the underlying photonic link. Lower chip coupling loss, of the order of 1.1 dB per facet, can be achieved in optical waveguides with inverse tapers [127]. Photonic link loss can be minimized by using an RF modulator with lower half-wave voltage (V_π), higher power laser source, and a higher power handling detector [544, 590]. Realistically, the insertion loss figure can be improved by 28 dB using the waveguide with inverse tapers, a modulator with half the , and a high photodetector current of 40 mA. This will lead to –2 dB insertion loss which is comparable to electronic RF filters, and is crucial to realize a filter with low noise figure and high spurious-free dynamic range (SFDR) [537, 591]. Such an improvement in the insertion loss will lead to a filter technology with all-optimized properties that is essential in modern RF systems and applications.

The filter central frequency stability in our setup is presently limited by the wavelength drifts of the pump and probe lasers. On the other hand, the stopband suppression stability is limited by the bias drifts of the electro-optic modulator. Stability improvement can be achieved by using a single laser as both pump and probe and to operate the modulator using a bias control circuitry. One can also satisfy the cancellation conditions using a phase modulator and a broadband optical filter, which will then operate bias free, to process one of the sidebands completely before interaction with the Brillouin scattering [592].

8.5 Comment: Comparison with Zhang and Minasian

At first glance, the initial implementation behind the cancellation filter looks similar to a body of work performed by, coincidentally, another group based in the University of Sydney [484, 593]. To provide clarity around this point, in the following we will briefly describe the circumstances under which the cancellation filter was initially explored at the start of 2013.

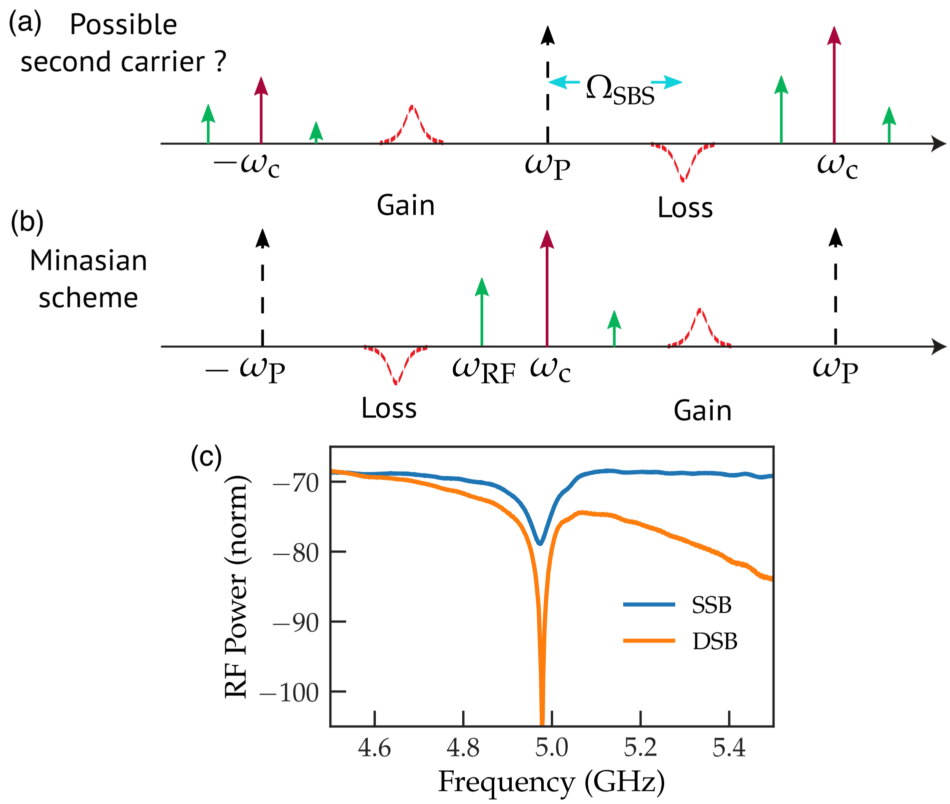

Figure 8.16: (a) Optical configuration when cancellation was first observed (b) Scheme of Zhang and Minasian [484] (c) Experimental measurements showing unexpected deep notch when second sideband was introduced.

The first results leading to the realisation of the cancellation filter were observed in February 2013. While performing the experiments outlined in section 8.2, B. Morrison, early into his studies and unaware of the broader literature, found that for some bias points of the DPMZM the measured filter response would suddenly, and significantly, increase in suppression. Following a number of discussions with D. Marpaung and R. Pant, the connection was made between the experimental observations and the recently published work of Zhang and Minasian [484]. However, the configuration in the experiment was quite distinct from that in the work of [484], where one RF sideband is processed with Brillouin gain and the other with Brillouin loss. Initial observations were presented in a wider group meeting on the 23rd February, and are shown in fig. 8.16.

Further experiments in the following weeks solidified and confirmed the initial observations. Following an intense discussion between B. Morrison, D. Marpaung and R. Pant, the realisation was formed that the observed cancellation was occurring due to the optical interaction with one sideband, while the other remained *unchanged*. This seemingly minor detail leads to a number of unique configurations and observations, as discussed in section 8.3.1. In particular, it became apparent that the conditions for localised cancellation could be met with a range of optical filters, not just Brillouin scattering. With this general understanding developed we have applied the cancellation technique to a broad range of devices and scenarios, including the passive ring resonator and forward Brillouin system discussed in the next chapter.

Chapter 9

Cancellation Filters with MPW Platforms

In the previous chapter we explored the use of Brillouin scattering to create a microwave photonic notch filter. We introduced a new scheme, the cancellation technique, enabling high filter suppression which is independent of the depth of the original optical response. In this chapter we apply the cancellation concept to two multiproject wafer platforms; silicon on insulator (SOI) from IMEC and Si_3N_4/SiO_2 (TriPleX) from LioNiX. For the SOI devices we utilise forward Brillouin scattering (FBS) in suspended nanowires, requiring a modification to the cancellation scheme. For the Si_3N_4 waveguides we explore the benefits the cancellation scheme provides to tunable ring resonators.

This chapter has sections based on the following publications:

9.2 A. Casas-Bedoya, **B. Morrison**, M. Pagani, D. Marpaung, B. J. Eggleton, "Tunable narrowband microwave photonic filter created by stimulated Brillouin scattering from a silicon nanowire", Optics Letters **40**, 4154 (2015)

9.3 D. Marpaung, **B. Morrison**, R. Pant, C. Roeloffzen, M. Hoekman, R. Heideman, B. J. Eggleton, "Si3N4 ring resonator-based microwave photonic notch filter with an ultrahigh peak rejection", Optics Express **21**, 23286 (2013)

9.1 Nonlinear Losses and Brillouin Scattering in Silicon

Silicon on insulator (SOI) is the current dominant platform for integrated optics due to its ease of fabrication and ability to be interfaced with silicon electronics. As discussed in section 3.2.1, for nonlinear optics silicon is quite attractive due to its large nonlinear refractive index and the ability to dope and control electrical carriers in the material. However, the generation of free carriers by two photon absorption at the telecommunications wavelength makes nonlinear optics quite problematic. Furthermore, the requirement of acoustic confinement for Brillouin scattering introduces further difficulties when using silicon, due to acoustic leakage into the SiO_2 substrate. In the following we discuss nonlinear losses and Brillouin scattering in silicon waveguides. For an overview of the historic developments of Brillouin scattering in silicon waveguides we refer the reader to section 2.4.2 and the thesis of Raphael Van Laer.

9.1.1 Brillouin Scattering with Nonlinear Losses

To understand the effects of nonlinear losses we consider the light attenuation through a waveguide in the presence of linear loss, two photon absorption (TPA) and free carrier absorption (FCA) [594, 595]. In the case of continuous wave (CW) pumping, or for optical pulses longer than the carrier lifetime, the reduction in optical power along the waveguide is given by

$$\frac{\mathrm{d}P(z)}{\mathrm{d}z} = -\alpha P(z) - \frac{\beta_{\mathrm{TPA}}}{A_{\mathrm{eff}}} P^2(z) - \sigma N(z) P(z) \tag{9.1}$$

where α is the linear loss coefficient, β_{TPA} is the TPA coefficient (at the wavelength of interest), σ is the free carrier cross section and $N(z)$ is the free carrier density. If the system has reached steady state, then $N(z)$ is determined by

$$N(z) = \frac{\beta_{\mathrm{TPA}} \lambda_{\mathrm{p}} \tau}{2hc} \frac{P^2(z)}{A_{\mathrm{eff}}^2}$$

where λ_{p} is the pump wavelength and τ is the carrier lifetime. In certain limits the above can be solved analytically [596], but in the general case a numerical solution to the eq. (9.1) is required. Individual parameters can vary depending on the waveguide geometry, fabrication process and operating wavelength. For 450 nm $\times$ 220 nm SOI nanowires from IMEC at 1550 nm typical parameters are; $\alpha = 2.25\,\mathrm{dB\,cm^{-1}}$, $\beta = 1.03 \times 10^{-11}\,\mathrm{m\,W^{-1}}$, $A_{\mathrm{eff}} = 0.1 \times 10^{-12}\,\mathrm{m^2}$, $\tau = 5 \times 10^{-9}\,\mathrm{s}$ and $\sigma = 1.45 \times 10^{-21}\,\mathrm{m^3}$. By solving the equation for a device length L, and varying the coupled pump power at $P(0)$, the excess nonlinear loss can be determined for a range of power levels. We compare the calculated and measured nonlinear loss for a silicon nanowire with 2.5 cm length in eq. (9.1). For coupled power levels beyond 50 mW the output power is completely saturated, as shown by the linear increase in total loss.

Equation (9.1) describes the attenuation of a single optical wave due to these multiple loss sources. When performing nonlinear optics the situation becomes more complicated. We will have multiple optical waves exchanging power along the medium through the respective nonlinear interactions, such as Kerr or Brillouin, while also being attenuated by a varying amount [595]. Wolff investigated this problem, numerically and analytically, using a coupled wave framework for the Brillouin and nonlinear interactions [107, 108]. A figure of merit is derived

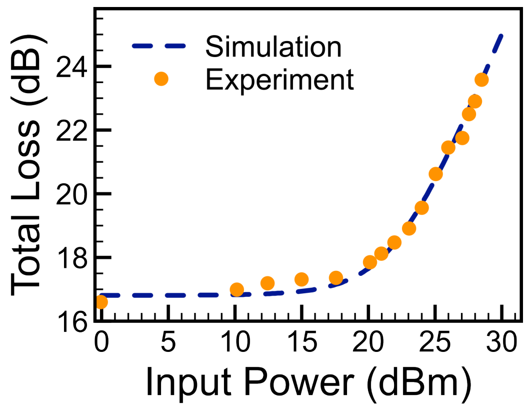

Figure 9.1: Nonlinear losses in a 2.5 cm long silicon nanowire

that can determine whether net amplification is possible, and the maximal gain available. It was found that to minimise the effects of nonlinear losses, for fixed material parameters, the use of long waveguides with low linear losses is the most viable approach. A similar strategy has been found when investigating the generation of idler waves using four wave mixing in the presence of nonlinear losses [532].

9.2 FBS in Silicon Based Cancellation Filter

Brillouin scattering is a light-sound interaction process that occurs when photons are scattered from a medium by induced acoustic waves [140][1]. Stimulated Brillouin scattering (SBS) is the strongest nonlinear process and manifest optically in ultra-narrow resonances, which have been harnessed in optical fibers for slow light, sensing, and laser applications [419, 489, 597–599]. Recently, there has been strong interest in harnessing SBS in integrated platforms and unlocking functionalities unreachable by other means [133]. This has been demonstrated in various glasses such as silica or chalcogenides [124]. Although impressive results were achieved, these devices cannot be monolithically integrated with on-chip electro-optic modulators and photodetectors, which are readily available in silicon [600], to create a compact tunable filter.

Unfortunately, for the CMOS-compatible silicon-on-insulator (SOI) platform, SBS has been elusive. The low elastic mismatch between the silicon core and the silicon dioxide substrate result in weak acoustic confinement, preventing build-up of the SBS process. To remedy this, a recent demonstration employed a hybrid approach to remove the substrate while holding the nanowire with Si_3N_4 [96]. Although these result harnessed SBS in Si nanowires, they required an extra material and fabrication step, increasing overall complexity.

A recent breakthrough achieved forward propagating Brillouin scattering FBS in a silicon nanowire [103] by partially releasing the nanowire from its substrate. Here, they showed that Brillouin interactions are enhanced at the nanoscale by radiation pressure contributions [95, 100, 103] and verified that electrostriction (a material property) in combination with radiation pressure (a geometrical property) increases the SBS gain. The amount of SBS gain that was reported, including this geometrical enhancement and novel fabrication methodology, was limited

[1]Parts of the following section have been published in *Optics Letters*: A. Casas-Bedoya et al., "Tunable narrowband microwave photonic filter created by stimulated Brillouin scattering from a silicon nanowire", Opt. Lett. **40**, 4154 (2015)

to around 4 dB [103], which is hardly usable for conventional signal processing applications.

In this paper we report the first functional device for signal processing based on SBS from a silicon nanowire. We employ a novel cancellation technique [447, 581] to harness this modest SBS gain in silicon, creating a high performance microwave photonic notch filter. We use only 0.98 dB of on-chip SBS gain to create a cancellation microwave photonic notch filter with 48 dB of suppression, 98 MHz linewidth, and 6 GHz frequency tuning. This demonstration establishes the path towards monolithic integration of high performance SBS microwave photonic filters in a CMOS compatible platform such as SOI.

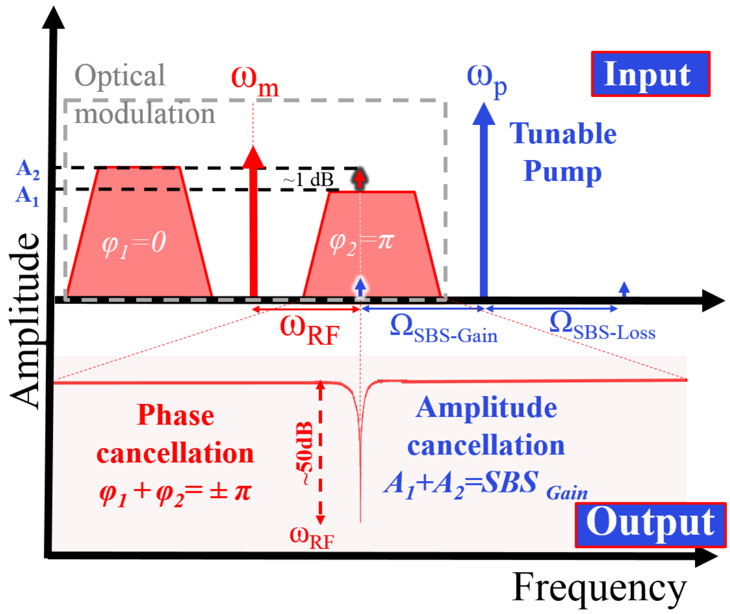

Figure 9.2: Radio frequency cancellation technique and working principle of the tunable narrowband microwave photonic filter created by SBS

9.2.1 Scheme and Characterisation

Figure 9.2 summarizes the RF cancellation technique and working principle of the narrowband microwave photonic filter created by SBS. Initially reported in [483], the technique uses heterodyne photodetection to generate two RF mixing products between an optical carrier (ω_m) and two modulation sidebands. These two mixing products, having the same frequency, interfere. Destructive interference however occurs only at the frequency (ω_{RF}) where the optical sidebands have the same amplitude (A) and are in antiphase ($\varphi_2 - \varphi_1 = \pm\pi$). This particular amplitude/phase relationship between the sidebands is achieved through SBS ($\Omega_{\mathrm{SBSGain}}$) on one of the sidebands. Therefore, in a frequency range equal to the SBS linewidth, the RF mixing products interfere destructively, resulting in a very narrowband, high-suppression electrical notch response. The centre frequency of this notch response can be tuned simply by changing position of the SBS resonance on the optical sideband, i.e. tuning the SBS pump wavelength (ω_{p}).

The silicon nanowire was fabricated at IMEC through ePIXfab. The nanowires were immersed in 10% diluted hydrofluoric acid with an etching rate of 40 nm/min for 5.2 min to partially release them from the silica substrate. This created a 1.25 cm silicon nanowire with a cross section of 220 by 480 nm which was supported by a silica pillar of 50 nm width [Fig (9.3-top)]. As reported in [103], such structure restricts the phonon leakage and guarantees high confinement of the optical and acoustic modes allowing an efficient SBS interaction.

We proceeded with the optical characterization of the structure. We coupled 1550 nm transverse-electric (TE)- polarized light using focus grating couplers [601] into the chip and measured 5.2 dB coupling loss. We used an optical frequency domain reflectometer (OFDR) to study the losses of our nanowire [434]. This methodology infers the time-domain response via Fourier transform from a modulated backscatter signal and consequently allows accurate measurement of the length of the nanowire and propagation losses as shown in Fig 9.3(a). Here, the first reflection peak is observed 722 cm away from the source. This length corresponds to the total length of our optical fibres just before the chip. The second reflected peak is observed 2.5 cm apart from this first reflection. This value corresponds to twice the length (L) of the nanowire as light is being reflected from the second grating coupler. Propagation losses (α) are also obtained with this technique by simply measuring the slope between both grating couplers reflections. This leads to an α= 2.06 dB cm^{-1} and an thus an effective length, $L_{\text{eff}} = (1 - \exp(-\alpha L))/\alpha = 0.94$ cm.

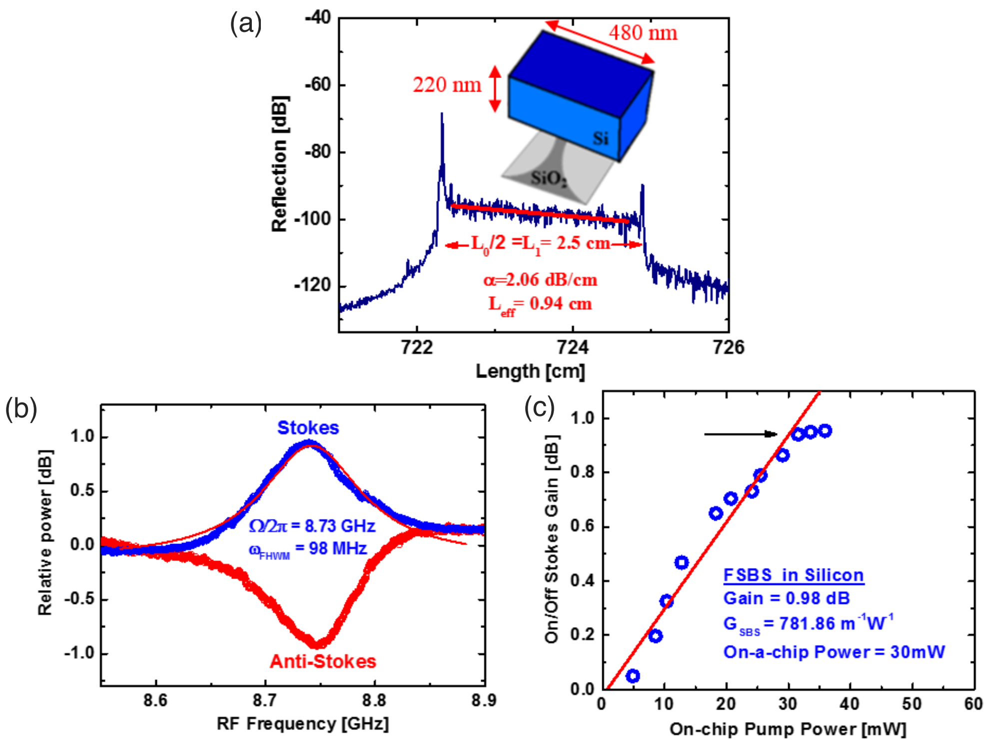

Figure 9.3: (a) Optical frequency domain reflectometer measurement of a 1.25 cm silicon nanowire. (Top-figure) Schematic representation of a partially suspended Silicon nanowire. Note that during this work we achieved a 50nm pillar width. (b) Measured Stokes (blue) and anti-Stokes (red) FBS frequency (c) Maximum Brillouin gain versus input pump power. The arrow indicates the SBS gain saturation at 30 mW due to nonlinear absorption. The red solid line is the fit performed to obtain the Brillouin gain coefficient (G_{SBS}).

We then measured the SBS gain response of the structure. With 30 mW of coupled pump power, we achieved a 0.98 dB of FBS gain, which was the highest gain we measured in our structure. The measured Stokes and anti-Stokes have a Lorentzian profile at $\Omega/2\pi$= 8.73 GHz and are combined and plotted in Fig.

9.3(b). The calculated linewidth was fitted with a Lorentzian curve (red solid line) and calculated to be $\Gamma/2\pi$ = 98 MHz. This leads to a quality factor of Q_m= 89.09 and a phonon life time $\tau = 1/\Gamma = 1.6$ ns.

We measured the maximum stokes gain for different pump powers and plot them in Fig 2 (c). On resonance, the maximum Brillouin gain as function of Pump power, P_p, is:

$$P_s(L) = P_s(0)\exp\left(G_{SBS}P_pL_{eff}\right), \tag{9.2}$$

where $I_s(L)$ and $I_s(0)$ are the probe intensity respectively at the output and input of the device [124]. We use equation 9.2 to infer the SBS gain coefficient (G_{SBS}) below nonlinear absorption saturation. Using a linear fitting in Fig. 9.3(c) we obtain a $G_{SBS} = 780\,\mathrm{m\,W^{-1}}$. This relatively low value is due to the phonon leakage through the post-processed Silica pillar [103]. However, we emphasise that creating notch filter do not require an ultra-high SBS gain or high pump powers. In fact we show below how using a modest SBS gain and the elegant RF cancellation technique we create a CMOS-compatible cancellation filter.

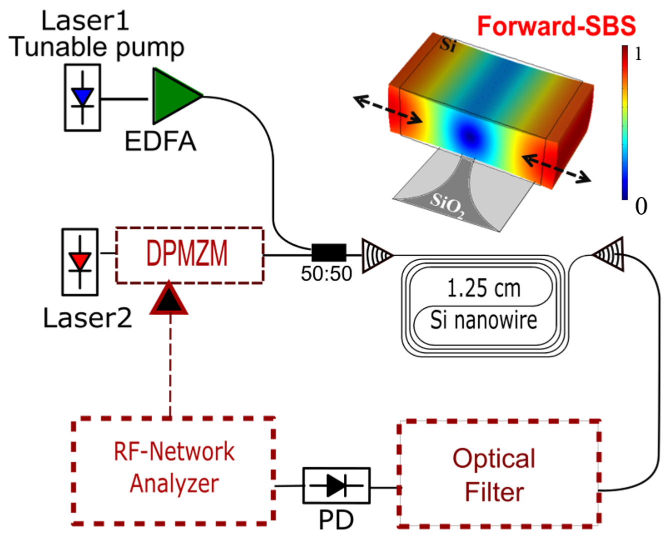

Figure 9.4: Set-up of the notch filter experiment. DPMZM: dual-parallel Mach-Zehnder modulator, PD: photodetector. (Top-right) Simulated transversal acoustic displacement, or forward SBS, from a silicon nanowire

9.2.2 Cancellation Filter with FBS

The experimental setup employed to create our notch filter relies on forward SBS. Therefore our measurement is based on transmission, not reflection as in [447], leading to a relatively simpler setup with less components. This approach is depicted schematically in Fig 9.4. Here, using a dual-parallel Mach-Zehnder modulator (DPMZM), a CW optical carrier is modulated with the input RF signal. The DPMZM bias is set such that the modulation sidebands are π out-of-phase, and with amplitude mismatch of 1 dB. The modulated carrier and the SBS pump then co-propagate along a 1.25 cm Si nanowire. The SBS pump frequency and power are set so that a FBS 0.98 dB gain resonance is induced on the weaker sideband. In this way, only at the center of the SBS gain the modulation sidebands have equal amplitude, as well as being π out-of-phase. The SBS pump is then removed using a bandpass filter, which selects the modulated carrier and sends it to a photodetector (PD). Upon photodetection, the sidebands and the carrier mix, resulting in the output RF signal. However, only in the center of the SBS gain the sideband reach equal amplitudes and the mixing products interfere destructively. This creates a high-suppression (>48 dB) notch response despite the low FBS gain, as shown in Fig. 9.5(a).

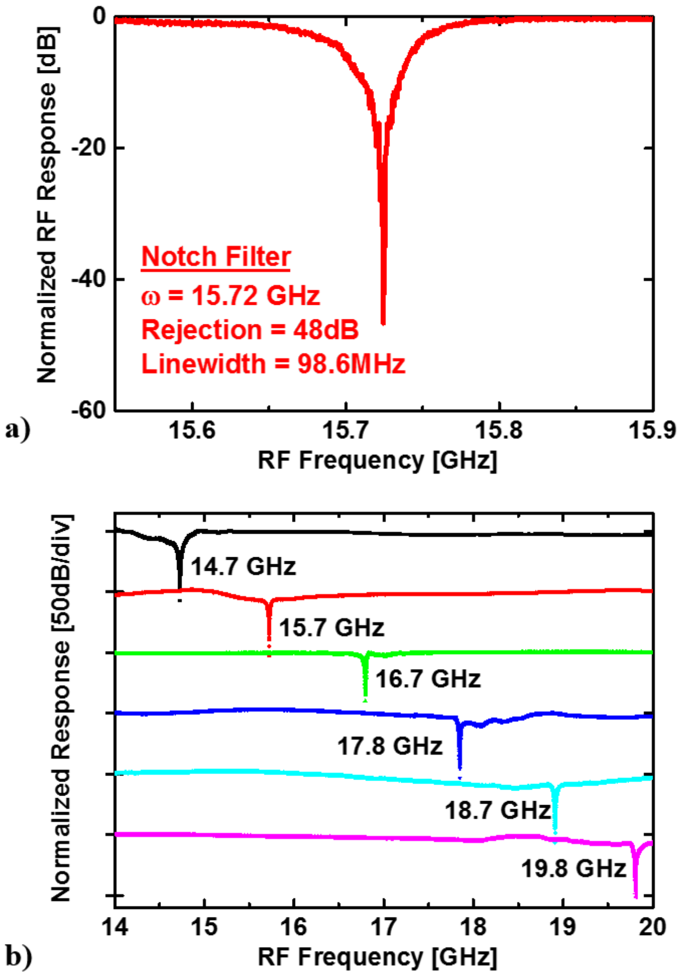

Figure 9.5: (a) Measured RF notch filter response at 15.72 GHz (b) Filter frequency tuning where the suppression was kept above 48 dB in all measurements

The centre frequency of the notch in the RF domain can be tuned simply by changing the frequency of the SBS pump. This tunability in principle, makes the filter frequency immune to small changes in the Stokes frequencies that could arise from external factors such as temperature variations. As shown in Fig. 9.5(b), we were able to continuously tune the notch frequency over a 6 GHz range, while maintaining the notch suppression above 48 dB. The 6 GHz tuning range achieved during this experiment was limited by the band-pass filter. Here, we use a filter with a 3dB bandwidth of 42 GHz centred at the optical carrier. As a consequence, the maximum accessible RF bandwidth was around 21 GHz while the lower frequency was determined by the filter roll-off and its ability of efficiently removing the SBS pump.

9.3 Si_3N_4 Ring Resonator Based Cancellation Filter

So far, we have demonstrated notch filters using Brillouin scattering and shown how the cancellation technique is capable of enhancing the suppression of the resulting microwave filter. In this section we apply the cancellation technique to a reconfigurable ring resonator, and highlight the benefits the scheme brings to this device[2]. A brief overview of waveguide based ring resonators is provided in section 6.1.1.

9.3.1 Tunable Coupling in Integrated Resonators

The depth of a ring resonator response is dependant on the round trip losses a and coupling coefficients, cross coupling κ and self coupling t. To achieve zero transmission in a ring with a single coupler, the self coupling needs to precisely match the round trip losses, i.e $t = a$. Due to fabrication imperfections this is difficult to achieve in planar circuits, and thus being able to reconfigure the coupling coefficients after device fabrication is highly beneficial. One way to achieve this is replacing the resonator coupling element, typically a directional coupler, with a reconfigurable Mach-Zehnder interferometer [461, 602]. The phase shifting mechanism can vary depending on the material platform, however the thermo-optic effect is one of the most commonly used due to the ease of integration of heating elements [603]. By altering the phase difference between the arms of the interferometer, the κ and t can be reconfigured. This allows for precise matching of the and high extinction ratios. If required, these reconfigurable couplers can be designed to enable broadband wavelength operation [604].

9.3.2 Limitations of Conventional Notch Filter

As we explored in the previous chapter, the simplest way to use an optical resonance as a tunable notch filter is by employing a single-sideband (SSB) modulation scheme, where the optical resonance is used to remove a portion of power in the optical sideband. This filtered optical spectrum is then mapped into the microwave spectrum via mixing with optical carrier during photodetection process. So far we have focused on the use of Brillouin scattering in this way, which suffers from this approach due to the requirement of large optical powers to achieve deep suppression. In this section following we will look at the limitation of the SSB approach when using an optical ring resonator.

A schematic of an all-pass ring resonator [462, 605], with the definition of the cross-coupling amplitude coefficient, κ, is shown in fig. 9.6a. By tuning κ, the magnitude and phase response of the ring can be reconfigured, as show in fig. 9.6b. The simplest way to use the ring resonance as a tunable notch filter is by employing a single-sideband (SSB) modulation scheme, where the optical resonance is used to remove a portion of power in the optical sideband. This filtered optical spectrum is then mapped into the microwave spectrum via mixing with optical carrier during photodetection process. This mechanism is illustrated in in fig. 9.6c.

From a notch filter perspective, tuning κ will change the filter bandwidth (full-width at half maximum, FWHM), and peak rejection, as depicted in fig. 9.6b.

[2]Parts of the following section have been published in *Optics Express*: D. Marpaung et al., "Si3N4 ring resonator-based microwave photonic notch filter with an ultrahigh peak rejection", Opt. Express **21**, 23286 (2013)

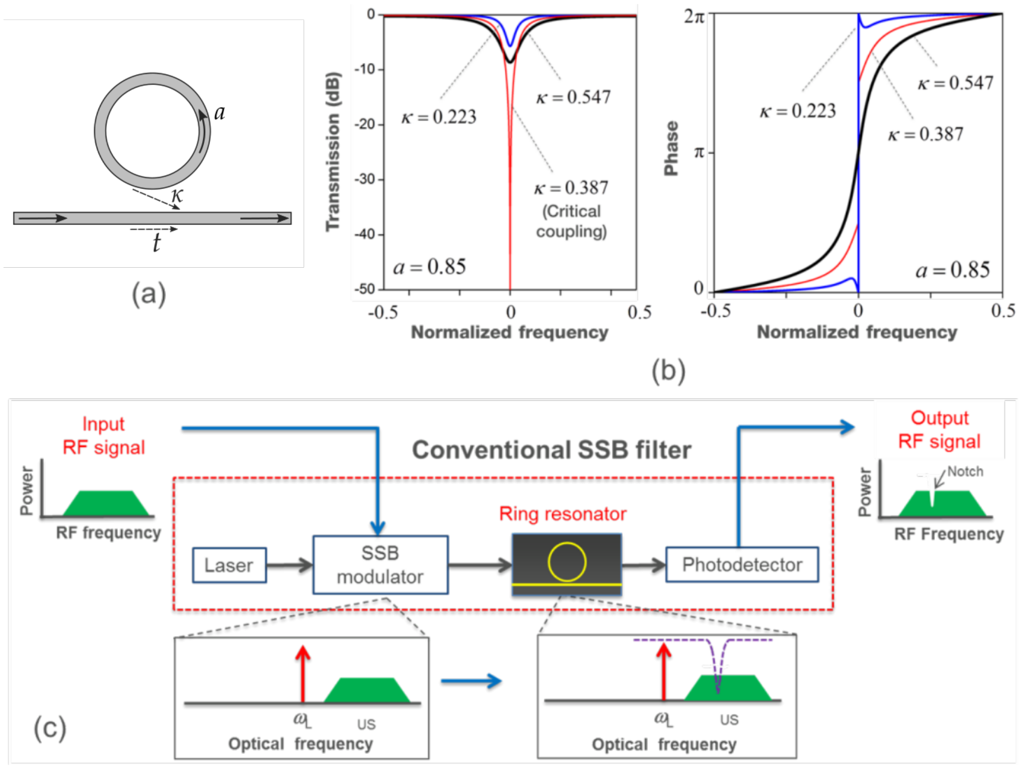

Figure 9.6: (a) All pass ring resonator, with the definition of the tunable coupling coefficients and loss. (b) Simulated transmission and phase response of a ring resonator with varied coupling coefficient. (c) Schematic of a conventional single sideband (SSB) notch filter where the optical resonance of the ring resonator is mapped to the microwave frequency to exhibit a notch filter response.

Given a ring resonator with a round trip length L, a round-trip loss a, and a self-coupling coefficient, t, where t^2=1+κ^2, the peak rejection at resonance is given by [462]

$$T_{\mathrm{p}} = \frac{(a-t)^2}{1-2at+(at)^2} \tag{9.3}$$

While the FWHM is given by

$$\mathrm{FWHM} = \frac{\lambda_{\mathrm{r}}^2(1-ta)}{\pi n_{\mathrm{g}} L\sqrt{ta}} \tag{9.4}$$

Here n_{g} is the group index and λ_{r} is the resonance wavelength.

For a given resonator loss (fixed a), according to eq. (9.3), the peak rejection of the filter is maximized when t=a, a condition known as critical coupling. On the other hand, according to eq. (9.4), the FWHM is minimized when t=1. For a non-lossless resonator, a is always smaller than unity (a<1), which means that in such a resonator one cannot simultaneously achieve minimum FWHM with maximized peak rejection. Thus, there is a trade-off between resolution and peak rejection for a conventional SSB-ring resonator microwave notch filter. For a low loss resonator, the FWHM at critical coupling is twice of the minimum FWHM.

This trade-off is clearly illustrated when we plot the peak rejection and FWHM for various values of κ as shown in fig. 9.7. In this simulation, we use parameters that correspond to the ring used in the experiment as the following: λ_{r}=1550 nm, L=8.783 mm, n_g=1.72, and a=0.974, which is equivalent to loss per unit length of 0.13 dB/cm. The minimum calculated FWHM of the ring was 166 MHz, which corresponds to an optical Q-factor [462] of 1.16 million. However, at this narrow bandwidth, the peak rejection is very low (< -0.5 dB). When κ increases, the FHWM monotonically increases but the peak rejection improves until it reaches maximum at critical coupling (κ=0.226), where the FWHM has doubled to 332 MHz.

We performed experiments using a Si_3N_4 racetrack ring resonator with a radius of 125 µm and a total path length of 8.783 mm. The ring was fabricated using the TriPleX^{TM} low-loss waveguide technology with double-stripe geometry [492, 606]. The group index of the optical waveguide was 1.72, leading to a free-spectral range of 19.8 GHz at 1550 nm, The propagation loss of the waveguide was previously reported in the order of 0.1 dB/cm [606]. Two chromium heaters were deposited on top of the waveguide layer to enable thermo-optics tuning [576, 606] to control the power coupling to the ring and the resonance frequency. The insertion loss of the ring away from the resonance wavelength was measured to be 13 dB, which was achieved by butt-coupling of standard single mode fibers. Using a setup as shown in fig. 9.6c, we measured the down-converted ring magnitude response in the RF spectrum for various values of κ. For each measurement, we put the measured peak rejection along theoretical curve in fig. 9.7, and we compared the measured FWHM with the calculated one. There is a good agreement between the measured and the simulated values. The lowest FWHM from our measurements was 238 MHz, which correspond to an optical Q=814,000. At this bandwidth, the filter peak rejection was only -6.2 dB, which is not sufficient for a microwave notch filter.

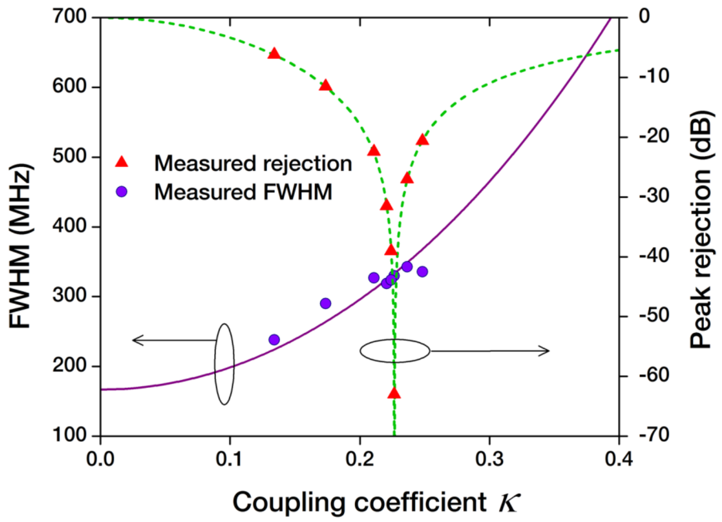

Figure 9.7: Simulated and experimentally measured FWHM and peak rejection for the notch filter using Si_3N_4 ring resonator with parameters: λ_r=1550 nm, L=8.783 mm, n_g=1.72, and a=0.974.

9.3.3 Novel notch filter principle and experiment

The novel technique to significantly improve the peak rejection of the ring-based notch filter is shown in fig. 9.8a. Instead of processing single sideband (SSB) signals, here we generate two sidebands with tunable amplitudes and phases [483]. The RF signal is encoded in the optical sidebands with unequal amplitudes and a phase difference, $\Delta\phi$ where $0 < \text{modulo}(\Delta\phi) < \pi$, using an electro-optic modulator (EOM). We then exploit both amplitude and phase responses of the ring to equalize these sidebands amplitudes and to produce an anti-phase relation between them ($\Delta\varphi = \pm\pi$), only in selected frequency region within the ring response. Upon

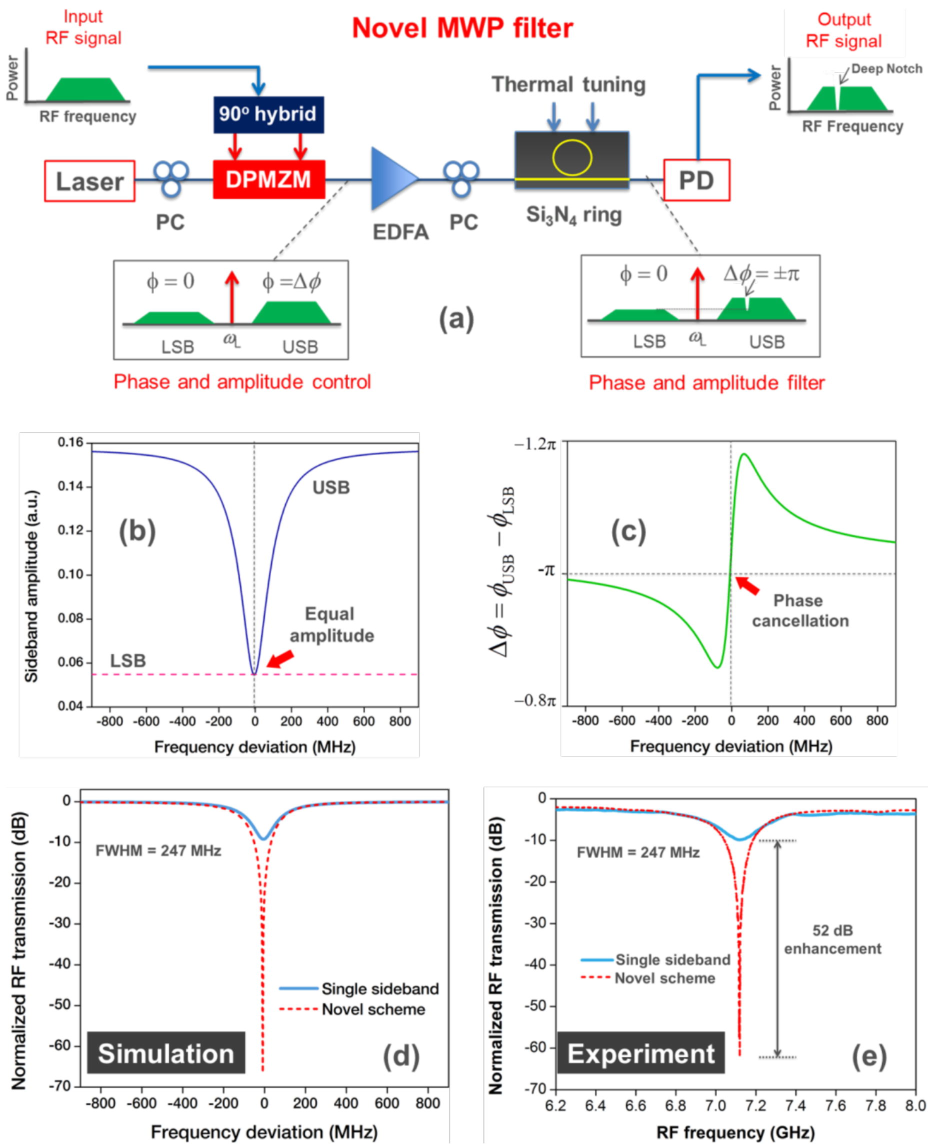

Figure 9.8: (a) Topology of novel MWP notch filter that exploits phase and amplitude responses of ring resonator to create ultra-high peak rejection. DPMZ: dual-parallel Mach-Zehnder modulator, PD: photodetector. Sidebands amplitude (b) and phase difference (c) after modification in the DPMZ and ring resonator. Simulated (d) and experimentally measured (e) notch filter response of the novel MWP filter (dashed line) and conventional single-sideband filter (solid line).

photodetection, the beat signals generated from the mixing of the optical carrier and the two sidebands perfectly cancel at a specific microwave frequency, forming a notch with an anomalously high stopband rejection [483]. This is a photonic implementation of an absorptive band-stop filter in microwaves [560–562], that exhibits quasi-infinite rejection.

The optical sidebands with tunable phase difference and amplitude ratio can be generated using a dual-parallel Mach-Zehnder modulator (DPMZM) driven through a 90º (quadrature) RF hybrid coupler [582]. Such a modulator consists of two parallel MZMs nested in a larger MZ interferometer structure with a tunable phase-modulator (PM) in one of its arms. The DPMZM has three biases, two for the MZMs (θ_{MZ1} and θ_{MZ2}) and one for the PM (θ_{PM}). We simulate the upper sideband (USB) and lower sideband (LSB) amplitudes and phase difference generated by the DPMZM at the output of our ring resonator (a=0.974, t=0.9873).

When the MZM bias angles are adjusted to be θ_{MZ1} =1.7603π, θ_{MZ2} =0.5488π, and θ_{PM} =1.879π, the conditions of equal amplitude and opposite phase of USB and LSB are met at the center of the ring resonance. The sidebands amplitudes and phase difference are depicted in fig. 9.8b and fig. 9.8c, respectively.

The simulated normalized RF transmission generated from the mixing of USB and LSB with the optical carrier is shown in fig. 9.8d, where it is compared to the filter response obtained from the conventional SSB scheme. Both filter responses have FWHM of 247 MHz, but the one generated with the novel phase cancellation scheme exhibited an ultra-high peak rejection of 70 dB, which is a 60 dB improvement from the peak rejection of the conventional SSB filter.

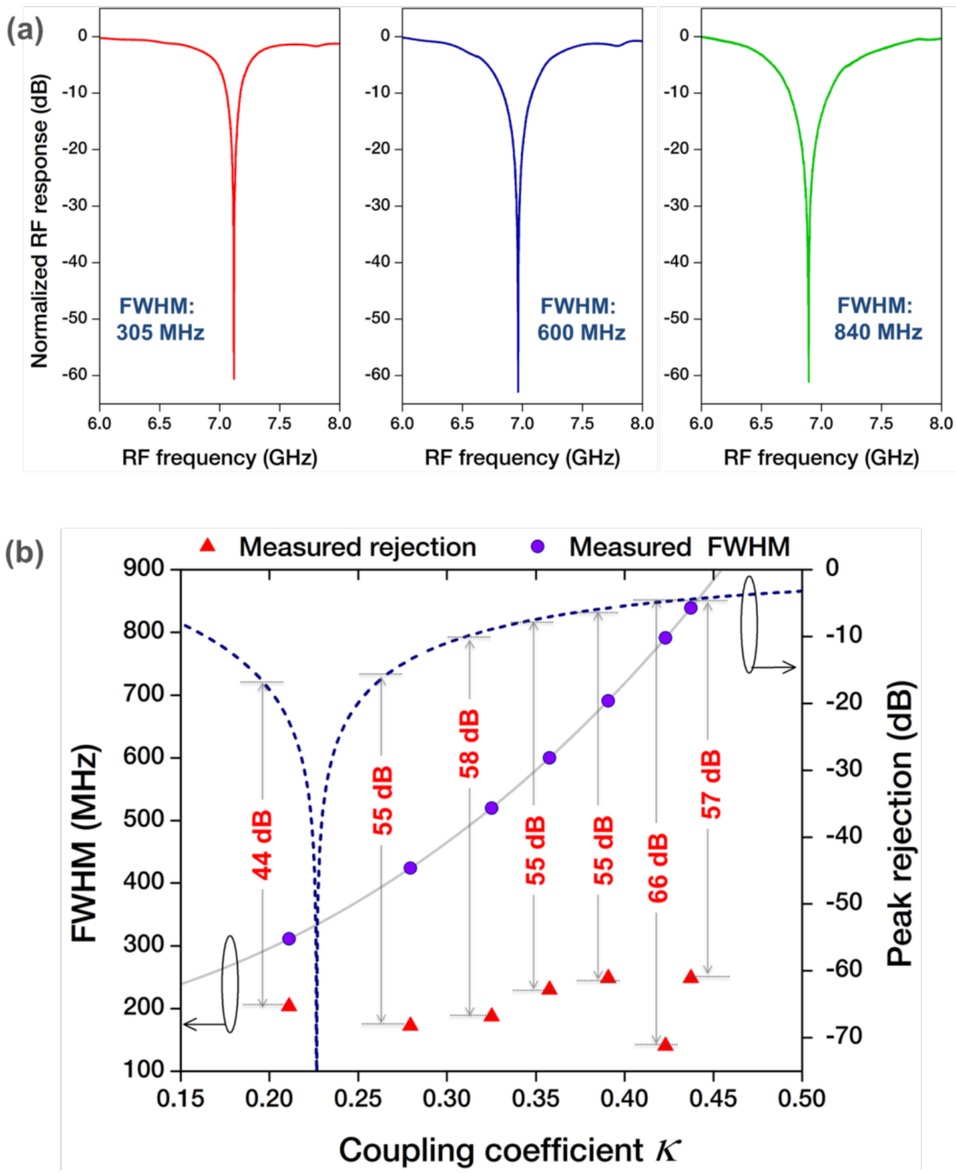

Figure 9.9: (a) Experimentally measured tunable bandwidth filter responses with at least 60 dB peak rejection. (b) Experimentally measured peak rejection of the novel MWP filter (triangle) compared to the peak rejection of a conventional SSB case (dashed curve) for various filter FWHMs.

To verify this simulation result, we performed experiments with the setup shown in fig. 9.8a. We used a 1550 nm, 100 mW DFB laser (Teraxion PureSpectrum), a 20 GHz DPMZM (Covega Mach 40-086) driven via a quadrature hybrid coupler (1.7-36 GHz, Krytar), and a high-speed photodetector (PD, u2t XPDV2120). A low noise EDFA was used to increase the optical power before coupling to the ring resonator. We thermally tuned the coupler to the ring resonator to achieve FWHM of 247 MHz. The RF filter response was measured using a vector network analyzer (VNA). To maximize filter peak rejection, we controlled the three bias voltages of the DPMZM using a multi-channel programmable power supply with 1 mV accuracy (Hameg HM7044G). The measured filter response exhibited a peak rejection of 62 dB, as shown in fig. 9.8e. This is a 52 dB improvement in peak rejection compared to the SSB filter.

Furthermore, we demonstrate a bandwidth tunable notch filter by repeating the measurements for several values of FWHM from 305 MHz to 840 MHz, as shown in fig. 9.9a. Each response exhibits a peak rejection of at least 60 dB. A slight notch frequency shift observed during the bandwidth reconfiguration was due to the thermo-optic effect. This shift can easily be compensated by tuning another heater placed on the ring waveguide path to keep the resonance frequency fixed [576]. fig. 9.9b highlights the main advantage of the novel filetering technique. Unlike the conventional SSB filter that suffers from trade-off between bandwidth and peak rejection when tuning the coupling of the ring (fig. 9.7), the novel filter shows ultra-high peak rejection for all measured filter bandwidths. We compare the peak rejection of this filter (triangles in fig. 9.9b) with the one of an SSB filter calculated from eq. (9.4) (dashed line in fig. 9.9b). The proposed filter shows impressive peak rejection enhancement, ranging from 44 dB up to 66 dB.

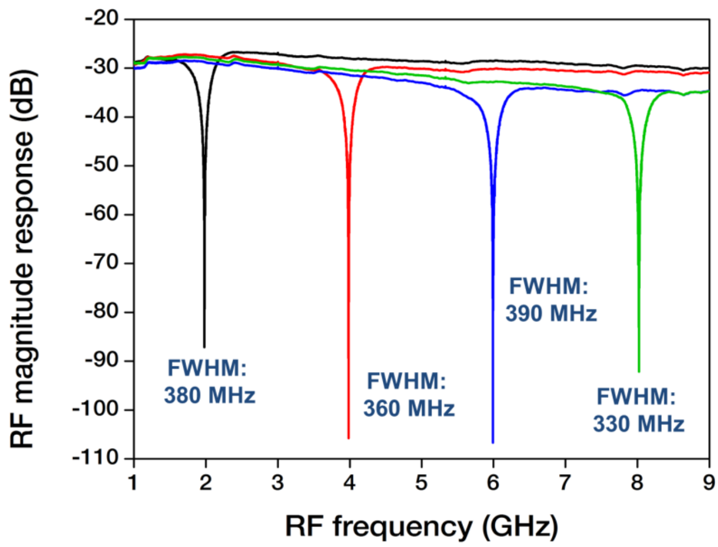

Figure 9.10: Experimental results of frequency tuning of the MWP notch filter, preserving a narrow bandwidth of 350 MHz and ultrahigh rejection of >55 dB.

Finally, we demonstrated the frequency tuning of the filter by tuning the central frequency of our laser. Since the FSR of the ring is 19.8 GHz and we essentially use a double sideband modulated signal, the filter tuning range is half of the FSR, which is 9.9 GHz. The tuned filter response in the range of 1-9 GHz is depicted in fig. 9.10. The insertion loss of the filter was in the order of -30 dB, which comprised the insertion loss of the DPMZ and the ring. The passband flatness degradation of the filter at higher frequency was attributed to the slope of the DPMZ frequency response. Over this tuning range, the filter showed peak rejection of at least 55 dB and maximum FWHM variation of 60 MHz.

9.3.4 Discussion

An important parameter for an RF filter is the RF insertion loss. In our case, this insertion loss can amount to -36 dB, which is limited by several factors. First, the insertion loss of the chip is relatively high (13 dB). This is due to the mode mismatch between the high index-contrast silicon nitride waveguide and the cleaved standard single mode fibers used in the experiments. A way to significantly reduce this loss is to incorporate on-chip spot-size converters, by tapering the width and height of the optical waveguides to control their mode field diameter [205]. Lensed coupling fibers can also be used, we measured 1.5 dB insertion loss per facet with 2 µm mode field diameter lensed fibers. The second source of loss was the electrical-to-optical (E/O) and optical-to-electrical (O/E) conversions in the MWP link. In the experiments, we were using a DPMZM with a relatively high half-wave voltage (V_π >5 V) and high insertion loss (L_{DPMZM} >7 dB). Using a DPMZM with lower half-wave voltage and insertion loss will lead to quadratic improvement in the filter RF loss. Finally, RF loss was also introduced by the novel filtering scheme itself. As shown in fig. 9.8c, opposite phase condition can also be met at frequencies other than the target notch frequency. In this case, signal reduction in the filter pass-band will occur, and will lead to an increase in the filter insertion loss. However, the impact of this loss will be minimal in the case of a ring with a relatively deep resonance, because the sidebands amplitude imbalance at frequencies away from the resonance peak is high.

Resonator vs SBS based Cancellation Filters

In the two previous chapters it has been demonstrated that the cancellation technique is capable of creating very high suppression microwave notch filters, from a variety of optical responses. From the perspective of integrated devices, it is fair question to ask, what are the advantages of SBS based devices compared to micro-resonators? We will discuss this question in the following section.

Linewidth One of the primary advantages of Brillouin based approaches over other integrated optical devices is based around the linewidth. Integrated waveguides formed of As_2S_3 posses linewidths in the 30 MHz to 40 MHz range, when clad with SiO_2. To attain similar intrinsic linewidths in integrated resonators requires losses in the 1 dB/m level, which is only just being reached in devices available in multi wafer programs [607]. If we compare this with the few MHz linewidths found in Si Brillouin waveguides [105, 110], this would require Q factors beyond 10^8, only currently possible with most advanced low index contrast waveguides [608]. To maintain wideband frequency operation resonator devices should also maintain a large FSR beyond 50 GHz, which is unable to be achieved in low index contrast waveguides which require large bending radii.

Dynamic Range Another drawback of using ultra-high Q resonators is the fact that these are accompanied with a very large *circulating* power, which can result in distortion and bistability due to thermal effects [609]. For example, in the few million Q ring resonators demonstrated in [607], coupled powers of 100 µW results in shifts of about a fifth of a linewidth, sufficient to change the output power. For the sake of linearity this represents the upper limit of operation and, as the modulated sideband power is directly related to the photonic link gain, this would significantly hinder the performance of a microwave photonic processor. This effect is even more significant in silicon based resonators, due to the additional thermal effects and dispersion associated with the photo-generated free carriers [610, 611]. Pump depletion may be a problem in Brillouin based devices, but this is only significant when the amplified probe powers become comparable to the pump. If operating in the low gain regime, or using the loss response which does not deplete, powers well over 10 mW do not represent an issue.

Noise The main advantage of microresonators is that they are optically passive, they do not add any additional noise. This is in contrast to Brillouin amplification/loss based approaches which add noise due to spontaneous Brillouin scattering. In the case when the Brillouin gain/loss is quite weak, < 3 dB for example, it is still unclear if the amount of noise due to spontaneous Brillouin scattering is significant compared to the shot noise and RIN from the local oscillator in a typical microwave photonic link. The spontaneous scattering is also weaker on the anti-Stokes/loss peak [612], with preliminary results demonstrating reduced additional noise using Brillouin loss [613].

From the above comparisons we can conclude that Brillouin scattering has unique advantages in applications which require very high selectivity, i.e. linewidths less than 100 MHz. For applications which need to work over the few GHz range, combining a series of integrated resonators with wider linewidths, which softens the loss requirements and reduces circulating power, is a sensible strategy. Combining Brillouin scattering and over-coupled rings has also been shown to improve the microwave photonic link performance [614].

Conclusion

In this chapter we have extended the cancellation concept to two additional integrated platforms. We have demonstrated the use of the cancellation filter with forward Brillouin scattering in a silicon nanowire. This is the first use of Brillouin scattering for signal processing in a silicon circuit. We also harnessed the cancellation technique with a low-loss Si_3N_4 ring resonator to achieve a tunable bandwidth microwave photonic notch filter with ultra-high peak rejection. This shows the wide applicability of the cancellation concept, which will potentially lead to creation of very high performance integrated MWP notch filters in the future.

Chapter 10

Conclusion

In this chapter we provide a summary of the results found within this thesis, as well as a perspective on future work and possible opportunities of Brillouin scattering in circuits.

10.1 Summary

Since SBS was first understood to limit the optical power in fiber systems designed for long haul communications, it has held the perception of being a nuisance, something to be inhibited and optimised around [44]. This perception only increased further when forward Brillouin scattering was found to be a limiting factor in the generation of squeezed states of light in optical fibers [61]. However, in the past two decades this understanding has been shifting and Brillouin scattering, due to its narrowband response and reconfigurability, can now be seen as an attractive optical signal processing tool [139]. This thesis was commenced at a time when Brillouin scattering in *integrated* photonic devices was still in its formative stages, with the demonstration of on-chip Brillouin scattering [124] occurring barely 2 years prior and thoughts of SBS in silicon waveguides were still just theory [95]. While the individual goals of this body of work changed over time, the publications of Shin in 2013 [96] and Van Laer in 2014 [103] certainly resulted in some readjustment, this work was driven by two main questions:

1. Can we utilise on-chip SBS to create high performance integrated microwave photonic processors?

2. How can we generate strong Brillouin interactions in photonic circuits?

The first question was born out of the earlier demonstrations of Pant [92] and Byrnes [94]. In these works, functionalities useful for microwave photonics, continuously tunable optical delay using slow light and narrowband bandpass filtering, were shown utilising the As_2S_3 waveguide platform. The general thrust of the group at that time was the further understanding of the limitations and applicability of previous demonstrations of SBS based microwave photonic processors to these soft glass waveguides. Chapter 8 details the work we performed exploring the effectiveness of on-chip SBS for the formation of narrowband microwave notch filters, another key functionality in microwave processing. Our first approach, found in Section 8.2, was mapping the optical response of the Brillouin loss of the As_2S_3 waveguide to the microwave domain, using single sideband modulation.

This resulted in relatively narrowband filters of around 100 MHz widths, and filter suppression up to 20 dB.

The initial notch filter demonstrations had one main problem, which was inherent to using the Brillouin loss and single sideband processing. As the filter suppression is directly proportional to the Brillouin response, achieving large suppression required high powers and operation close to the damage threshold. Quite fortuitously, during these experiments it was observed that for certain bias voltages of the Dual Parallel Mach-Zehnder Modulator (DPMZM) the measured microwave filter suppression was far beyond that of the optical response. We termed this the cancellation technique and it is described in Section 8.3. In essence, the technique relies upon tailoring the optical amplitude and phase of two modulated sidebands, resulting in a subtraction in the electrical domain upon optical detection on a fast photodiode. The separation of suppression from the depth of the optical response opened up new possibilities, such as the use of the Brillouin *gain* to make a narrowband electrical *notch*. We applied the cancellation technique to our previous As_2S_3 waveguide devices and demonstrated a reconfigurable filter with wideband frequency operation over 10s of GHz, while maintaining large suppression. We also showed other benefits of the scheme, such as improving the RF insertion loss over the filter depth, in section 8.4. In Chapter 9 we applied the cancellation technique to two circuits obtained from multi-project wafer (MPW) foundries, an SOI chip from imec and a TriPleX circuit from LioniX, exploring the benefits of the technique to these different technologies.

The second question originated from the desire to develop higher levels of integration of Brillouin process with platforms accessible for mass manufacturing and the components required for microwave signal processing. We initiated work in this direction by investigating the performance of the previous As_2S_3 rib waveguides used in our group. To consistently perform these comparisons over a number of years we adopted a high resolution pump-probe scheme which enabled accurate measurements of the frequency shift, natural linewidth and gain coefficient of our devices. We describe this scheme in Chapter 5, along with many measurements and the context in which they were made. Through optimisation of the waveguide geometry and cladding material, we demonstrated improved gain coefficients of $500\,\mathrm{m}^{-1}\,\mathrm{W}^{-1}$, enabling an on-off Brillouin amplification in excess of 50 dB. This is a 10^3 times improvement in amplification over previous As_2S_3 devices [92, 124] and more than 10^4 times greater than the best results in suspended silicon waveguides [104, 110]. The large amplification available in these new structures has been utilised effectively within our group, with improved microwave photonic processors [89, 451] and an integrated photonic-phononic memory [450] two examples of recent work.

Having well established the large Brillouin gain available in As_2S_3, the focus then shifted to bringing this material onto more widely available photonic platforms. The ubiquity of SOI, with its well proven library of passive and active components, lead us to focus on the integration of As_2S_3 with this platform. Although a few different geometries were studied, such as hybrid slot waveguides [615], we settled on a fully etched As_2S_3 waveguide which was embedded within a larger SOI circuit. In Chapter 6 we demonstrate the successful hybrid integration of As_2S_3 into a silicon circuit, with the SOI chip obtained through a standard MPW run from imec. To achieve this we were required to fit the As_2S_3 components within an area of less than $0.1\,\mathrm{mm}^2$, an orders of magnitude reduction in area compared to previous As_2S_3 device. We adapted techniques from the literature, primarily the use of adiabatic bend shapes based on the Euler curve [206], to minimise losses at the circuit level which may have arisen from the heavily multi-moded fully etched structures. In doing so, we demonstrated on-off amplification beyond 20 dB in a highly compact 6 cm long spiral. Going beyond a simple spiral structure, we fabricated a compact spiral resonator with a free spectral range matched to the Brillouin frequency shift. This enabled the first demonstration of Brillouin lasing in *any* planar integrated circuit. Key to the success of this work was the development of a standardised fabrication process and photonic design kit by our collaborators at The Australian National University and RMIT University. This work was the first step towards circuit level Brillouin processing, utilising soft glasses, in highly integrated photonic circuits. Some key results of this thesis are shown in fig. 10.1.

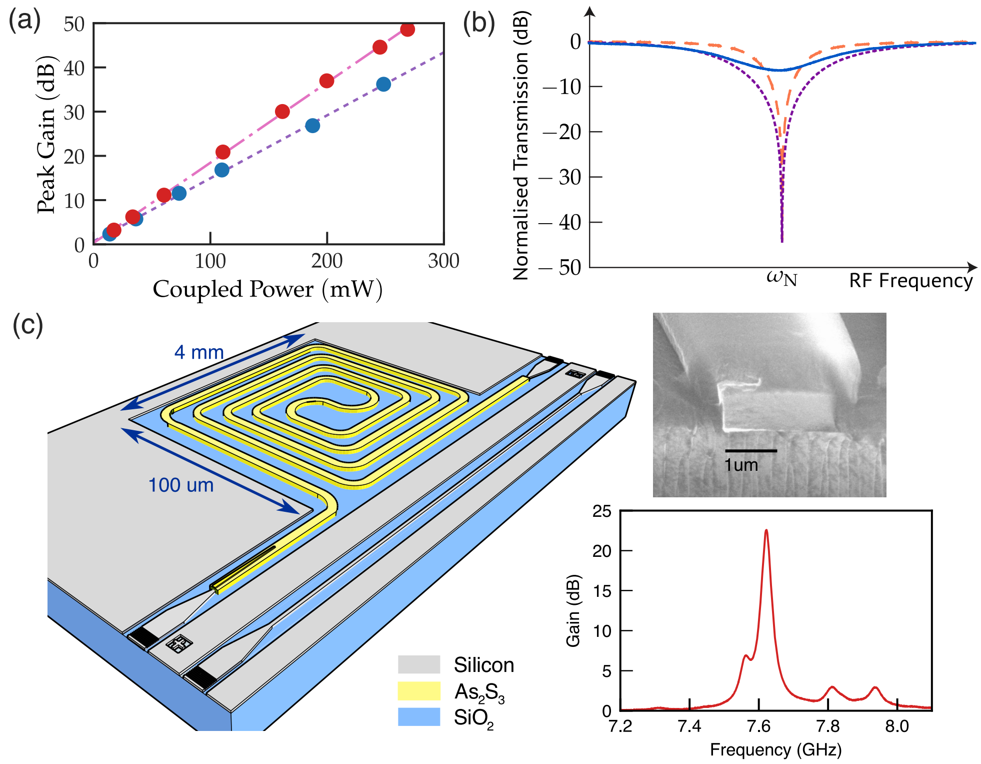

Figure 10.1: Some key results from the thesis (a) 50 dB amplification in As_2S_3 rib waveguides in Chapter 5 (b) Cancellation filter introduced in Chapter 8 (c) Hybrid integration of As_2S_3 onto SOI circuit, with amplification generated in compact sub mm^2 spiral from Chapter 6.

10.2 State of the Art Integrated Microwave Photonic Devices

Here we discuss the possibility of creating high resolution reconfigurable optical circuits and improvements to cancellation filters.

10.2.1 High Resolution Reconfigurable Optical Circuits

Reconfigurable optical circuits are of increasing interest to integrated optics systems, in particular to quantum information [616–618] and microwave photonics [552, 619, 620]. By cascading a series of tunable Mach-Zehnder interferometers, it is possible to create truly universal linear processors, which are capable of performing any "legal" linear operation [621]. The extensive theory work of Miller has established a number of properties of these devices, showing that they can be characterised fully with external detectors, are quite tolerant to fabrication imperfections and can even be programmed to be self aligning [622]. In microwave photonics the focus has been on mesh structures, with hexagonal mesh designs being the most space efficient [623]. The first experimental results were demonstrated by Zhuang in 2015 [552], where a square lattice mesh of 2 unit cells was reconfigured to form optical filters, a delay line and a Hilbert transformer. Quite recently Perez has demonstrated a hexagonal mesh system using SOI, with 7 unit cells enabling the replication of 21 unique optical functionalities including ring cavities and ring-loaded filters [624].

While undoubtedly powerful, these reconfigurable circuits have some inherent trade-offs. The most significant is the choice of length of the unit cell, which will effect the minimum frequency spacing and optical quality factor of configured components (discussed in the supplementary of [624]). It is here that SBS could play a key role in future devices. The spectral response of SBS has a width on the order of 10 MHz, equivalent to a 10^6 Q-factor resonator. By broadening the pump source, or using multiple individual tones, the combined Brillouin response can be arbitrarily tailored [369, 625, 626]. This tailoring is of frequent use in microwave photonics, and can be performed using an electro-optic modulator driven by an arbitrary waveform generator. Integrated electronic logic, such as an FPGA, required to control the complex reconfigurable optical circuit, could be used generate RF signals to tailor the SBS pump. Thus by combining an efficient Brillouin waveguide within the optical circuit, a high resolution reconfigurable circuit could be created. Using inter-modal Brillouin scattering will allow for the pump to be removed from the circuit, preventing cross-talk and the requirement for optical isolators.

10.2.2 Beyond The Cancellation Filter

The simplicity of the cancellation concept means that it is capable of being extended in a number of ways. The work based on the cancellation filter has already been extended by other members of the group. By using multiple pump waves, from different lasers or generated through modulation, multiple notch filters can be created simultaneously in a wide frequency band [89]. The creation of sharp bandstop filters was also shown to be possible, by satisfying the cancellation condition over a continuous frequency band [627]. To do this two probe lasers were used, each modulated with single sideband modulation to generate a single electrical beatnote at the same frequency, and a delay line was used to match the phase response of a broadened Brillouin pump. An interesting scheme was implemented by Liu [614], where a standard intensity modulator was combined with an over coupled ring resonator to provide a frequency localised π phase shift. The Brillouin pump was tailored to match the amplitude response of the ring, allowing for localised cancellation with a net improvement to the link gain in the passband of the filter. These are just a few examples of how the cancellation filter concept has already been extended in the literature. We expect that as the improvements to reconfigurable optical circuits continue the cancellation concept is bound to find a wide range of uses.

10.3 New Materials and Fabrication Techniques

Here we will summarise alternative materials to As_2S_3 and possibilities for integration with active photonic platforms.

10.3.1 Soft Glasses

As_2S_3 is undoubtedly a very suitable material for Brillouin scattering in photonic circuits, however it does have some drawbacks. It is quite a difficult material to etch, resulting in only modest propagation losses in sub-µm waveguides, preventing single mode operation. It can be damaged if contacted with basic chemicals, preventing use with lift-off fabrication processes, which introduces additional complexities during the hybrid integration process. And its glass softening temperatures are relatively low, bringing about questions of long term stability.

Are there any viable alternatives to As_2S_3 for Brillouin scattering in planar circuits? After investigating parts of the literature, in particular articles providing photoelastic parameters and figures of merit for acousto optic devices [407, 412–414, 628] it seems a few options may exist.

For single pass devices we require large Brillouin gain coefficients. Thus we want glasses with high refractive indexes and large photoelastic coefficients or moderately strong electrostriction but with low scattering losses allowing for tight confinement and small A_{eff}. In this category glasses with Germanium (Ge) seem to be a good choice, such as GeAsSe, GeSbSe or GeSbS glasses, due to the higher softening temperatures of these materials [405]. The exact composition needs to be chosen to prevent any TPA [629–632], however the lack of free carriers and modest CW operation means this is not as strict as a requirement for semiconductors. In Section 5.4.4 of this thesis we characterised $Ge_{11.5}As_{24}Se_{64.5}$, and found it to have a large gain coefficient, warranting further interest. In the wider integrated optics community there has been significant amount of focus on one Ge based glass – $Ge_{23}Sb_7S_{70}$. This material is capable of low losses in single mode geometries [633, 634], is compatible with lift-off fabrication [635], has a reasonably high nonlinear index [636], can be integrated on flexible substrates [637], and can even stabilise 2D materials [638]. Brillouin scattering has not been characterised in this exact glass composition, possibly due to the frequent use of polymer claddings, however micro-structured fibers with slightly lower germanium content have demonstrated peak gain factors slightly below As_2S_3 [421]. Bulk glass measurements of a range of compositions have shown that, for systems with low Sb content, acousto optic figures of merit close to As_2S_3 can be expected [639–642]. Moving forward, this particular chalcogenide is a highly suitable material for back-end and hybrid integration with SOI circuits.

For Brillouin lasers, and other resonant components, the requirements are somewhat different to single pass devices. The most important criteria is achieving the lowest possible losses of the waveguide. This means that choosing a lower index material, which can also be fabricated with minimal surface roughness, is generally a preferred option. The material should also be capable of handling very high circulating powers which will occur in high-Q designs. A chalcogenide which fits these requirements is TeO_2 glass, which we investigated in section 5.4.4 [404, 409, 458]. Tellurite glasses are considered some of the most stable of the chalcogenides, with high softening temperatures and minimal effects due to photosensitivity [404]. Losses below 0.1 dB/cm have been measured in large mode area waveguides, with no indications that this is a fundamental material or technology limit [404]. Polymer claddings can be utilised to increase the acoustic damping [432, 502], enabling a more direct transition the linewidth narrowing regime [465]. The lower peak gain coefficient of the TeO_2, due to the reduced refractive index, will be compensated in high-Q resonator designs. In fact, recent work investigating Brillouin lasing at cryogenic temperatures indicates that a smaller gain coefficient is beneficial for achieving a narrower Brillouin laser [643]. As such, TeO_2 glass may be an effective soft glass for Brillouin lasing in future integrated devices.

10.3.2 Semiconductors

While silicon photonics has captured the attention of the bulk of integrated optics researchers, it is just one of a number of semiconductor based material platforms for integrated optics. Of these, one material in particular could be of significant interest to Brillouin scattering, GaAs. GaAs, and its close relative $Al_xGa_{1\text{-}x}As$, possess a high refractive index around 3.3 and significantly larger photoelastic coefficients than silicon. Cavity optomechanics devices harnessing these strong photoelastic forces have been demonstrated, with efficient operation even at room temperature [644]. GaAs also possesses piezo electric properties, enabling external electrical signals to directly induce phonons in the medium and opening up interesting signal processing regimes [645, 646]. For Brillouin scattering GaAs is intriguing primarily as it possesses strong electrostrictive properties, and it may also be capable of acoustic confinement with a SiO_2 cladding. For certain crystal axis it has comparable stiffness to SiO_2 [644], but twice the density, and preliminary calculations in NumBAT indicate that acoustic guidance can occur. If we assume bulk parameters, focusing solely on the electrostriction and the same linewidth as As_2S_3, then the peak gain coefficient is on the order of that measured in the As_2S_3 waveguides. While traditionally grown on top of other layers of III-V semiconductor material [647, 648], researchers in DTU are currently developing an AlGaAs-on-insulator platform [649]. It is quite possible that Brillouin scattering would be observed in these waveguides, though the the remaining polymer resist may need to be removed from the waveguides. Considering the fact that materials based on GaAs have been effectively integrated with SOI for hybrid evanescent lasers [305], this is a promising semiconductor material for Brillouin scattering and warrants further study.

The primary issue preventing strong Brillouin interactions in SOI at 1550 nm is nonlinear losses, particularly the excess absorption from photo-generated carriers. A common practice for reducing the effects of free carriers is the use of p-n junctions in deeply etched rib waveguides [229]. The requirement for acoustic confinement has currently prevented the use of p-n junctions. The other alternative is to shift the operating wavelength beyond 2 µm, where the two photon absorption (and hence free carriers) will become diminished [221, 650, 651]. The Brillouin gain coefficient will be reduced slightly at the longer wavelengths, however this would be compensated by the increased power handling of the circuit. Just as crucially, photonic integration at this wavelength range is relatively mature as the standard set of active components have all been demonstrated near 2 µm [652, 653]. At longer wavelengths Ge-on-Si has become of interest [650], with passive devices showing effective operation at 5 µm. Theoretical work indicates that this material platform is highly suitable for Brillouin scattering, and is capable of acoustic confinement without under etching [654]. Moving to wavelengths beyond the standard telecommunications band will thus be beneficial to the future harnessing of Brillouin scattering in semiconductor circuits.

Before moving on, it is worth discussing the fact that acoustic confinement is not a necessary requirement for low threshold Brillouin lasing. While this is not immediately intuitive, a free space optical beam passing through a bulk medium will certainly generate Brillouin scattering if at suitable power levels. In the case of a resonator formed with a waveguide with no acoustic confinement [432], as long as the spontaneously scattered light is strong enough to result in stimulated scattering, corresponding to powers on the order of nW, then net amplification on a round trip will result in buildup and oscillation. To compensate the reduced gain coefficient, caused by the low opto-acoustic overlap and acoustic lifetimes, exceedingly high quality factors are required to achieve a low threshold. Two recent results demonstrate such high-Q integrated resonators and Brillouin laser action, though linewidth narrowing was not explicitly mentioned in either case and bending radii for both devices was beyond 1 mm [655, 656]. Thin high aspect ratio Si_3N_4 waveguides achieved loaded Q factors beyond 20×10^6 with a Brillouin threshold of 12.7 mW [655]. Large mode volume integrated SiO_2 ridge waveguide have demonstrated record Q factors for integrated resonators, with values beyond 100×10^6 and an observed Brillouin threshold of 0.8 mW [656]. Considering the sensitivity of the narrowing factor with the linewidth of the acoustic mode, further theoretical research is required to understand the effects generating lasing while overlapped with a large number of radiative acoustic modes with varying lifetimes [121, 432, 643].

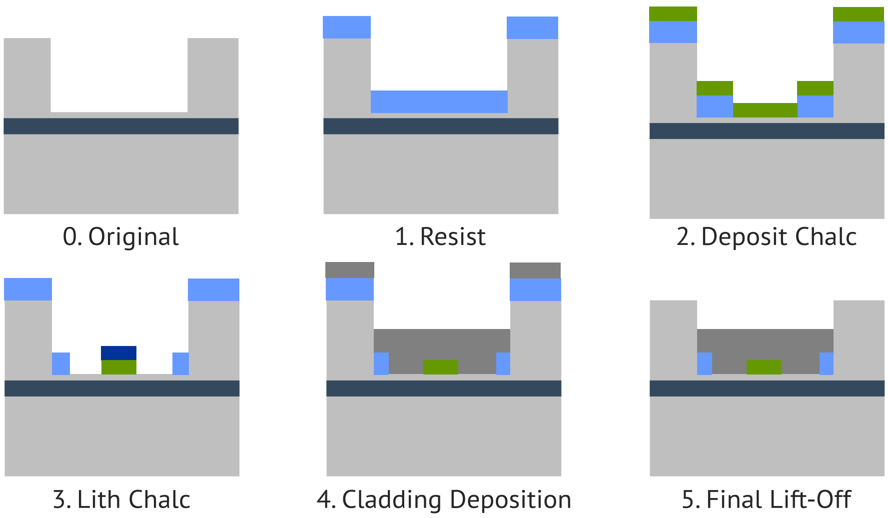

Figure 10.2: Schematic of possible integration strategy of soft glass material with silicon waveguides.

10.3.3 Future Integration Strategies

To successfully integrate soft glasses with active photonic circuits new techniques will need to be adopted. In the following we describe possible integration strategies which may be compatible with integration in imec's current active platform iSiPP50G [329, 657].

Etched Glass Waveguides A schematic of this possible strategy is shown in fig. 10.2. An option available in the iSiPP50G platform of imec is to etch through the SiO_2 cladding down to the silicon waveguide. This nominally results in a thin layer of SiO_2, however extra SiO_2 may need to be deposited to achieve an optimum field concentration in the soft glass waveguide. A resist is spun coat to protect the wafer, and processed with lithography to define the region where the soft glass will be deposited. After removing the processed resist, the soft glass is deposited onto the wafer. This is followed by a further resist lithography and etching process to define the soft glass waveguide. This is followed by cladding deposition: on the order of 1 μm is sufficient to protect the waveguide and the full trench does not need to be filled. Finally the original resist is removed with a lift-off process, returning the rest of the wafer to its original state. Some resist may be present in the cladded region, but this should not pose an issue considering the low index of the most resits, provided sufficient spacing is given ($> 2\,\mu m$) around the soft glass waveguide. Appropriate coupling to the silicon circuit, using tapers with the multiple etch levels of the silicon waveguides should allow for low loss coupling.

Etch-less Structures Another option in imecs platform is light pass (LPASS), where the silicon nitride layer, which is used for electrical isolation, is removed to reduce reflections when coupling to the circuit. This layer also prevents any metallic routing in this region, generating errors during the design rule checking stage. By locally etching the thermal oxide cladding, we can gain access to the photonic layer and integrate our soft glass material. An interesting possibility is using the etched trench to form the shape of the waveguide, as introduced recently by LioniX [658]. A schematic of this process is shown in fig. 10.3. As before, a resist is spun coat and processed with lithography. Now a trench is directly etched into the SiO_2 top cladding. The soft glass is deposited, filling the trench, and followed by a cladding. A final lift-off step removes the initial resist. This procedure has the advantage of less lithography and etch steps, however it is quite sensitive to the trench depth proximity to the silicon photonic layer. Evanescent coupling can be performed between two layers with slowly tapered waveguides [308], to interface the soft-glass and front end waveguides. Alternatively, the use of gratings between the optical layers can be less sensitive to the trench depth precision [659].

Figure 10.3: Schematic of etch-less integration strategy of soft glass material with silicon waveguides.

10.4 Opportunities Enabled By Brillouin Scattering Within Circuits

As Brillouin scattering is successfully integrated into future photonic circuits it will enable a new degree of freedom in device design. Thus it is important to begin considering what opportunities Brillouin components will enable in these circuits. We provide perspectives for new devices enabled by integration of Brillouin components and close with a discussion on possibilities enabled by circuit level design.

10.4.1 Possible Opportunities

Narrow linewidth lasers are crucial for a number of applications, in particular coherent telecommunications operating at high modulation formats [660]. State of the art hybrid silicon lasers, using InP semiconductor gain media embedded in optical cavities formed of silicon, are currently capable of achieving linewidths on the order of 50 kHz [661, 662]. These integrated lasers could be used to pump high-Q Brillouin active cavities, which will generate spectrally purified narrow linewidth lasers [121, 465]. Rather than using a single resonator matched to the Brillouin frequency shift, multiple compact resonators can be coupled to tailor the optical density of states [663–667]. This density of states engineering has a further advantage that higher order Stokes waves could be suppressed, enabling large output powers and narrower Schawlow-Townes linewidths [121, 643]. In doing so, widely tunable Hz linewidth lasers will be available in integrated devices.

As integrated lasers become more advanced and move to longer optical wavelengths, circuit characterisation at these new frontiers becomes incredibly important. One technology that allows for high resolution spectral analysis is based on Brillouin scattering, the Brillouin optical spectrum analyser (BOSA) [487]. BOSA devices are capable of sub pm resolution [668], can achieve high dynamic range [669], and can capture phase and amplitude information [670]. But the most powerful characteristic of the BOSA is its simplicity; it only requires a tunable pump laser, Brillouin scattering and a photodetector. A range of materials would be suitable for generating Brillouin scattering in these circuits, including chalcogenides and semiconduntors such as Germanium. Successful integration of BOSA systems into photonic circuits, which operate in the near and far infrared, could accelerate the transition to these longer operational wavelengths.

10.4.2 New Devices and Concluding Remarks

Now that the understanding of Brillouin scattering in photonic circuits has been well established in a number of platforms over the past few years [89, 95, 96, 103–105, 124, 389], the field is transitioning to a new regime where a circuit level approach is being taken to device optimisation. A good example of this is the recent work demonstrating forward intermodal Brillouin scattering [110], enabled through the use of silicon mode couplers [671], and the work in this thesis on hybrid integration of As_2S_3 and SOI [479], which required adiabatic bends to fit within a compact working area. Intermodal scattering has since been utilised for the recent results of Brillouin lasing in a silicon circuit [672]. In the following we briefly outline future directions for researchers in this field.

Working on a circuit level provides multiple opportunities when harnessing Brillouin scattering in resonators. The requirement for the free spectral range to satisfy the Brillouin frequency shift can be met in more ways than just varying the resonator length. The degenerate cavity modes can be split, using multiple resonators or self coupling in the same resonator mode [663–667], to satisfy this condition. The resonator can be made to be transparent to one of the waves, by using intermodal scattering or wavelength sensitive couplers [673], akin to systems using optical isolators to prevent one wave from circulating [126]. One could even choose to use multiple materials within a single resonator, having a Brillouin gain medium embedded within a larger external cavity, providing another path to higher quality factors. Clearly, a wealth of opportunities are available and new demonstrations will rapidly occur in the next few years.

For travelling wave devices there are also interesting possibilities. Perhaps the strongest is the adoption of slow light systems to generate large Brillouin gain in ultra-compact devices. The use of an optically written Bragg grating has demonstrated that Brillouin scattering scales appropriately in slow light systems [90]. Future devices will utilise lithographically defined components to increase the slow down factors, with photonic crystals [242] and coupled ring devices [239, 244] both viable options. The affect of waveguide geometry on the phononic system certainly needs to be considered in these devices, but if performed correctly large gain coefficients well over 10^5 could be attained and perhaps leading to unexplored physical regimes [674]. Another opportunity is splitting Brillouin amplifier devices into multiple discrete elements, to inhibit the build up of spontaneous Brillouin scattering [368]. Adopting circuit design strategies will certainly enable efficient, compact and low noise Brillouin amplifiers in the near future.

This thesis has set out to provide a definitive reference material for future students and researchers exploring Brillouin scattering in photonic circuits. This has required covering a wealth of material from somewhat disparate areas: from the historical development of Brillouin scattering and the theory of optical waveguides and photonic circuits, to the latest technologies and materials for photonic integration. We have definitively demonstrated that chalcogenide glasses are capable of strong Brillouin interactions in photonic circuits, and that these materials can be interfaced with standard platforms without any cost to performance. The understanding developed in this thesis will be of use to those studying Brillouin scattering and photonic circuits alike, as the progress in these fields continues to accelerate in the coming years.

Appendices

Appendix A

Elasticity Theory Notation

We begin by considering a solid body. Under an external force this body will become deformed, the strain is the relative change in distance between particles within the body due to the deformation. For a simple 1D case with a uniform deformation we will have

$$\epsilon = \frac{l' - l}{l}$$

where l' is the deformed length and l is the original length. In a more general sense we need to consider a point in 3D in the solid, with its spatial position by the vector $\mathbf{x}$. If acted on by the external force then this original position is deformed to a new position $\mathbf{x}'$. The displacement, due to the strain, can then be defined simply as

$$\mathbf{u} = \mathbf{x}' - \mathbf{x}$$

By considering how much an infinitesimal length $\mathbf{dx}$ changes under the displacement $\mathbf{u}$ we can derive the *finite strain tensor*, which is then given by

$$\epsilon_{ij} = \frac{1}{2}\left(\frac{\partial u_i}{\partial x_j} + \frac{\partial u_j}{\partial x_i} + \frac{\partial u_k}{\partial x_i}\frac{\partial u_k}{\partial x_j}\right)$$

For small strains the 3rd term is very small, and we can thus write the *linearized strain tensor* as

$$\epsilon_{ij} = \frac{1}{2}\left(\frac{\partial u_i}{\partial x_j} + \frac{\partial u_j}{\partial x_i}\right)$$

which can be expressed in matrix form as

$$\epsilon_{ij} = \begin{pmatrix} \frac{\partial u_x}{\partial x} & \frac{1}{2}\left(\frac{\partial u_x}{\partial y} + \frac{\partial u_y}{\partial x}\right) & \frac{1}{2}\left(\frac{\partial u_x}{\partial z} + \frac{\partial u_z}{\partial x}\right) \\ \frac{1}{2}\left(\frac{\partial u_x}{\partial y} + \frac{\partial u_y}{\partial x}\right) & \frac{\partial u_y}{\partial y} & \frac{1}{2}\left(\frac{\partial u_y}{\partial z} + \frac{\partial u_z}{\partial y}\right) \\ \frac{1}{2}\left(\frac{\partial u_x}{\partial z} + \frac{\partial u_z}{\partial x}\right) & \frac{1}{2}\left(\frac{\partial u_y}{\partial z} + \frac{\partial u_z}{\partial y}\right) & \frac{\partial u_z}{\partial z} \end{pmatrix} \tag{A.1}$$

It is important to note that this tensor is symmetric, i.e $\epsilon_{ij} = \epsilon_{ji}$ and can thus be represented by 6 terms only. It is also important to note that the strain tensor does not describe the complete deformation, just the part of the deformation that changes the size and shape of parts of the solid.

The description above shows how displacements in a continuous media are related to the strain, which are due to some external forces acting on the body. A solid body can experience two types of general forces, a body force, which acts on all points in the body simultaneously, or a traction force, which is applied at the boundary. The traction force is transmitted to the interior of the body via internal forces, i.e stresses. The *stress tensor* is thus defined at a single point as the force per unit area acting *on a plane* oriented at that point. It is a 2nd rank tensor given by:

$$\sigma_{ij} = \begin{pmatrix} \sigma_{xx} & \sigma_{xy} & \sigma_{xz} \\ \sigma_{yx} & \sigma_{yy} & \sigma_{yx} \\ \sigma_{zx} & \sigma_{zy} & \sigma_{zz} \end{pmatrix} \tag{A.2}$$

The off diagonal terms result in shear stresses, where the diagonal terms result in normal stress components. Positive normal stresses are outwards from the body. The stress and the strain are linearly related through a set of constitutive relations, essentially the 3D version of Hooke's law.

$$\sigma_{ij} = \mathbf{c}_{ijkl}\epsilon_{kl} \tag{A.3}$$

$$\epsilon_{ij} = \mathbf{s}_{ijkl}\sigma_{kl} \tag{A.4}$$

where $\mathbf{c}$ is known as the *stiffness tensor* and $\mathbf{s}$ is the *compliance tensor*. Expanding out even a single term of the above is clearly quite intensive, with nine terms over the entire elastic tensor on the right hand side. If the interaction is devoid of body-torques then the stress tensor becomes symmetric, i.e $\sigma_{ij} = \sigma_{ji}$ and we can compact down all the above summations quite heavily with the use of Voigt notation. We can introduce the *stress vector* and *strain vector*, $\mathbf{T}$ and $\mathbf{S}$, which are given by

$$\mathbf{T} = \begin{pmatrix} \sigma_{xx} \\ \sigma_{xy} \\ \sigma_{zz} \\ \sigma_{yz} \\ \sigma_{zx} \\ \sigma_{xy} \end{pmatrix} = \begin{pmatrix} T_1 \\ T_2 \\ T_3 \\ T_4 \\ T_5 \\ T_6 \end{pmatrix} \qquad \mathbf{S} = \begin{pmatrix} \epsilon_{xx} \\ \epsilon_{xy} \\ \epsilon_{zz} \\ \epsilon_{yz} \\ \epsilon_{zx} \\ \epsilon_{xy} \end{pmatrix} = \begin{pmatrix} S_1 \\ S_2 \\ S_3 \\ S_4 \\ S_5 \\ S_6 \end{pmatrix} \tag{A.5}$$

Hooke's law can then be re-expressed in more simplified terms as, focusing just for the stiffness tensor,

$$\mathbf{T} = \mathbf{c} : \mathbf{S}$$

Finally, the stiffness tensor is still an array of six by six terms, explicitly given by individual c_{ij} values. Many of the terms inside the stiffness tensor are zero or equal, depending on the different crystal or material classes. For cubic and isotropic media, the only types of materials investigated in this thesis, the stiffness tensor is symmetric and is determined by only three elastic constants, c_{11}, c_{12} and c_{44}, such that

$$\mathbf{c} = \begin{pmatrix} c_{11} & c_{12} & c_{12} & 0 & 0 & 0 \\ & c_{11} & c_{12} & 0 & 0 & 0 \\ & & c_{11} & 0 & 0 & 0 \\ & & & c_{44} & 0 & 0 \\ & & & & c_{44} & 0 \\ & & & & & c_{44} \end{pmatrix} \tag{A.6}$$

where $c_{44} = (c_{11} - c_{12})/2$ in the case of isotropic media, such as amorphous glasses.

Appendix B

Integrated Optics: A Pre History

Modern integrated optical devices consist of wafer scale produced circuits with many individual components approaching (or indeed, below) the wavelength of the guided electromagnetic waves. From this perspective, one may be led to believe that the birth of integrated optics followed from the development of lithographic tools for micro electronics. This is true, however, and quite remarkably, modern style integrated optical circuits were predicted only a few years after the very first demonstrations of photolithographically produced electronic circuits in the early 1970s. Here we provide a brief description of the early interest in guided electromagnetic waves, which leads into the famous edition of Bell Labs System Journal.

B.1 Microwave Waveguides

Before we get ahead of ourselves, what is the first example of a work investigating *guided* electromagnetic waves? Like many aspects of electromagnetism, Lord Rayleigh (in *1897*) was first to investigate the waveguide modes propagating through hollow metallic tubes [675]. The rectangular and circular (and perfectly conducting) waveguides explored in Rayleigh's work allowed exact solutions to be formed. Significant early contributions also came from the works of Arnold Sommerfeld, in particular the derivation of the waves guided by a solid lossy cylindrical wire in 1899 [676]. But for integrated optics early theory work, perhaps the key work, was performed by Hondros and Debye in 1910 [677], where the authors studied the mode propagation in a purely dielectric rod without any conductors.

While the wireless transmission of radio waves was a broad research topic in the early 1900s, predated by impressive experimental work by J. C. Bose as highlighted by Emerson [678], waveguides did not receive significant focus within the wider literature again until the 1930s. Two papers stimulated the field: G. Southworth from Bell Laboratories and W. Barrow from MIT, who presented similar work, theory and experiment, focusing on guided waves in cylindrical metallic tubes, filled with dielectric or air. The key results leading to these works, and the interactions between the researchers at the time, are described in detail by K. Packard [679]. Of note is the fact that the researchers were unaware of Rayleigh's paper for a number of years and developed theory and intuition from scratch. While experimental results were based on the conducting rods, descriptions and intuition for purely dielectric waveguides is also provided in these works [680, 681]. An accompanying paper from colleagues of Southworth in the same issue of *Bell System Technical Journal* describes the theory of these waveguides, and focuses purely on dielectric rods, even discussing the conditions for cut-off [682]. This theory work was key to later developments of early optical fibers. Following this, Southworth performed a number of talks on the properties of waveguides (such as modes and cutoff frequencies) and even presented public demonstrations of his experimental systems.

These key results were followed by a flurry of activity, particularly by Barrow and his colleagues, as interests in waveguides grew due to their the use in a number of applications, in particular communication and Radar. A thorough treatise of the electromagnetic waves in hollow rectangular tubes was published by L. Chu and W. Barrow [683]. What is remarkable in this work is the thorough, and clear, detail to which this system is explored, with experiments measuring various properties and even calculations of mode fields. An extensively detailed treatise was also developed by S. Schelkunoff (also from Bell Labs) [684]. In this work Schelkunoff approaches the problem from the perspective of transmission lines and impedances, which was the style of the time for microwave resonance structured but the first time for guided wave systems. The results of the work include plots of some interesting waveguide shapes and overall the results were similar to the work of Chu, but greatly expanded the understanding and approaches available to physicists and engineers of the period. These works inspired a great deal of further research from hundreds of individuals in many institutions around the world.

B.2 Optical Waveguides

Dielectric waveguides received significant further exploration at microwave wavelengths, in particular for the use of leaky wave antennas. However, at this point we diverge from a focus on microwave theory and shift to early works on waveguides at *optical* frequencies. Two articles published back to back in *Nature* in 1954 investigate the use of optical fiber for flexible conduits for imaging, termed fibrescopes [685, 686]. These structures consisted of large bundles of individual fibers, with structures of the size that were large enough that the dynamics could be described by geometric ray optics alone [687]. As fabrication capabilities improved, individual fibers were made smaller in an effort to improve the spatial resolution of the imaging, to the point that they were within a few wavelengths (or below!) that of the guided light [688]. This surprised researchers at the time as it was thought that guidance would be for fibers with core diameters smaller than 10 wavelengths! At this point, waveguiding effects were observable, along with significant mode coupling when only a single fiber is excited, producing fringes and distorting the images the researchers where attempting to capture. They went back to the earlier modal theory of dielectric rods for microwaves and made extensions to cover the new observations [689] and figure out how to minimise the waveguiding effects.

In the same year that Kapany and Bourke were minimising the waveguiding effects, 1961, Snitzer and Osterberg observed the modes of a fiber when illuminated with visible light [690]. Theory developed by Snitzer [691] allowed for an understanding of ways to illuminate the fiber such that individual modes could be imaged. These modal images have a remarkable clarity and are reminiscent of modern undergraduate experiments investigating spatial modes of a free space cavity. Interest in optical fiber continued over the next few years, with a continued focus of the use of for a communications medium. Considerable momentum in optical fibers was built after the definitive work of C. Kao in 1966 [43], for which Kao received the Nobel Prize in 2009. This work explored the theory, and experiment, of various properties of guided waves of glass fibers of different material types. The investigated properties included sources of losses, optical dispersion, power handling and how these different properties affected information capacity in real devices. The commonly acknowledged key result was the possibility of making fibers with *orders* of magnitude lower losses than the multi dB /m, which was the state of the art of the time. The work of Kao received some attention in the wider research community and only a few years later in 1971, Corning fabricated optical fibers with losses of 20 dB /km at the 633 nm He-Ne line, an incredible loss reduction over such a short period of time and suitable for early communications purposes.

While fiber devices rapidly progressed, early works on planar waveguides was quite rudimentary. It is acknowledged that many of the groups that explored fibers also performed calculations on thin films, due to the more straightforward mathematical formulation, however the literature does not seem to hold many results. Researchers at the Wheeler laboratories (formed by a pioneer of microwave systems Harold Wheeler) published a number of papers investigating optical waveguides during the 60s. The first of these works was a slab waveguide, consisting of a liquid core sandwiched between two pieces of optically polished glass [692]. The liquid core was used to provide a smooth interface and also provide flexibility of the core index, allowing for controlled investigations of modal behaviour. Initially they adjusted the index so the waveguide was multimode, and proceeded to excite different modes by changing the input angle. They then reduced the index contrast and would only observe a single guided mode as they varied the angle. Another work of Wheeler laboratories used a Nd doped glass slab as a waveguide core, immersed in a liquid bath [693]. The doped glass was pumped and single mode lasing output was observed, with a diffraction limited beam (in the transverse direction of wave guiding). If the temperature of the liquid was varied such that $n_{\text{clad}} > n_{\text{core}}$ than no lasing output was observed. The single mode operation of the demonstrated laser was superior to the unstable multi-mode output of an earlier an Nd doped fiber waveguide.

The work of Wheeler labs was based on slab optical waveguides formed of glass with no lateral confinement. In the prescient work by Anderson [694], "*Applications of microphotolithography to millimeter and infrared devices*", descriptions of microwave and infrared waveguides formed using microlithography techniques, with semiconductor materials, are given. This work realised the applicability of applying microfabrication techniques, still very early from microelectronics, to planar optical waveguides. The waveguides were formed by processing silica on top a doped silicon slab. No numbers of waveguide performance are given, though a sidewall roughness of 200 nm RMS is quoted, images of standing waves in guided structures are provided showing guidance. Anderson also highlights work on p-n junctions in GaAs and GaP in Bell Labs, for the use of electro optic modulators [695]. The works of Yariv [696, 697], and the descriptive but clear work from Ashkin [698], show the possibility of guiding light near the depletion layer of p-n junctions in semiconductors, due to the slight changes of material index in this region. These early works focusing on semiconductors and microlithography herald the absolute explosion of research in integrated optical devices in the 1970s and beyond, propelled by an edition of Bell Labs Journal in 1969, as discussed in the next section.

B.3 Bell Labs Journal Issue: Heralding Integrated Optical *Circuits*

In 1969, the real beginnings of modern integrated optics was initiated in volume 48 of *The Bell System Technical Journal*. This volume contains 4 articles [171, 699–701], including a summary article, covering different aspects of integrated optical systems, and highlights the opportunities of creating integrated optical *circuits* rather than just single devices. The abstract from the summary article "*Integrated Optics: An Introduction*" by S. Miller [171] is as follows:

> This paper outlines a proposal for a miniature form of laser beam circuitry. Index of refraction changes of the order of 10^{-2} or 10^{-3} in a substrate such as glass allow guided laser beams of width near 10 microns. Photolithographic techniques may permit simultaneous construction of complex circuit patterns. This paper also indicates possible miniature forms for a laser, modulator, and hybrids. If realized, this new art would facilitate isolating the laser circuit assembly from thermal, mechanical, and acoustic ambient changes through small overall size; economy should ultimately result.

The desire for these new integrated systems is quite intriguing. In the introduction of his article, Miller outlines how current repeater experiments using lasers (over a range of wavelengths even at that time) is akin to "interconnecting the oscillators, modulators, detectors, and so on, using a form of extremely short-range radio". The general thought was by integrating all these components significant advantages over free space optics could be achieved in sensitivity and compactness, no doubt assisting the development of devices for communications systems.

Undoubtedly inspired by the well developed literature of microwave waveguides, this volume covers an astonishing number of aspects integrated optical circuitry. In the remaining of the summary article Miller covers points from the other articles and summarises a number of possible components which, clear even at that time, should be realisable if technology is approved. The components included:

- Integrated lasers with resonators formed using distributed partially reflective mirrors. Possible schemes for optical pumping and electrical pumping are indicated.

- Optical modulators, using electro-optic material that is embedded or as a thin layer over the main waveguide. Driving voltages of only a few Volts were expected.

- Directional couplers and waveguide crossings.

- Frequency selective filters, using a scheme which looks very similar to a Mach Zhender interferometer with resonators in the arms.

The remaining articles cover a number of the technical and theoretical details which were summarised by Miller. In "*Dielectric Rectangular Waveguide and Directional Coupler for Integrated Optics*", E. Marcatili explores the theory and properties of rectangular waveguides and directional couplers [700]. He finds conditions for single mode operation, effective index properties with changing dimensions and ways of suppressing modes with absorbing (i.e metal) layers on some interfaces.

For directional couplers it was found that, for a spacing similar to the waveguide dimension, a 3 dB coupler could be formed with only a few 100's of um length. Another article by Marcatili [699],"*Bends in Optical Dielectric Guides*", investigates the properties of bends for waveguides of different types. This thorough treatise (30 pages long) identifies loss sources for bends in waveguides through theory and simulation, identifying that small single-mode geometries are capable of tight bends below 100 um radius and that in multi-mode structures significant issues will arise from mode coupling between bent and straight waveguides. Finally, the paper by J. Goell [701], "*A Circular-Harmonic Computer Analysis of Rectangular Dielectric Waveguides*", provides theory and simulations of optical mode properties such as effective indices and also mode profiles of different waveguide cases.

Cumulatively these articles have received just under 4,000 citations as of 2017. This is really quite remarkable when you consider that there was no actual experimental measurements or physical devices presented in these works. These papers where published to extend the theory of the time and to stimulate the broader scientific community into studying this new and emerging, fascinating area. To quote the end of Miller's article:

> Finally, a word of caution is needed. Work is just beginning in the directions indicated, and we have identified goals rather than accomplishments. We recognize these are difficult goals; but we believe they are worth the serious effort required to achieve them.

Considering just one benefit of integrated optics on modern society (i.e telecommunications based on ubiquitous lithium niobate modulators), the goals suggested in these works were indeed worth the effort extorted by hundreds of researchers over the proceeding decades.

Complete Bibliography

[1]J. W. Strutt, "XV. On the light from the sky, its polarization and colour", Philos. Mag. Ser. 4 **41**, 107–120 (1871) (cit. on p. 6).

[2]L. Rayleigh, "On the transmission of light through an atmosphere containing small particles in suspension, and on the origin of the blue of the sky", Philos. Mag. Ser. 5 **47**, 375–384 (1899) (cit. on p. 6).

[3]J. Larmor, "The principle of molecular scattering of radiation", Philos. Mag. Ser. 6 **37**, 161–163 (1919) (cit. on p. 6).

[4]C. V. RAMAN, "Optical Observation of the Thermal Agitation of the Atoms in Crystals.", Nature **109**, 42–42 (1922) (cit. on p. 6).

[5]P. Debye, "Zur Theorie der spezifischen Wärmen", Ann. Phys. **344**, 789–839 (1912) (cit. on p. 6).

[6]A. Einstein, "Theorie der Opaleszenz von homogenen Flüssigkeiten und Flüssigkeitsgemischen in der Nähe des kritischen Zustandes", Ann. Phys. **338**, 1275–1298 (1910) (cit. on p. 6).

[7]K. Krishnan, "LXXV. On the molecular scattering of light in liquids", Philos. Mag. Ser. 6 **50**, 697–715 (1925) (cit. on p. 7).

[8]C. V. RAMAN and K. S. KRISHNAN, "A New Type of Secondary Radiation", Nature **121**, 501–502 (1928) (cit. on p. 7).

[9]C. V. RAMAN and K. S. KRISHNAN, "The Optical Analogue of the Compton Effect", Nature **121**, 711–711 (1928) (cit. on p. 7).

[10]C. V. RAMAN and K. S. KRISHNAN, "The Negative Absorption of Radiation", Nature **122**, 12–13 (1928) (cit. on p. 7).

[11]C. V. Raman, *A Change of Wave-length in Light Scattering*, 1928 (cit. on p. 7).

[12]R. S. Krishnan and R. K. Shankar, "Raman effect: History of the discovery", J. Raman Spectrosc. **10**, 1–8 (1981) (cit. on p. 7).

[13]R. Singh and F. Riess, "The 1930 Nobel Prize for Physics: A close decision?", Notes Rec. R. Soc. **55**, 267–283 (2001) (cit. on p. 7).

[14]A. C. MENZIES, "The Raman Effect.", Nature **125**, 205–207 (1930) (cit. on p. 7).

[15]J. R. Nielsen, "THE RAMAN EFFECT", Sch. Sci. Math. **29**, 581–589 (1929) (cit. on p. 7).

[16]I. L. Fabelinskii, "The discovery of combinational scattering of light (the Raman effect)", Sov. Phys. Uspekhi **21**, 780–797 (1978) (cit. on pp. 8, 29).

[17]L. N. Brillouin, "Diffusion de la lumi'ere et des rayons x par un corps transparent homog´ene", Ann. Phys. **17**, 88–122 (1922) (cit. on p. 8).

[18]P. Debye and F. W. Sears, "On the Scattering of Light by Supersonic Waves", Proc. Natl. Acad. Sci. **18**, 409–414 (1932) (cit. on pp. 8, 9).

[19]C. V. RAMAN and C. S. VENKATESWARAN, "Optical Observation of the Debye Heat Waves in Crystals", Nature **142**, 250–250 (1938) (cit. on pp. 8, 10).

[20]E. Gross, “Change of Wave-length of Light due to Elastic Heat Waves at Scattering in Liquids.”, Nature **126**, 201–202 (1930) (cit. on p. 9).

[21]B. V. Raghavendra Rao, “The doppler effect in light scattered by liquds”, Proc. Indian Acad. Sci. - Sect. A **1**, 765–767 (1935) (cit. on pp. 9, 10).

[22]C. Raman and N. Nath, “The diffraction of light by high frequency sound waves: Part I”, Proc. Indian Acad. Sci. **2**, 406–412 (1935) (cit. on p. 10).

[23]V. Chandrasekharan, “Thermal scattering of light in crystals - Part II: Diamond”, Proc. Indian Acad. Sci. - Sect. A **32**, 379 (1950) (cit. on p. 10).

[24]V. Chandrasekharan, “Thermal scattering of light in crystals - Part III: Theory for Birefringent Crystals”, Proc. Indian Acad. Sci. - Sect. A **33**, 183 (1951) (cit. on p. 10).

[25]R. S. Krishnan, “The scattering of light in fused quartz and its Raman spectrum”, Proc. Indian Acad. Sci. - Sect. A **37**, 377–384 (1953) (cit. on p. 10).

[26]R. S. Krishnan, “Elastic constants of crystals from light scattering measurements”, Proc. Indian Acad. Sci. - Sect. A **41**, 91–97 (1955) (cit. on p. 10).

[27]T. H. MAIMAN, “Stimulated Optical Radiation in Ruby”, Nature **187**, 493–494 (1960) (cit. on p. 11).

[28]F. J. McClung and R. W. Hellwarth, “Giant Optical Pulsations from Ruby”, J. Appl. Phys. **33**, 828–829 (1962) (cit. on p. 11).

[29]E. J. Woodbury and W. K. Ng, “Ruby Laser Operation in the Near IR”, Proc. IRE **50**, 2365–2383 (1962) (cit. on p. 11).

[30]G. Eckhardt, R. W. Hellwarth, F. J. McClung, S. E. Schwarz, D. Weiner, and E. J. Woodbury, “Stimulated Raman Scattering From Organic Liquids”, Phys. Rev. Lett. **9**, 455–457 (1962) (cit. on p. 11).

[31]R. W. Hellwarth, “Theory of Stimulated Raman Scattering”, Phys. Rev. **130**, 1850–1852 (1963) (cit. on p. 11).

[32]V. A. Zubov, M. M. Sushchinskii, and I. K. Shuvalov, “STIMULATED RAMAN SCATTERING OF LIGHT”, Sov. Phys. Uspekhi **7**, 419–433 (1964) (cit. on p. 11).

[33]R. W. Minck, R. W. Terhune, and W. G. Rado, “LASER-STIMULATED RAMAN EFFECT AND RESONANT FOUR-PHOTON INTERACTIONS IN GASES H2 , D2 , AND CH 4”, Appl. Phys. Lett. **3**, 181–184 (1963) (cit. on p. 11).

[34]B. Stoicheff, “Characteristics of stimulated raman radiation generated by coherent light”, Phys. Lett. **7**, 186–188 (1963) (cit. on p. 11).

[35]E. Garmire, F. Pandarese, and C. H. Townes, “Coherently Driven Molecular Vibrations and Light Modulation”, Phys. Rev. Lett. **11**, 160–163 (1963) (cit. on p. 12).

[36]R. Y. Chiao, C. H. Townes, and B. P. Stoicheff, “Stimulated brillouin scattering and coherent generation of intense hypersonic waves”, Phys. Rev. Lett. **12**, 592–595 (1964) (cit. on p. 12).

[37]R. Y. Chiao and B. P. Stoicheff, “Brillouin Scattering in Liquids Excited by the He-Ne Maser”, J. Opt. Soc. Am. **54**, 1286–1287 (1964) (cit. on p. 13).

[38]N. M. Kroll, “Excitation of Hypersonic Vibrations by Means of Photoelastic Coupling of High-Intensity Light Waves to Elastic Waves”, J. Appl. Phys. **36**, 34–43 (1965) (cit. on p. 13).

[39]C. L. Tang, “Saturation and Spectral Characteristics of the Stokes Emission in the Stimulated Brillouin Process”, J. Appl. Phys. **37**, 2945–2955 (1966) (cit. on pp. 13, 18, 76, 87).

[40]D. Pohl, M. Maier, and W. Kaiser, “Phonon Lifetimes Measured in Amplifiers for Brillouin Radiation”, Phys. Rev. Lett. **20**, 366–368 (1968) (cit. on pp. 13, 89).

[41]E. P. Ippen, “Low-power quasi-cw raman oscillator”, Appl. Phys. Lett. **16**, 303–305 (1970) (cit. on p. 13).

[42] R. H. Stolen, E. P. Ippen, and A. R. Tynes, “Raman Oscillation in Glass Optical Waveguide”, Appl. Phys. Lett. **20**, 62–64 (1972) (cit. on p. 13).

[43] K. Kao and G. Hockham, “Dielectric-fibre surface waveguides for optical frequencies”, Proc. Inst. Electr. Eng. **113**, 1151–1158 (1966) (cit. on pp. 14, 192).

[44] R. G. Smith, “Optical Power Handling Capacity of Low Loss Optical Fibers as Determined by Stimulated Raman and Brillouin Scattering”, Appl. Opt. **11**, 2489 (1972) (cit. on pp. 14, 79, 87, 93, 177).

[45] E. Ippen and R. Stolen, “Stimulated Brillouin scattering in optical fibers”, Appl. Phys. Lett. **21**, 539–541 (1972) (cit. on pp. 14, 70).

[46] D. Cotter, “Stimulated Brillouin Scattering in Monomode Optical Fiber”, J. Opt. Commun. **4**, 10–19 (1983) (cit. on pp. 14, 29).

[47] K. O. Hill, B. S. Kawasaki, and D. C. Johnson, “cw Brillouin laser”, Appl. Phys. Lett. **28**, 608–609 (1976) (cit. on pp. 14, 15).

[48] K. O. Hill, D. C. Johnson, and B. S. Kawasaki, “Cw generation of multiple Stokes and anti-Stokes Brillouin-shifted frequencies”, Appl. Phys. Lett. **29**, 185–187 (1976) (cit. on p. 15).

[49] L. F. Stokes, M. Chodorow, and H. J. Shaw, “All-single-mode fiber resonator”, Opt. Lett. **7**, 288 (1982) (cit. on pp. 15, 109).

[50] L. F. Stokes, M. Chodorow, and H. J. Shaw, “All-fiber stimulated Brillouin ring laser with submilliwatt pump threshold”, Opt. Lett. **7**, 509 (1982) (cit. on pp. 15, 109).

[51] J. R. Sandercock, “Brillouin-Scattering Measurements on Silicon and Germanium”, Phys. Rev. Lett. **28**, 237–240 (1972) (cit. on p. 15).

[52] J. R. Sandercock, “Structure in the Brillouin Spectra of Thin Films”, Phys. Rev. Lett. **29**, 1735–1738 (1972) (cit. on pp. 15, 16).

[53] N. Rowell, V. C.-Y. So, and G. I. Stegeman, “Brillouin scattering in a thin-film waveguide”, Appl. Phys. Lett. **32**, 154–155 (1978) (cit. on p. 16).

[54] N. L. Rowell, P. J. Thomas, H. M. van Driel, and G. I. Stegeman, “Brillouin spectrum of single-mode optical fibers”, Appl. Phys. Lett. **34**, 139–141 (1979) (cit. on pp. 16, 19).

[55] P. J. Thomas, N. L. Rowell, H. M. van Driel, and G. I. Stegeman, “Normal acoustic modes and Brillouin scattering in single-mode optical fibers”, Phys. Rev. B **19**, 4986–4998 (1979) (cit. on pp. 16, 19, 80, 92).

[56] W. May, H. Kiefte, M. J. Clouter, and G. I. Stegeman, “Automated data acquisition and stabilization system for Fabry-Perot interferometry.”, Appl Opt **17**, 1603–1605 (1978) (cit. on pp. 16, 92).

[57] R. H. Stolen, “The early years of fiber nonlinear optics”, J. Light. Technol. **26**, 1021–1031 (2008) (cit. on pp. 17, 29, 43).

[58] D. F. Walls, “Squeezed states of light”, Nature **306**, 141–146 (1983) (cit. on p. 17).

[59] R. M. Shelby, M. D. Levenson, and P. W. Bayer, “Guided acoustic-wave Brillouin scattering”, Phys. Rev. B **31**, 5244–5252 (1985) (cit. on pp. 17, 70).

[60] R. M. Shelby, M. D. Levenson, and P. W. Bayer, “Resolved forward Brillouin scattering in optical fibers”, Phys. Rev. Lett. **54**, 939–942 (1985) (cit. on pp. 17, 70, 80).

[61] R. M. Shelby, M. D. Levenson, D. F. Walls, A. Aspect, and G. J. Milburn, “Generation of squeezed states of light with a fiber-optic ring interferometer”, Phys. Rev. A **33**, 4008–4025 (1986) (cit. on pp. 17, 177).

[62] R. M. Shelby, M. D. Levenson, S. H. Perlmutter, R. G. DeVoe, and D. F. Walls, “Broad-Band Parametric Deamplification of Quantum Noise in an Optical Fiber”, Phys. Rev. Lett. **57**, 691–694 (1986) (cit. on p. 17).

[63] P. Henry, “Lightwave primer”, IEEE J. Quantum Electron. **21**, 1862–1879 (1985) (cit. on p. 18).

[64]A. Chraplyvy and R. Tkach, “Narrowband tunable optical filter for channel selection in densely packed WDM systems”, Electron. Lett. **22**, 1084 (1986) (cit. on pp. 18, 79).

[65]N. Olsson and J. Van Der Ziel, “Characteristics of a semiconductor laser pumped brillouin amplifier with electronically controlled bandwidth”, J. Light. Technol. **5**, 147–153 (1987) (cit. on p. 18).

[66]R. W. Tkach and A. R. Chraplyvy, “Fibre Brillouin amplifiers”, Opt. Quantum Electron. **21**, S105–S112 (1989) (cit. on pp. 18, 79).

[67]R. Mears, L. Reekie, I. Jauncey, and D. Payne, “Low-noise erbium-doped fibre amplifier operating at 1.54um”, Electron. Lett. **23**, 1026 (1987) (cit. on p. 18).

[68]R. Laming, M. Zervas, and D. Payne, “Erbium-doped fiber amplifier with 54 dB gain and 3.1 dB noise figures”, IEEE Photonics Technol. Lett. **4**, 1345–1347 (1992) (cit. on p. 18).

[69]J. L. Zyskind, C. R. Giles, J. R. Simpson, and D. J. DiGiovanni, “Erbium-Doped Fiber Amplifiers and the Next Generation of Lightwave Systems”, AT&T Tech. J. **71**, 53–62 (1992) (cit. on p. 18).

[70]B. Y. Kim, H. E. Engan, H. J. Shaw, and J. N. Blake, “All-fiber acousto-optic frequency shifter”, Opt. Lett. **11**, 389 (1986) (cit. on pp. 18, 19).

[71]P. Russell, D. Culverhouse, and F. Farahi, “Theory of forward stimulated Brillouin scattering in dual-mode single-core fibers”, IEEE J. Quantum Electron. **27**, 836–842 (1991) (cit. on pp. 18, 19, 71).

[72]P. Russell, D. Culverhouse, and F. Farahi, “Experimental observation of forward stimulated Brillouin scattering in dual-mode single-core fibre”, Electron. Lett. **26**, 1195 (1990) (cit. on pp. 18, 19, 21, 71).

[73]Y. Ohmachi and J. Noda, “LiNbO3 TE-TM mode converter using collinear acoustooptic interaction”, IEEE J. Quantum Electron. **13**, 43–46 (1977) (cit. on p. 18).

[74]S. Wang, M. Shah, and J. D. Crow, “Studies of the Use of Gyrotropic and Anisotropic Materials for Mode Conversion in Thin-Film Optical-Waveguide Applications”, J. Appl. Phys. **43**, 1861–1875 (1972) (cit. on p. 18).

[75]H. E. Engan, B. Y. Kim, J. N. Blake, and H. J. Shaw, “Propagation and Optical Interaction of Guided Acoustic Waves in Two-Mode Optical Fibers”, J. Light. Technol. **6**, 428–436 (1988) (cit. on p. 18).

[76]T. Birks, P. Russell, and D. Culverhouse, “The acousto-optic effect in single-mode fiber tapers and couplers”, J. Light. Technol. **14**, 2519–2529 (1996) (cit. on pp. 19, 80).

[77]Chen Kuei Jen, A. Safaai-Jazi, and G. Farnell, “Leaky Modes in Weakly Guiding Fiber Acoustic Waveguides”, IEEE Trans. Ultrason. Ferroelectr. Freq. Control **33**, 634–643 (1986) (cit. on p. 20).

[78]N. Shibata, Y. Azuma, T. Horiguchi, and M. Tateda, “Identification of longitudinal acoustic modes guided in the core region of a single-mode optical fiber by Brillouin gain spectra measurements”, Opt. Lett. **13**, 595 (1988) (cit. on pp. 20, 80, 96).

[79]N. Shibata, K. Okamoto, and Y. Azuma, “Longitudinal acoustic modes and Brillouin-gain spectra for GeO_2-doped-core single-mode fibers”, J. Opt. Soc. Am. B **6**, 1167 (1989) (cit. on p. 20).

[80]A. Yeniay, J.-M. Delavaux, and J. Toulouse, “Spontaneous and stimulated Brillouin scattering gain spectra in optical fibers”, J. Light. Technol. **20**, 1425–1432 (2002) (cit. on pp. 20, 88, 89, 95, 115, 155).

[81]P. Russell, E. Marin, A. Diez, S. Guenneau, and A. Movchan, “Sonic band gaps in PCF preforms: enhancing the interaction of sound and light”, Opt. Express **11**, 2555 (2003) (cit. on p. 20).

[82]P. Dainese, P. S. J. Russell, N. Joly, J. C. Knight, G. S. Wiederhecker, H. L. Fragnito, V. Laude, and A. Khelif, “Stimulated Brillouin scattering from multi-GHz-guided acoustic phonons in nanostructured photonic crystal fibres”, Nat. Phys. **2**, 388–392 (2006) (cit. on pp. 20, 81).

[83]P. Dainese, P. S. Russell, G. S. Wiederhecker, N. Joly, H. L. Fragnito, V. Laude, and A. Khelif, "Raman-like light scattering from acoustic phonons in photonic crystal fiber", Opt. Express **14**, 4141 (2006) (cit. on p. 21).

[84]M. S. Kang, A. Nazarkin, A. Brenn, and P. S. J. Russell, "Tightly trapped acoustic phonons in photonic crystal fibres as highly nonlinear artificial Raman oscillators", Nat. Phys. **5**, 276–280 (2009) (cit. on pp. 21, 22, 70, 77, 78).

[85]M. S. Kang, A. Brenn, and P. St.j.Russell, "All-optical control of gigahertz acoustic resonances by forward stimulated interpolarization scattering in a photonic crystal fiber", Phys. Rev. Lett. **105**, 2–5 (2010) (cit. on pp. 21, 22, 71, 81, 82).

[86]A. Brenn, G. S. Wiederhecker, M. S. Kang, H. Hundertmark, N. Joly, and P. S. Russell, "Influence of air-filling fraction on forward Raman-like scattering by transversely trapped acoustic resonances in photonic crystal fibers", J. Opt. Soc. Am. B **26**, 1641 (2009) (cit. on pp. 21, 71, 81, 82).

[87]M. S. Kang, A. Butsch, and P. S. J. Russell, "Reconfigurable light-driven opto-acoustic isolators in photonic crystal fibre", Nat. Photonics **5**, 549–553 (2011) (cit. on p. 21).

[88]R. Pant, C. G. Poulton, D.-y. Choi, H. Mcfarlane, S. Hile, E. Li, L. Thevenaz, B. Luther-Davies, S. J. Madden, and B. J. Eggleton, "On-chip stimulated Brillouin scattering", Opt. Express **19**, 8285 (2011) (cit. on pp. 21, 23, 145, 147).

[89]A. Choudhary, B. Morrison, I. Aryanfar, S. Shahnia, M. Pagani, Y. Liu, K. Vu, S. Madden, D. Marpaung, and B. J. Eggleton, "Advanced Integrated Microwave Signal Processing With Giant On-Chip Brillouin Gain", J. Light. Technol. **35**, 846–854 (2017) (cit. on pp. 22, 23, 25, 100, 110, 113, 114, 118, 122, 178, 180, 185).

[90]M. Merklein, I. V. Kabakova, T. F. S. Büttner, D.-y. Choi, B. Luther-Davies, S. J. Madden, and B. J. Eggleton, "Enhancing and inhibiting stimulated Brillouin scattering in photonic integrated circuits", Nat. Commun. **6**, 6396 (2015) (cit. on pp. 22, 23, 29, 186).

[91]C. Florea, M. Bashkansky, Z. Dutton, J. Sanghera, P. Pureza, and I. Aggarwal, "Stimulated Brillouin scattering in single-mode As2S3 and As2Se3 chalcogenide fibers", Opt. Express **14**, 12063 (2006) (cit. on pp. 21, 88).

[92]R. Pant, A. Byrnes, C. G. Poulton, E. Li, D.-Y. Choi, S. Madden, B. Luther-Davies, and B. J. Eggleton, "Photonic-chip-based tunable slow and fast light via stimulated Brillouin scattering", Opt. Lett. **37**, 969 (2012) (cit. on pp. 22, 25, 110, 122, 145, 177, 178).

[93]R. Pant, E. Li, C. G. Poulton, D.-Y. Choi, S. Madden, B. Luther-Davies, and B. J. Eggleton, "Observation of Brillouin dynamic grating in a photonic chip.", Opt. Lett. **38**, 305–7 (2013) (cit. on p. 22).

[94]A. Byrnes, R. Pant, E. Li, D.-Y. Choi, C. G. Poulton, S. Fan, S. Madden, B. Luther-Davies, and B. J. Eggleton, "Photonic chip based tunable and reconfigurable narrowband microwave photonic filter using stimulated Brillouin scattering", Opt. Express **20**, 18836 (2012) (cit. on pp. 22, 145, 148, 152, 157, 177).

[95]P. T. Rakich, C. Reinke, R. Camacho, P. Davids, and Z. Wang, "Giant Enhancement of Stimulated Brillouin Scattering in the Subwavelength Limit", Phys. Rev. X **2**, 011008 (2012) (cit. on pp. 22, 23, 81, 110, 164, 177, 185).

[96]H. Shin, W. Qiu, R. Jarecki, J. a. Cox, R. H. Olsson, A. Starbuck, Z. Wang, and P. T. Rakich, "Tailorable stimulated Brillouin scattering in nanoscale silicon waveguides", Nat. Commun. **4**, 1–10 (2013) (cit. on pp. 23, 25, 152, 164, 177, 185).

[97]M. Eichenfield, J. Chan, R. M. Camacho, K. J. Vahala, and O. Painter, "Optomechanical crystals.", Nature **462**, 78–82 (2009) (cit. on p. 22).

[98]M. Aspelmeyer, T. J. Kippenberg, and F. Marquardt, "Cavity optomechanics", Rev. Mod. Phys. **86**, 1391–1452 (2014) (cit. on pp. 22, 81).

[99]A. H. Safavi-Naeini and O. Painter, "Optomechanical Crystal Devices", in *Cavity optomech.* (2014), pp. 195–231 (cit. on p. 22).

[100]P. T. Rakich, P. Davids, and Z. Wang, “Tailoring optical forces in waveguides through radiation pressure and electrostrictive forces”, Opt. Express **18**, 14439 (2010) (cit. on pp. 22, 81, 164).

[101]W. Qiu, P. T. Rakich, H. Shin, H. Dong, M. Soljačić, and Z. Wang, “Stimulated Brillouin scattering in nanoscale silicon step-index waveguides: a general framework of selection rules and calculating SBS gain”, Opt. Express **21**, 31402 (2013) (cit. on pp. 23, 75, 81, 82).

[102]H. Shin, J. a. Cox, R. Jarecki, A. Starbuck, Z. Wang, and P. T. Rakich, “Control of coherent information via on-chip photonic–phononic emitter–receivers”, Nat. Commun. **6**, 6427 (2015) (cit. on p. 24).

[103]R. Van Laer, B. Kuyken, D. Van Thourhout, and R. Baets, “Interaction between light and highly confined hypersound in a silicon photonic nanowire”, Nat. Photonics **9**, 199–203 (2015) (cit. on pp. 24, 25, 73, 77, 78, 82, 91, 110, 115, 121, 122, 134, 152, 157, 164–167, 177, 185).

[104]E. A. Kittlaus, H. Shin, and P. T. Rakich, “Large Brillouin amplification in silicon”, Nat. Photonics **10**, 463–467 (2016) (cit. on pp. 24, 25, 70, 78, 82, 91, 110, 111, 113–116, 122, 134, 178, 185).

[105]R. V. Laer, A. Bazin, B. Kuyken, R. Baets, and D. V. Thourhout, “Net on-chip Brillouin gain based on suspended silicon nanowires”, New J. Phys. **17**, 115005 (2015) (cit. on pp. 25, 91, 110, 115, 116, 121, 122, 175, 185).

[106]C. Wolff, R. V. Laer, M. J. Steel, B. J. Eggleton, and C. G. Poulton, “Brillouin resonance broadening due to structural variations in nanoscale waveguides”, New J. Phys. **18**, 025006 (2016) (cit. on pp. 25, 111, 115).

[107]C. Wolff, P. Gutsche, M. J. Steel, B. J. Eggleton, and C. G. Poulton, “Impact of nonlinear loss on stimulated Brillouin scattering”, J. Opt. Soc. Am. B **32**, 1968 (2015) (cit. on pp. 25, 111, 115, 163).

[108]C. Wolff, P. Gutsche, M. J. Steel, B. J. Eggleton, and C. G. Poulton, “Power limits and a figure of merit for stimulated Brillouin scattering in the presence of third and fifth order loss”, Opt. Express **23**, 26628 (2015) (cit. on pp. 25, 111, 115, 163).

[109]E. A. Kittlaus, N. T. Otterstrom, and P. T. Rakich, “On-chip Inter-modal Brillouin Scattering”, (2016) (cit. on pp. 25, 71).

[110]E. A. Kittlaus, N. T. Otterstrom, and P. T. Rakich, “On-chip inter-modal Brillouin scattering”, Nat. Commun. **8**, 15819 (2017) (cit. on pp. 26, 134, 175, 178, 185).

[111]K. J. Vahala, “Optical microcavities”, Nature **424**, 839–846 (2003) (cit. on p. 26).

[112]S. M. Spillane, T. J. Kippenberg, and K. J. Vahala, “Ultralow-threshold Raman laser using a spherical dielectric microcavity”, Nature **415**, 621–623 (2002) (cit. on p. 26).

[113]D. K. Armani, T. J. Kippenberg, S. M. Spillane, and K. J. Vahala, “Ultra-high-Q toroid microcavity on a chip”, Nature **421**, 925–928 (2003) (cit. on p. 26).

[114]T. J. Kippenberg, S. M. Spillane, D. K. Armani, and K. J. Vahala, “Ultralow-threshold microcavity Raman laser on a microelectronic chip”, Opt. Lett. **29**, 1224 (2004) (cit. on p. 26).

[115]M. Tomes and T. Carmon, “Photonic Micro-Electromechanical Systems Vibrating at X-band (11-GHz) Rates”, Phys. Rev. Lett. **102**, 113601 (2009) (cit. on pp. 26, 27, 116).

[116]I. S. Grudinin, A. B. Matsko, and L. Maleki, “Brillouin Lasing with a CaF2 Whispering Gallery Mode Resonator”, Phys. Rev. Lett. **102**, 043902 (2009) (cit. on pp. 26, 27, 116).

[117]D. Braje, L. Hollberg, and S. Diddams, “Brillouin-Enhanced hyperparametric generation of an optical frequency comb in a monolithic highly nonlinear fiber cavity pumped by a cw laser”, Phys. Rev. Lett. **102**, 1–4 (2009) (cit. on pp. 26, 27).

[118]G. Bahl, J. Zehnpfennig, M. Tomes, and T. Carmon, “Stimulated optomechanical excitation of surface acoustic waves in a microdevice”, Nat. Commun. **2**, 403 (2011) (cit. on pp. 27, 28).

[119]G. Bahl, M. Tomes, F. Marquardt, and T. Carmon, "Observation of spontaneous Brillouin cooling", Nat. Phys. **8**, 203–207 (2012) (cit. on pp. 27, 28).

[120]H. Lee, T. Chen, J. Li, K. Y. Yang, S. Jeon, O. Painter, and K. J. Vahala, "Chemically etched ultrahigh-Q wedge-resonator on a silicon chip", Nat. Photonics **6**, 369–373 (2012) (cit. on pp. 28, 48, 51, 116).

[121]J. Li, H. Lee, T. Chen, and K. J. Vahala, "Characterization of a high coherence, Brillouin microcavity laser on silicon", Opt. Express **20**, 20170 (2012) (cit. on pp. 28, 109, 110, 183, 185).

[122]J. Li, H. Lee, and K. J. Vahala, "Microwave synthesizer using an on-chip Brillouin oscillator", Nat. Commun. **4**, 2097 (2013) (cit. on pp. 28, 109, 110).

[123]J. Li, M.-G. Suh, and K. Vahala, "Microresonator Brillouin gyroscope", Optica **4**, 346 (2017) (cit. on pp. 28, 111).

[124]R. Pant, C. G. Poulton, D.-y. Choi, H. Mcfarlane, S. Hile, E. Li, L. Thevenaz, B. Luther-Davies, S. J. Madden, and B. J. Eggleton, "On-chip stimulated Brillouin scattering", Opt. Express **19**, 8285 (2011) (cit. on pp. 28, 88, 98, 99, 153, 164, 167, 177, 178, 185).

[125]R. Pant, E. Li, D.-Y. Choi, C. G. Poulton, S. J. Madden, B. Luther-Davies, and B. J. Eggleton, "Cavity enhanced stimulated Brillouin scattering in an optical chip for multiorder Stokes generation", Opt. Lett. **36**, 3687 (2011) (cit. on pp. 29, 110).

[126]I. V. Kabakova, R. Pant, D.-Y. Choi, S. Debbarma, B. Luther-Davies, S. J. Madden, and B. J. Eggleton, "Narrow linewidth Brillouin laser based on chalcogenide photonic chip", Opt. Lett. **38**, 3208 (2013) (cit. on pp. 29, 99, 110, 185).

[127]S. Madden, Z. Jin, D. Choi, S. Debbarma, D. Bulla, and B. Luther-Davies, "Low loss coupling to sub-micron thick rib and nanowire waveguides by vertical tapering", Opt. Express **21**, 3582 (2013) (cit. on pp. 29, 97–99, 150, 159).

[128]T. F. S. Büttner, M. Merklein, I. V. Kabakova, D. D. Hudson, D.-Y. Choi, B. Luther-Davies, S. J. Madden, and B. J. Eggleton, "Phase-locked, chip-based, cascaded stimulated Brillouin scattering", Optica **1**, 311 (2014) (cit. on p. 29).

[129]T. F. S. Büttner, I. V. Kabakova, D. D. Hudson, R. Pant, C. G. Poulton, A. C. Judge, and B. J. Eggleton, "Phase-locking and pulse generation in multi-frequency brillouin oscillator via four wave mixing.", Sci. Rep. **4**, 5032 (2014) (cit. on p. 29).

[130]W. A. Gambling, "The rise and rise of optical fibers", IEEE J. Sel. Top. Quantum Electron. **6**, 1084 (2000) (cit. on p. 29).

[131]E. Garmire, "Perspectives on stimulated Brillouin scattering", New J. Phys. **19**, 011003 (2017) (cit. on p. 29).

[132]A. Kobyakov, M. Sauer, and D. Chowdhury, "Stimulated Brillouin scattering in optical fibers", Adv. Opt. Photonics **2**, 1 (2009) (cit. on pp. 29, 66, 79, 109).

[133]B. J. Eggleton, C. G. Poulton, and R. Pant, "Inducing and harnessing stimulated Brillouin scattering in photonic integrated circuits", Adv. Opt. Photonics **5**, 536 (2013) (cit. on pp. 29, 61, 98, 164).

[134]M. Merklein, A. Casas-Bedoya, D. Marpaung, T. Buttner, M. Pagani, B. Morrison, I. Kabakova, and B. Eggleton, "Stimulated Brillouin scattering in photonic integrated circuits: novel applications and devices", IEEE J. Sel. Top. Quantum Electron. **22**, 1–1 (2016) (cit. on p. 29).

[135]H. J. Kong, J. Y. Lee, Y. S. Shin, J. O. Byun, H. S. Park, and H. Kim, "Beam Recombination Characteristics in Array Laser Amplification Using Stimulated Brillouin Scattering Phase Conjugation", Opt. Rev. **4**, 277–283 (1997) (cit. on p. 30).

[136]C. a. Galindez-Jamioy and J. M. López-Higuera, "Brillouin Distributed Fiber Sensors: An Overview and Applications", J. Sensors **2012**, 1–17 (2012) (cit. on p. 30).

[137]A. Motil, A. Bergman, and M. Tur, "[INVITED] State of the art of Brillouin fiber-optic distributed sensing", Opt. Laser Technol. **78**, 81–103 (2016) (cit. on p. 30).

[138]Z. Meng, A. J. Traverso, C. W. Ballmann, M. Troyanova-Wood, and V. V. Yakovlev, "Seeing cells in a new light: a renaissance of Brillouin spectroscopy", Adv. Opt. Photonics **8**, 300–327 (2016) (cit. on p. 30).

[139]R. Pant, D. Marpaung, I. V. Kabakova, B. Morrison, C. G. Poulton, and B. J. Eggleton, "On-chip stimulated brillouin scattering for microwave signal processing and generation", Laser Photonics Rev. **8**, 653–666 (2014) (cit. on pp. 30, 110, 122, 177).

[140]R. W. Boyd, *Nonlinear Optics, Third Edition* (2008), p. 640 (cit. on pp. 32, 39–41, 62, 64, 77, 164).

[141]B. E. A. Saleh and M. C. Teich, *Fundamentals of Photonics* (1991) (cit. on pp. 33, 34).

[142]G. Agrawal, "Nonlinear Fiber Optics", in *Nonlinear fiber opt. (fifth ed.* Fifth Edit (2013), pp. 1–25 (cit. on pp. 39, 41, 42, 87).

[143]G. New, *Introduction to Nonlinear Optics* (2011) (cit. on p. 39).

[144]G. Stegeman, E. Wright, N. Finlayson, R. Zanoni, and C. Seaton, "Third order nonlinear integrated optics", J. Light. Technol. **6**, 953–970 (1988) (cit. on pp. 39, 49).

[145]I. Rukhlenko, M. Premaratne, and G. Agrawal, "Nonlinear Silicon Photonics: Analytical Tools", IEEE J. Sel. Top. Quantum Electron. **16**, 200–215 (2010) (cit. on pp. 40, 51).

[146]I. D. Rukhlenko, M. Premaratne, and G. P. Agrawal, "Effective mode area and its optimization in silicon-nanocrystal waveguides", Opt. Lett. **37**, 2295 (2012) (cit. on p. 40).

[147]E. Wooten, K. Kissa, A. Yi-Yan, E. Murphy, D. Lafaw, P. Hallemeier, D. Maack, D. Attanasio, D. Fritz, G. McBrien, and D. Bossi, "A review of lithium niobate modulators for fiber-optic communications systems", IEEE J. Sel. Top. Quantum Electron. **6**, 69–82 (2000) (cit. on p. 40).

[148]A. Vatarescu, "Light conversion in nonlinear monomode optical fibers", J. Light. Technol. **5**, 1652–1659 (1987) (cit. on p. 42).

[149]J. Hansryd, P. Andrekson, M. Westlund, Jie Li, and P.-O. Hedekvist, "Fiber-based optical parametric amplifiers and their applications", IEEE J. Sel. Top. Quantum Electron. **8**, 506–520 (2002) (cit. on p. 42).

[150]R. H. Stolen, J. E. Bjorkholm, and A. Ashkin, "Phase-matched three-wave mixing in silica fiber optical waveguides", Appl. Phys. Lett. **24**, 308–310 (1974) (cit. on p. 43).

[151]R. Stolen, "Phase-matched-stimulated four-photon mixing in silica-fiber waveguides", IEEE J. Quantum Electron. **11**, 100–103 (1975) (cit. on p. 43).

[152]D. Gloge, "Weakly Guiding Fibers", Appl. Opt. **10**, 2252 (1971) (cit. on p. 43).

[153]D. Gloge, "Dispersion in Weakly Guiding Fibers", Appl. Opt. **10**, 2442 (1971) (cit. on p. 43).

[154]R. Stolen and J. Bjorkholm, "Parametric amplification and frequency conversion in optical fibers", IEEE J. Quantum Electron. **18**, 1062–1072 (1982) (cit. on pp. 43, 50).

[155]P. S. Russell, "Photonic-Crystal Fibers", J. Light. Technol. **24**, 4729–4749 (2006) (cit. on p. 43).

[156]H. Fukuda, K. Yamada, T. Shoji, M. Takahashi, T. Tsuchizawa, T. Watanabe, J.-I. Takahashi, and S.-I. Itabashi, "Four-wave mixing in silicon wire waveguides.", Opt. Express **13**, 4629–4637 (2005) (cit. on pp. 44, 132).

[157]M. A. Foster, A. C. Turner, J. E. Sharping, B. S. Schmidt, M. Lipson, and A. L. Gaeta, "Broad-band optical parametric gain on a silicon photonic chip", Nature **441**, 960–963 (2006) (cit. on p. 44).

[158]M. a. Foster, A. C. Turner, R. Salem, M. Lipson, and A. L. Gaeta, "Broad-band continuous-wave parametric wavelength conversion in silicon nanowaveguides", Opt. Express **15**, 12949 (2007) (cit. on p. 44).

[159]M. R. Lamont, C. M. de Sterke, and B. J. Eggleton, "Dispersion engineering of highly nonlinear As_2S_3 waveguides for parametric gain and wavelength conversion", Opt. Express **15**, 9458 (2007) (cit. on pp. 44, 89).

[160]M. R. Lamont, B. Luther-Davies, D.-Y. Choi, S. Madden, X. Gai, and B. J. Eggleton, "Net-gain from a parametric amplifier on a chalcogenide optical chip", Opt. Express **16**, 20374 (2008) (cit. on p. 44).

[161]M. R. Lamont, B. Luther-Davies, D.-Y. Choi, S. Madden, and B. J. Eggleton, "Supercontinuum generation in dispersion engineered highly nonlinear (γ = 10 /W/m) As_2S_3 chalcogenide planar waveguide", Opt. Express **16**, 14938 (2008) (cit. on p. 44).

[162]B. Kuyken, P. Verheyen, P. Tannouri, X. Liu, J. Van Campenhout, R. Baets, W. M. J. Green, and G. Roelkens, "Generation of 3.6 μm radiation and telecom-band amplification by four-wave mixing in a silicon waveguide with normal group velocity dispersion", Opt. Lett. **39**, 1349 (2014) (cit. on p. 44).

[163]X. Liu, B. Kuyken, G. Roelkens, R. Baets, R. M. Osgood, and W. M. J. Green, "Bridging the mid-infrared-to-telecom gap with silicon nanophotonic spectral translation", Nat. Photonics **6**, 667–671 (2012) (cit. on p. 44).

[164]X. Liu, R. M. Osgood, Y. A. Vlasov, and W. M. J. Green, "Mid-infrared optical parametric amplifier using silicon nanophotonic waveguides", Nat. Photonics **4**, 557–560 (2010) (cit. on p. 44).

[165]J. Riemensberger, K. Hartinger, T. Herr, V. Brasch, R. Holzwarth, and T. J. Kippenberg, "Dispersion engineering of thick high-Q silicon nitride ring-resonators via atomic layer deposition", Opt. Express **20**, 27661 (2012) (cit. on p. 44).

[166]P. Apiratikul, J. J. Wathen, G. a. Porkolab, B. Wang, L. He, T. E. Murphy, and C. J. K. Richardson, "Enhanced continuous-wave four-wave mixing efficiency in nonlinear AlGaAs waveguides", Opt. Express **22**, 26814 (2014) (cit. on pp. 44, 130).

[167]R. M. Osgood, Jr., N. C. Panoiu, J. I. Dadap, X. Liu, X. Chen, I.-W. Hsieh, E. Dulkeith, W. M. Green, and Y. A. Vlasov, "Engineering nonlinearities in nanoscale optical systems: physics and applications in dispersion-engineered silicon nanophotonic wires", Adv. Opt. Photonics **1**, 162 (2009) (cit. on pp. 44, 49, 130).

[168]S. a. Schulz, L. O'Faolain, D. M. Beggs, T. P. White, A. Melloni, and T. F. Krauss, "Dispersion engineered slow light in photonic crystals: a comparison", J. Opt. **12**, 104004 (2010) (cit. on pp. 44, 51).

[169]T. Baba, "Slow light in photonic crystals", Nat. Photonics **2**, 465–473 (2008) (cit. on pp. 44, 51).

[170]K. Suzuki and T. Baba, "Nonlinear light propagation in chalcogenide photonic crystal slow light waveguides.", Opt. Express **18**, 26675–85 (2010) (cit. on p. 44).

[171]S. E. Miller, "Integrated Optics: An Introduction", Bell Syst. Tech. J. **48**, 2059–2069 (1969) (cit. on pp. 44, 47, 193).

[172]W. Bogaerts, P. Dumon, V. Wiaux, J. Wouters, S. Beckx, and D. Taillaert, "Nanophotonic waveguides in silicon-on-insulator fabricated with CMOS technology", J. Light. Technol. **23**, 401–412 (2005) (cit. on pp. 45, 48).

[173]P. Dumon, G. Priem, L. R. Nunes, W. Bogaerts, D. Van Thourhout, P. Bienstman, T. K. Liang, M. Tsuchiya, P. Jaenen, S. Beckx, J. Wouters, and R. Baets, "Linear and Nonlinear Nanophotonic Devices Based on Silicon-on-Insulator Wire Waveguides", Jpn. J. Appl. Phys. **45**, 6589–6602 (2006) (cit. on p. 45).

[174]M. Settle, M. Salib, A. Michaeli, and T. F. Krauss, "Low loss silicon on insulator photonic crystal waveguides made by 193nm optical lithography.", Opt. Express **14**, 2440–2445 (2006) (cit. on p. 45).

[175]S. Selvaraja, P. Jaenen, W. Bogaerts, D. Van Thourhout, P. Dumon, and R. Baets, "Fabrication of Photonic Wire and Crystal Circuits in Silicon-on-Insulator Using 193-nm Optical Lithography", J. Light. Technol. **27**, 4076–4083 (2009) (cit. on pp. 45, 58).

[176]W. Bogaerts, S. K. Selvaraja, P. Dumon, J. Brouckaert, K. De Vos, D. Van Thourhout, and R. Baets, "Silicon-on-Insulator Spectral Filters Fabricated With CMOS Technology", IEEE J. Sel. Top. Quantum Electron. **16**, 33–44 (2010) (cit. on p. 45).

[177] S. K. Selvaraja, P. De Heyn, G. Winroth, P. Ong, G. Lepage, C. Cailler, A. Rigny, K. Bourdelle, W. Bogaerts@ugent.be, D. VanThourhout, J. Van Campenhout, and P. Absil, "Highly uniform and low-loss passive silicon photonics devices using a 300mm CMOS platform", in Opt. fiber commun. conf. (2014), Th2A.33 (cit. on pp. 45, 48, 58, 127).

[178] T. Horikawa, D. Shimura, and T. Mogami, "Low-loss silicon wire waveguides for optical integrated circuits", MRS Commun. **6**, 9–15 (2016) (cit. on pp. 45, 48).

[179] V. Subramaniam, G. De Brabander, D. Naghski, and J. Boyd, "Measurement of mode field profiles and bending and transition losses in curved optical channel waveguides", J. Light. Technol. **15**, 990–997 (1997) (cit. on pp. 46, 47, 53).

[180] E. A. J. Marcatili and S. E. Miller, "Improved Relations Describing Directional Control in Electromagnetic Wave Guidance", Bell Syst. Tech. J. **48**, 2161–2188 (1969) (cit. on p. 47).

[181] D. Marcuse, "Radiation Losses of Dielectric Waveguides in Terms of the Power Spectrum of the Wall Distortion Function", Bell Syst. Tech. J. **48**, 3233–3242 (1969) (cit. on p. 47).

[182] S. Suzuki, M. Yanagisawa, Y. Hibino, and K. Oda, "High-density integrated planar lightwave circuits using SiO2-GeO2 waveguides with a high refractive index difference", J. Light. Technol. **12**, 790–796 (1994) (cit. on p. 47).

[183] A. Himeno, K. Kato, and T. Miya, "Silica-based planar lightwave circuits", IEEE J. Sel. Top. Quantum Electron. **4**, 913–924 (1998) (cit. on p. 47).

[184] C. R. Doerr and K. Okamoto, "Advances in Silica Planar Lightwave Circuits", J. Light. Technol. **24**, 4763–4789 (2006) (cit. on pp. 47, 52, 53).

[185] Y. A. Vlasov and S. J. McNab, "Losses in single-mode silicon-on-insulator strip waveguides and bends", Opt. Express **12**, 1622 (2004) (cit. on p. 48).

[186] C. G. Poulton, C. Koos, M. Fujii, A. Pfrang, T. Schimmel, J. Leuthold, and W. Freude, "Radiation Modes and Roughness Loss in High Index-Contrast Waveguides", IEEE J. Sel. Top. Quantum Electron. **12**, 1306–1321 (2006) (cit. on pp. 48, 112).

[187] D. Marcuse, "Mode Conversion Caused by Surface Imperfections of a Dielectric Slab Waveguide", Bell Syst. Tech. J. **48**, 3187–3215 (1969) (cit. on p. 48).

[188] F. P. Payne and J. P. R. Lacey, "A theoretical analysis of scattering loss from planar optical waveguides", Opt. Quantum Electron. **26**, 977–986 (1994) (cit. on p. 48).

[189] P. K. Tien, "Light Waves in Thin Films and Integrated Optics", Appl. Opt. **10**, 2395 (1971) (cit. on p. 48).

[190] K. K. Lee, D. R. Lim, L. C. Kimerling, J. Shin, and F. Cerrina, "Fabrication of ultralow-loss Si/SiO_2 waveguides by roughness reduction", Opt. Lett. **26**, 1888 (2001) (cit. on p. 48).

[191] P. Dumon, W. Bogaerts, V. Wiaux, J. Wouters, S. Beckx, J. Van Campenhout, D. Taillaert, B. Luyssaert, P. Bienstman, D. Van Thourhout, and R. Baets, "Low-Loss SOI Photonic Wires and Ring Resonators Fabricated With Deep UV Lithography", IEEE Photonics Technol. Lett. **16**, 1328–1330 (2004) (cit. on p. 48).

[192] M. Kohtoku, T. Kominato, Y. Nasu, and T. Shibata, "New waveguide fabrication techniques for next-generation PLCs", NTT Tech. Rev. **3**, 37–41 (2005) (cit. on pp. 48, 53).

[193] H. Lee, T. Chen, J. Li, O. Painter, and K. J. Vahala, "Ultra-low-loss optical delay line on a silicon chip", Nat. Commun. **3**, 867 (2012) (cit. on p. 48).

[194] W. Bogaerts and S. K. Selvaraja, "Compact Single-Mode Silicon Hybrid Rib/Strip Waveguide With Adiabatic Bends", IEEE Photonics J. **3**, 422–432 (2011) (cit. on pp. 48, 53).

[195] Kuan Pei Yap, A. Delage, J. Lapointe, B. Lamontagne, J. Schmid, P. Waldron, B. Syrett, and S. Janz, "Correlation of Scattering Loss, Sidewall Roughness and Waveguide Width in Silicon-on-Insulator (SOI) Ridge Waveguides", J. Light. Technol. **27**, 3999–4008 (2009) (cit. on p. 48).

[196]P. Dong, W. Qian, S. Liao, H. Liang, C.-C. Kung, N.-N. Feng, R. Shafiiha, J. Fong, D. Feng, A. V. Krishnamoorthy, and M. Asghari, "Low loss shallow-ridge silicon waveguides.", Opt. Express **18**, 14474–14479 (2010) (cit. on pp. 48, 53).

[197]A. Biberman, M. J. Shaw, E. Timurdogan, J. B. Wright, and M. R. Watts, "Ultralow-loss silicon ring resonators", Opt. Lett. **37**, 4236 (2012) (cit. on p. 48).

[198]T. G. Nguyen, R. S. Tummidi, T. L. Koch, and A. Mitchell, "Lateral leakage of TM-like mode in thin-ridge Silicon-on-Insulator bent waveguides and ring resonators", Opt. Express **18**, 7243 (2010) (cit. on p. 48).

[199]D. Dai, Z. Wang, N. Julian, and J. E. Bowers, "Compact broadband polarizer based on shallowly-etched silicon-on-insulator ridge optical waveguides", Opt. Express **18**, 27404 (2010) (cit. on p. 48).

[200]A. Hope, T. Nguyen, A. Mitchell, and W. Bogaerts, "Quantitative analysis of TM lateral leakage in foundry fabricated silicon rib waveguides", IEEE Photonics Technol. Lett. **PP**, 1–1 (2015) (cit. on p. 48).

[201]A. Oliner, Song-Tsuen Peng, Ting-Ih Hsu, and A. Sanchez, "Guidance and Leakage Properties of a Class of Open Dielectric Waveguides: Part II–New Physical Effects", IEEE Trans. Microw. Theory Tech. **29**, 855–869 (1981) (cit. on p. 48).

[202]J. F. Bauters, M. J. R. Heck, D. D. John, J. S. Barton, C. M. Bruinink, A. Leinse, R. G. Heideman, D. J. Blumenthal, and J. E. Bowers, "Planar waveguides with less than 01 dB/m propagation loss fabricated with wafer bonding", Opt. Express **19**, 24090 (2011) (cit. on p. 48).

[203]M. Gould, A. Pomerene, C. Hill, S. Ocheltree, Y. Zhang, T. Baehr-Jones, and M. Hochberg, "Ultra-thin silicon-on-insulator strip waveguides and mode couplers", Appl. Phys. Lett. **101**, 221106 (2012) (cit. on p. 48).

[204]D. T. Spencer, J. F. Bauters, M. J. R. Heck, and J. E. Bowers, "Integrated waveguide coupled Si_3N_4 resonators in the ultrahigh-Q regime", Optica **1**, 153 (2014) (cit. on p. 48).

[205]K. Wörhoff, R. G. Heideman, A. Leinse, and M. Hoekman, "TriPleX: a versatile dielectric photonic platform", Adv. Opt. Technol. **4**, 189–207 (2015) (cit. on pp. 48, 58, 175).

[206]M. Cherchi, S. Ylinen, M. Harjanne, M. Kapulainen, and T. Aalto, "Dramatic size reduction of waveguide bends on a micron-scale silicon photonic platform", Opt. Express **21**, 17814 (2013) (cit. on pp. 48, 54, 112, 120, 126–128, 178).

[207]G. Li, J. Yao, H. Thacker, A. Mekis, X. Zheng, I. Shubin, Y. Luo, J.-h. Lee, K. Raj, J. E. Cunningham, and A. V. Krishnamoorthy, "Ultralow-loss, high-density SOI optical waveguide routing for macrochip interconnects", Opt. Express **20**, 12035 (2012) (cit. on pp. 48, 53).

[208]D. Melati, A. Melloni, and F. Morichetti, "Real photonic waveguides: guiding light through imperfections", Adv. Opt. Photonics **6**, 156 (2014) (cit. on p. 49).

[209]F. Morichetti, A. Canciamilla, C. Ferrari, M. Torregiani, A. Melloni, and M. Martinelli, "Roughness Induced Backscattering in Optical Silicon Waveguides", Phys. Rev. Lett. **104**, 033902 (2010) (cit. on pp. 49, 54, 131).

[210]M. Á. Guillén-Torres, K. Murray, H. Yun, M. Caverley, E. Cretu, L. Chrostowski, and N. A. F. Jaeger, "Effects of backscattering in high-Q, large-area silicon-on-insulator ring resonators", Opt. Lett. **41**, 1538 (2016) (cit. on p. 49).

[211]S. Afshar V. and T. M. Monro, "A full vectorial model for pulse propagation in emerging waveguides with subwavelength structures part I: Kerr nonlinearity", Opt. Express **17**, 2298 (2009) (cit. on p. 49).

[212]S. Afshar V., W. Q. Zhang, H. Ebendorff-Heidepriem, and T. M. Monro, "Small core optical waveguides are more nonlinear than expected: experimental confirmation", Opt. Lett. **34**, 3577 (2009) (cit. on p. 49).

[213]V. Shahraam Afshar, T. M. Monro, and C. M. de Sterke, “Understanding the contribution of mode area and slow light to the effective Kerr nonlinearity of waveguides”, Opt. Express **21**, 18558 (2013) (cit. on p. 49).

[214]W. Zhang, S. Serna, N. Dubreuil, and E. Cassan, “Nonlinear optimization of slot Si waveguides: TPA minimization with FOM_TPA up to 425”, Opt. Lett. **40**, 1212 (2015) (cit. on pp. 49, 51).

[215]C. Koos, L. Jacome, C. Poulton, J. Leuthold, and W. Freude, “Nonlinear silicon-on-insulator waveguides for all-optical signal processing”, Opt. Express **15**, 5976 (2007) (cit. on pp. 49, 51, 56).

[216]J. Toulouse, “Optical nonlinearities in fibers: review, recent examples, and systems applications”, J. Light. Technol. **23**, 3625–3641 (2005) (cit. on pp. 50, 87).

[217]C. C. Wang, “Empirical Relation between the Linear and the Third-Order Nonlinear Optical Susceptibilities”, Phys. Rev. B **2**, 2045–2048 (1970) (cit. on p. 50).

[218]N. Boling, A. Glass, and A. Owyoung, “Empirical relationships for predicting nonlinear refractive index changes in optical solids”, IEEE J. Quantum Electron. **14**, 601–608 (1978) (cit. on p. 50).

[219]T. M. Monro and H. Ebendorff-Heidepriem, “Progress In Microstructured Optical Fibers”, Annu. Rev. Mater. Res. **36**, 467–495 (2006) (cit. on p. 50).

[220]K. J. A. Ooi, D. K. T. Ng, T. Wang, A. K. L. Chee, S. K. Ng, Q. Wang, L. K. Ang, A. M. Agarwal, L. C. Kimerling, and D. T. H. Tan, “Pushing the limits of CMOS optical parametric amplifiers with USRN:Si7N3 above the two-photon absorption edge”, Nat. Commun. **8**, 13878 (2017) (cit. on pp. 50, 51).

[221]X. Gai, Y. Yu, B. Kuyken, P. Ma, S. J. Madden, J. Van Campenhout, P. Verheyen, G. Roelkens, R. Baets, and B. Luther-Davies, “Nonlinear absorption and refraction in crystalline silicon in the mid-infrared”, Laser Photon. Rev. **7**, 1054–1064 (2013) (cit. on pp. 50, 51, 182).

[222]T. Liang and H. Tsang, “Nonlinear Absorption and Raman Scattering in Silicon-on-Insulator Optical Waveguides”, IEEE J. Sel. Top. Quantum Electron. **10**, 1149–1153 (2004) (cit. on p. 50).

[223]W. C. Hurlbut, Y.-S. Lee, K. L. Vodopyanov, P. S. Kuo, and M. M. Fejer, “Multiphoton absorption and nonlinear refraction of GaAs in the mid-infrared”, Opt. Lett. **32**, 668 (2007) (cit. on p. 50).

[224]J. Harbold, F. Ilday, F. Wise, and B. Aitken, “Highly nonlinear Ge-As-Se and Ge-As-S-Se glasses for all-optical switching”, IEEE Photonics Technol. Lett. **14**, 822–824 (2002) (cit. on p. 50).

[225]A. Zakery and S. R. Elliott, “Optical properties and applications of chalcogenide glasses: A review”, J. Non. Cryst. Solids **330**, 1–12 (2003) (cit. on pp. 50, 87).

[226]G. Lenz, J. Zimmermann, T. Katsufuji, M. E. Lines, H. Y. Hwang, S. Spälter, R. E. Slusher, S.-W. Cheong, J. S. Sanghera, and I. D. Aggarwal, “Large Kerr effect in bulk Se-based chalcogenide glasses”, Opt. Lett. **25**, 254 (2000) (cit. on pp. 50, 87).

[227]S. Krishnamurthy, Z. G. Yu, L. P. Gonzalez, and S. Guha, “Temperature- and wavelength-dependent two-photon and free-carrier absorption in GaAs, InP, GaInAs, and InAsP”, J. Appl. Phys. **109**, 033102 (2011) (cit. on p. 51).

[228]J. Leuthold, C. Koos, and W. Freude, “Nonlinear silicon photonics”, Nat. Photonics **4**, 535–544 (2010) (cit. on pp. 51, 114, 127, 130).

[229]A. C. Turner-Foster, M. a. Foster, J. S. Levy, C. B. Poitras, R. Salem, A. L. Gaeta, and M. Lipson, “Ultrashort free-carrier lifetime in low-loss silicon nanowaveguides”, Opt. Express **18**, 3582 (2010) (cit. on pp. 51, 182).

[230]H. Rong, R. Jones, A. Liu, O. Cohen, D. Hak, A. Fang, and M. Paniccia, “A continuous-wave Raman silicon laser.”, Nature **433**, 725–728 (2005) (cit. on p. 51).

[231]H. Rong, S. Xu, Y.-H. Kuo, V. Sih, O. Cohen, O. Raday, and M. Paniccia, “Low-threshold continuous-wave Raman silicon laser”, Nat. Photonics **1**, 232–237 (2007) (cit. on p. 51).

[232]J. R. Ong, R. Kumar, R. Aguinaldo, and S. Mookherjea, “Efficient CW Four-Wave Mixing in Silicon-on-Insulator Micro-Rings With Active Carrier Removal”, IEEE Photonics Technol. Lett. **25**, 1699–1702 (2013) (cit. on p. 51).

[233]T. W. Baehr-Jones and M. J. Hochberg, “Polymer Silicon Hybrid Systems: A Platform for Practical Nonlinear Optics”, J. Phys. Chem. C **112**, 8085–8090 (2008) (cit. on p. 51).

[234]C. Koos, P. Vorreau, T. Vallaitis, P. Dumon, W. Bogaerts, R. Baets, B. Esembeson, I. Biaggio, T. Michinobu, F. Diederich, W. Freude, and J. Leuthold, “All-optical high-speed signal processing with silicon-organic hybrid slot waveguides”, Nat. Photonics **3**, 216–219 (2009) (cit. on p. 51).

[235]T. Vallaitis, S. Bogatscher, L. Alloatti, P. Dumon, R. Baets, M. L. Scimeca, I. Biaggio, F. Diederich, C. Koos, W. Freude, and J. Leuthold, “Optical properties of highly nonlinear silicon-organic hybrid (SOH) waveguide geometries”, Opt. Express **17**, 17357 (2009) (cit. on pp. 51, 56).

[236]J. J. Wathen, P. Apiratikul, C. J. K. Richardson, G. A. Porkolab, G. M. Carter, and T. E. Murphy, “Efficient continuous-wave four-wave mixing in bandgap-engineered AlGaAs waveguides”, Opt. Lett. **39**, 3161 (2014) (cit. on p. 51).

[237]E. Dulkeith, F. Xia, L. Schares, W. M. Green, L. Sekaric, and Y. a. Vlasov, “Group index and group velocity dispersion in silicon-on-insulator photonic wires: errata”, Opt. Express **14**, 6372 (2006) (cit. on p. 51).

[238]C. Monat, B. Corcoran, M. Ebnali-Heidari, C. Grillet, B. J. Eggleton, T. P. White, L. O’Faolain, and T. F. Krauss, “Slow light enhancement of nonlinear effects in silicon engineered photonic crystal waveguides”, Opt. Express **17**, 2944 (2009) (cit. on p. 51).

[239]F. Morichetti, C. Ferrari, A. Canciamilla, and A. Melloni, “The first decade of coupled resonator optical waveguides: bringing slow light to applications”, Laser Photon. Rev. **6**, 74–96 (2012) (cit. on pp. 51, 186).

[240]C. Monat, M. de Sterke, and B. J. Eggleton, “Slow light enhanced nonlinear optics in periodic structures”, J. Opt. **12**, 104003 (2010) (cit. on p. 51).

[241]B. Corcoran, C. Monat, C. Grillet, D. J. Moss, B. J. Eggleton, T. P. White, L. O’Faolain, and T. F. Krauss, “Green light emission in silicon through slow-light enhanced third-harmonic generation in photonic-crystal waveguides”, Nat. Photonics **3**, 206–210 (2009) (cit. on p. 51).

[242]J. Li, L. O’Faolain, and T. F. Krauss, “Four-wave mixing in slow light photonic crystal waveguides with very high group index”, Opt. Express **20**, 17474 (2012) (cit. on pp. 51, 186).

[243]A. Martin, S. Combrié, and A. D. Rossi, “Photonic crystal waveguides based on wide-gap semiconductor alloys”, J. Opt. **19**, 033002 (2017) (cit. on p. 51).

[244]F. Morichetti, A. Canciamilla, C. Ferrari, A. Samarelli, M. Sorel, and A. Melloni, “Travelling-wave resonant four-wave mixing breaks the limits of cavity-enhanced all-optical wavelength conversion.”, Nat. Commun. **2**, 296 (2011) (cit. on pp. 51, 186).

[245]C. Caer, X. Le Roux, and E. Cassan, “Enhanced localization of light in slow wave slot photonic crystal waveguides.”, Opt. Lett. **37**, 3660–2 (2012) (cit. on p. 51).

[246]C. Caër, S. Combrié, X. Le Roux, E. Cassan, and A. De Rossi, “Extreme optical confinement in a slotted photonic crystal waveguide”, Appl. Phys. Lett. **105**, 121111 (2014) (cit. on p. 51).

[247]A. Martin, D. Sanchez, S. Combrié, A. de Rossi, and F. Raineri, “GaInP on oxide nonlinear photonic crystal technology”, Opt. Lett. **42**, 599 (2017) (cit. on p. 51).

[248]J. F. McMillan, M. Yu, D.-l. Kwong, and C. W. Wong, “Observation of four-wave mixing in slow-light silicon photonic crystal waveguides”, Opt. Express **18**, 15484 (2010) (cit. on p. 51).

[249]J. E. Heebner and R. W. Boyd, “Enhanced all-optical switching by use of a nonlinear fiber ring resonator”, Opt. Lett. **24**, 847 (1999) (cit. on p. 51).

[250]J. E. Heebner, N. N. Lepeshkin, A. Schweinsberg, G. W. Wicks, R. W. Boyd, R. Grover, and P.-T. Ho, "Enhanced linear and nonlinear optical phase response of AlGaAs microring resonators", Opt. Lett. **29**, 769 (2004) (cit. on p. 51).

[251]K. J. Vahala, "Optical microcavities", Nature **424**, 839–846 (2003) (cit. on p. 51).

[252]T. J. Kippenberg, R. Holzwarth, and S. A. Diddams, "Microresonator-Based Optical Frequency Combs", Science **332**, 555–559 (2011) (cit. on p. 51).

[253]D. J. Moss, R. Morandotti, A. L. Gaeta, and M. Lipson, "New CMOS-compatible platforms based on silicon nitride and Hydex for nonlinear optics", Nat. Photonics **7**, 597–607 (2013) (cit. on pp. 51, 59, 127, 131).

[254]X. Ji, F. A. S. Barbosa, S. P. Roberts, A. Dutt, J. Cardenas, Y. Okawachi, A. Bryant, A. L. Gaeta, and M. Lipson, "Ultra-low-loss on-chip resonators with sub-milliwatt parametric oscillation threshold", Optica **4**, 619 (2017) (cit. on p. 51).

[255]T. Herr, V. Brasch, J. D. Jost, C. Y. Wang, N. M. Kondratiev, M. L. Gorodetsky, and T. J. Kippenberg, "Temporal solitons in optical microresonators", Nat. Photonics **8**, 145–152 (2013) (cit. on p. 51).

[256]T. Herr, M. L. Gorodetsky, and T. J. Kippenberg, "Dissipative Kerr solitons in optical microresonators", 1–39 (2015) (cit. on p. 51).

[257]X. Yi, Q.-F. Yang, K. Y. Yang, M.-G. Suh, and K. Vahala, "Soliton frequency comb at microwave rates in a high-Q silica microresonator", Optica **2**, 1078 (2015) (cit. on p. 51).

[258]Q. Li, T. C. Briles, D. A. Westly, T. E. Drake, J. R. Stone, B. R. Ilic, S. A. Diddams, S. B. Papp, and K. Srinivasan, "Stably accessing octave-spanning microresonator frequency combs in the soliton regime", Optica **4**, 193 (2017) (cit. on p. 51).

[259]M.-G. Suh, Q.-F. Yang, K. Y. Yang, X. Yi, and K. J. Vahala, "Microresonator soliton dual-comb spectroscopy", Science **354**, 600–603 (2016) (cit. on p. 51).

[260]Y. Xuan, Y. Liu, L. T. Varghese, A. J. Metcalf, X. Xue, P.-H. Wang, K. Han, J. A. Jaramillo-Villegas, A. Al Noman, C. Wang, S. Kim, M. Teng, Y. J. Lee, B. Niu, L. Fan, J. Wang, D. E. Leaird, A. M. Weiner, and M. Qi, "High-Q silicon nitride microresonators exhibiting low-power frequency comb initiation", Optica **3**, 1171 (2016) (cit. on p. 51).

[261]K. Y. Yang, D. Y. Oh, S. H. Lee, Q.-F. Yang, X. Yi, B. Shen, H. Wang, and K. Vahala, "Bridging ultrahigh-Q devices and photonic circuits", Nat. Photonics **12**, 297–302 (2018) (cit. on p. 51).

[262]L. Chrostowski and M. Hochberg, *Silicon Photonics Design* (2015) (cit. on pp. 52, 55).

[263]M. L. Dakss, L. Kuhn, P. F. Heidrich, and B. A. Scott, "Grating coupler for efficient excitation of optical guided waves in thin films", Appl. Phys. Lett. **16**, 523–525 (1970) (cit. on p. 52).

[264]D. Vermeulen, S. Selvaraja, P. Verheyen, G. Lepage, W. Bogaerts, P. Absil, D. Van Thourhout, and G. Roelkens, "High-efficiency fiber-to-chip grating couplers realized using an advanced CMOS-compatible Silicon-On-Insulator platform", Opt. Express **18**, 18278 (2010) (cit. on p. 52).

[265]D. Taillaert, W. Bogaerts, P. Bienstman, T. Krauss, P. Van Daele, I. Moerman, S. Verstuyft, K. De Mesel, and R. Baets, "An out-of-plane grating coupler for efficient butt-coupling between compact planar waveguides and single-mode fibers", IEEE J. Quantum Electron. **38**, 949–955 (2002) (cit. on p. 52).

[266]D. Taillaert, F. Van Laere, M. Ayre, W. Bogaerts, D. Van Thourhout, P. Bienstman, and R. Baets, "Grating Couplers for Coupling between Optical Fibers and Nanophotonic Waveguides", Jpn. J. Appl. Phys. **45**, 6071–6077 (2006) (cit. on pp. 52, 111).

[267]Y. Wang, W. Shi, X. Wang, Z. Lu, M. Caverley, R. Bojko, L. Chrostowski, and N. A. F. Jaeger, "Design of broadband subwavelength grating couplers with low back reflection", Opt. Lett. **40**, 4647 (2015) (cit. on p. 52).

[268]Y. Li, D. Vermeulen, Y. De Koninck, G. Yurtsever, G. Roelkens, and R. Baets, "Compact grating couplers on silicon-on-insulator with reduced backreflection", Opt. Lett. **37**, 4356 (2012) (cit. on p. 52).

[269]Y. Li, L. Li, B. Tian, G. Roelkens, and R. G. Baets, "Reflectionless Tilted Grating Couplers With Improved Coupling Efficiency Based on a Silicon Overlay", IEEE Photonics Technol. Lett. **25**, 1195–1198 (2013) (cit. on p. 52).

[270]W. S. Zaoui, A. Kunze, W. Vogel, M. Berroth, J. Butschke, F. Letzkus, and J. Burghartz, "Bridging the gap between optical fibers and silicon photonic integrated circuits", Opt. Express **22**, 1277 (2014) (cit. on p. 52).

[271]L. Vivien, D. Pascal, S. Lardenois, D. Marris-Morini, E. Cassan, F. Grillot, S. Laval, J. M. Fédéli, and L. El Melhaoui, "Light injection in SOI microwaveguides using high-efficiency grating couplers", J. Light. Technol. **24**, 3810–3815 (2006) (cit. on p. 52).

[272]C. R. Doerr, L. Chen, Y.-K. Chen, and L. L. Buhl, "Wide Bandwidth Silicon Nitride Grating Coupler", IEEE Photonics Technol. Lett. **22**, 1461–1463 (2010) (cit. on p. 52).

[273]J. Zou, Y. Yu, M. Ye, L. Liu, S. Deng, and X. Zhang, "Ultra efficient silicon nitride grating coupler with bottom grating reflector", Opt. Express **23**, 26305 (2015) (cit. on p. 52).

[274]P. Dumon, W. Bogaerts, D. Van Thourhout, D. Taillaert, R. Baets, J. Wouters, S. Beckx, and P. Jaenen, "Compact wavelength router based on a Silicon-on-insulator arrayed waveguide grating pigtailed to a fiber array", Opt. Express **14**, 664 (2006) (cit. on p. 52).

[275]A. Mekis, S. Gloeckner, G. Masini, A. Narasimha, T. Pinguet, S. Sahni, and P. De Dobbelaere, "A Grating-Coupler-Enabled CMOS Photonics Platform", IEEE J. Sel. Top. Quantum Electron. **17**, 597–608 (2011) (cit. on p. 52).

[276]S. Janz, P. Cheben, D. Dalacu, A. Delge, A. Densmore, B. Lamontagne, M.-J. Picard, E. Post, J. H. Schmid, P. Waldron, D.-X. Xu, K. P. Yap, and W. N. Ye, "Microphotonic Elements for Integration on the Silicon-on-Insulator Waveguide Platform", IEEE J. Sel. Top. Quantum Electron. **12**, 1402–1415 (2006) (cit. on p. 52).

[277]T. Aalto, M. Cherchi, M. Harjanne, M. Kapulainen, and S. Ylinen, "Dense photonics integration on a micron-scale SOI waveguide platform", in 10th int. conf. gr. iv photonics, Vol. 2 (2013), pp. 107–108 (cit. on p. 52).

[278]T. Shoji, T. Tsuchizawa, T. Watanabe, K. Yamada, and H. Morita, "Low loss mode size converter from 0.3 um square Si wire waveguides to singlemode fibres", Electron. Lett. **38**, 1669 (2002) (cit. on p. 52).

[279]V. R. Almeida, R. R. Panepucci, and M. Lipson, "Nanotaper for compact mode conversion.", Opt. Lett. **28**, 1302–1304 (2003) (cit. on p. 52).

[280]J. Cardenas, C. Poitras, K. Luke, L.-W. Luo, P. Morton, and M. Lipson, "High Coupling Efficiency Etched Facet Tapers in Silicon Waveguides", IEEE Photonics Technol. Lett. **26**, 2380–2382 (2014) (cit. on p. 52).

[281]R. Takei, M. Suzuki, E. Omoda, S. Manako, T. Kamei, M. Mori, and Y. Sakakibara, "Silicon knife-edge taper waveguide for ultralow-loss spot-size converter fabricated by photolithography", Appl. Phys. Lett. **102** (2013) `10.1063/1.4795308` (cit. on p. 52).

[282]M. Pu, L. Liu, H. Ou, K. Yvind, and J. M. Hvam, "Ultra-low-loss inverted taper coupler for silicon-on-insulator ridge waveguide", Opt. Commun. **283**, 3678–3682 (2010) (cit. on p. 52).

[283]Z. Xiao, X. Luo, T.-Y. Liow, P. H. Lim, P. Prabhathan, J. Zhang, and F. Luan, "Design and characterization of low loss 50 picoseconds delay line on SOI platform", Opt. Express **21**, 21285 (2013) (cit. on p. 53).

[284]M. A. Guillen-Torres, M. Caverley, E. Cretu, N. A. F. Jaeger, and L. Chrostowski, "Large-area, high-Q SOI ring resonators", in 2014 ieee photonics conf. 1 (2014), pp. 336–337 (cit. on p. 53).

[285]Y. Fu, T. Ye, W. Tang, and T. Chu, "Efficient adiabatic silicon-on-insulator waveguide taper", Photonics Res. **2**, A41 (2014) (cit. on pp. 53, 116, 121).

[286]A. Melloni, F. Carniel, R. Costa, and M. Martinelli, "Determination of bend mode characteristics in dielectric waveguides", J. Light. Technol. **19**, 571–577 (2001) (cit. on p. 53).

[287]M. Heiblum and J. Harris, "Analysis of curved optical waveguides by conformal transformation", IEEE J. Quantum Electron. **11**, 75–83 (1975) (cit. on p. 53).

[288]T. Hirono, M. Kohtoku, Y. Yoshikuni, W. Lui, and K. Yokoyama, "Optimized offset to eliminate first-order mode excitation at the junction of straight and curved multimode waveguides", IEEE Photonics Technol. Lett. **10**, 982–984 (1998) (cit. on p. 53).

[289]A. Melloni, P. Monguzzi, R. Costa, and M. Martinelli, "Design of curved waveguides: the matched bend", J. Opt. Soc. Am. A **20**, 130 (2003) (cit. on pp. 53, 112).

[290]L. Chrostowski and M. Hochberg, *Silicon Photonics Design* (2015) (cit. on pp. 54, 121).

[291]Wangqing Yuan, C. S. Seibert, and D. C. Hall, "Single-Facet Teardrop Laser With Matched-Bends Design", IEEE J. Sel. Top. Quantum Electron. **17**, 1662–1669 (2011) (cit. on p. 53).

[292]W. Yuan and D. C. Hall, "A General Scaling Rule for Matched Bend Waveguides", J. Light. Technol. **29**, 3786–3796 (2011) (cit. on p. 53).

[293]B. a. Dorin and W. N. Ye, "Two-mode division multiplexing in a silicon-on-insulator ring resonator", Opt. Express **22**, 4547 (2014) (cit. on p. 54).

[294]M. Cherchi, S. Ylinen, M. Harjanne, M. Kapulainen, T. Vehmas, and T. Aalto, "Low-loss spiral waveguides with ultra-small footprint on a micron scale SOI platform", Proc. SPIE **8990**, 899005 (2014) (cit. on pp. 54, 56).

[295]C. J. Oton, O. Lemonnier, M. Fournier, and C. Kopp, "Adiabatic bends in silicon multi-mode waveguides", in 2016 ieee 13th int. conf. gr. iv photonics, Vol. 2016-Novem (2016), pp. 108–109 (cit. on p. 54).

[296]J. F. Bauters, M. L. Davenport, M. J. R. Heck, J. K. Doylend, A. Chen, A. W. Fang, and J. E. Bowers, "Silicon on ultra-low-loss waveguide photonic integration platform", Opt. Express **21**, 544 (2013) (cit. on pp. 54, 56).

[297]D. Dai, Y. Tang, and J. E. Bowers, "Mode conversion in tapered submicron silicon ridge optical waveguides", Opt. Express **20**, 13425 (2012) (cit. on p. 54).

[298]A. Yariv, "Coupled-mode theory for guided-wave optics", IEEE J. Quantum Electron. **9**, 919–933 (1973) (cit. on p. 55).

[299]W.-P. Huang, "Coupled-mode theory for optical waveguides: an overview", J. Opt. Soc. Am. A **11**, 963 (1994) (cit. on p. 55).

[300]B. Little and T. Murphy, "Design rules for maximally flat wavelength-insensitive optical power dividers using Mach-Zehnder structures", IEEE Photonics Technol. Lett. **9**, 1607–1609 (1997) (cit. on p. 55).

[301]Z. Lu, H. Yun, Y. Wang, Z. Chen, F. Zhang, N. a. F. Jaeger, and L. Chrostowski, "Broadband silicon photonic directional coupler using asymmetric-waveguide based phase control", Opt. Express **23**, 3795 (2015) (cit. on p. 55).

[302]D. Melati, F. Morichetti, G. G. Gentili, and A. Melloni, "Optical radiative crosstalk in integrated photonic waveguides", Opt. Lett. **39**, 3982 (2014) (cit. on p. 55).

[303]K. Murray, Z. Lu, H. Jayatilleka, and L. Chrostowski, "Dense dissimilar waveguide routing for highly efficient thermo-optic switches on silicon", Opt. Express **23**, 19575 (2015) (cit. on p. 56).

[304]A. Khavasi, L. Chrostowski, Z. Lu, and R. Bojko, "Significant Crosstalk Reduction Using All-Dielectric CMOS-Compatible Metamaterials", IEEE Photonics Technol. Lett. **28**, 2787–2790 (2016) (cit. on p. 56).

[305]A. W. Fang, H. Park, O. Cohen, R. Jones, M. J. Paniccia, and J. E. Bowers, "Electrically pumped hybrid AlGaInAs-silicon evanescent laser", Opt. Express **14**, 9203 (2006) (cit. on pp. 56, 182).

[306]A. Milton and W. Burns, "Mode coupling in optical waveguide horns", IEEE J. Quantum Electron. **13**, 828–835 (1977) (cit. on p. 56).

[307]R. Palmer, L. Alloatti, D. Korn, W. Heni, P. C. Schindler, J. Bolten, M. Karl, M. Waldow, T. Wahlbrink, W. Freude, C. Koos, and J. Leuthold, “Low-loss silicon strip-to-slot mode converters”, IEEE Photonics J. **5** (2013) 10.1109/JPHOT.2013.2239283 (cit. on p. 56).

[308]W. D. Sacher, Y. Huang, G.-q. Lo, and J. K. S. Poon, “Multilayer Silicon Nitride-on-Silicon Integrated Photonic Platforms and Devices”, J. Light. Technol. **33**, 901–910 (2015) (cit. on pp. 56, 58, 59, 184).

[309]M. J. R. Heck, J. F. Bauters, M. L. Davenport, D. T. Spencer, and J. E. Bowers, “Ultra-low loss waveguide platform and its integration with silicon photonics”, Laser Photonics Rev. **8**, 667–686 (2014) (cit. on p. 56).

[310]N. Matsuda, P. Karkus, H. Nishi, T. Tsuchizawa, W. J. Munro, H. Takesue, and K. Yamada, “On-chip generation and demultiplexing of quantum correlated photons using a silicon-silica monolithic photonic integration platform”, Opt. Express **22**, 22831 (2014) (cit. on p. 56).

[311]H. Nishi, T. Tsuchizawa, R. Kou, H. Shinojima, T. Yamada, H. Kimura, Y. Ishikawa, K. Wada, and K. Yamada, “Monolithic integration of a silica AWG and Ge photodiodes on Si photonic platform for one-chip WDM receiver”, Opt. Express **20**, 9312 (2012) (cit. on p. 56).

[312]H. Nishi, K. Takeda, T. Tsuchizawa, T. Fujii, S. Matsuo, K. Yamada, and T. Yamamoto, “Monolithic Integration of InP Wire and SiOx Waveguides on Si Platform”, IEEE Photonics J. **7**, 1–8 (2015) (cit. on p. 56).

[313]M. J. R. Heck, J. F. Bauters, M. L. Davenport, J. K. Doylend, S. Jain, G. Kurczveil, S. Srinivasan, Y. Tang, and J. E. Bowers, “Hybrid Silicon Photonic Integrated Circuit Technology”, IEEE J. Sel. Top. Quantum Electron. **19**, 6100117–6100117 (2013) (cit. on p. 56).

[314]G. Roelkens, L. Liu, D. Liang, R. Jones, A. Fang, B. Koch, and J. Bowers, “III-V/silicon photonics for on-chip and intra-chip optical interconnects”, Laser Photon. Rev. **4**, 751–779 (2010) (cit. on p. 56).

[315]D. Liang and J. E. Bowers, “Recent progress in lasers on silicon”, Nat. Photonics **4**, 511–517 (2010) (cit. on p. 56).

[316]T. W. Baehr-Jones and M. J. Hochberg, “Polymer Silicon Hybrid Systems: A Platform for Practical Nonlinear Optics”, J. Phys. Chem. C **112**, 8085–8090 (2008) (cit. on p. 56).

[317]J. Leuthold, C. Koos, W. Freude, L. Alloatti, R. Palmer, D. Korn, J. Pfeifle, M. Lauermann, R. Dinu, S. Wehrli, M. Jazbinsek, P. Günter, M. Waldow, T. Wahlbrink, J. Bolten, H. Kurz, M. Fournier, J. M. Fedeli, H. Yu, and W. Bogaerts, “Silicon-Organic hybrid electro-optical devices”, IEEE J. Sel. Top. Quantum Electron. **19**, 3401413–1–3401413–13 (2013) (cit. on p. 56).

[318]L. Chang, M. H. P. Pfeiffer, N. Volet, M. Zervas, J. D. Peters, C. L. Manganelli, E. J. Stanton, Y. Li, T. J. Kippenberg, and J. E. Bowers, “Heterogeneous integration of lithium niobate and silicon nitride waveguides for wafer-scale photonic integrated circuits on silicon”, Opt. Lett. **42**, 803 (2017) (cit. on p. 56).

[319]P. O. Weigel, M. Savanier, C. T. DeRose, A. T. Pomerene, A. L. Starbuck, A. L. Lentine, V. Stenger, and S. Mookherjea, “Lightwave Circuits in Lithium Niobate through Hybrid Waveguides with Silicon Photonics”, Sci. Rep. **6**, 22301 (2016) (cit. on p. 56).

[320]J. Kim, W. J. Sung, O. Eknoyan, and C. K. Madsen, “Linear photonic frequency discriminator on As2S3-ring-on-Ti:LiNbO_3 hybrid platform”, Opt. Express **21**, 24566 (2013) (cit. on p. 56).

[321]X. Xia, Y. Zhou, and C. K. Madsen, “Analysis of As2S3-Ti: LiNbO3 Taper Couplers Using Supermode Theory”, Opt. Photonics J. **2**, 344–351 (2012) (cit. on p. 56).

[322]A. Rao, A. Patil, J. Chiles, M. Malinowski, S. Novak, K. Richardson, P. Rabiei, and S. Fathpour, “Heterogeneous microring and Mach-Zehnder modulators based on lithium niobate and chalcogenide glasses on silicon”, Opt. Express **23**, 22746 (2015) (cit. on p. 56).

[323]L. Chang, Y. Li, N. Volet, L. Wang, J. Peters, and J. Bowers, "Thin film wavelength converters for photonic integrated circuits", Optica **3**, 531–535 (2016) (cit. on p. 56).

[324]S. Jin, L. Xu, H. Zhang, and Y. Li, "LiNbO 3 Thin-Film Modulators Using Silicon Nitride Surface Ridge Waveguides", IEEE Photonics Technol. Lett. **28**, 736–739 (2016) (cit. on p. 56).

[325]J. Chiles and S. Fathpour, "Mid-infrared integrated waveguide modulators based on silicon-on-lithium-niobate photonics", Optica **1**, 350–355 (2014) (cit. on p. 56).

[326]J. D. Witmer, J. T. Hill, and A. H. Safavi-Naeini, "Design of nanobeam photonic crystal resonators for a silicon-on-lithium-niobate platform", Opt. Express **24**, 5876 (2016) (cit. on p. 56).

[327]G. Kurczveil, P. Pintus, M. J. R. Heck, J. D. Peters, and J. E. Bowers, "Characterization of Insertion Loss and Back Reflection in Passive Hybrid Silicon Tapers", IEEE Photonics J. **5**, 6600410–6600410 (2013) (cit. on p. 56).

[328]M. Hochberg and T. Baehr Jones, "Towards fabless silicon photonics", Nat. Photonics **4**, 492–494 (2010) (cit. on p. 57).

[329]M. Pantouvaki, S. A. Srinivasan, Y. Ban, P. De Heyn, P. Verheyen, G. Lepage, H. Chen, J. De Coster, N. Golshani, S. Balakrishnan, P. Absil, and J. Van Campenhout, "Active Components for 50 Gb/s NRZ-OOK Optical Interconnects in a Silicon Photonics Platform", J. Light. Technol. **35**, 631–638 (2017) (cit. on pp. 57, 58, 183).

[330]P. Dumon, W. Bogaerts, R. Baets, J.-M. Fedeli, and L. Fulbert, "Towards foundry approach for silicon photonics: silicon photonics platform ePIXfab", Electron. Lett. **45**, 581 (2009) (cit. on p. 57).

[331]A. E.-J. Lim, Junfeng Song, Qing Fang, Chao Li, Xiaoguang Tu, Ning Duan, Kok Kiong Chen, R. P.-C. Tern, and Tsung-Yang Liow, "Review of Silicon Photonics Foundry Efforts", IEEE J. Sel. Top. Quantum Electron. **20**, 405–416 (2014) (cit. on pp. 58, 127).

[332]P. P. Absil, P. De Heyn, H. Chen, P. Verheyen, G. Lepage, M. Pantouvaki, J. De Coster, A. Khanna, Y. Drissi, D. Van Thourhout, and J. Van Campenhout, "Imec iSiPP25G silicon photonics: a robust CMOS-based photonics technology platform", in Spie sil phot x, Vol. 9367 (2015), p. 93670V (cit. on p. 58).

[333]D. Knoll, S. Lischke, A. Awny, and L. Zimmermann, "(Invited) SiGe BiCMOS for Optoelectronics", ECS Trans. **75**, 121–139 (2016) (cit. on p. 58).

[334]B. Goll, D. J. Thomson, L. Zimmermann, H. Porte, F. Y. Gardes, Y. Hu, D. Knoll, S. Lischke, B. Tillack, G. T. Reed, and H. Zimmermann, "A monolithically integrated silicon modulator with a 10 Gb/s 5 Vpp or 5.6 Vpp driver in 0.25 um SiGe:C BiCMOS", Front. Phys. **2**, 1–11 (2014) (cit. on p. 58).

[335]A. Novack, M. Streshinsky, R. Ding, Y. Liu, A. E.-J. Lim, G.-Q. Lo, T. Baehr-Jones, and M. Hochberg, "Progress in silicon platforms for integrated optics", Nanophotonics **3**, 205–214 (2014) (cit. on p. 58).

[336]C. Baudot, A. Fincato, D. Fowler, D. Perez-Galacho, A. Souhaité, S. Messaoudène, R. Blanc, C. Richard, J. Planchot, C. De-Buttet, B. Orlando, F. Gays, C. Mezzomo, E. Bernard, D. Marris-Morini, L. Vivien, C. Kopp, and F. Boeuf, "DAPHNE silicon photonics technological platform for research and development on WDM applications", in Spie sil phot v, Vol. 9891 (2016), p. 98911D (cit. on p. 58).

[337]M. Smit, X. Leijtens, H. Ambrosius, E. Bente, J. van der Tol, B. Smalbrugge, T. de Vries, E.-J. Geluk, J. Bolk, R. van Veldhoven, L. Augustin, P. Thijs, D. D'Agostino, H. Rabbani, K. Lawniczuk, S. Stopinski, S. Tahvili, A. Corradi, E. Kleijn, D. Dzibrou, M. Felicetti, E. Bitincka, V. Moskalenko, J. Zhao, R. Santos, G. Gilardi, W. Yao, K. Williams, P. Stabile, P. Kuindersma, J. Pello, S. Bhat, Y. Jiao, D. Heiss, G. Roelkens, M. Wale, P. Firth, F. Soares, N. Grote, M. Schell, H. Debregeas, M. Achouche, J.-L. Gentner, A. Bakker, T. Korthorst, D. Gallagher, A. Dabbs, A. Melloni, F. Morichetti, D. Melati, A. Wonfor, R. Penty, R. Broeke, B. Musk, and D. Robbins, "An introduction to InP-based generic integration technology", Semicond. Sci. Technol. **29**, 083001 (2014) (cit. on p. 58).

[338]K. A. Williams, E. A. J. M. Bente, D. Heiss, Y. Jiao, K. Ławniczuk, X. J. M. Leijtens, J. J. G. M. van der Tol, and M. K. Smit, "InP photonic circuits using generic integration [Invited]", Photonics Res. **3**, B60 (2015) (cit. on p. 58).

[339]T. Aalto, M. Cherchi, M. Harjanne, S. Ylinen, M. Kapulainen, and T. Vehmas, "Launching of multi-project wafer runs in ePIXfab with micron-scale silicon rib waveguide technology", in Proc. spie, Vol. 8990 (2014), p. 899003 (cit. on pp. 58, 126–128).

[340]M. Cherchi, S. Ylinen, M. Harjanne, M. Kapulainen, T. Vehmas, and T. Aalto, "Low-loss spiral waveguides with ultra-small footprint on a micron scale SOI platform", in Proc. spie, Vol. 8990 (2014), p. 899005 (cit. on pp. 59, 126–129).

[341]M. Liehr, D. Coolbaugh, J. E. Bowers, R. Alferness, M. Watts, L. Kimerling, and T. L. Koch, "AIM Photonics-What merging photonics with nano-electronics will do", in 2016 ieee opt. interconnects conf. Vol. 1 (2016), pp. 22–23 (cit. on p. 59).

[342]M. H. P. Pfeiffer, A. Kordts, V. Brasch, M. Zervas, M. Geiselmann, J. D. Jost, and T. J. Kippenberg, "Photonic Damascene process for integrated high-Q microresonator based nonlinear photonics", Optica **3**, 20 (2016) (cit. on p. 59).

[343]J. E. Bowers, A. Beling, D. Blumenthal, A. Bluestone, S. M. Bowers, T. C. Briles, L. Chang, S. A. Diddams, G. Fish, H. Guo, T. J. Kippenberg, T. Komljenovic, E. Norberg, S. Papp, M. H. P. Pfeiffer, K. Srinivasan, L. Theogarajan, K. J. Vahala, and N. Volet, "Chip-scale optical resonator enabled synthesizer (CORES) miniature systems for optical frequency synthesis", in 2016 ieee int. freq. control symp. (2016), pp. 1–5 (cit. on p. 59).

[344]A. B. Ruffin, M.-J. Li, X. Chen, A. Kobyakov, and F. Annunziata, "Brillouin gain analysis for fibers with different refractive indices", Opt. Lett. **30**, 3123 (2005) (cit. on p. 64).

[345]C. Wolff, M. J. Steel, B. J. Eggleton, and C. G. Poulton, "Acoustic build-up in on-chip stimulated Brillouin scattering", Sci. Rep. **5**, 13656 (2015) (cit. on pp. 65, 98).

[346]K. Y. Song, Y. H. Kim, and B. Y. Kim, "Intermodal stimulated Brillouin scattering in two-mode fibers", Opt. Lett. **38**, 1805 (2013) (cit. on p. 70).

[347]K. Y. Song and Y. H. Kim, "Characterization of stimulated Brillouin scattering in a few-mode fiber", Opt. Lett. **38**, 4841 (2013) (cit. on p. 70).

[348]Wei-Wei Ke, Xiao-Jun Wang, and Xuan Tang, "Stimulated Brillouin Scattering Model in Multi-Mode Fiber Lasers", IEEE J. Sel. Top. Quantum Electron. **20**, 305–314 (2014) (cit. on p. 70).

[349]Y. H. Kim and K. Y. Song, "Mapping of intermodal beat length distribution in an elliptical-core two-mode fiber based on Brillouin dynamic grating.", Opt. Express **22**, 17292–302 (2014) (cit. on p. 70).

[350]J. R. Koehler, R. E. Noskov, A. A. Sukhorukov, A. Butsch, D. Novoa, and P. S. J. Russell, "Resolving the mystery of milliwatt-threshold opto-mechanical self-oscillation in dual-nanoweb fiber", APL Photonics **1**, 056101 (2016) (cit. on p. 71).

[351]W. H. Renninger, P. Kharel, R. O. Behunin, and P. T. Rakich, "Bulk crystalline optomechanics", arXiv, 1703.08231 (2017) (cit. on p. 72).

[352]C. Wolff, M. J. Steel, and C. G. Poulton, "Formal selection rules for Brillouin scattering in integrated waveguides and structured fibers", Opt. Express **22**, 32489 (2014) (cit. on pp. 75, 82).

[353]F. S. Gokhan and G. Yilmaz, "Numerical solution of Brillouin and Raman fiber amplifiers using bvp6c", COMPEL Int. J. Comput. Math. Electr. Electron. Eng. **29**, 824–839 (2010) (cit. on p. 76).

[354]Y. H. Ja, "Using the shooting method to solve boundary-value problems involving nonlinear coupled-wave equations", Opt. Quantum Electron. **15**, 539–546 (1983) (cit. on p. 76).

[355]M. Pagani, E. H. W. Chan, and R. a. Minasian, "A Study of the Linearity Performance of a Stimulated Brillouin Scattering-Based Microwave Photonic Bandpass Filter", J. Light. Technol. **32**, 999–1005 (2014) (cit. on pp. 76, 77).

[356]M. van Deventer and A. Boot, "Polarization properties of stimulated Brillouin scattering in single-mode fibers", J. Light. Technol. **12**, 585–590 (1994) (cit. on p. 77).

[357]A. Zadok, E. Zilka, A. Eyal, L. Thévenaz, and M. Tur, "Vector analysis of stimulated Brillouin scattering amplification in standard single-mode fibers.", Opt. Express **16**, 21692–707 (2008) (cit. on pp. 77, 147).

[358]C. Wolff, B. Stiller, B. J. Eggleton, M. J. Steel, and C. G. Poulton, "Cascaded forward Brillouin scattering to all Stokes orders", New J. Phys. **19**, 023021 (2017) (cit. on p. 78).

[359]P. Kharel, R. O. Behunin, W. H. Renninger, and P. T. Rakich, "Noise and dynamics in forward Brillouin interactions", Phys. Rev. A **93**, 063806 (2016) (cit. on pp. 78, 79).

[360]A. Casas-Bedoya, B. Morrison, M. Pagani, D. Marpaung, and B. J. Eggleton, "Tunable narrowband microwave photonic filter created by stimulated Brillouin scattering from a silicon nanowire", Opt. Lett. **40**, 4154 (2015) (cit. on pp. 78, 110, 116, 164).

[361]A. Yeniay, J.-M. Delavaux, and J. Toulouse, "Spontaneous and stimulated Brillouin scattering gain spectra in optical fibers", J. Light. Technol. **20**, 1425–1432 (2002) (cit. on p. 79).

[362]R. W. Boyd, K. Rzaewski, and P. Narum, "Noise initiation of stimulated Brillouin scattering", Phys. Rev. A **42**, 5514–5521 (1990) (cit. on p. 79).

[363]A. L. Gaeta and R. W. Boyd, "Stochastic dynamics of stimulated Brillouin scattering in an optical fiber", Phys. Rev. A **44**, 3205–3209 (1991) (cit. on p. 79).

[364]R. B. Jenkins, R. M. Sova, and R. I. Joseph, "Steady-State Noise Analysis of Spontaneous and Stimulated Brillouin Scattering in Optical Fibers", J. Light. Technol. **25**, 763–770 (2007) (cit. on p. 79).

[365]M. F. Ferreira, J. F. Rocha, and J. L. Pinto, "Analysis of the gain and noise characteristics of fibre Brillouin amplifiers", Opt. Quantum Electron. **26**, 35–44 (1994) (cit. on p. 79).

[366]L. Stépien, S. Randoux, and J. Zemmouri, "Origin of spectral hole burning in Brillouin fiber amplifiers and generators", Phys. Rev. A **65**, 053812 (2002) (cit. on p. 79).

[367]L. Xing, L. Zhan, S. Luo, and Y. Xia, "High-Power Low-Noise Fiber Brillouin Amplifier for Tunable Slow-Light Delay Buffer", IEEE J. Quantum Electron. **44**, 1133–1138 (2008) (cit. on p. 79).

[368]L. Yi, W. Wei, M. Shi, Y. Jaouen, and W. Hu, "Design and performance evaluation of narrowband rectangular optical filter based on stimulated Brillouin scattering in fiber", Photonic Netw. Commun. **31**, 336–344 (2016) (cit. on pp. 79, 186).

[369]W. Wei, L. Yi, Y. Jaouen, M. Morvan, and W. Hu, "Brillouin Rectangular Optical Filter with Improved Selectivity and Noise Performance", IEEE Photonics Technol. Lett. **27**, 1593–1596 (2015) (cit. on pp. 79, 180).

[370]Y. Souidi, F. Taleb, J. Zheng, M. W. Lee, F. D. Burck, and V. Roncin, "Low-noise and high-gain Brillouin optical amplifier for narrowband active optical filtering based on a pump-to-signal optoelectronic tracking", Appl. Opt. **55**, 248 (2016) (cit. on p. 79).

[371]S. M. F. Raupach, A. Koczwara, and G. Grosche, "Brillouin amplification supports uncertainty in optical frequency transfer over 1400 km of underground fibe", Phys. Rev. A **92**, 021801 (2015) (cit. on pp. 79, 110).

[372]K. Predehl, G. Grosche, S. M. F. Raupach, S. Droste, O. Terra, J. Alnis, T. Legero, T. W. Hansch, T. Udem, R. Holzwarth, and H. Schnatz, "A 920-Kilometer Optical Fiber Link for Frequency Metrology at the 19th Decimal Place", Science **336**, 441–444 (2012) (cit. on pp. 79, 110).

[373]A. Lorences-Riesgo, M. Mazur, T. A. Eriksson, P. A. Andrekson, and M. Karlsson, "Self-homodyne 24x32-QAM superchannel receiver enabled by all-optical comb regeneration using brillouin amplification", Opt. Express **24**, 29714 (2016) (cit. on p. 79).

[374]R. Tkach, A. Chraplyvy, and R. Derosier, "Spontaneous Brillouin scattering for single-mode optical-fibre characterisation", Electron. Lett. **22**, 1011 (1986) (cit. on pp. 80, 92).

[375]E. Picholle, J. Botineau, and D. Bahloul, “Effective stimulated Brillouin gain in single-mode optical fibres”, Electron. Lett. **31**, 2032–2034 (1995) (cit. on p. 80).

[376]W. Zou, Z. He, and K. Hotate, “Two-Dimensional Finite-Element Modal Analysis of Brillouin Gain Spectra in Optical Fibers”, IEEE Photonics Technol. Lett. **18**, 2487–2489 (2006) (cit. on p. 80).

[377]W. Zou, Z. He, and K. Hotate, “Acoustic modal analysis and control in w-shaped triple-layer optical fibers with highly-germanium-doped core and F-doped inner cladding”, Opt. Express **16**, 10006 (2008) (cit. on p. 80).

[378]J. E. McElhenny, R. K. Pattnaik, J. Toulouse, K. Saitoh, and M. Koshiba, “Unique characteristic features of stimulated Brillouin scattering in small-core photonic crystal fibers”, J. Opt. Soc. Am. B **25**, 582 (2008) (cit. on p. 80).

[379]S. Dasgupta, F. Poletti, S. Liu, P. Petropoulos, D. J. Richardson, L. Gruner-Nielsen, and S. Herstrom, “Modeling Brillouin Gain Spectrum of Solid and Microstructured Optical Fibers Using a Finite Element Method”, J. Light. Technol. **29**, 22–30 (2011) (cit. on p. 80).

[380]X. Qian, B. Han, and Q. Wang, “NUMERICAL RESEARCH ON GAIN SPECTRUM OF STIMULATED BRILLOUIN SCATTERING IN PHOTONICS CRYSTAL FIBER”, Instrum. Sci. Technol. **41**, 175–186 (2013) (cit. on p. 80).

[381]Y. Koyamada, S. Sato, S. Nakamura, H. Sotobayashi, and W. Chujo, “Simulating and Designing Brillouin Gain Spectrum in Single-Mode Fibers”, J. Light. Technol. **22**, 631–639 (2004) (cit. on p. 80).

[382]S. Afshar V., V. P. Kalosha, X. Bao, and L. Chen, “Enhancement of stimulated Brillouin scattering of higher-order acoustic modes in single-mode optical fiber”, Opt. Lett. **30**, 2685 (2005) (cit. on p. 80).

[383]A. McCurdy, “Modeling of stimulated Brillouin scattering in optical fibers with arbitrary radial index profile”, J. Light. Technol. **23**, 3509–3516 (2005) (cit. on p. 80).

[384]Liang Dong, “Formulation of a Complex Mode Solver for Arbitrary Circular Acoustic Waveguides”, J. Light. Technol. **28**, 3162–3175 (2010) (cit. on p. 80).

[385]L. Dong, “Limits of stimulated brillouin scattering suppression in optical fibers with transverse acoustic waveguide designs”, J. Light. Technol. **28**, 3156–3161 (2010) (cit. on p. 80).

[386]T. J. Kippenberg and K. J. Vahala, “Cavity Optomechanics: Back-Action at the Mesoscale”, Science **321**, 1172–1176 (2008) (cit. on p. 81).

[387]P. T. Rakich, Z. Wang, and P. Davids, “Scaling of optical forces in dielectric waveguides: rigorous connection between radiation pressure and dispersion”, Opt. Lett. **36**, 217 (2011) (cit. on p. 81).

[388]C. Wolff, M. J. Steel, B. J. Eggleton, and C. G. Poulton, “Stimulated Brillouin scattering in integrated photonic waveguides: Forces, scattering mechanisms, and coupled-mode analysis”, Phys. Rev. A **92**, 013836 (2015) (cit. on pp. 82, 83).

[389]O. Florez, P. F. Jarschel, Y. A. V. Espinel, C. M. B. Cordeiro, T. P. Mayer Alegre, G. S. Wiederhecker, and P. Dainese, “Brillouin scattering self-cancellation”, Nat. Commun. **7**, 11759 (2016) (cit. on pp. 82, 83, 185).

[390]J.-C. Beugnot and V. Laude, “Electrostriction and guidance of acoustic phonons in optical fibers”, Phys. Rev. B **86**, 224304 (2012) (cit. on p. 83).

[391]V. Laude and J. C. Beugnot, “Generation of phonons from electrostriction in small-core optical waveguides”, AIP Adv. **3** (2013) `10.1063/1.4801936` (cit. on p. 83).

[392]Y. Pennec, V. Laude, N. Papanikolaou, B. Djafari-Rouhani, M. Oudich, S. El Jallal, J. C. Beugnot, J. M. Escalante, and A. Martínez, “Modeling light-sound interaction in nanoscale cavities and waveguides”, Nanophotonics **3**, 1–29 (2014) (cit. on p. 83).

[393]B. Stiller, M. Delqué, J.-C. Beugnot, M. W. Lee, G. Mélin, H. Maillotte, V. Laude, and T. Sylvestre, “Frequency-selective excitation of guided acoustic modes in a photonic crystal fiber.”, Opt. Express **19**, 7689–94 (2011) (cit. on p. 83).

[394]J.-C. Beugnot, S. Lebrun, G. Pauliat, H. Maillotte, V. Laude, and T. Sylvestre, "Brillouin light scattering from surface acoustic waves in a subwavelength-diameter optical fibre.", Nat. Commun. **5**, 5242 (2014) (cit. on p. 83).

[395]P. Szriftgiser, A. Kudlinski, D. Bacquet, G. Bouwmans, M. Dossou, J.-C. Beugnot, and V. Laude, "Enhanced structural sensitivity of hybrid-mode acoustic phonons in axially-varying photonic crystal fiber", Opt. Express **23**, 23329 (2015) (cit. on p. 83).

[396]C. J. Sarabalis, J. T. Hill, and A. H. Safavi-Naeini, "Guided acoustic and optical waves in silicon-on-insulator for Brillouin scattering and optomechanics", APL Photonics **1**, 071301 (2016) (cit. on p. 83).

[397]R. G. Decorby, N. Ponnampalam, M. M. Pai, H. T. Nguyen, P. K. Dwivedi, T. J. Clement, C. J. Haugen, J. N. McMullin, and S. O. Kasap, "High index contrast waveguides in chalcogenide glass and polymer", IEEE J. Sel. Top. Quantum Electron. **11**, 539–546 (2005) (cit. on p. 87).

[398]X. Gai, T. Han, A. Prasad, S. Madden, D.-Y. Choi, R. Wang, D. Bulla, and B. Luther-Davies, "Progress in optical waveguides fabricated from chalcogenide glasses", Opt. Express **18**, 26635 (2010) (cit. on pp. 87, 102).

[399]D. Hewak, D. Brady, R. Curry, G. Elliott, C. Huang, M. Hughes, K. Knight, A. Mairaj, M. Petrovich, R. Simpson, and C. Sproat, "Chalcogenide glasses for photonics device applications", in *Photonic glas. glas.* (2010), pp. 29–102 (cit. on p. 87).

[400]B. J. Eggleton, B. Luther-Davies, and K. Richardson, "Chalcogenide photonics", Nat Phot. **5**, 141–148 (2011) (cit. on pp. 87, 157).

[401]A. R. Hilton, "Nonoxide Chalcogenide Glasses as Infrared Optical Materials", Appl. Opt. **5**, 1877 (1966) (cit. on p. 87).

[402]M.-L. Anne, J. Keirsse, V. Nazabal, K. Hyodo, S. Inoue, C. Boussard-Pledel, H. Lhermite, J. Charrier, K. Yanakata, O. Loreal, J. Le Person, F. Colas, C. Compère, and B. Bureau, "Chalcogenide Glass Optical Waveguides for Infrared Biosensing", Sensors **9**, 7398–7411 (2009) (cit. on p. 87).

[403]N. Mehta, "Applications of chalcogenide glasses in electronics and optoelectronics: A review", J. Sci. Ind. Res. (India). **65**, 777–786 (2006) (cit. on p. 87).

[404]S. J. Madden and K. T. Vu, "High-Performance Integrated Optics with Tellurite Glasses: Status and Prospects", Int. J. Appl. Glas. Sci. **3**, 289–298 (2012) (cit. on pp. 87, 103, 181).

[405]G. E. Snopatin, V. S. Shiryaev, V. G. Plotnichenko, E. M. Dianov, and M. F. Churbanov, "High-purity chalcogenide glasses for fiber optics", Inorg. Mater. **45**, 1439–1460 (2009) (cit. on pp. 87, 181).

[406]M. Asobe, "Nonlinear Optical Properties of Chalcogenide Glass Fibers and Their Application to All-Optical Switching", Opt. Fiber Technol. **3**, 142–148 (1997) (cit. on p. 87).

[407]A. B. Seddon and M. J. Laine, "A Review of Amorphous Chalcogenides as Materials For Infrared Bulk Acousto-Optic Devices", Phys. Appl. Non-Crystalline Semicond. Optoelectron., 327–336 (1997) (cit. on pp. 87, 181).

[408]A. Warner and D. Pinnow, "Miniature acoustooptic modulators for optical communications", IEEE J. Quantum Electron. **9**, 1155–1157 (1973) (cit. on pp. 87, 102).

[409]T. Yano, A. Fukumoto, and A. Watanabe, "Tellurite glass: A new acousto-optic material", J. Appl. Phys. **42**, 3674–3676 (1971) (cit. on pp. 87, 103, 181).

[410]J. T. Krause, C. R. Kurkjian, D. A. Pinnow, and E. A. Sigety, "Low acoustic loss chalcogenide glasses - A new category of materials for acoustic and acousto-optic applications", Appl. Phys. Lett. **17**, 367–368 (1970) (cit. on pp. 87, 102).

[411]K. Ogusu, H. Li, and M. Kitao, "Brillouin-gain coefficients of chalcogenide glasses", J. Opt. Soc. Am. B **21**, 1302 (2004) (cit. on p. 87).

[412]D. Pinnow, "Guide lines for the selection of acoustooptic materials", IEEE J. Quantum Electron. **6**, 223–238 (1970) (cit. on pp. 87, 181).

[413]N. Uchida and N. Niizeki, "Acoustooptic deflection materials and techniques", Proc. IEEE **61**, 1073–1092 (1973) (cit. on pp. 87, 181).

[414]M. Gottlieb, "Acousto-optic properties of some chalcogenide crystals", J. Appl. Phys. **45**, 5145 (1974) (cit. on pp. 87, 181).

[415]K. S. Abedin, "Observation of strong stimulated Brillouin scattering in single-mode As2Se3 chalcogenide fiber", Opt. Express **13**, 10266 (2005) (cit. on pp. 87, 88).

[416]R. E. Slusher, G. Lenz, J. Hodelin, J. Sanghera, L. B. Shaw, and I. D. Aggarwal, "Large Raman gain and nonlinear phase shifts in high-purity As_2Se_3 chalcogenide fibers", J. Opt. Soc. Am. B **21**, 1146 (2004) (cit. on p. 87).

[417]K. S. Abedin, "Brillouin amplification and lasing in a single-mode As2Se3 chalcogenide fiber", Opt. Lett. **31**, 1615 (2006) (cit. on p. 88).

[418]K. Y. Song, K. S. Abedin, K. Hotate, M. González Herráez, and L. Thévenaz, "Highly efficient Brillouin slow and fast light using As 2 Se 3 chalcogenide fiber", Opt. Express **14**, 5860 (2006) (cit. on p. 88).

[419]L. Thévenaz, "Slow and fast light in optical fibres", Nat. Photonics **2**, 474–481 (2008) (cit. on pp. 88, 110, 164).

[420]K. S. Abedin, "Stimulated Brillouin scattering in single-mode tellurite glass fiber.", Opt. Express **14**, 11766–11772 (2006) (cit. on p. 88).

[421]C. Fortier, J. Fatome, S. Pitois, F. Smektala, G. Millot, J. Troles, F. Desevedavy, P. Houizot, L. Brilland, and N. Traynor, "Experimental investigation of Brillouin and Raman scattering in a 2SG sulfide glass microstructured chalcogenide fiber.", Opt. Express **16**, 9398–9404 (2008) (cit. on pp. 88, 181).

[422]J. Fatome, C. Fortier, T. N. Nguyen, T. Chartier, F. Smektala, K. Messaad, B. Kibler, S. Pitois, G. Gadret, C. Finot, J. Troles, F. Desevedavy, P. Houizot, G. Renversez, L. Brilland, and N. Traynor, "Linear and Nonlinear Characterizations of Chalcogenide Photonic Crystal Fibers", J. Light. Technol. **27**, 1707–1715 (2009) (cit. on p. 88).

[423]J. S. Sanghera, L. B. Shaw, P. Pureza, V. Q. Nguyen, D. Gibson, L. Busse, I. D. Aggarwal, C. M. Florea, and F. H. Kung, "Nonlinear Properties of Chalcogenide Glass Fibers", Int. J. Appl. Glas. Sci. **1**, 296–308 (2010) (cit. on p. 88).

[424]K. H. Tow, Y. Léguillon, S. Fresnel, P. Besnard, L. Brilland, D. Méchin, D. Trégoat, J. Troles, and P. Toupin., "Linewidth-narrowing and intensity noise reduction of the 2nd order Stokes component of a low threshold Brillouin laser made of Ge_10As_22Se_68 chalcogenide fiber", Opt. Express **20**, B104 (2012) (cit. on p. 88).

[425]K. H. Tow, Y. Léguillon, P. Besnard, L. Brilland, J. Trolès, P. Toupin, D. Méchin, D. Trégoat, and M. Doisy, "Brillouin fiber laser using As38Se62 suspended-core chalcogenide fiber", in Proc. spie 8426, Vol. 8426 (2012), p. 842611 (cit. on pp. 88, 109).

[426]K. H. Tow, Y. Léguillon, P. Besnard, L. Brilland, J. Troles, P. Toupin, D. Méchin, D. Trégoat, and S. Molin, "Relative intensity noise and frequency noise of a compact Brillouin laser made of As_38Se_62 suspended-core chalcogenide fiber", Opt. Lett. **37**, 1157 (2012) (cit. on p. 88).

[427]P. Toupin, L. Brilland, J. Trolès, and J.-L. Adam, "Small core Ge-As-Se microstructured optical fiber with single-mode propagation and low optical losses", Opt. Mater. Express **2**, 1359 (2012) (cit. on p. 88).

[428]K. Ogusu, "Analysis of steady-state cascaded stimulated Brillouin scattering in a fiber Fabry-Perot resonator", IEEE Photonics Technol. Lett. **14**, 947–949 (2002) (cit. on p. 88).

[429]G. Qin, H. Sotobayashi, M. Tsuchiya, A. Mori, T. Suzuki, and Y. Ohishi, "Stimulated Brillouin Scattering in a Single-Mode Tellurite Fiber for Amplification, Lasing, and Slow Light Generation", J. Light. Technol. **26**, 492–498 (2008) (cit. on p. 88).

[430]B. Eggleton, T. Vo, R. Pant, J. Schr, M. Pelusi, D. Yong Choi, S. Madden, and B. Luther-Davies, "Photonic chip based ultrafast optical processing based on high nonlinearity dispersion engineered chalcogenide waveguides", Laser Photon. Rev. **6**, 97–114 (2012) (cit. on pp. 88, 127).

431 C. B. Dane, W. a. Neuman, and L. a. Hackel, "Pulse-shape dependence of stimulated-Brillouin-scattering phase-conjugation fidelity for high input energies", Opt. Lett. **17**, 1271 (1992) (cit. on p. 89).

432 C. G. Poulton, R. Pant, and B. J. Eggleton, "Acoustic confinement and Stimulated Brillouin Scattering in integrated optical waveguides", J. Opt. Soc. Am. B **30**, 2657 (2013) (cit. on pp. 89–91, 99, 101, 123, 133, 134, 181, 183).

433 J. Hu and C. R. Menyuk, "Understanding leaky modes: slab waveguide revisited", Adv. Opt. Photonics **1**, 58 (2009) (cit. on p. 89).

434 B. J. Soller, D. K. Gifford, M. S. Wolfe, and M. E. Froggatt, "High resolution optical frequency domain reflectometry for characterization of components and assemblies", Opt. Express **13**, 666 (2005) (cit. on pp. 92, 166).

435 S. Dwivedi, A. Ruocco, M. Vanslembrouck, T. Spuesens, P. Bienstman, P. Dumon, T. Van Vaerenbergh, and W. Bogaerts, "Experimental Extraction of Effective Refractive Index and Thermo-Optic Coefficients of Silicon-on-Insulator Waveguides Using Interferometers", J. Light. Technol. **33**, 4471–4477 (2015) (cit. on p. 92).

436 D. Melati, A. Alippi, and A. Melloni, "Waveguide-based technique for wafer-level measurement of phase and group effective refractive indices", J. Light. Technol. **34**, 1–1 (2015) (cit. on p. 92).

437 A. Ruffin, "Stimulated brillouin scattering: an overview of measurements, system impairments, and applications", in Tech. dig. symp. opt. fiber meas. 2004. 3 (2004), pp. 23–28 (cit. on p. 93).

438 M. Nikles, L. Thevenaz, and P. Robert, "Brillouin gain spectrum characterization in single-mode optical fibers", J. Light. Technol. **15**, 1842–1851 (1997) (cit. on p. 94).

439 A. Loayssa, R. Hernández, D. Benito, and S. Galech, "Characterization of stimulated Brillouin scattering spectra by use of optical single-sideband modulation.", Opt. Lett. **29**, 638–640 (2004) (cit. on pp. 94, 114).

440 M. Izutsu, S. Shikama, and T. Sueta, "Integrated optical SSB modulator/frequency shifter", IEEE J. Quantum Electron. **17**, 2225–2227 (1981) (cit. on p. 94).

441 Y. Mizuno and K. Nakamura, "Enhancement of Brillouin Scattering Signal in Optical Fibers by Use of Pulsed Pump Light", Appl. Phys. Express **5**, 032501 (2012) (cit. on p. 95).

442 Y. Mizuno, M. Kishi, K. Hotate, T. Ishigure, and K. Nakamura, "Observation of stimulated Brillouin scattering in polymer optical fiber with pump–probe technique", Opt. Lett. **36**, 2378 (2011) (cit. on p. 96).

443 D. Y. Choi, A. Wade, S. Madden, R. Wang, D. Bulla, and B. Luther-Davies, "Photo-induced and thermal annealing of chalcogenide films for waveguide fabrication", Phys. Procedia **48**, 196–205 (2013) (cit. on pp. 97, 112).

444 S. J. Madden, D.-Y. Choi, D. A. Bulla, A. V. Rode, B. Luther-Davies, V. G. Ta'eed, M. D. Pelusi, and B. J. Eggleton, "Long, low loss etched As2S3 chalcogenide waveguides for all-optical signal regeneration", Opt. Express **15**, 14414 (2007) (cit. on p. 97).

445 D.-Y. Choi, S. Maden, A. Rode, R. Wang, and B. Luther-Davies, "Plasma etching of As2S3 films for optical waveguides", J. Non. Cryst. Solids **354**, 3179–3183 (2008) (cit. on p. 97).

446 R. Van Laer, B. Kuyken, D. Van Thourhout, and R. Baets, "Interaction between light and highly confined hypersound in a silicon photonic nanowire: Supplementary Information", Nat. Photonics **9**, 199–203 (2015) (cit. on p. 98).

447 D. Marpaung, B. Morrison, M. Pagani, R. Pant, D.-Y. Choi, B. Luther-Davies, S. J. Madden, and B. J. Eggleton, "Low-power, chip-based stimulated Brillouin scattering microwave photonic filter with ultrahigh selectivity", Optica **2**, 76 (2015) (cit. on pp. 98, 153, 165, 167).

[448]G. Pillet, L. Morvan, M. Brunel, F. Bretenaker, D. Dolfi, M. Vallet, J.-P. Huignard, and A. Le Floch, "Dual-Frequency Laser at 1.5 um for Optical Distribution and Generation of High-Purity Microwave Signals", J. Light. Technol. **26**, 2764–2773 (2008) (cit. on p. 99).

[449]J. Maxin, G. Pillet, B. Steinhausser, L. Morvan, O. Llopis, and D. Dolfi, "Widely Tunable Opto-Electronic Oscillator Based on a Dual-Frequency Laser", J. Light. Technol. **31**, 2919–2925 (2013) (cit. on p. 99).

[450]M. Merklein, B. Stiller, K. Vu, S. J. Madden, and B. J. Eggleton, "A chip-integrated coherent photonic-phononic memory", Nat. Commun. **8**, 574 (2017) (cit. on pp. 100, 178).

[451]A. Choudhary, Y. Liu, B. Morrison, K. Vu, D.-Y. Choi, P. Ma, S. Madden, D. Marpaung, and B. J. Eggleton, "High-resolution, on-chip RF photonic signal processor using Brillouin gain shaping and RF interference", Sci. Rep. **7**, 5932 (2017) (cit. on pp. 101, 178).

[452]A. Prasad, C.-j. Zha, R.-p. Wang, A. Smith, S. Madden, and B. Luther-Davies, "Properties of Ge_x As_y Se_1-x-y glasses for all-optical signal processing", Opt. Express **16**, 2804 (2008) (cit. on p. 102).

[453]X. Gai, S. Madden, D.-Y. Choi, D. Bulla, and B. Luther-Davies, "Dispersion engineered Ge11.5 As24 Se64.5 nanowires with a nonlinear parameter of 136W^-1m^-1 at 1550nm", Opt. Express **18**, 18866 (2010) (cit. on p. 102).

[454]X. Su, R. Wang, B. Luther-Davies, and L. Wang, "The dependence of photosensitivity on composition for thin films of Ge x As y Se1–x–y chalcogenide glasses", Appl. Phys. A **113**, 575–581 (2013) (cit. on p. 102).

[455]D. A. P. Bulla, R. P. Wang, A. Prasad, A. V. Rode, S. J. Madden, and B. Luther-Davies, "On the properties and stability of thermally evaporated Ge–As–Se thin films", Appl. Phys. A **96**, 615–625 (2009) (cit. on p. 102).

[456]S. J. Madden and K. T. Vu, "Very low loss reactively ion etched Tellurium Dioxide planar rib waveguides for linear and non-linear optics.", Opt. Express **17**, 17645–17651 (2009) (cit. on p. 103).

[457]S. M. Pietralunga, M. Lanata, M. Ferè, D. Piccinin, G. Cusmai, M. Torregiani, and M. Martinelli, "High-contrast waveguides in sputtered pure TeO2 glass thin films.", Opt. Express **16**, 21662–70 (2008) (cit. on p. 103).

[458]K. T. Vu and S. J. Madden, "Reactive ion etching of tellurite and chalcogenide waveguides using hydrogen, methane, and argon", J. Vac. Sci. Technol. A Vacuum, Surfaces, Film. **29**, 011023 (2011) (cit. on pp. 103, 181).

[459]K. Vu and S. Madden, "Tellurium dioxide Erbium doped planar rib waveguide amplifiers with net gain and 2.8 dB/cm internal gain.", Opt. Express **18**, 19192–19200 (2010) (cit. on p. 103).

[460]A. Yariv, "Universal relations for coupling of optical power between microresonators and dielectric waveguides", Electron. Lett. **36**, 321 (2000) (cit. on p. 106).

[461]a. Yariv, "Critical coupling and its control in optical waveguide-ring resonator systems", IEEE Photonics Technol. Lett. **14**, 483–485 (2002) (cit. on pp. 106, 108, 169).

[462]W. Bogaerts, P. De Heyn, T. Van Vaerenbergh, K. De Vos, S. Kumar Selvaraja, T. Claes, P. Dumon, P. Bienstman, D. Van Thourhout, and R. Baets, "Silicon microring resonators", Laser Photonics Rev. **6**, 47–73 (2012) (cit. on pp. 106, 169–171).

[463]P. P. Absil, J. V. Hryniewicz, B. E. Little, P. S. Cho, R. a. Wilson, L. G. Joneckis, and P. T. Ho, "Wavelength conversion in GaAs micro-ring resonators.", Opt. Lett. **25**, 554–556 (2000) (cit. on p. 108).

[464]M. J. Strain, C. Lacava, L. Meriggi, I. Cristiani, and M. Sorel, "Tunable Q-factor silicon microring resonators for ultra-low power parametric processes.", Opt. Lett. **40**, 1274–7 (2015) (cit. on p. 108).

[465]A. Debut, S. Randoux, and J. Zemmouri, "Experimental and theoretical study of linewidth narrowing in Brillouin fiber ring lasers", J. Opt. Soc. Am. B **18**, 556–567 (2001) (cit. on pp. 109, 181, 185).

[466]I. S. Grudinin, H. Lee, O. Painter, and K. J. Vahala, "Phonon Laser Action in a Tunable Two-Level System", Phys. Rev. Lett. **104**, 083901 (2010) (cit. on p. 109).

[467]A. Debut, S. Randoux, and J. Zemmouri, "Linewidth narrowing in Brillouin lasers: Theoretical analysis", Phys. Rev. A **62**, 1–4 (2000) (cit. on pp. 109, 110, 122).

[468]S. Molin, G. Baili, M. Alouini, D. Dolfi, and J.-P. Huignard, "Experimental investigation of relative intensity noise in Brillouin fiber ring lasers for microwave photonics applications.", Opt. Lett. **33**, 1681–1683 (2008) (cit. on p. 109).

[469]J. Zhou, Y. Jaouen, L. Yi, and P. Gallion, "Pump to Stokes Waves Intensity Noise Transfer in Cascaded Brillouin Fiber Lasers", IEEE Photonics Technol. Lett. **20**, 912–914 (2008) (cit. on p. 109).

[470]M. Digonnet and H. Shaw, "Analysis of a Tunable Single Mode Optical Fiber Coupler", IEEE Trans. Microw. Theory Tech. **30**, 592–600 (1982) (cit. on p. 109).

[471]V. Lecoeuche, S. Randoux, B. Ségard, and J. Zemmouri, "Dynamics of stimulated Brillouin scattering with feedback", Quantum Semiclassical Opt. J. Eur. Opt. Soc. Part B **8**, 1109–1145 (1996) (cit. on p. 109).

[472]S. Randoux, V. Lecoeuche, B. Segard, and J. Zemmouri, "Dynamical analysis of Brillouin fiber lasers: An experimental approach", Phys. Rev. A **51**, R4345–R4348 (1995) (cit. on p. 109).

[473]S. Norcia, S. Tonda-Goldstein, D. Dolfi, J. P. Huignard, and R. Frey, "Efficient single-mode Brillouin fiber laser for low-noise optical carrier reduction of microwave signals.", Opt. Lett. **28**, 1888–1890 (2003) (cit. on p. 109).

[474]G. Wang, L. Zhan, J. Liu, T. Zhang, J. Li, L. Zhang, J. Peng, and L. Yi, "Watt-level ultrahigh-optical signal-to-noise ratio single-longitudinal-mode tunable Brillouin fiber laser", Opt. Lett. **38**, 19 (2013) (cit. on p. 109).

[475]G. J. Cowle and D. Y. Stepanov, "Hybrid Brillouin/erbium fiber laser", Opt. Lett. **21**, 1250 (1996) (cit. on p. 109).

[476]T. Kippenberg, S. Spillane, B. Min, and K. Vahala, "Theoretical and Experimental Study of Stimulated and Cascaded Raman Scattering in Ultrahigh-Q Optical Microcavities", IEEE J. Sel. Top. Quantum Electron. **10**, 1219–1228 (2004) (cit. on pp. 109, 116, 118).

[477]S. R. Mirnaziry, C. Wolff, M. J. Steel, B. J. Eggleton, and C. G. Poulton, "Stimulated Brillouin scattering in integrated ring resonators", J. Opt. Soc. Am. B **34**, 937 (2017) (cit. on p. 109).

[478]S. R. Mirnaziry, C. Wolff, M. J. Steel, B. Morrison, B. J. Eggleton, and C. G. Poulton, "Lasing in ring resonators by stimulated Brillouin scattering in the presence of nonlinear loss", Opt. Express **25**, 23619 (2017) (cit. on p. 109).

[479]B. Morrison, A. Casas-Bedoya, G. Ren, K. Vu, Y. Liu, A. Zarifi, T. G. Nguyen, D.-Y. Choi, D. Marpaung, S. J. Madden, A. Mitchell, and B. J. Eggleton, "Compact Brillouin devices through hybrid integration on silicon", Optica **4**, 847 (2017) (cit. on pp. 110, 185).

[480]G. Agrawal, "Stimulated Raman Scattering", in *Nonlinear fiber opt.* (2013), pp. 295–352 (cit. on p. 110).

[481]Z. Zhu, D. J. Gauthier, and R. W. Boyd, "Stored Light in an Optical Fiber via Stimulated Brillouin Scattering", Science **318**, 1748–1750 (2007) (cit. on p. 110).

[482]B. Vidal, M. A. Piqueras, and J. Martí, "Tunable and reconfigurable photonic microwave filter based on stimulated Brillouin scattering", Opt. Lett. **32**, 23 (2007) (cit. on pp. 110, 145).

[483]D. Marpaung, B. Morrison, R. Pant, and B. J. Eggleton, "Frequency agile microwave photonic notch filter with anomalously high stopband rejection", Opt. Lett. **38**, 4300 (2013) (cit. on pp. 110, 150, 165, 171, 172).

[484] W. Zhang and R. Minasian, "Ultrawide Tunable Microwave Photonic Notch Filter Based on Stimulated Brillouin Scattering", IEEE Photonics Technol. Lett. **24**, 1182–1184 (2012) (cit. on pp. 110, 145, 159, 160).

[485] K. Y. Song, W. Zou, Z. He, and K. Hotate, "All-optical dynamic grating generation based on Brillouin scattering in polarization-maintaining fiber.", Opt. Lett. **33**, 926–928 (2008) (cit. on p. 110).

[486] M. Santagiustina, S. Chin, N. Primerov, L. Ursini, and L. Thévenaz, "All-optical signal processing using dynamic Brillouin gratings.", Sci. Rep. **3**, 1594 (2013) (cit. on p. 110).

[487] J. Domingo, J. Pelayo, F. Villuendas, C. Heras, and E. Pellejer, "Very high resolution optical spectrometry by stimulated Brillouin scattering", IEEE Photonics Technol. Lett. **17**, 855–857 (2005) (cit. on pp. 110, 185).

[488] X. S. Yao, "High-quality microwave signal generation by use of Brillouin scattering in optical fibers", Opt. Lett. **22**, 1329 (1997) (cit. on p. 110).

[489] S. P. Smith, F. Zarinetchi, and S. Ezekiel, "Narrow-linewidth stimulated Brillouin fiber laser and applications", Opt. Lett. **16**, 393 (1991) (cit. on pp. 110, 164).

[490] J. Geng, S. Staines, Z. Wang, J. Zong, M. Blake, and S. Jiang, "Highly stable low-noise brillouin fiber laser with ultranarrow spectral linewidth", IEEE Photonics Technol. Lett. **18**, 1813–1815 (2006) (cit. on p. 110).

[491] M. C. Gross, P. T. Callahan, T. R. Clark, D. Novak, R. B. Waterhouse, and M. L. Dennis, "Tunable millimeter-wave frequency synthesis up to 100 GHz by dual-wavelength Brillouin fiber laser.", Opt. Express **18**, 13321–30 (2010) (cit. on p. 110).

[492] D. Marpaung, C. Roeloffzen, R. Heideman, A. Leinse, S. Sales, and J. Capmany, "Integrated microwave photonics", Laser Photon. Rev. **7**, 506–538 (2013) (cit. on pp. 110, 127, 131, 133, 137, 144, 145, 171).

[493] H. Shin, W. Qiu, R. Jarecki, J. a. Cox, R. H. Olsson, A. Starbuck, Z. Wang, and P. T. Rakich, "Tailorable stimulated Brillouin scattering in nanoscale silicon waveguides: Supplementary", Nat. Commun. **4**, 1944 (2013) (cit. on pp. 110, 121, 122).

[494] M. Merklein, B. Stiller, I. V. Kabakova, U. S. Mutugala, K. Vu, S. J. Madden, B. J. Eggleton, and R. Slavík, "Widely tunable, low phase noise microwave source based on a photonic chip", Opt. Lett. **41**, 4633 (2016) (cit. on p. 111).

[495] Y. Liu, D. Marpaung, A. Choudhary, and B. J. Eggleton, "Lossless and high-resolution RF photonic notch filter", Opt. Lett. **41**, 5306 (2016) (cit. on pp. 111, 158).

[496] E. Kittlaus, N. T. Otterstrom, and P. T. Rakich, "Inter-modal Brillouin Scattering in an Integrated Waveguide", in Conf. lasers electro-optics (2017), STu3N.3 (cit. on pp. 114, 122).

[497] R. Claps, V. Raghunathan, D. Dimitropoulos, and B. Jalali, "Influence of nonlinear absorption on Raman amplification in Silicon waveguides", Opt. Express **12**, 2774 (2004) (cit. on p. 114).

[498] Y. Zhou, X. Xia, W. T. Snider, J. Kim, Q. Chen, W. C. Tan, and C. K. Madsen, "Two-Stage Taper Enhanced Ultra-High Q As2S3 Ring Resonator on LiNbO3", IEEE Photonics Technol. Lett. **23**, 1195–1197 (2011) (cit. on p. 117).

[499] S. Levy, M. Klebanov, and A. Zadok, "High-Q ring resonators directly written in As2S3 chalcogenide glass films", Photonics Res. **3**, 63 (2015) (cit. on p. 117).

[500] T. Kawanishi and M. Izutsu, "Linear Single-Sideband Modulation for High-SNR Wavelength Conversion", IEEE Photonics Technol. Lett. **16**, 1534–1536 (2004) (cit. on p. 119).

[501] G. Smith, D. Novak, and Z. Ahmed, "Technique for optical SSB generation to overcome dispersion penalties in fibre-radio systems", Electron. Lett. **33**, 74 (1997) (cit. on p. 119).

[502] J.-C. Beugnot, R. Ahmad, M. Rochette, V. Laude, H. Maillotte, and T. Sylvestre, "Reduction and control of stimulated Brillouin scattering in polymer-coated chalcogenide optical microwires", Opt. Lett. **39**, 482 (2014) (cit. on pp. 123, 181).

[503] R. Soref, "Silicon-based optoelectronics", Proc. IEEE **81**, 1687–1706 (1993) (cit. on p. 125).

[504]G. T. Reed, W. R. Headley, and C. E. J. Png, "Silicon photonics: the early years", in Proc. spie, Vol. 5730 (2005), p. 1 (cit. on p. 125).

[505]R. Soref, "The Past, Present, and Future of Silicon Photonics", IEEE J. Sel. Top. Quantum Electron. **12**, 1678–1687 (2006) (cit. on p. 125).

[506]B. Jalali and S. Fathpour, "Silicon Photonics", J. Light. Technol. **24**, 4600–4615 (2006) (cit. on pp. 125, 127).

[507]S. A. Miller, M. Yu, X. Ji, A. G. Griffith, J. Cardenas, A. L. Gaeta, and M. Lipson, "Low-loss silicon platform for broadband mid-infrared photonics", Optica **4**, 707 (2017) (cit. on p. 125).

[508]I. Day, I. Evans, A. Knights, F. Hopper, S. Roberts, J. Johnston, S. Day, J. Luff, H. Tsang, and M. Asghari, "Tapered silicon waveguides for low insertion loss highly-efficient high-speed electronic variable optical attenuators", in Ofc 2003 opt. fiber commun. conf. 2003. (2003), 249–251 vol.1 (cit. on p. 125).

[509]A. Martin, J. Luff, D. Feng, and M. Asghari, "Technical Challenges for 100Gb/s Silicon Photonics Transceivers for Data Center Applications", Opt. Fiber Commun. Conf. 2016 **1**, 1–3 (2016) (cit. on pp. 125, 126).

[510]A. Rickman, "The commercialization of silicon photonics", Nat. Photonics **8**, 579–582 (2014) (cit. on p. 125).

[511]D. Feng, W. Qian, H. Liang, C.-C. Kung, Z. Zhou, Z. Li, J. S. Levy, R. Shafiiha, J. Fong, B. Jonathan Luff, and M. Asghari, "High-Speed GeSi Electroabsorption Modulator on the SOI Waveguide Platform", IEEE J. Sel. Top. Quantum Electron. **19**, 64–73 (2013) (cit. on p. 126).

[512]Dazeng Feng, Wei Qian, Hong Liang, B. J. Luff, and M. Asghari, "High-Speed Receiver Technology on the SOI Platform", IEEE J. Sel. Top. Quantum Electron. **19**, 3800108–3800108 (2013) (cit. on p. 126).

[513]D. Feng, J. Luff, S. Jatar, and M. Asghari, "Micron-scale Silicon Photonic Devices and Circuits", in Opt. fiber commun. conf. Vol. 3, 4-5 (2014), Th4C.1 (cit. on p. 126).

[514]G. Przyrembel, "Design and fabrication of arrayed waveguide grating multiplexers on silicon-on-insulator platforms", Opt. Eng. **46**, 094602 (2007) (cit. on p. 126).

[515]K. Solehmainen, "Fabrication of microphotonic waveguide components on silicon", PhD thesis (2007) (cit. on p. 126).

[516]T. Aalto, M. Harjanne, B.-J. Offrein, C. Caër, C. Neumeyr, A. Malacarne, M. Guina, R. N. Sheehan, F. H. Peters, and P. Melanen, "Integrating III-V, Si, and polymer waveguides for optical interconnects: RAPIDO", in Opt. interconnects xvi, Vol. 9753 (2016), p. 97530D (cit. on p. 126).

[517]M. Pagani, B. Morrison, Y. Zhang, A. Casas-Bedoya, T. Aalto, M. Harjanne, M. Kapulainen, B. J. Eggleton, and D. Marpaung, "Low-error and broadband microwave frequency measurement in a silicon chip", Optica **2**, 751 (2015) (cit. on pp. 127, 131, 133).

[518]M. Estevez, M. Alvarez, and L. Lechuga, "Integrated optical devices for lab-on-a-chip biosensing applications", Laser Photon. Rev. **6**, 463–487 (2012) (cit. on p. 127).

[519]B. Morrison, Y. Zhang, M. Pagani, B. Eggleton, and D. Marpaung, "Four-wave mixing and nonlinear losses in thick silicon waveguides", Opt. Lett. **41**, 2418 (2016) (cit. on p. 127).

[520]O. Boyraz, T. Indukuri, and B. Jalali, "Self-phase-modulation induced spectral broadening in silicon waveguides.", Opt. Express **12**, 829–834 (2004) (cit. on pp. 127, 128).

[521]J. B. Driscoll, R. R. Grote, X. Liu, J. I. Dadap, N. C. Panoiu, and R. M. Osgood, "Directionally anisotropic Si nanowires: on-chip nonlinear grating devices in uniform waveguides.", Opt. Lett. **36**, 1416–8 (2011) (cit. on p. 130).

[522]J. S. Levy, A. Gondarenko, M. A. Foster, A. C. Turner-Foster, A. L. Gaeta, and M. Lipson, "CMOS-compatible multiple-wavelength oscillator for on-chip optical interconnects", Nat. Photonics **4**, 37–40 (2010) (cit. on p. 130).

[523] C. J. Krückel, V. Torres-Company, P. A. Andrekson, D. T. Spencer, J. F. Bauters, M. J. R. Heck, and J. E. Bowers, “Continuous wave-pumped wavelength conversion in low-loss silicon nitride waveguides”, Opt. Lett. **40**, 875 (2015) (cit. on pp. 130, 131).

[524] M. Ferrera, L. Razzari, D. Duchesne, R. Morandotti, Z. Yang, M. Liscidini, J. E. Sipe, S. Chu, B. E. Little, and D. J. Moss, “Low-power continuous-wave nonlinear optics in doped silica glass integrated waveguide structures”, Nat. Photonics **2**, 737–740 (2008) (cit. on p. 130).

[525] A. Biberman, B. G. Lee, A. C. Turner-Foster, M. a. Foster, M. Lipson, A. L. Gaeta, and K. Bergman, “Wavelength multicasting in silicon photonic nanowires.”, Opt. Express **18**, 18047–18055 (2010) (cit. on pp. 131, 134).

[526] Q. Lin, O. J. Painter, and G. P. Agrawal, “Nonlinear optical phenomena in silicon waveguides: modeling and applications.”, Opt. Express **15**, 16604–16644 (2007) (cit. on pp. 131, 132).

[527] A. C. Peacock, P. Mehta, P. Horak, and N. Healy, “Nonlinear pulse dynamics in multimode silicon core optical fibers.”, Opt. Lett. **37**, 3351–3 (2012) (cit. on p. 131).

[528] M. Asghari and A. V. Krishnamoorthy, “Silicon photonics: Energy-efficient communication”, Nat. Photonics **5**, 268–270 (2011) (cit. on p. 131).

[529] Q. Lin, J. Zhang, P. M. Fauchet, and G. P. Agrawal, “Ultrabroadband parametric generation and wavelength conversion in silicon waveguides.”, Opt. Express **14**, 4786–4799 (2006) (cit. on p. 131).

[530] H. Rong, A. Liu, R. Nicolaescu, M. Paniccia, O. Cohen, and D. Hak, “Raman gain and nonlinear optical absorption measurements in a low-loss silicon waveguide”, Appl. Phys. Lett. **85**, 2196 (2004) (cit. on p. 133).

[531] D. Dimitropoulos, R. Jhaveri, R. Claps, J. C. S. Woo, and B. Jalali, “Lifetime of photogenerated carriers in silicon-on-insulator rib waveguides”, Appl. Phys. Lett. **86**, 071115 (2005) (cit. on p. 133).

[532] L. Jia, M. Geng, L. Zhang, L. Yang, P. Chen, Y. Liu, Q. Fang, and M. Yu, “Effects of waveguide length and pump power on the efficiency of wavelength conversion in silicon nanowire waveguides.”, Opt. Lett. **34**, 3502–3504 (2009) (cit. on pp. 133, 164).

[533] Y. S. Mamdem, E. Burov, L.-A. de Montmorillon, Y. Jaouën, G. Moreau, R. Gabet, and F. Taillade, “Importance of residual stresses in the Brillouin gain spectrum of single mode optical fibers”, Opt. Express **20**, 1790 (2012) (cit. on p. 134).

[534] W. Ye, D.-X. Xu, S. Janz, P. Cheben, M.-J. Picard, B. Lamontagne, and N. Tarr, “Birefringence control using stress engineering in silicon-on-insulator (SOI) waveguides”, J. Light. Technol. **23**, 1308–1318 (2005) (cit. on p. 134).

[535] D.-X. Xu, P. Cheben, D. Dalacu, A. Delâge, S. Janz, B. Lamontagne, M.-J. Picard, and W. N. Ye, “Eliminating the birefringence in silicon-on-insulator ridge waveguides by use of cladding stress”, Opt. Lett. **29**, 2384 (2004) (cit. on p. 134).

[536] J. Capmany, B. Ortega, and D. Pastor, “A tutorial on microwave photonic filters”, J. Light. Technol. **24**, 201–229 (2006) (cit. on pp. 137, 144, 145).

[537] J. Capmany, J. Mora, I. Gasulla, J. Sancho, J. Lloret, and S. Sales, “Microwave Photonic Signal Processing”, J. Light. Technol. **31**, 571–586 (2013) (cit. on pp. 137, 159).

[538] A. Seeds, “Microwave photonics”, IEEE Trans. Microw. Theory Tech. **50**, 877–887 (2002) (cit. on p. 137).

[539] A. J. Seeds and K. J. Williams, “Microwave Photonics”, J. Light. Technol. **24**, 4628–4641 (2006) (cit. on p. 137).

[540] J. Capmany and D. Novak, “Microwave photonics combines two worlds”, Nat. Photonics **1**, 319–330 (2007) (cit. on p. 137).

[541] J. Yao, “Microwave Photonics”, J. Light. Technol. **27**, 314–335 (2009) (cit. on p. 137).

[542] T. Berceli and P. R. Herczfeld, “Microwave Photonics-A Historical Perspective”, IEEE Trans. Microw. Theory Tech. **58**, 2992–3000 (2010) (cit. on pp. 137, 142).

[543]A. J. Seeds, H. Shams, M. J. Fice, and C. C. Renaud, "TeraHertz photonics for wireless communications", J. Light. Technol. **33**, 579–587 (2015) (cit. on p. 137).

[544]C. H. Cox, E. I. Ackerman, G. E. Betts, and J. L. Prince, "Limits on the performance of RF-over-fiber links and their impact on device design", IEEE Trans. Microw. Theory Tech. **54**, 906–920 (2006) (cit. on pp. 137, 150, 159).

[545]D. A. Marpaung, "High dynamic range analog photonic links : design and implementation", (2009) 10.3990/1.9789036528603 (cit. on pp. 137, 142).

[546]G. Smith, D. Novak, and Z. Ahmed, "Technique for optical SSB generation to overcome dispersion penalties in fibre-radio systems", Electron. Lett. **33**, 74 (1997) (cit. on p. 142).

[547]K. Jackson, S. Newton, B. Moslehi, M. Tur, C. Cutler, J. Goodman, and H. Shaw, "Optical Fiber Delay-Line Signal Processing", IEEE Trans. Microw. Theory Tech. **33**, 193–210 (1985) (cit. on p. 142).

[548]R. Hernandez, A. Loayssa, and D. Benito, "Optical vector network analysis based on single-sideband modulation", Opt. Eng. **43**, 2418 (2004) (cit. on p. 143).

[549]J. E. Román, M. Y. Frankel, and R. D. Esman, "Spectral characterization of fiber gratings with high resolution", Opt. Lett. **23**, 939 (1998) (cit. on p. 143).

[550]M. Xue, Y. Zhao, X. Gu, and S. Pan, "Performance analysis of optical vector analyzer based on optical single-sideband modulation", J. Opt. Soc. Am. B **30**, 928 (2013) (cit. on p. 143).

[551]M. Xue, S. Pan, and Y. Zhao, "Accurate optical vector network analyzer based on optical single-sideband modulation and balanced photodetection", Opt. Lett. **40**, 569 (2015) (cit. on p. 143).

[552]L. Zhuang, C. G. H. Roeloffzen, M. Hoekman, K.-J. Boller, and A. J. Lowery, "Programmable photonic signal processor chip for radiofrequency applications", Optica **2**, 854 (2015) (cit. on pp. 144, 179, 180).

[553]L. R. Chen, "Silicon Photonics for Microwave Photonics Applications", J. Light. Technol. **35**, 824–835 (2017) (cit. on p. 144).

[554]L. R. Chen, J. Li, M. Spasojevic, and R. Adams, "Nanowires and sidewall Bragg gratings in silicon as enabling technologies for microwave photonic filters.", Opt. Express **21**, 19624–33 (2013) (cit. on p. 144).

[555]X. Xue and A. M. Weiner, "Microwave photonics connected with microresonator frequency combs", Front. Optoelectron. **9**, 238–248 (2016) (cit. on p. 144).

[556]D. Cabric, I. O'Donnell, M.-W. Chen, and R. Brodersen, "Spectrum sharing radios", IEEE Circuits Syst. Mag. **6**, 30–45 (2006) (cit. on p. 144).

[557]Beibei Wang and K. J. R. Liu, "Advances in cognitive radio networks: A survey", IEEE J. Sel. Top. Signal Process. **5**, 5–23 (2011) (cit. on p. 144).

[558]Y.-R. Chien, "Design of GPS Anti-Jamming Systems Using Adaptive Notch Filters", IEEE Syst. J. **9**, 451–460 (2015) (cit. on p. 144).

[559]G. Aiello and G. Rogerson, "Ultra-Wideband Wireless Systems", IEEE Microw. Mag. **4**, 36–47 (2003) (cit. on p. 144).

[560]T. Snow, J. Lee, and W. J. Chappell, "Tunable high quality-factor absorptive bandstop filter design", in 2012 ieee/mtt-s int. microw. symp. dig. (2012), pp. 1–3 (cit. on pp. 144, 158, 159, 172).

[561]J. Lee, T. C. Lee, and W. J. Chappell, "Lumped-Element Realization of Absorptive Bandstop Filter With Anomalously High Spectral Isolation", IEEE Trans. Microw. Theory Tech. **60**, 2424–2430 (2012) (cit. on pp. 144, 172).

[562]B. Kim, J. Lee, J. Lee, B. Jung, and W. J. Chappell, "RF CMOS Integrated On-Chip Tunable Absorptive Bandstop Filter Using Q-Tunable Resonators", IEEE Trans. Electron Devices **60**, 1730–1737 (2013) (cit. on pp. 144, 158, 159, 172).

[563]R. Minasian, K. Alameh, and E. Chan, "Photonics-based interference mitigation filters", IEEE Trans. Microw. Theory Tech. **49**, 1894–1899 (2001) (cit. on pp. 144, 145).

[564]J. Sancho, J. Bourderionnet, J. Lloret, S. Combrié, I. Gasulla, S. Xavier, S. Sales, P. Colman, G. Lehoucq, D. Dolfi, J. Capmany, and A. De Rossi, "Integrable microwave filter based on a photonic crystal delay line", Nat. Commun. **3**, 1075 (2012) (cit. on pp. 144, 145, 159).

[565]V. R. Supradeepa, C. M. Long, R. Wu, F. Ferdous, E. Hamidi, D. E. Leaird, and A. M. Weiner, "Comb-based radiofrequency photonic filters with rapid tunability and high selectivity", Nat. Photonics **6**, 186–194 (2012) (cit. on pp. 144, 159).

[566]M. Rasras, Kun-Yii Tu, D. Gill, Young-Kai Chen, A. White, S. Patel, A. Pomerene, D. Carothers, J. Beattie, M. Beals, J. Michel, and L. Kimerling, "Demonstration of a Tunable Microwave-Photonic Notch Filter Using Low-Loss Silicon Ring Resonators", J. Light. Technol. **27**, 2105–2110 (2009) (cit. on pp. 144, 145, 159).

[567]Jianji Dong, Li Liu, Dingshan Gao, Yuan Yu, Aoling Zheng, Ting Yang, and Xinliang Zhang, "Compact Notch Microwave Photonic Filters Using On-Chip Integrated Microring Resonators", IEEE Photonics J. **5**, 5500307–5500307 (2013) (cit. on pp. 144, 145, 159).

[568]A. A. Savchenkov, W. Liang, A. B. Matsko, V. S. Ilchenko, D. Seidel, and L. Maleki, "Narrowband tunable photonic notch filter", Opt. Lett. **34**, 1318 (2009) (cit. on pp. 144, 145).

[569]X. Yao, "Brillouin selective sideband amplification of microwave photonic signals", IEEE Photonics Technol. Lett. **10**, 138–140 (1998) (cit. on p. 145).

[570]A. Loayssa and F. Lahoz, "Broad-band RF photonic phase shifter based on stimulated Brillouin scattering and single-sideband modulation", IEEE Photonics Technol. Lett. **18**, 208–210 (2006) (cit. on pp. 145, 152).

[571]Y. Okawachi, M. S. Bigelow, J. E. Sharping, Z. Zhu, A. Schweinsberg, D. J. Gauthier, R. W. Boyd, and A. L. Gaeta, "Tunable All-Optical Delays via Brillouin Slow Light in an Optical Fiber", Phys. Rev. Lett. **94**, 153902 (2005) (cit. on p. 145).

[572]K. Y. Song, M. G. Herraez, and L. Thevenaz, "Observation of pulse delaying and advancement in optical fibers using stimulated Brillouin scattering", Opt. Express **13**, 82 (2005) (cit. on p. 145).

[573]S. Chin, L. Thévenaz, J. Sancho, S. Sales, J. Capmany, P. Berger, J. Bourderionnet, and D. Dolfi, "Broadband true time delay for microwave signal processing, using slow light based on stimulated Brillouin scattering in optical fibers.", Opt. Express **18**, 22599–613 (2010) (cit. on p. 145).

[574]W. Zhang and R. A. Minasian, "Widely Tunable Single-Passband Microwave Photonic Filter Based on Stimulated Brillouin Scattering", IEEE Photonics Technol. Lett. **23**, 1775–1777 (2011) (cit. on pp. 145, 152).

[575]J. Lloret, J. Sancho, M. Pu, I. Gasulla, K. Yvind, S. Sales, and J. Capmany, "Tunable complex-valued multi-tap microwave photonic filter based on single silicon-on-insulator microring resonator.", Opt. Express **19**, 12402–12407 (2011) (cit. on p. 145).

[576]M. Burla, D. Marpaung, L. Zhuang, C. Roeloffzen, M. R. Khan, A. Leinse, M. Hoekman, and R. Heideman, "On-chip CMOS compatible reconfigurable optical delay line with separate carrier tuning for microwave photonic signal processing", Opt. Express **19**, 21475 (2011) (cit. on pp. 145, 171, 174).

[577]B. Morrison, D. Marpaung, R. Pant, E. Li, D.-Y. Choi, S. Madden, B. Luther-Davies, and B. J. Eggleton, "Tunable microwave photonic notch filter using on-chip stimulated Brillouin scattering", Opt. Commun. **313**, 85–89 (2014) (cit. on p. 145).

[578]J. E. McElhenny, R. Pattnaik, and J. Toulouse, "Polarization dependence of stimulated Brillouin scattering in small-core photonic crystal fibers", J. Opt. Soc. Am. B **25**, 2107 (2008) (cit. on p. 147).

[579]H. W. Bode, *Wave filter*, 1936 (cit. on p. 151).

[580]D. Jachowski, "Passive enhancement of resonator Q in microwave notch filters", in 2004 ieee mtt-s int. microw. symp. dig. Vol. 3 (2004), pp. 1315–1318 (cit. on p. 151).

[581]D. Marpaung, M. Pagani, B. Morrison, and B. J. Eggleton, "Nonlinear Integrated Microwave Photonics", J. Light. Technol. **32**, 3421–3427 (2014) (cit. on pp. 152, 165).

[582]E. H. W. Chan, W. Zhang, and R. a. Minasian, "Photonic RF Phase Shifter Based on Optical Carrier and RF Modulation Sidebands Amplitude and Phase Control", J. Light. Technol. **30**, 3672–3678 (2012) (cit. on pp. 152, 172).

[583]D. Marpaung, B. Morrison, M. Pagani, R. Pant, and B. J. Eggleton, "Ultra-high suppression microwave photonic bandstop filters", Chinese Sci. Bull. **59**, 2684–2692 (2014) (cit. on p. 152).

[584]P. Ghelfi, F. Laghezza, F. Scotti, G. Serafino, A. Capria, S. Pinna, D. Onori, C. Porzi, M. Scaffardi, A. Malacarne, V. Vercesi, E. Lazzeri, F. Berizzi, and A. Bogoni, "A fully photonics-based coherent radar system", Nature **507**, 341–345 (2014) (cit. on p. 153).

[585]S. Koenig, D. Lopez-Diaz, J. Antes, F. Boes, R. Henneberger, A. Leuther, A. Tessmann, R. Schmogrow, D. Hillerkuss, R. Palmer, T. Zwick, C. Koos, W. Freude, O. Ambacher, J. Leuthold, and I. Kallfass, "Wireless sub-THz communication system with high data rate", Nat. Photonics **7**, 977–981 (2013) (cit. on p. 153).

[586]D. Marpaung, B. Morrison, R. Pant, C. Roeloffzen, A. Leinse, M. Hoekman, R. Heideman, and B. J. Eggleton, "Si3N4 ring resonator-based microwave photonic notch filter with an ultrahigh peak rejection", Opt. Express **21**, 23286 (2013) (cit. on pp. 159, 169).

[587]E. J. Naglich, A. C. Guyette, and D. Peroulis, "High-Q intrinsically-switched quasi-absorptive tunable bandstop filter with electrically-short resonators", in 2014 ieee mtt-s int. microw. symp. (2014), pp. 1–4 (cit. on p. 159).

[588]I. Reines, Sang-June Park, and G. M. Rebeiz, "Compact Low-Loss Tunable X-Band Bandstop Filter With Miniature RF-MEMS Switches", IEEE Trans. Microw. Theory Tech. **58**, 1887–1895 (2010) (cit. on pp. 158, 159).

[589]D. Jachowski, "Compact, frequency-agile, absorptive bandstop filters", in Ieee mtt-s int. microw. symp. dig. 2005. Vol. 2005, C (2005), pp. 513–516 (cit. on p. 158).

[590]E. I. Ackerman, G. E. Betts, W. K. Burns, J. C. Campbell, C. H. Cox, N. Duan, J. L. Prince, M. D. Regan, and H. V. Roussell, "Signal-to-Noise Performance of Two Analog Photonic Links Using Different Noise Reduction Techniques", in 2007 ieee/mtt-s int. microw. symp. (2007), pp. 51–54 (cit. on p. 159).

[591]D. Marpaung, C. Roeloffzen, A. Leinse, and M. Hoekman, "A photonic chip based frequency discriminator for a high performance microwave photonic link", Opt. Express **18**, 27359 (2010) (cit. on p. 159).

[592]S. Shahnia, M. Pagani, B. Morrison, B. J. Eggleton, and D. Marpaung, "Independent manipulation of the phase and amplitude of optical sidebands in a highly-stable RF photonic filter", Opt. Express **23**, 23278 (2015) (cit. on p. 160).

[593]W. Zhang and R. a. Minasian, "Switchable and Tunable Microwave Photonic Brillouin-Based Filter", IEEE Photonics J. **4**, 1443–1455 (2012) (cit. on p. 160).

[594]A. L. A. Liu, H. R. H. Rong, R. Jones, O. Cohen, D. Hak, and M. Paniccia, "Optical amplification and lasing by stimulated Raman scattering in silicon waveguides", J. Light. Technol. **24**, 1440–1455 (2006) (cit. on p. 163).

[595]V. Raghunathan, R. Claps, D. Dimitropoulos, and B. Jalali, "Parametric Raman wavelength conversion in scaled silicon waveguides", J. Light. Technol. **23**, 2094–2102 (2005) (cit. on p. 163).

[596]Y. Zhang, C. Husko, J. Schröder, and B. J. Eggleton, "Pulse evolution and phase-sensitive amplification in silicon waveguides", Opt. Lett. **39**, 5329 (2014) (cit. on p. 163).

[597]X. Bao and L. Chen, "Recent Progress in Brillouin Scattering Based Fiber Sensors", Sensors **11**, 4152–4187 (2011) (cit. on p. 164).

[598]M. Damzen, V. Vlad, V. Babin, and A. Mocofanescu, *Stimulated Brillouin Scattering*, Vol. 20034312 (2003) (cit. on p. 164).

[599]M. Lee, R. Pant, and M. a. Neifeld, "Improved slow-light delay performance of a broadband stimulated Brillouin scattering system using fiber Bragg gratings", Appl. Opt. **47**, 6404 (2008) (cit. on p. 164).

[600]Y. Li, Q. Li, Y. Liu, T. Baehr-Jones, M. Hochberg, and K. Bergman, "Integrated on-chip C-band optical spectrum analyzer using dual-ring resonators", in Cleo 2015 (2015), SM1I.4 (cit. on p. 164).

[601]F. Van Laere, T. Claes, J. Schrauwen, S. Scheerlinck, W. Bogaerts, D. Taillaert, L. O'Faolain, D. Van Thourhout, and R. Baets, "Compact Focusing Grating Couplers for Silicon-on-Insulator Integrated Circuits", IEEE Photonics Technol. Lett. **19**, 1919–1921 (2007) (cit. on p. 166).

[602]C. Madsen, G. Lenz, A. Bruce, M. Cappuzzo, L. Gomez, and R. Scotti, "Integrated all-pass filters for tunable dispersion and dispersion slope compensation", IEEE Photonics Technol. Lett. **11**, 1623–1625 (1999) (cit. on p. 169).

[603]N. C. Harris, Y. Ma, J. Mower, T. Baehr-Jones, D. Englund, M. Hochberg, and C. Galland, "Efficient, compact and low loss thermo-optic phase shifter in silicon", Opt. Express **22**, 10487 (2014) (cit. on p. 169).

[604]J. Van Campenhout, W. M. Green, S. Assefa, and Y. A. Vlasov, "Low-power, 2×2 silicon electro-optic switch with 110-nm bandwidth for broadband reconfigurable optical networks", Opt. Express **17**, 24020 (2009) (cit. on p. 169).

[605]G. Lenz, B. Eggleton, C. Madsen, C. Giles, and G. Nykolak, "Optimal dispersion of optical filters for WDM systems", IEEE Photonics Technol. Lett. **10**, 567–569 (1998) (cit. on p. 169).

[606]L. Zhuang, D. Marpaung, M. Burla, W. Beeker, A. Leinse, and C. Roeloffzen, "Low-loss, high-index-contrast Si_3N_4/SiO_2 optical waveguides for optical delay lines in microwave photonics signal processing", Opt. Express **19**, 23162 (2011) (cit. on p. 171).

[607]M. H. P. Pfeiffer, J. Liu, A. S. Raja, T. Morais, B. Ghadiani, and T. J. Kippenberg, "Ultra-smooth silicon nitride waveguides based on the Damascene reflow process: fabrication and loss origins", Optica **5**, 884 (2018) (cit. on p. 175).

[608]K. Y. Yang, D. Y. Oh, S. H. Lee, Q.-F. Yang, X. Yi, B. Shen, H. Wang, and K. Vahala, "Bridging ultrahigh-Q devices and photonic circuits", Nat. Photonics **12**, 297–302 (2018) (cit. on p. 175).

[609]T. Carmon, L. Yang, and K. J. Vahala, "Dynamical thermal behavior and thermal self-stability of microcavities", Opt. Express **12**, 4742 (2004) (cit. on p. 175).

[610]Q. Xu and M. Lipson, "Carrier-induced optical bistability in silicon ring resonators", Opt. Lett. **31**, 341 (2006) (cit. on p. 176).

[611]T. J. Johnson, M. Borselli, and O. Painter, "Self-induced optical modulation of the transmission through a high-Q silicon microdisk resonator", Opt. Express **14**, 817 (2006) (cit. on p. 176).

[612]G. Qin, T. Suzuki, and Y. Ohishi, "Power dependence of Brillouin linewidths in a silica fiber", Opt. Lett. **32**, 3155 (2007) (cit. on p. 176).

[613]A. Choudhary, Y. Liu, D. Marpaung, and B. J. Eggleton, "Brillouin Filtering with Enhanced Noise Performance and Linearity Using Anti-Stokes Interactions", in Conf. lasers electro-optics (2018), STu4F.2 (cit. on p. 176).

[614]Y. Liu, D. Marpaung, A. Choudhary, and B. J. Eggleton, "Lossless and high-resolution RF photonic notch filter", Opt. Lett. **41**, 5306 (2016) (cit. on pp. 176, 180).

[615]S. R. Mirnaziry, C. Wolff, M. J. Steel, B. J. Eggleton, and C. G. Poulton, "Stimulated Brillouin scattering in silicon/chalcogenide slot waveguides", Opt. Express **24**, 4786 (2016) (cit. on p. 178).

[616]N. C. Harris, D. Bunandar, M. Pant, G. R. Steinbrecher, J. Mower, M. Prabhu, T. Baehr-Jones, M. Hochberg, and D. Englund, "Large-scale quantum photonic circuits in silicon", Nanophotonics **5**, 456–468 (2016) (cit. on p. 179).

[617]N. C. Harris, G. R. Steinbrecher, M. Prabhu, Y. Lahini, J. Mower, D. Bunandar, C. Chen, F. N. C. Wong, T. Baehr-Jones, M. Hochberg, S. Lloyd, and D. Englund, "Quantum transport simulations in a programmable nanophotonic processor", Nat. Photonics **11**, 447–452 (2017) (cit. on p. 179).

[618]J. Carolan, C. Harrold, C. Sparrow, E. Martin-Lopez, N. J. Russell, J. W. Silverstone, P. J. Shadbolt, N. Matsuda, M. Oguma, M. Itoh, G. D. Marshall, M. G. Thompson, J. C. F. Matthews, T. Hashimoto, J. L. O'Brien, and A. Laing, "Universal linear optics", Science **349**, 711–716 (2015) (cit. on p. 179).

[619]D. Pérez, I. Gasulla, and J. Capmany, "Software-defined reconfigurable microwave photonics processor", Opt. Express **23**, 14640 (2015) (cit. on p. 179).

[620]E. J. Norberg, R. S. Guzzon, J. S. Parker, L. A. Johansson, and L. A. Coldren, "Programmable Photonic Microwave Filters Monolithically Integrated in InP–InGaAsP", J. Light. Technol. **29**, 1611–1619 (2011) (cit. on p. 179).

[621]D. a. B. Miller, "All linear optical devices are mode converters", Opt. Express **20**, 23985 (2012) (cit. on p. 179).

[622]D. A. B. Miller, "Perfect optics with imperfect components", Optica **2**, 747 (2015) (cit. on p. 180).

[623]D. Pérez, I. Gasulla, J. Capmany, and R. A. Soref, "Reconfigurable lattice mesh designs for programmable photonic processors", Opt. Express **24**, 12093 (2016) (cit. on p. 180).

[624]D. Pérez, I. Gasulla, L. Crudgington, D. J. Thomson, A. Z. Khokhar, K. Li, W. Cao, G. Z. Mashanovich, and J. Capmany, "Multipurpose silicon photonics signal processor core", Nat. Commun. **8**, 636 (2017) (cit. on p. 180).

[625]Y. Stern, K. Zhong, T. Schneider, R. Zhang, Y. Ben-Ezra, M. Tur, and A. Zadok, "Tunable sharp and highly selective microwave-photonic band-pass filters based on stimulated Brillouin scattering", Photonics Res. **2**, B18 (2014) (cit. on p. 180).

[626]W. Wei, L. Yi, Y. Jaouën, and W. Hu, "Software-defined microwave photonic filter with high reconfigurable resolution", Sci. Rep. **6**, 35621 (2016) (cit. on p. 180).

[627]I. Aryanfar, A. Choudhary, S. Shahnia, M. Pagani, Y. Liu, D. Marpaung, and B. J. Eggleton, "Signal interference RF photonic bandstop filter", Opt. Express **24**, 14995 (2016) (cit. on p. 180).

[628]I. C. Chang, "Selection Of Materials For Acousto-Optic Devices", Opt. Eng. **24**, 297–299 (1985) (cit. on p. 181).

[629]T. Wang, X. Gai, W. Wei, R. Wang, Z. Yang, X. Shen, S. Madden, and B. Luther-Davies, "Systematic z-scan measurements of the third order nonlinearity of chalcogenide glasses", Opt. Mater. Express **4**, 1011 (2014) (cit. on p. 181).

[630]M. Olivier, J. C. Tchahame, P. Nemec, M. Chauvet, V. Besse, C. Cassagne, G. Boudebs, G. Renversez, R. Boidin, E. Baudet, and V. Nazabal, "Structure, nonlinear properties, and photosensitivity of (GeSe2)(100-x)(Sb2Se3)(x) glasses", Opt. Mater. Express **4**, 525–540 (2014) (cit. on p. 181).

[631]S. Dai, F. Chen, Y. Xu, Z. Xu, X. Shen, T. Xu, R. P. Wang, and W. Ji, "Mid-infrared optical nonlinearities of chalcogenide glasses in Ge-Sb-Se ternary system", Opt. Express **23**, 1300 (2015) (cit. on p. 181).

[632]M. Zhang, Z. Yang, L. Li, Y. Wang, J. Qiu, A. Yang, H. Tao, and D. Tang, "The effects of germanium addition on properties of Ga-Sb-S chalcogenide glasses", J. Non. Cryst. Solids **452**, 114–118 (2016) (cit. on p. 181).

[633]Q. Du, Y. Huang, J. Li, D. Kita, J. Michon, H. Lin, L. Li, S. Novak, K. Richardson, W. Zhang, and J. Hu, "Low-loss photonic device in Ge-Sb-S chalcogenide glass", Opt. Lett. **41**, 3090 (2016) (cit. on p. 181).

[634]J. Chiles, M. Malinowski, A. Rao, S. Novak, K. Richardson, and S. Fathpour, "Low-loss, submicron chalcogenide integrated photonics with chlorine plasma etching", Appl. Phys. Lett. **106**, 111110 (2015) (cit. on p. 181).

[635]J. Hu, V. Tarasov, N. Carlie, N.-N. Feng, L. Petit, A. Agarwal, K. Richardson, and L. Kimerling, "Si-CMOS-compatible lift-off fabrication of low-loss planar chalcogenide waveguides", Opt. Express **15**, 11798 (2007) (cit. on p. 181).

[636]J. W. Choi, Z. Han, B.-u. Sohn, G. F. R. Chen, C. Smith, L. C. Kimerling, K. A. Richardson, A. M. Agarwal, and D. T. H. Tan, "Nonlinear characterization of GeSbS chalcogenide glass waveguides", Sci. Rep. **6**, 39234 (2016) (cit. on p. 181).

[637]L. Li, H. Lin, S. Qiao, Y. Zou, S. Danto, K. Richardson, J. D. Musgraves, N. Lu, and J. Hu, "Integrated flexible chalcogenide glass photonic devices", Nat. Photonics **8**, 643–649 (2014) (cit. on p. 181).

[638]H. Lin, Y. Song, Y. Huang, D. Kita, K. Wang, L. Li, J. Li, H. Zheng, S. Novak, C.-c. Huang, D. Hewak, K. Richardson, J. Kong, and J. Hu, "Chalcogenide Glass-on-Graphene Photonics", 5–6 (2017) (cit. on p. 181).

[639]P. P. Shtets, V. I. Fedelesh, V. M. Kabatsij, V. I. Malesh, I. I. Shpak, and A. A. Gorvat, "Structure, dielectric and photoelastic properties of glasses in the system Ge-Sb-S", J. Optoelectron. Adv. Mater. **3**, 937–940 (2001) (cit. on p. 181).

[640]J. Galbraith, J. Zwanziger, and B. Aitken, "Correlating structure with stress-optic response in non-oxide glasses", J. Non. Cryst. Solids **404**, 1–6 (2014) (cit. on p. 181).

[641]I. I. Shpak, R. M. Yevych, S. I. Perechinskii, É. M. Hryha, Z. P. Gad'mashi, D. I. Bletskan, Y. M. Vysochanskii, and V. Y. Slivka, "Rayleigh-Brillouin light scattering in chalcogenide glasses of the Ge-Sb-S system", Opt. Spectrosc. **98**, 411–414 (2005) (cit. on p. 181).

[642]I. I. Shpak, R. M. Yevych, A. I. Shpak, S. I. Perechinskiĭ, D. I. Bletskan, and Y. M. Vysochanskiĭ, "Rayleigh and Mandelstam–Brillouin Light Scattering in Chalcogenide Glasses of the (Sb2S3) x (GeS2)100–x System", J. Appl. Spectrosc. **84**, 567–572 (2017) (cit. on p. 181).

[643]M.-G. Suh, Q.-F. Yang, and K. J. Vahala, "Phonon-Limited-Linewidth of Brillouin Lasers at Cryogenic Temperatures", Phys. Rev. Lett. **119**, 143901 (2017) (cit. on pp. 182, 183, 185).

[644]K. C. Balram, M. Davanço, J. Y. Lim, J. D. Song, and K. Srinivasan, "Moving boundary and photoelastic coupling in GaAs optomechanical resonators: Supplementary", Optica **1**, 414 (2014) (cit. on p. 182).

[645]K. C. Balram, M. Davanco, J. D. Song, and K. Srinivasan, "Coherent coupling between radio frequency, optical, and acoustic waves in piezo-optomechanical circuits", Nat. Photonics **10**, 1–20 (2015) (cit. on p. 182).

[646]K. C. Balram, M. I. Davanço, B. R. Ilic, J. H. Kyhm, J. D. Song, and K. Srinivasan, "Acousto-Optic Modulation and Optoacoustic Gating in Piezo-Optomechanical Circuits", Phys. Rev. Appl. **7**, 1–9 (2017) (cit. on p. 182).

[647]C. P. Dietrich, A. Fiore, M. G. Thompson, M. Kamp, and S. Höfling, "GaAs integrated quantum photonics: Towards compact and multi-functional quantum photonic integrated circuits", Laser Photon. Rev. **10**, 870–894 (2016) (cit. on p. 182).

[648]K. Dolgaleva, W. C. Ng, L. Qian, and J. S. Aitchison, "Compact highly-nonlinear AlGaAs waveguides for efficient wavelength conversion", Opt. Express **19**, 12440 (2011) (cit. on p. 182).

[649]M. Pu, L. Ottaviano, E. Semenova, and K. Yvind, "Efficient frequency comb generation in AlGaAs-on-insulator", Optica **3**, 823 (2016) (cit. on p. 182).

[650]L. Zhang, A. M. Agarwal, L. C. Kimerling, and J. Michel, "Nonlinear Group IV photonics based on silicon and germanium: from near-infrared to mid-infrared", Nanophotonics **3**, 247–268 (2014) (cit. on p. 182).

[651]B. Kuyken, X. Liu, G. Roelkens, R. Baets, R. M. Osgood, Jr., and W. M. J. Green, "50 dB parametric on-chip gain in silicon photonic wires", Opt. Lett. **36**, 4401 (2011) (cit. on p. 182).

[652]R. Wang, A. Vasiliev, M. Muneeb, A. Malik, S. Sprengel, G. Boehm, M.-C. Amann, I. Šimonytė, A. Vizbaras, K. Vizbaras, R. Baets, and G. Roelkens, "III–V-on-Silicon Photonic Integrated Circuits for Spectroscopic Sensing in the 2–4 μm Wavelength Range", Sensors **17**, 1788 (2017) (cit. on p. 182).

[653]N. Li, Purnawirman, Z. Su, E. Salih Magden, P. T. Callahan, K. Shtyrkova, M. Xin, A. Ruocco, C. Baiocco, E. P. Ippen, F. X. Kärtner, J. D. B. Bradley, D. Vermeulen, and M. R. Watts, "High-power thulium lasers on a silicon photonics platform", Opt. Lett. **42**, 1181 (2017) (cit. on p. 182).

[654]C. Wolff, R. Soref, C. Poulton, and B. Eggleton, "Germanium as a material for stimulated Brillouin scattering in the mid-infrared", Opt. Express **22**, 30735 (2014) (cit. on p. 182).

[655]S. Gundavarapu, M. Puckett, T. Huffman, R. Behunin, J. Wu, T. Qiu, G. M. G. Brodnik, C. Pinho, D. Bose, P. T. P. Rakich, J. Nohava, K. K. D. Nelson, M. Salit, and D. D. J. Blumenthal, "Integrated Waveguide Brillouin Laser", ArXiv E-prints **1709.04512**, 1–15 (2017) (cit. on p. 183).

[656]K. Y. Yang, D. Y. Oh, S. H. Lee, Q.-F. Yang, X. Yi, and K. Vahala, "Integrated Ultra-High-Q Optical Resonator", ArXiv E-prints **1702.05076**, 1–8 (2017) (cit. on p. 183).

[657]P. P. Absil, P. Verheyen, P. De Heyn, M. Pantouvaki, G. Lepage, J. De Coster, and J. Van Campenhout, "Silicon photonics integrated circuits: a manufacturing platform for high density, low power optical I/O's", Opt. Express **23**, 9369 (2015) (cit. on p. 183).

[658]J. P. Epping, M. Hoekman, R. Mateman, A. Leinse, R. G. Heideman, A. van Rees, P. J. van der Slot, C. J. Lee, and K.-J. Boller, "High confinement, high yield Si_3N_4 waveguides for nonlinear optical applications", Opt. Express **23**, 642 (2015) (cit. on p. 184).

[659]M. Sodagar, R. Pourabolghasem, A. A. Eftekhar, and A. Adibi, "High-efficiency and wideband interlayer grating couplers in multilayer Si/SiO_2/SiN platform for 3D integration of optical functionalities", Opt. Express **22**, 16767 (2014) (cit. on p. 184).

[660]D. Pan, C. Ke, S. Fu, Y. Liu, D. Liu, and A. E. Willner, "All-optical spectral linewidth reduction of lasers for coherent optical communication", Opt. Lett. **38**, 5220 (2013) (cit. on p. 185).

[661]T. Komljenovic, S. Srinivasan, E. Norberg, M. Davenport, G. Fish, and J. E. Bowers, "Widely Tunable Narrow-Linewidth Monolithically Integrated External-Cavity Semiconductor Lasers", IEEE J. Sel. Top. Quantum Electron. **21**, 214–222 (2015) (cit. on p. 185).

[662]T. Komljenovic and J. E. Bowers, "Monolithically Integrated High-Q Rings for Narrow Linewidth Widely Tunable Lasers", IEEE J. Quantum Electron. **51**, 1–10 (2015) (cit. on p. 185).

[663]S. A. Miller, Y. Okawachi, S. Ramelow, K. Luke, A. Dutt, A. Farsi, A. L. Gaeta, and M. Lipson, "Tunable frequency combs based on dual microring resonators", Opt. Express **23**, 21527 (2015) (cit. on p. 185).

[664]Y. A. V. Espinel, F. G. S. Santos, G. O. Luiz, T. P. M. Alegre, and G. S. Wiederhecker, "Brillouin Optomechanics in Coupled Silicon Microcavities", Sci. Rep. **7**, 43423 (2017) (cit. on p. 185).

[665]L. A. M. Barea, F. Vallini, G. F. M. De Rezende, and N. C. Frateschi, "Spectral engineering with CMOS compatible SOI photonic molecules", IEEE Photonics J. **5** (2013) `10.1109/JPHOT.2013.2289977` (cit. on p. 185).

[666]G. Gao, D. Li, Y. Zhang, S. Yuan, A. Armghan, Q. Huang, Y. Wang, J. Yu, and J. Xia, "Tuning of resonance spacing over whole free spectral range based on Autler-Townes splitting in a single microring resonator", Opt. Express **23**, 26895 (2015) (cit. on p. 185).

[667]B. Peng, Ş. K. Özdemir, W. Chen, F. Nori, and L. Yang, "What is and what is not electromagnetically induced transparency in whispering-gallery microcavities", Nat. Commun. **5**, 5082 (2014) (cit. on p. 185).

[668]S. Preussler, A. Wiatrek, K. Jamshidi, and T. Schneider, "Ultrahigh-resolution spectroscopy based on the bandwidth reduction of stimulated brillouin scattering", IEEE Photonics Technol. Lett. **23**, 1118–1120 (2011) (cit. on p. 185).

[669] S. Preussler, A. Zadok, A. Wiatrek, M. Tur, and T. Schneider, "Enhancement of spectral resolution and optical rejection ratio of Brillouin optical spectral analysis using polarization pulling", Opt. Express **20**, 14734 (2012) (cit. on p. 185).

[670] A. Villafranca, J. Lasobras, R. Alonso, F. Lopez, and I. Garces, "Complex Spectrum Analysis of Modulated Optical Signals Using Stimulated Brillouin Scattering", IEEE Photonics Technol. Lett. **20**, 1938–1940 (2008) (cit. on p. 185).

[671] D. Dai, J. Wang, and Y. Shi, "Silicon mode (de)multiplexer enabling high capacity photonic networks-on-chip with a single-wavelength-carrier light", Opt. Lett. **38**, 1422 (2013) (cit. on p. 185).

[672] N. T. Otterstrom, R. O. Behunin, E. A. Kittlaus, Z. Wang, and P. T. Rakich, "A silicon Brillouin laser", (2017) (cit. on p. 185).

[673] Jae Chul Yong, L. Thevenaz, and Byoung Yoon Kim, "Brillouin fiber laser pumped by a DFB laser diode", J. Light. Technol. **21**, 546–554 (2003) (cit. on p. 185).

[674] K. P. Huy, J.-C. Beugnot, J.-C. Tchahame, and T. Sylvestre, "Strong coupling between phonons and optical beating in backward Brillouin scattering", Phys. Rev. A **94**, 043847 (2016) (cit. on p. 186).

[675] L. Rayleigh, "XVIII. On the passage of electric waves through tubes, or the vibrations of dielectric cylinders", Philos. Mag. Ser. 5 **43**, 125–132 (1897) (cit. on p. 190).

[676] A. Sommerfeld, "Ueber die Fortpflanzung elektrodynamischer Wellen längs eines Drahtes", Ann. der Phys. und Chemie **303**, 233–290 (1899) (cit. on p. 190).

[677] D. Hondros and P. Debye, "Elektromagnetische Wellen an dielektrischen Drähten", Ann. Phys. **337**, 465–476 (1910) (cit. on p. 190).

[678] D. Emerson, "The work of Jagadis Chandra Bose: 100 years of millimeter-wave research", IEEE Trans. Microw. Theory Tech. **45**, 2267–2273 (1997) (cit. on p. 190).

[679] K. Packard, "The Origin of Waveguides: A Case of Multiple Rediscovery", IEEE Trans. Microw. Theory Tech. **32**, 961–969 (1984) (cit. on p. 190).

[680] G. C. Southworth, "Hyper-Frequency Wave Guides-General Considerations and Experimental Results", Bell Syst. Tech. J. **15**, 284–309 (1936) (cit. on p. 190).

[681] W. Barrow, "Transmission of Electromagnetic Waves in Hollow Tubes of Metal", Proc. IRE **24**, 1298–1328 (1936) (cit. on p. 190).

[682] J. R. Carson, S. P. Mead, and S. A. Schelkunoff, "Hyper-Frequency Wave Guides-Mathematical Theory", Bell Syst. Tech. J. **15**, 310–333 (1936) (cit. on p. 191).

[683] L. Chu and W. Barrow, "Electromagnetic Waves in Hollow Metal Tubes of Rectangular Cross Section", Proc. IRE **26**, 1520–1555 (1938) (cit. on p. 191).

[684] S. Schelkunoff, "Transmission Theory of Plane Electromagnetic Waves", Proc. IRE **25**, 1457–1492 (1937) (cit. on p. 191).

[685] H. H. HOPKINS and N. S. KAPANY, "A Flexible Fibrescope, using Static Scanning", Nature **173**, 39–41 (1954) (cit. on p. 191).

[686] A. C. S. VAN HEEL, "A New Method of transporting Optical Images without Aberrations", Nature **173**, 39–39 (1954) (cit. on p. 191).

[687] N. S. Kapany, "Fiber Optics. Part I. Optical Properties of Certain Dielectric Cylinders", J. Opt. Soc. Am. **47**, 413 (1957) (cit. on p. 191).

[688] N. S. KAPANY, "High-Resolution Fibre Optics Using Sub-Micron Multiple Fibres", Nature **184**, 881–883 (1959) (cit. on p. 191).

[689] N. S. Kapany and J. J. Burke, "Fiber Optics IX Waveguide Effects", J. Opt. Soc. Am. **51**, 1067 (1961) (cit. on p. 191).

[690] E. Snitzer and H. Osterberg, "Observed Dielectric Waveguide Modes in the Visible Spectrum", J. Opt. Soc. Am. **51**, 499–505 (1961) (cit. on p. 191).

[691] E. Snitzer, "Cylindrical Dielectric Waveguide Modes", J. Opt. Soc. Am. **51**, 491 (1961) (cit. on p. 191).

[692] R. Kaplan, "Optical waveguide of macroscopic dimensions in single-mode operation", Proc. IEEE **51**, 1144–1145 (1963) (cit. on p. 192).

[693] R. Flam and E. Schineller, "A single-mode waveguide laser", Proc. IEEE **56**, 195–196 (1968) (cit. on p. 192).

[694] D. Anderson and R. August, "Applications of microphotolithography to millimeter and infrared devices", Proc. IEEE **54**, 657–661 (1966) (cit. on p. 192).

[695] D. F. Nelson and F. K. Reinhart, "Light modulation by the electro-optic effect in reverse-biased GaP p-n junctions", Appl. Phys. Lett. **5**, 148–150 (1964) (cit. on p. 192).

[696] A. Yariv and R. C. C. Leite, "DIELECTRIC-WAVEGUIDE MODE OF LIGHT PROPAGATION IN p-n JUNCTIONS", Appl. Phys. Lett. **2**, 55–57 (1963) (cit. on p. 192).

[697] W. L. Bond, B. G. Cohen, R. C. C. Leite, and A. Yariv, "OBSERVATION OF THE DIELECTRIC-WAVEGUIDE MODE OF LIGHT PROPAGATION IN p-n JUNCTIONS", Appl. Phys. Lett. **2**, 57–59 (1963) (cit. on p. 192).

[698] A. Ashkin and M. Gershenzon, "Reflection and Guiding of Light at p-n Junctions", J. Appl. Phys. **34**, 2116–2119 (1963) (cit. on p. 192).

[699] E. A. J. Marcatili, "Bends in Optical Dielectric Guides", Bell Syst. Tech. J. **48**, 2103–2132 (1969) (cit. on pp. 193, 194).

[700] E. A. J. Marcatili, "Dielectric Rectangular Waveguide and Directional Coupler for Integrated Optics", Bell Syst. Tech. J. **48**, 2071–2102 (1969) (cit. on p. 193).

[701] J. E. Goell, "A Circular-Harmonic Computer Analysis of Rectangular Dielectric Waveguides", Bell Syst. Tech. J. **48**, 2133–2160 (1969) (cit. on pp. 193, 194).